A NUMERICAL AND EXPERIMENTAL STUDY OF INITIAL DEFIBRATION OF WOOD

STEFAN HOLMBERG

A NUMERICAL AND EXPERIMENTAL STUDY OF INITIAL DEFIBRATION OF WOOD

STEFAN HOLMBERG

To
Rebecka,
Karl and Jakob

Acknowledgements

Lund in September 1998

Stefan Holmberg

FORSKARSKOLAN
TRÄ OCH TRÄFIBER

Abstract

A major drawback of the defibration or refining process in manufacturing pulp is that of its large energy requirements. If the mechanics of the process were better understood, large amounts of energy could probably be saved. The initial defibration seems to be crucial for both the quality of the pulp and the total consumption of energy. Numerical simulations by means of the finite element method represent a powerful tool that can be used to analyse and simulate different defibration processes. The present study was undertaken with the aim of gaining more thorough knowledge both of suitable material modelling approaches for this type of simulation and of the mechanics of the initial defibration. Both experimental and numerical work is presented.

The experimental study involves three types of tests. The chip shearing tests serve to illustrate the complex behaviour of wood when loaded perpendicular to the grain under conditions resembling those present during refining. In particular, the influence of specimen orientation versus loading direction was investigated. The combined compression and shear tests, in turn, concern the behaviour of wood when loaded by both radial compression and shear. The tensile tests, finally, deal with the effect of the loading rate on fracture mechanical properties. The experiments show that the mechanical behaviour of wood loaded perpendicular to the grain is very complex and is characterized by the development of cracks and, in the case of earlywood subjected to compression, by large volumetric changes. It is also shown that the mechanical properties of earlywood are very different from those of latewood and that the specimen orientation versus loading direction has a strong effect on both the failure process and energy consumption. On the basis of the combined compression and shear tests, it could be concluded that the combined loading modes require about the same energy as pure compression does, although the cell collapse produced by the combined loading appears to be more well-defined than that obtained through pure compression. An increase in fracture energy was found as loading rates increased. A strong effect of moisture content on the mechanical properties of wood was also demonstrated.

When numerical analyses of initial defibration processes are to be performed, two main approaches may be applied in the modelling of the wooden material. One approach is to use continuum models based on smeared material properties. The other approach is to develop models of the cellular microstructure involving modelling of the individual fibres. Numerical simulations, related to initial defibration processes, using each of these two approaches, are presented in the thesis. The simulations were performed using the finite element method, taking both the nonlinear material behaviour and geometric nonlinearity into account.

The continuum modelling approach involves use of a foam plasticity model and a

fictitious crack model. The inhomogeneity of the material was taken into account by separating the earlywood from the latewood and also by assuming small variations in properties in the radial direction within the earlywood zone. Several simulations of the chip shearing tests and the combined compression and shear tests were carried out using this modelling approach. Close agreement between the simulations and the experiments was obtained. The effect of loading rate on the failure process and on energy consumption was investigated, loading rates of up to 50 m/s being considered. The effect of the knife design on wood cutting was also studied.

At the microstructural level, the consequences of making different constitutive assumptions for the cell wall material, ranging from the basic assumption of linear elasticity to more sophisticated approaches involving both plastic behavior and microcracking, were investigated. The effect of the ray cells and of friction within the cell lumens was also studied, results of the simulations and the experiments being compared.

Notations

Notations and symbols are explained in the text where they first appear. A list of main notations used is given below.

General notations

$\Delta(\ )$	incremental quantity
$d(\ )$	differential quantity
$\dot{(\ )}$	time differentiation of ( )
$\ddot{(\ )}$	second time differentiation of ( )
$\bar{(\ )}$	quantity referred to local system
$(\ )_n^i$	quantity at increment n and iteration i

Roman upper case letters

A	transformation matrix for stress and strain vectors
B	transformation matrix for crack elements
C	Jacobian matrix of constitutive model
D	rate of deformation tensor
D	material parameter defining strain rate dependence for foam plasticity model
E	modulus of elasticity
F	yield function
G	out of balance force vector
G	shear modulus
G_F	fracture energy
H_{fn}	ratio of normal softening stress at current loading rate to the stress at reference loading rate
H_{fs}	ratio of shear softening stress at current loading rate to the stress at reference loading rate
H_p	ratio of yield stress at nonzero strain rate to static yield stress
I	identity tensor
J	ratio of current to original volume
J^{el}	elastic part of the ratio of current to original volume
J^{pl}	plastic part of the ratio of current to original volume
K	tangent stiffness matrix

$\mathbf{K}_{load}$	load stiffness matrix
$\hat{\mathbf{K}}$	Jacobian matrix
$\mathbf{L}$	velocity gradient
$\mathbf{M}$	mass matrix
M	constant used in yield function for foam plasticity model
$\mathbf{N}$	interpolation functions
$\mathbf{P}^{ext}$	external forces
$\mathbf{P}^{int}$	internal forces
$\Delta\mathbf{R}$	rotation increment
$\mathbf{S}$	deviatoric part of Cauchy stress tensor
$T,\ R,\ L$	tangential, radial and longitudinal direction
V	volume
V_0	volume in reference configuration
$\mathbf{W}$	spin tensor
$\mathbf{X}$	material coordinates

Roman lower case letters

$\mathbf{a}$	nodal displacements
$\mathbf{b}$	body force vector
$\mathbf{c}$	parameters used to approximate weight functions $\mathbf{v}$
$\mathbf{e}$	strain vector
e	nominal strain
f^d	yield stress at nonzero strain rate
f^0	static yield stress
f_s	shear strength
f_t	tensile strength
f_t^0	shear strength at reference loading rate
h	potential function for plasticity
k_1	initial stiffness of crack elements
k_2	slope of the first softening branch for crack elements
l	length
l_c	critical length of specimen for stable test performance
l_0	initial length
m,n	coupling parameter for mixed mode fracturing
m_0	weight of wood in oven-dry condition
m_w	weight of wood with moisture content w
$\mathbf{n}$	unit normal vector
p	equivalent pressure stress
p_c	yield stress in hydrostatic compression
$p_{c/0}$	initial yield stress in hydrostatic compression
p_t	strength in hydrostatic tension
q	von Mises equivalent stress
r	material parameter defining strain rate dependence for foam plasticity model
$\mathbf{s}$	stress vector

t	traction vector
t	time
u	displacement vector
u_h	horizontal displacement in combined compression and shear tests
u_v	vertical displacement in combined compression and shear tests
v	vector of weight functions
w	moisture content
x	spatial coordinates

Greek letters

α	parameter for numerical damping
β	parameter used in Newmark's algorithm
γ	parameter used in Newmark's algorithm
δ	relative displacement at fracture zone
δ_n	relative normal displacement at fracture zone
δ_s	relative shear displacement at fracture zone
δ_{n0}	relative normal displacement for zero normal stress
δ_{s0}	relative shear displacement for zero shear stress
δ_{n1}	relative normal displacement at breakpoint on normal stress-displacement curve
δ_{s1}	relative shear displacement at breakpoint on shear stress-displacement curve
$\boldsymbol{\epsilon}$	total strain
$\dot{\boldsymbol{\epsilon}}$	strain rate tensor
$\dot{\boldsymbol{\epsilon}}^{el}$	elastic part of strain rate tensor
$\dot{\boldsymbol{\epsilon}}^{pl}$	plastic part of strain rate tensor
ϵ_{log}	logarithmic strain
ϵ_{vol}	volumetric strain
ϵ_{vol}^{el}	elastic part of volumetric strain
ϵ_{vol}^{pl}	plastic part of volumetric strain
θ, θ_1-θ_3	angles
$\Delta\lambda$	plastic multiplier
μ	coefficient of friction
ν	Poisson's ratio
ρ	current density
ρ_0	density referred to the reference volume
ρ_1-ρ_4	breakpoints defining the density variation over a growth ring
ρ_c	density of a cell
ρ_{c0}	cell wall bulk density
ρ_e	average density of the earlywood region
ρ_l	average density of the transitionwood region
ρ_t	average density of the latewood region
ρ_t	average density of the growth ring
$\boldsymbol{\sigma}$	Cauchy stress tensor

σ_n	normal stress at fracture zone
σ_{n1}	normal stress at breakpoint on stress-displacement curve
σ_n^0	normal stress at fracture zone for reference loading rate
σ_p	contact pressure at fracture zone
σ_s	shear stress at fracture zone
σ_{s1}	shear stress at breakpoint on stress-displacement curve
σ_n^0	shear stress at fracture zone for reference loading rate
σ_0	initial yield stress in uniaxial compression
$\boldsymbol{\tau}$	Kirchhoff stress tensor
$\hat{\boldsymbol{\tau}}$	Jaumann rate of Kirchhoff stress tensor
$\dot{\boldsymbol{\tau}}$	material time rate of Kirchhoff stress tensor
$\bar{\varphi}$	orientation of local coordinate system for crack elements
φ_a, φ_b	orientation of crack element boundaries
ξ	angle defining direction of loading in combined compression and shear test
ψ	mixed mode fracture angle

Contents

Chapter 1

Introduction

1.1   General Remarks

The pulp and paper manufacturing industry is of great importance to Sweden, which is one of the leading pulp and paper exporting nations of the world. There are two main types of pulp, chemical and mechanical. In chemical pulping, the wood fibres are separated by chemical means, whereas in mechanical pulping they are separated by mechanical processes. Mechanical pulping has several advantages in comparison with chemical pulping, such as its having a very high pulp yield and low investment costs. Because of its unique properties, mechanical pulp is used extensively in many printing paper and paper board grades. Newsprint and magazine papers are mainly produced through use of mechanical pulp. A major disadvantage of mechanical pulping, however, is the large energy consumption it results in. In Sweden approximately 5 TWh of electrical energy are needed annually for producing some 3 million tons of mechanical pulp. Only a small percentage of the electrical energy supplied is utilized to create well-refined pulp fibres, however. The majority of the energy is converted to heat without it having much effect on the properties of the pulp. There is thus a large potential for saving energy [35]. If the mechanical pulp industry is to remain competitive, energy efficiency needs to be increased. The fact that the mechanics of the defibration processes are incompletely understood, however, prevents the development of improved defibration methods.

1.2   Aim and Scope of Investigation

Numerical simulations by means of the finite element method represent a powerful tool that can be used to analyse and simulate different defibration processes. For instance, the influence of different combinations of loading modes, loading direction and loading rate can be studied numerically in order to find more optimal combinations with respect to energy consumption and fibre properties. This information can then be used to optimize the mechanical pulping processes currently employed, or to develop new processes and defibration techniques. The main application dealt with in this thesis is that of mechanical pulping. It should be emphasized, however, that there

are also other industrial processes that aim at disintegrating wooden materials, such as sawing, wood chipping and lumber cutting. For these applications as well, finite element simulations could be very useful for improving and further developing the techniques currently employed.

Numerical simulations of such complex processes require the use of proper constitutive models. From a mechanical point of view, wood is a very advanced material. Its anisotropy and inhomogeneity as well as its elastic, plastic and fracture mechanical properties need to be taken into account in order for realistic numerical simulations to be performed.

The thesis deals with different aspects of the material modelling of wood when disintegration and defibration of wood are simulated. The major aim of the study is to increase knowledge of suitable material modelling approaches for simulation of this type. One of the main issues involved is the level of modelling. Two modelling approaches are considered in the thesis, one involving continuum models and the other modelling at the microstructural level. Continuum modelling is needed in order to simulate the initial breakdown of the wooden chips, and micro-modelling in order to analyse the later stages of defibration. Numerical simulations related to initial defibration processes, using the two modelling approaches just referred to, are presented and are compared with experimental results.

A significant part of the work performed involved experimental investigations. The mechanical behaviour of wood chips subjected to a number of well-defined loading modes was studied. Material tests concerned with elastic, plastic and fracturing characteristics were also carried out. These tests were performed in order to obtain input for the material models, as well as to contribute to a basic understanding of the complex mechanical behaviour of the wooden material. A further aim of the project was to obtain improved insight into the mechanics of the initial defibration processes.

The study focuses on the initial conversion of wood to fibres rather than on the final transformation of the individual fibres through further treatment, aimed at giving them suitable paper-making properties. This is based on the fact that the initial defibration has a crucial effect on both the final quality of the pulp and the total energy consumption required. It is essential to be able to control the initial defibration so that breakdown occurs in the best possible way. A tough initial defibration, for example, may result in a considerably more favourable initiation of fractures in the wood structure than defibration does which is carried out under milder conditions.

The study is limited to wood loaded perpendicular to the grain. This direction of loading is of considerable interest in connection with mechanical pulping applications, in which it is highly important to obtain well-collapsed fibres so that the pulp will possess good paper-making properties. Also, only clear wood is dealt with; inhomogeneities such as knots and anomalies are not considered. Defibration is a very complex process, and not much is known about how chip disintegration and fibre separation and preparation take place. In order to be able to perform simulations and gain sound knowledge of wood defibration, a number of limiting choices were made, resulting in the conditions used differing from those present in defibration processes used commercially. The aim is thus not to take all parameters of importance into account. Instead, certain specific parameters that could be controlled both in simulations and

in experiments are studied. The differences between the conditions and parameters considered in this study and the conditions in actual industrial defibration processes are pointed out in Table 1.1.

Table 1.1: Comparison between conditions in current industrial defibration processes and parameters considered in this study.

Variables	Defibration	Experiments	Simulations
Raw material	Mainly spruce	Spruce	Spruce
Moisture content	Normally above 30 %	12, 28 %	12, 28 %
Temperature	$\approx 150°$ C	$\approx 20°$ C	$\approx 20°$ C
Loading rate	Up to 100 m/s	Mainly quasi-static	0-50 m/s
Loading mode	Random	Well-defined	Well-defined
Pre-treatment of chips	Chemical or mechanical	None	None

The study was carried out during the past five years in collaboration with other Swedish researchers. Certain parts of the work presented in the thesis has been published previously, in a licentiate thesis [28], a refereed paper [29], internal reports [33, 34] and in conference papers [30, 31, 32, 69].

1.3 Outline

The general background to the study is considered in Chapter 2. A description of the structure and the mechanical properties of softwoods, which constitute the main raw material for mechanical pulping, are presented together with a brief description of mechanical pulping. The major processes in use, the modes of fibre separation, properties of the pulp and of the fibres as well as the huge energy consumption, are discussed. Chapter 3 deals with experimental work, three different types of tests being dealt with: compression and shear tests concerning the behaviour of wood when loaded in radial compression and tangential shear as well as in different combinations of compression and shear; tensile tests dealing with the fracture mechanical behaviour of wood; and chip shearing tests demonstrating the complex behaviour of wood when loaded perpendicular to the grain under conditions resembling those present during refining. In particular, the influence of specimen orientation versus loading direction is studied.

Chapter 4 concerns the constitutive modelling of wood. Modelling at both the macro- and the microstructural level is considered, modelling approaches for both these structural levels being taken up. A mixed-mode fracture model is presented. In Chapter 5 the procedure used for the numerical simulations dealt with in the two subsequent

chapters is outlined. The finite element formulation, the solution techniques employed, and the implementation of the fracture mechanics model are described. Chapter 6 concerns numerical simulations of wood disintegration at the macrostructural level. Several numerical examples are presented and comparisons are made with experimental results. The effect of the loading rate on fracturing behaviour is also studied. In Chapter 7, numerical examples of modelling at the microstructural level are presented. The effects of different constitutive assumptions on the behaviour of the cell structure are investigated. In Chapter 8, finally, concluding remarks are presented and possible future work is discussed.

Chapter 2

General Background

2.1 Introduction

This chapter considers the background to the present work. The first section contains a brief description of softwoods, which represent the most suitable raw material for manufacturing mechanical pulps, spruce being particularly good in this respect. The spruce fibre is relatively long and has a cross section favourable in order to give it a suitable flexibility by mechanical treatment. The softwood structure is described at the macro, the micro and the cell wall level, the mechanical properties likewise being discussed. For a more complete description of the structure and properties of softwoods, see e. g. Bodig and Jayne [7], Dinwoodie [9], [10] and Kollmann and Côté [45]. The second section of the chapter deals with mechanical pulping and focuses on refining, which is the dominating mechanical pulping process. The mode of fibre separation, the properties of the pulp and the fibres, and the huge energy consumption are discussed as well.

2.2 Structure and Properties of Softwoods

2.2.1 Macrostructure

Wood is a cellular material with a high degree of anisotropy. Figure 2.1 shows a wedge-shaped segment cut from a twelve-year-old softwood tree. The tree consists of a central core containing conductive tissues on the inside and dead protective outer bark on the outside. The central core is composed mainly of wood in the inner parts and of the inner and living layer of bark towards the outside, with a cambium layer separating the two. The innermost part is called the pith. The growth and formation of new cells takes place in the cambium, which is a zone of cells capable of repeated cell divisions. Each growing season, the cambium forms a new layer of wood and a certain amount of additional bark over the entire surface of the stem, resulting in an increase in stem diameter. The growth and formation of new cells can be characterized as proceeding rapidly in the early spring and slowing down late in the summer, before finally ceasing in the fall. Such a growth pattern results in different kinds of wood being formed in

various seasons in the year. The light-coloured portion of the growth ring, termed earlywood, is formed in the spring, whereas the darker part, the latewood, is formed later in the season, mainly during the summer.
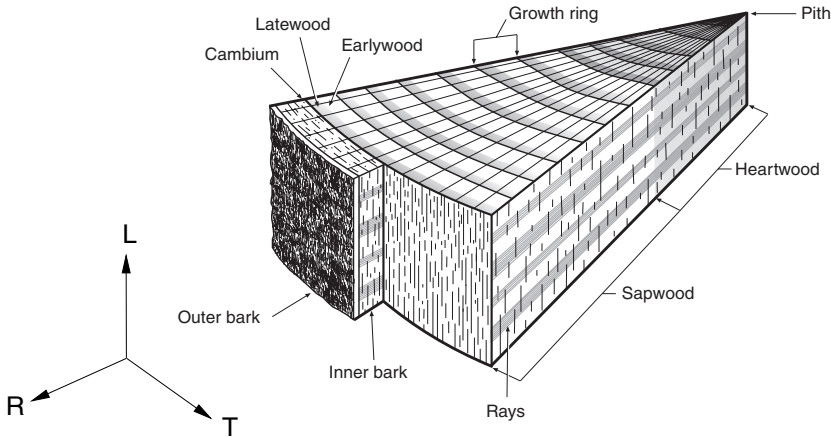
Figure 2.1: A wedge-shaped segment cut from a twelve-year-old softwood tree. R, T and L denote the radial, tangential and longitudinal directions, respectively.

The wood material in the outer growth rings of the stem, called the sapwood, serves to conduct water and nutrients to the crown of the tree. The wood material inside the sapwood where there is no transportation of water and nutrients is called the heartwood. The primary difference between the heartwood and the sapwood is the appearance of extractable chemicals. These are primarily responsible for giving the heartwood its unique properties, such as its high resistance to insects and to decay, an increase in density, and for some species a darker colour.

Because of the manner in which a tree grows and the arrangements of the wood cells within the stem, three principal directions are usually referred to in describing the properties of wood. These are the longitudinal, the radial and the tangential direction (the latter being in the direction of the growth ring), these being denoted as L, R and T, respectively.

2.2.2   Microstructure

Softwoods contain different cell types. By far the major part of the wood in softwoods (90-95%) is composed of long slender cells known as longitudinal tracheids. Ray cells constitute most of the remainder of the wood in softwoods. Although a few other types of cells may occur, these make up an insignificant part of the volume.

The longitudinal tracheids are oriented almost parallel to the axis of the stem. Longitudinal tracheids are normally 3-5 mm long and only 25-45 μm thick, which means

that they are about 100 times greater in length than in cross dimensions. These tracheids are almost rectangular in cross section and have hollow centers (lumens), which are closed at the ends. The main functions of these cells are to provide mechanical support in the stem and to transport water and nutrients to the crown of the tree. The transportation of water and nutrients is restricted to the living cells, specifically the sapwood tracheids, whereas both the sapwood and heartwood cells are active in supporting the tree. The ray cells are oriented perpendicular to the longitudinal tracheids. They extend in radial direction from the pith to the bark. Their function is primarily that of water and nutrient transportation in the radial direction.

The cellular structure of softwood is illustrated in Figure 2.2 in which earlywood tracheids, latewood tracheids and ray cells are shown. At this level of magnification, it is easy to see with the unaided eye why wood formed in the latter part of a growing season appears different than that formed earlier in the year. The latewood tissue is of greater density, being composed of cells of relatively small radial diameter, thick cell walls and small lumens. It is this tissue that forms the darker-coloured portion of the growth ring. Characteristic for softwoods is that the cells are aligned in straight parallel rows, combined with straight rays that cross them.
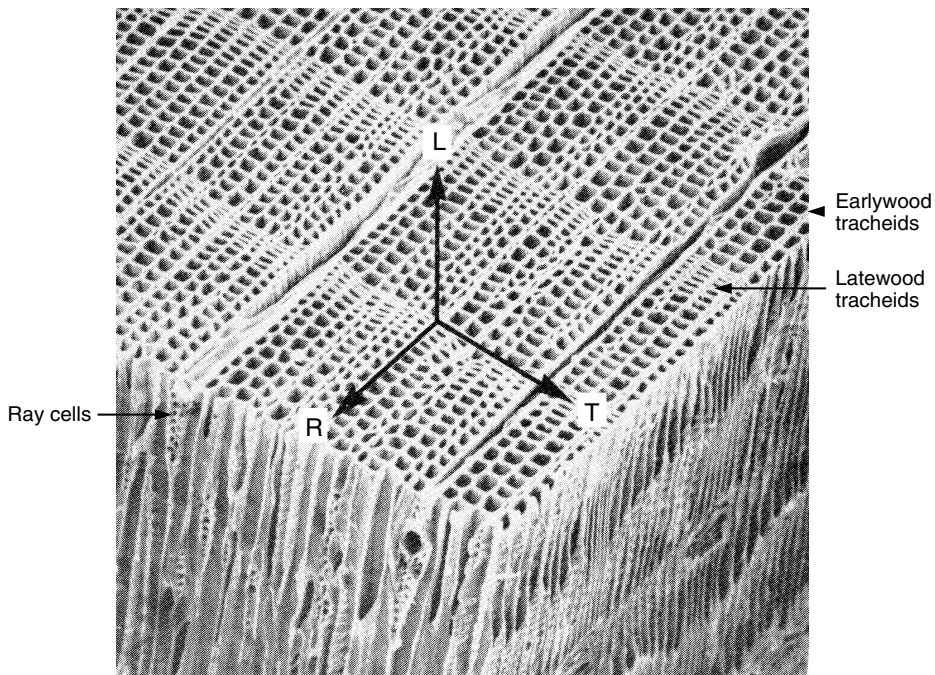
Figure 2.2: Cellular structure of softwood. R, T and L denote the radial, tangential and longitudinal directions, respectively. From Barrett [5].

2.2.3   Cell wall

Wood can be regarded as a composite material with a cellular structure, the cells being built up of small units called microfibrils, which are embedded in a matrix consisting of lignin and hemicellulose. The cells in turn are embedded in a matrix of lignin. The microfibrils consist of cellulose chains and have a thickness of 10-20 nm and a length of approximately 5000 nm.

The cell wall consists of several layers, differing mainly in their microfibrillar orientation, see Figure 2.3. The outermost layer, or the primary wall (P), is a thin layer with randomly-oriented microfibrils. Inside this, there is a secondary wall consisting of three distinct layers: a thin outer layer with crosswise-oriented microfibrils; a thick central layer with the microfibrils nearly parallel to the cell axis; and a thin inner layer composed of microfibrils roughly parallel to those in the outer layer, except that they are not oriented crosswise. The three layers are designated as S1, S2 and S3, respectively. The S2 layer is the thickest, constituting the bulk of the cell wall (approximately 70-80%). Consequently, this layer has a major influence on the mechanical behavior of the cell. Between the cells there is a layer consisting mainly of lignin. This layer, referred to as the middle lamella (ML), serves as a bonding medium holding the fibres together.
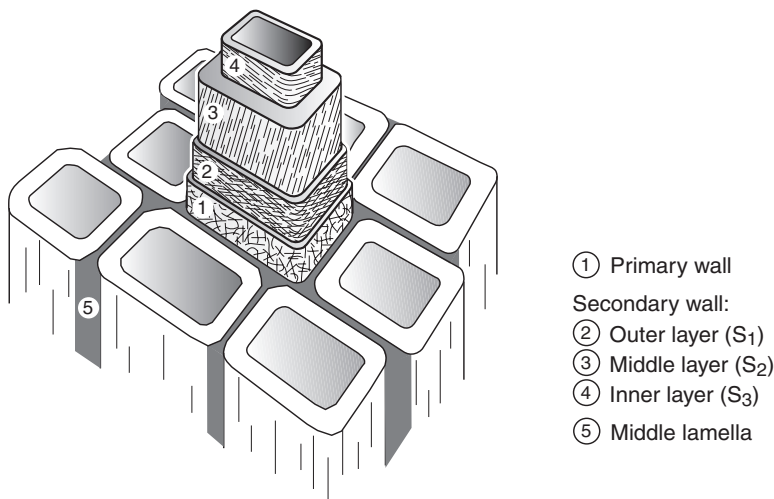
Figure 2.3: Schematic illustration of the cell wall structure indicating the microfibrillar orientation within the layers.

The volumetric fractions, the chemical composition and the microfibril angle of the different cell wall layers are given in Table 2.1. The values of the microfibrillar angle given in the table are only average values for the layers. The microfibrillar angle appears to vary systematically along the length of the fibre as well as across the wall thickness. Systematic differences in microfibrillar orientation between radial and tangential walls have also been found.

Table 2.1: Volumetric fractions, chemical composition and microfibril angles of the cell wall layers in spruce tracheids according to Fengel [12] and Dinwoodie [9].

Layer	Thickness [μm]		Chemical composition [%]			Microfibril
	Earlyw.	Latew.	Cellulose	Hemicellulose	Lignin	angle [°]
ML	0.5	0.5	12 (ML+P)	26 (ML+P)	62 (ML+P)	-
P	0.1	0.1	12 (ML+P)	26 (ML+P)	62 (ML+P)	Random
S1	0.2	0.3	35	35	30	$\pm$50-70
S2	1.4	4.0	56 (S2+S3)	14 (S2+S3)	30 (S2+S3)	10-30
S3	0.03	0.04	56 (S2+S3)	14 (S2+S3)	30 (S2+S3)	60-90

2.2.4 Mechanical properties

Due to its cellular structure, wood is a highly anisotropic material. Because of the manner in which a tree grows and the arrangement of the wood cells within the stem, wood can basically be considered as a cylindrical orthotropic material, one that possesses three principal directions: the longitudinal (fibre direction), the radial and the tangential, denoted by L, R and T respectively, see Figure 2.2. Hooke's generalized law for a linear elastic orthotropic material can with these indices be written as

$$
\begin{bmatrix}
\epsilon_{LL} \\
\epsilon_{RR} \\
\epsilon_{TT} \\
\gamma_{LR} \\
\gamma_{LT} \\
\gamma_{RT}
\end{bmatrix}
=
\begin{bmatrix}
\frac{1}{E_L} & -\frac{\nu_{RL}}{E_R} & -\frac{\nu_{TL}}{E_T} & 0 & 0 & 0 \\
-\frac{\nu_{LR}}{E_L} & \frac{1}{E_R} & -\frac{\nu_{TR}}{E_T} & 0 & 0 & 0 \\
-\frac{\nu_{LT}}{E_L} & -\frac{\nu_{RT}}{E_R} & \frac{1}{E_T} & 0 & 0 & 0 \\
0 & 0 & 0 & \frac{1}{G_{LR}} & 0 & 0 \\
0 & 0 & 0 & 0 & \frac{1}{G_{LT}} & 0 \\
0 & 0 & 0 & 0 & 0 & \frac{1}{G_{RT}}
\end{bmatrix}
\begin{bmatrix}
\sigma_{LL} \\
\sigma_{RR} \\
\sigma_{TT} \\
\tau_{LR} \\
\tau_{LT} \\
\tau_{RT}
\end{bmatrix}
\tag{2.1}
$$

or shorter as

$$
\mathbf{e}^e = \mathbf{Cs} \tag{2.2}
$$

or in the inverse form

$$
\mathbf{s} = \mathbf{De}^e, \qquad \mathbf{D} = \mathbf{C}^{-1} \tag{2.3}
$$

where $\mathbf{e}^e$ is the elastic strain vector, $\mathbf{s}$ is the stress vector, $\mathbf{C}$ the flexibility or compliance matrix and $\mathbf{D}$ the material stiffness matrix. The parameters E_L, E_R and E_T are the moduli of elasticity in the three orthotropic directions and G_{LR}, G_{LT} and G_{RT} are the shear moduli in the respective orthotropic planes. The parameters ν_{LR}, ν_{LT}, ν_{RL}, ν_{RT},

ν_{TL} and ν_{TR} are Poisson's ratios. The compliance matrix is symmetric, which implies that

$$\frac{\nu_{RL}}{E_R} = \frac{\nu_{LR}}{E_L}, \qquad \frac{\nu_{TL}}{E_T} = \frac{\nu_{LT}}{E_L}, \qquad \frac{\nu_{TR}}{E_T} = \frac{\nu_{RT}}{E_R}. \qquad (2.4)$$

There are thus nine independent parameters describing the stiffness of an orthotropic material. If the principal orthotropic material directions do not coincide with those of the global coordinate system, a transformation of the constitutive matrices must be made. For a change of coordinate system, the stress vector transforms according to

$$\mathbf{s}' = \mathbf{As}, \qquad (2.5)$$

where $\mathbf{s}'$ is the stress vector with reference to the global directions, $\mathbf{s}$ is the stress vector in the local material directions and $\mathbf{A}$ is the transformation matrix. Since the strain energy $\mathbf{s}^T\mathbf{e}$ is invariant it can be concluded that the strain vector transforms according to

$$\mathbf{e} = \mathbf{A}^T\mathbf{e}'. \qquad (2.6)$$

By using Eq. (2.5) and (2.6) the transformation rules for the constitutive matrices $\mathbf{C}$ and $\mathbf{D}$, expressed with reference to the local material directions, into $\mathbf{C}'$ and $\mathbf{D}'$, with reference to the global directions, can be established

$$\mathbf{C}' = (\mathbf{A}^T)^{-1}\mathbf{CA}^{-1}, \qquad \mathbf{D}' = \mathbf{ADA}^T. \qquad (2.7)$$

The strength and stiffness of wood are considerably greater in the longitudinal than in the perpendicular directions. This is easily understood since 90-95% of the fibres are oriented longitudinally. There is also a difference in properties between the radial and tangential directions. Reasons for the difference in stiffness between the two directions perpendicular to the grain are the presence of the rays, which are oriented in the radial direction, the difference in cellular structure between the radial and tangential directions and possibly also different orientations of the microfibrils for radially and tangentially cell walls. The elastic moduli vary with species, moisture content, temperature etc. but in general the moduli are related according to the following ratios [7]:

$$E_L : E_R : E_T \approx 20 : 1.6 : 1$$

$$G_{LR} : G_{LT} : G_{RT} \approx 10 : 9.4 : 1$$

$$E_L : G_{LR} \approx 14 : 1.$$

By using the transformation rules, Eq. (2.7), the elastic moduli for arbitrary material orientations can be determined. In Figure 2.4 the modulus of elasticity perpendicular to the grain E_y is shown as a function of the annual ring orientation. The example is based on the stiffness ratios given above and assuming a value of the modulus of elasticity in the longitudinal direction of E_L=10000 MPa. This yields the following values of the moduli perpendicular to the grain: E_R=800 MPa, E_T=500 MPa and

G_{RT}=71 MPa. Poisson' s ratio ν_{TR} is set equal to 0.25. The annual ring orientation is defined by the angle θ. For the case of θ=0° the global direction coincides with that of the radial direction and E_y=E_R, and for θ=90° the global direction coincides with that of the tangential and E_y=E_T. For many of the intermediate orientations the modulus of elasticity E_y is considerably lower than E_T. The lowest values are even lower than half of that of E_T and are obtained at an angle of about 45°. The reason for the low stiffness values is the low modulus in rolling shear G_{RT}. Low values of the modulus of elasticity perpendicular to the grain have also been determined experimentally. Gustafsson and Enquist [20] report values for Pinus Sylvestris L. as low as 95 MPa for tensile loading and 161 MPa for compressive loading.
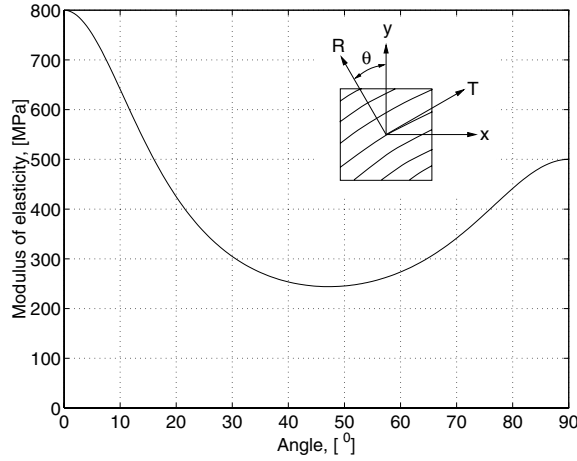
Figure 2.4: Modulus of elasticity perpendicular to the grain as a function of the annual ring orientation.

The moisture content has a considerable influence on the elastic properties. The reduction in stiffness as the moisture content increases is approximately linear up to the point of fibre saturation; further increase in moisture content has no influence on the stiffness. The influence of moisture content is significantly greater on the radial and tangential elastic moduli than on the longitudinal moduli [15]. The stiffness perpendicular to the grain at the point of fibre saturation is only about half of that under dry conditions [45]. The influence of moisture content on strength is also of considerable importance, up to the point of fibre saturation. The moisture content w is here defined as

$$w = \frac{m_w - m_0}{m_0} \tag{2.8}$$

where m_w is the weight of the wood with the moisture content w and m_0 is the weight in oven-dry condition. The point of fibre saturation for spruce corresponds to a moisture content slightly below 30 %.

There is also a dependence of the temperature on the elastic properties; strength and stiffness decrease with increasing temperature. The relations between these properties and the temperature are often treated as linear and reversible up to a temperature of about 90-95°. At higher temperatures, thermal degradation of the wood substance takes place which may result in permanent stiffness and strength reduction. It has also been shown that the influence of temperature is greater the higher the moisture content [7, 15].

The stiffness and strength properties of wood are strongly dependent on the density. Normally, the larger the density, the higher the stiffness and strength. This is obvious since density is a function of the cell wall thickness to the cell diameter. Due to the large difference in cell wall thickness between earlywood and latewood, the density of wood varies considerably over a growth ring. Figure 2.5 shows the fraction of the cell wall area to the total area over some growth rings. Due to the large difference in density between earlywood and latewood, the mechanical properties differ markedly between the two phases. The stiffness and strength are considerably higher for latewood than for earlywood, and the latewood acts as a stiff reinforcement.
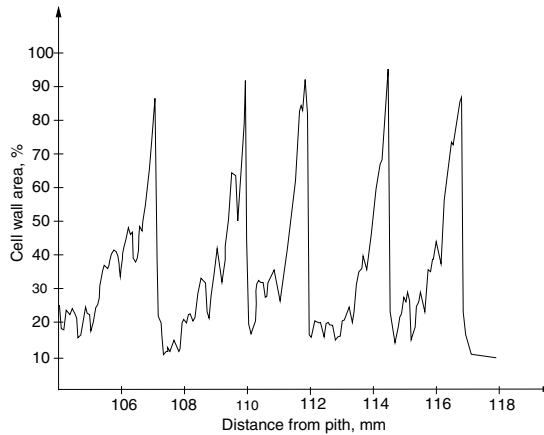
Figure 2.5: Variation in density, in the radial direction, over some growth rings, Wigge [88].

For wood, several ways of defining the density are used. One common measure is the oven-dry weight divided by the volume in the green condition; other measures are those of the oven-dry weight divided by the oven-dry volume or the oven-dry weight divided by the volume at a specified moisture content. In this study, density in terms of the oven-dry weight divided by the volume in the green condition is used.

When wood is loaded beyond the elastic region, irreversible changes in the material take place. Wood behaves highly nonlinear above the limit of proportionality, and its behavior is influenced by several factors such as density, moisture content, temperature, duration of loading etc. Typical stress-strain curves for wood in dry condition loaded in compression and tension in different directions are shown in Figure 2.6. When loaded in

compression the response can, for all three main directions, be characterized by a initial elastic region, followed by a plateau region and finally a region with rapidly increasing stress. Compression in the tangential direction gives a smooth stress-strain curve rising gently throughout the plateau, whereas compression in the radial direction may give a slightly irregular stress plateau often starting with a small drop in stress after the linear elastic region has been passed. The tangential and radial yield stresses are about equal. The yield stress in the axial direction is considerably higher than that in the radial and tangential directions, and the plateau region is serrated [16]. For compression perpendicular to the grain, three basic failure patterns can be distinguished, depending on the orientation of the growth rings in relation to the direction of loading, Figure 2.7. For radial compression, crushing failure occurs in the earlywood zone. Tangential compression may result in buckling of the growth rings, whereas shear failure often occurs for loading at an angle to the growth rings.
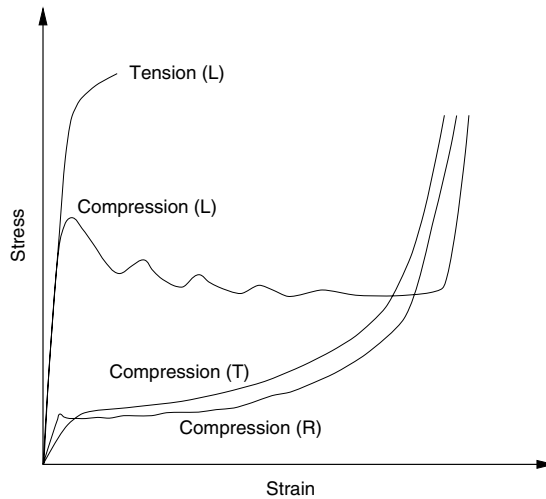
Figure 2.6: Typical stress-strain curves for wood loaded in compression in the longitudinal, radial and tangential directions and for tension in the longitudinal direction.

The compressive behavior of wet spruce loaded perpendicular to the grain has been studied by Uhmeier [83], Uhmeier, Vansteenkiste and Salmén [84] and Vansteenkiste [86]. In [83] the influence of various parameters such as loading rate and temperature on the mechanical response of spruce compressed radially was investigated. In [84] the influence of specimen height and of loading rate was investigated, results of both radial and tangential compression tests of earlywood being presented. From these investigations it was concluded that the compressive response is clearly dependent on the loading rate: the higher the loading rate the higher the stress in the plateau region. The influence of the loading rate was greatest for the highest loading rate, probably due to a high resistance in squeezing out the lumen water from the saturated specimens [84]. Higher temperatures result in lower stress plateau values, and the influence of temperature
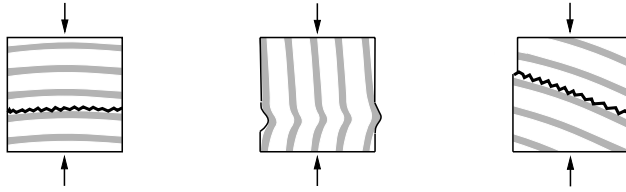
Figure 2.7: Failure types in compression perpendicular to the grain. Adopted from [7]. Left: crushing of earlywood. Middle: buckling of growth rings. Right: shear failure.

was found to be linear for all strain rates in the temperature and strain rate interval studied. In [86] the response of earlywood, latewood and a mix of earlywood and latewood loaded in tangential compression was investigated. The tests were performed on spruce in wet condition (saturated) and at low strain rates. It was found that the latewood was considerably stiffer (and stronger) than the earlywood, the plateau stress being higher and the plateau region shorter and steeper for the specimens containing latewood.

The aim in mechanical pulping is to create fractures in the wood so that the fibres are separated. In wood, eight systems of crack propagation might be identified, as illustrated in Figure 2.8. Each system is identified by two letters, the first indicating the normal to the crack surface and the second the direction of crack growth. Due to the density gradient in the growth rings, a microscopic asymmetry is introduced. The + sign means that the crack propagates away from the center of the tree whereas the - sign that it propagates towards the center. For each of the eight cases defined above fracture can occur in three different modes, see Figure 2.9. Mode I represents symmetric opening perpendicular to the crack surface, while Modes II and III denote antisymmetric shear separations. For wood, cracks may then arise in 24 different manners. The resistance to crack propagation across the grain (the LT and LR systems) is much higher than in the other systems. The ray cells are of great importance since they act as crack initiators in the TL and TR systems and as crack arrestors in the RL and RT.

Tensile loading perpendicular to the grain gives rise to three different failure patterns: tensile fracture in the earlywood for radial loading; tensile failure in the wood rays for tangential loading and shear failure along a growth ring when loaded at an angle to the growth rings. At the microstructural level the crack propagation for Mode I loading may occur in two different ways, Figure 2.10. The crack may advance across the cell walls (cell wall breaking), or it may propagate between two adjacent cells close to the middle lamella (cell wall peeling). The cell wall breaking type propagation is in general not considered desirable in mechanical pulping since it gives rise to damaged fibres. The cell wall peeling type with fracturing at the S1 or S2 layer of the secondary wall is preferred, whereas fracturing in the middle lamella should be avoided. Crack propagation in thin-walled earlywood is commonly caused by cell wall breaking. When cracks propagate in the TR direction, the peeling type predominates [7]. Cracks in the TR direction seek rays and then propagate along them, Johnson [43]. The peeling
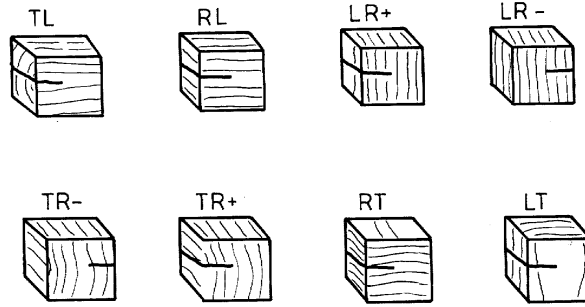
Figure 2.8: Eight crack propagation systems in wood. The distinction between R+ and R- directions arises due to the asymmetric structure of the growth ring. Gibson and Ashby [16].

type is favoured by thick cell walls [7] and high temperatures. At room temperature the failure commonly occurs in the primary wall and in the S1 layer of the secondary wall, whereas in the case of high temperatures the crack path, due to the softening of the lignin and the hemicellulose, is gradually transferred towards the middle lamella, Koran [47], [48], Koran and Salmen [50].

An important parameter for characterizing fracture mechanical properties is the fracture energy G_F, defined as the energy needed to bring a unit area of the material to complete fracture. Different test methods for determining fracture mechanics properties of wood have been developed [19] and the most comprehensive studies have been performed in Mode I fracture perpendicular to the grain. One method used to determine the fracture energy for Mode I tensile fracture perpendicular to the grain is
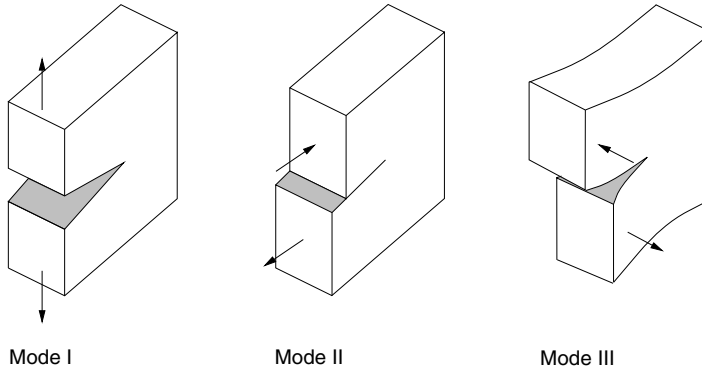
Figure 2.9: The three different modes of fracture. Mode I: the opening or cleavage mode, Mode II: the forward shear or sliding mode, and mode III: the transverse shear or tearing mode.
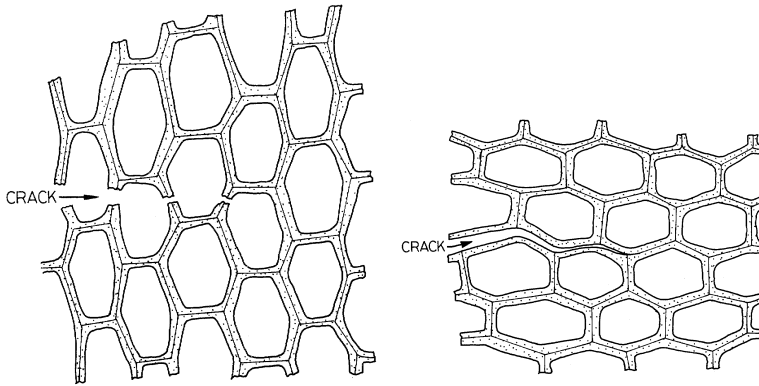
Figure 2.10: Crack propagation at the microstructural level for Mode I loading. Left: cell wall breaking. Right: cell wall peeling. Gibson and Ashby [16].

a three-point bending test of a notched beam composed of three pieces of wood glued together. The fracture energy is evaluated as the total work to fracture divided by the area of the fracture cross section. The main assumption made in the evaluation is that no less and no more than the external work goes into creating the fracture surface. This method has been applied by several investigators, e. g. [53, 55, 71, 76]. Another type of test is fracture softening tests. In this type of test the stress versus deformation performance of the material is recorded, including the descending branch of the curve showing the gradual decrease in stress at increasing deformation. One problem with this type of test is achieving sufficient stable test performance and avoiding unstable brittle failure. This implies that the length of the specimen must be small; the critical specimen length for spruce is in the range of 2-4 mm. Also, the cross section needs to be small in order to get as uniform stress distribution over the fracture zone as possible. The specimen must be large enough to enable accurate handling during preparation and gluing, however. This type of test thus involves some difficulties concerning specimen design and preparation; on the other hand, it yields much information and material data that are needed in cohesive fracture models. This test method can be applied to evaluate fracturing properties for tension perpendicular to the grain [8, 63], forward shear [8, 71, 87] and combined tension and shear [87]. The effect of the grain orientation on the fracturing properties in Mode I tension perpendicular to the grain was examined by Boström [8]. He investigated fracturing in the RL and TL modes and also for one orientation between RL and TL. It was found that the curves had the same shape for all three orientations with an initial rapid decrease in stress after peak stress, followed by a region with considerably slower decrease with increasing deformation. The differences in tensile strength and fracture energy between the directions examined were about 20 %. Investigations of the shear fracturing properties treat longitudinal shearing exclusively; references to the properties in rolling shear fracture were not found in the literature. Typical values of the fracture energy for softwoods at low moisture contents and at low temperatures for the case of Mode I tangential

tensile fracture are in the range of 300-500 Nm/m^2 and for Mode II shearing about 800-1000 Nm/m^2, i. e the fracture energy in longitudinal shear is about three times as high as that for tensile fracture. By comparing fracture energy values reported in the literature, it can be concluded that higher values of the fracture energy are often obtained from the three-point bending test than from stable tensile tests. This is because the major assumption made when evaluating G_F from the test results is not fulfilled, i. e due to inelastic response of the material outside the fracture zone and/or external work being transferred to kinetic energy which is lost by damping [19, 67].

The moisture content is, perhaps, the most important environmental parameter that has to be taken into account for the fracturing of wood. There is no doubt about the influence of moisture content, but there is no agreement on how the moisture affects the resistance to cracking [85]. The effect of the moisture content on the Mode I fracture energy using the three-point bending specimen has been investigated by e. g. Kretschman [53], Smith [76] and Rug et al. [73]. Kretschman found that the fracture energy of Southern Pine increases linearly with increasing moisture content for moisture contents varying between 4 % and 18 %. The fracture energy was found to be about 30 % higher for the highest moisture content than for the lowest. Smith studied the influence of the moisture content on the fracture energy of Red Pine for moisture contents between 5 % and 28 %. He found that the fracture energy increases with increasing moisture content up to a moisture content of 18 %. For higher values of the moisture content, the fracture energy decreases with increasing moisture content. The maximum value of G_F for a moisture content of 18 % was 64 % higher than the corresponding value at a moisture content of 5 %, and 24 % higher than the value obtained at 28 % moisture content. In [73] Rug et al. report values of the Mode I fracture energy at three different moisture levels, 12, 18 and 24 %, for Pinus Sylvestris. They concluded that there was a small decrease in fracture energy when going from 12 % to 18 % moisture content and no change when going from 18 % to 24 %.

The influence of temperature on the fracture mechanical properties is of great importance for mechanical pulping applications. Results of how fracture energy varies with temperature have been presented by Koran in e. g. [46] and [49]. The tests performed by Koran were unstable however, and the recorded work-to-maximum-load is not a proper measure of the fracture energy of the material. Unfortunately, no conclusions regarding the influence of temperature on the fracture energy can therefore be drawn from Koran's investigations, see Holmberg [34].

2.3   Mechanical Pulping

2.3.1   General remarks

The objective in producing pulp is to separate the wood fibres and give them properties suitable for making paper. There are two main types of pulp. In chemical pulp, the fibres are separated by removing the lignin by chemical means. (Lignin is the binding agent holding the fibres together.) In mechanical pulp, the fibres are separated by mechanical processes. Two main types of processes are employed in manufacturing mechanical pulp. In the grinding process (groundwood pulp), logs are pressed against

a revolving stone, water being used as a lubricant. In the refining or defibration process (refiner pulp), wood chips are disintegrated, the fibres being prepared in the small gap between parallel and patterned refiner discs, where either one or both discs revolve. An elementary presentation of the different processes involved in producing chemical and mechanical pulps is given in [82].

The advantages of mechanical pulp over chemical pulp is that the mechanical pulp making process is relatively simple, the investment costs are lower, the pulp yield is very high and the optical properties are better. Drawbacks are that the mechanical pulp has lower strength than chemical pulp and that its aging behavior reduces its use.

The optical properties of groundwood are excellent, but their poor mechanical properties make it necessary to reinforce them with chemical pulp fibres. Refiner pulp is significantly stronger than groundwood pulp and the need for chemical pulp fibres is eliminated or reduced. The broader supply of raw materials is another advantage of refining over grinding. (Remnants from sawmills, material from thinnings and distorted wood can be utilized since the wood is subdivided into chips.) This study is focused on the refining process, since it is the dominating mechanical pulping process. Approximately 80 % (1995) of the mechanical pulp manufactured in Sweden is refiner pulp. The various types of pulp differ in their properties, regarding both paper strength and printability, and they are therefore used in different products. Mechanical pulp is mainly used for newsprint and magazine papers. Other areas of use are the production of paper boards, tissues and fluff. Approximately one quarter of all pulp produced in Sweden is of the mechanical type.

A major drawback of the mechanical pulping processes is their large energy consumption. A substantial part of the total energy production in Sweden is in fact consumed in manufacturing mechanical pulps.

2.3.2   The refining process

When refiner pulps are manufactured, the logs are first subdivided into chips with an average length of about 20-25 mm in the grain direction, a thickness of about 3-5 mm and a width of about 10-20 mm [83]. The chips are fed, randomly oriented, to the center of two refiner discs. In a single-disc refiner, only one of the discs revolves, whereas in a double-disc refiner both discs revolve, in opposite directions, see Figure 2.11. The chips are successively disintegrated, the fibres being separated while moving towards the periphery of the discs.

An example of a disc pattern is shown in Figure 2.12. The discs have a system of elevated parts called bars and of lower parts called grooves. Forces are applied by the bars to the chips and fibre bundles. In the grooves, the wooden particles are transported in the radial direction towards the periphery. There are also restrictions, called dams, located in the grooves. These force the pulp out from the grooves so that it can be subjected to further treatment. The wooden material first reaches the breaker bar zone, then the intermediate zone and finally the refining zone before being discharged from the refiner. The design of the refiner discs has mainly been based on empirical knowledge, since the course of events in the refiner is quite complex. Normally, the discs have a coarse pattern near the center (breaker bar zone), whereas the bars of
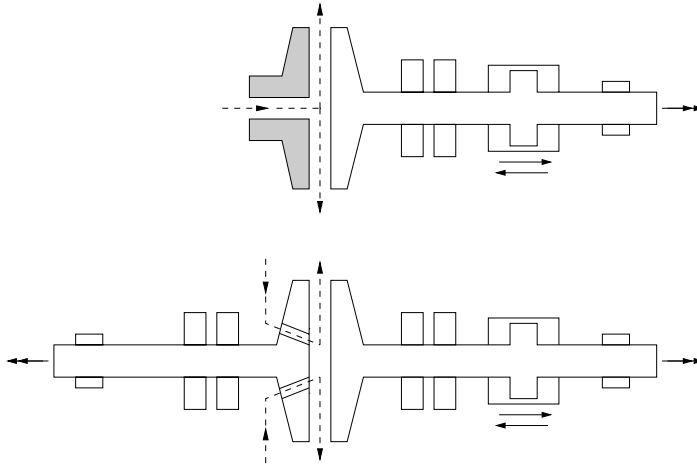
Figure 2.11: View of a single-disc and a double-disc refiner. The upper shaded disc does not rotate.

the discs possess much finer cross-sectional dimensions at the periphery. The discs can be up to 1.5 m in diameter. They operate at between 1200 and 1800 revolutions per minute, resulting in loading rates at the periphery of up to about 100 m/s. The gap between the two plates decreases from the center to the periphery, where it can be as small as 0.1 mm. The loading caused by the two discs is illustrated in cross section in Figure 2.13. The residence time for the wooden material in the refiner is only about a few seconds.
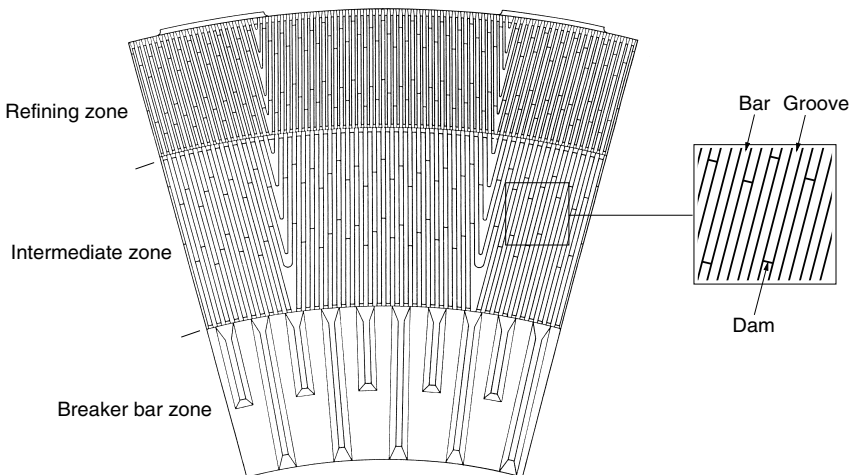
Figure 2.12: Example of a disc pattern.
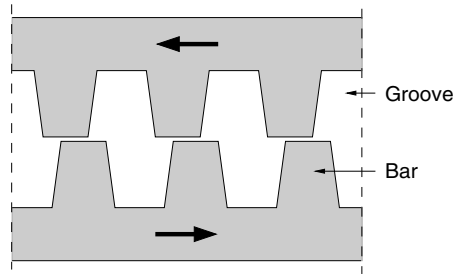
Figure 2.13: The loading caused by the refiner discs.

The mechanisms basic to the refining process are incompletely known. The process can essentially be divided into two main phases. In the first phase, the wooden material is separated into fibres and fibre bundles. This phase is referred to as the phase of initial fibre separation or initial defibration and takes place in the breaker bar zone. The separated fibres are not yet ready to be used for making good-quality paper and need to be further refined in order to possess better papermaking properties. In this phase, the fibrillation phase, the fibres are given suitable properties, such as good optical properties, improved flexibility and fibre-bonding ability. In addition, debris and fibrillar materials, or so-called fines, are produced which significantly contribute to the fibre bonding and the optical and printability properties of the paper.

There are several modifications to the original refiner mechanical pulp (RMP) process. In the thermomechanical pulp (TMP) process, the wood chips are pre-heated with steam prior to refining. The refining zone is pressurized and the refining is performed either in one stage or in two stages. In two-stage refining, untreated fibre bundles from the primary refiner (rejects) are separated and further refined in a pressurized or atmospheric refiner. About 60 % of the heat evolved during the refining process is recovered as steam. This process was developed in the late sixties and has expanded extensively since then. The TMP fibres are stronger than the RMP fibres, but the process requires more energy than RMP. In the chemical thermomechanical pulp (CTMP) a small amount of chemicals are added to the wood chips prior to refining. The CTMP pulps are somewhat stronger than TMP pulps. The energy consumption is higher, the wood yield lower and the opacity much lower, however [35].

2.3.3 Fibre and pulp properties

High opacity and high brightness are desirable optical properties for all printing papers. In order to get a good printability the surface smoothness needs to be high. Mechanical properties such as high strength and stiffness are also desirable. The fibre separation and preparation should be done so that these optical, printability and mechanical properties of the paper can be achieved. The structure of a paper for newsprint is shown in Figure 2.14. It is essential that the fibres are collapsed, see Figure 2.15. This gives good fibre bonding abilities, which is essential for the stiffness and strength of the
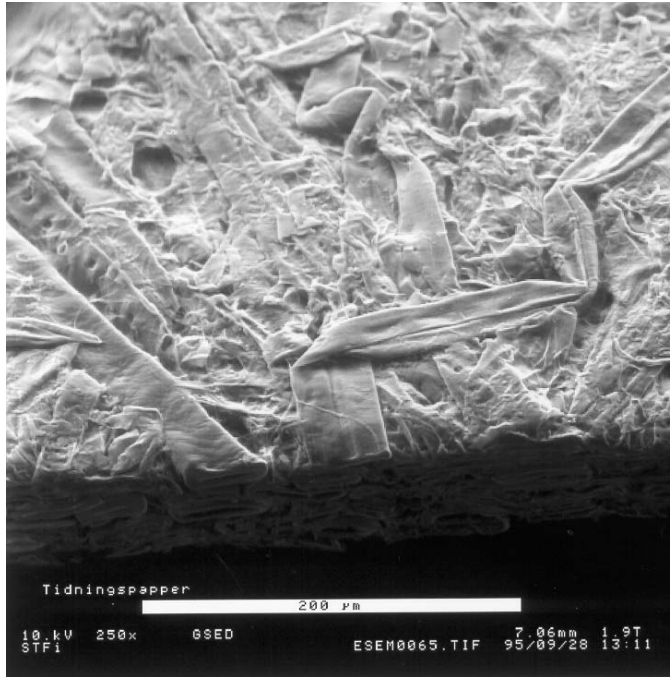
Figure 2.14: Micrograph of a paper for newsprint. From STFI.

paper, and high bending flexibility of the fibre, which prevents or limits fibre rising. The fibre should also have sufficient axial stiffness and strength. According to Hartler [21] refiner pulp fibers contain a large amount of axial microcompressions. These give rise to reduced fibre stiffness and strength. This may not reduce the strength of the paper, however, since the bond strength normally is the critical factor for mechanical pulps, Hartler [21]. The following requirements are thus desirable in the refining process: high brightness of the pulp, high degree of fibre collapse, optimum combination of strength and stiffness, high opacity and a low content of fibres with low bonding ability.

It should be emphasized that the pulp is a mixture of different fibre types (early- and latewood, juvenile and mature wood etc) and fibre fragments of various size (shives and fines). This means that very different paper qualities can be achieved by varying
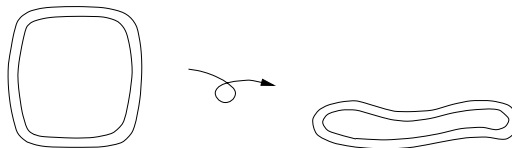
Figure 2.15: Undeformed and collapsed fibre.

this mixture. Pulps intended for different use are mainly characterized by their different distributions between long, middle and fine fibre fractions.

The most important properties used in characterizing the pulp are the shive content and the freeness of the pulp. Shives are coarse, stiff fibre bundles with poor bonding ability, and the shive content should normally be as low as possible. Freeness is a measure of the dewatering capacity of the pulp and gives a good indication of the strength of the pulp and the final quality of the paper. Freeness is measured using a standard test and given in ml CSF (Canadian Standard Freeness).

2.3.4   Fibre separation

The mode of fibre separation in the refining process is not well known. Atack and May [1] observed that the wood chips in a double disc refiner were, in the breaker bar zone, reduced to small matchstick-like particles of rather uniform size with their main axes in the grain direction. In [3], however, Atack et al. state that the chips are disintegrated into coarse pulp at the inlet of the refiner before entering the breaker bar zone. According to May [59] the chips are broken down by fracture along the grain in fairly well-defined stages. First, they are split into matchstick-like material, then into more slender pin chips, larger fibre bundles, smaller bundles and finally into separate fibres as they move towards the periphery of the refining zone.

The importance of the conditions present during the initial defibration has been pointed out in a number of studies in recent years. Investigations of two-stage refining, carried out by Falk et al. [11], showed that primary-stage refining is largely responsible for establishing the characteristic properties of the pulp, whereas secondary refining has only marginal influence. Stationwala and Karnis [78] studied a method for producing pulp based on a combination of refining and grinding. They found that the manner in which the fibres were separated during the initial stage of wood disintegration is important in determining the final properties of the pulp. They also concluded that the differences in quality between groundwood and refiner-mechanical pulp arise from the difference in the way in which the initial fibre separation occurs. The importance of the initial defibration step has also been emphasized by Heikkurinen et al. [23] and Stationwala et al. [79].

2.3.5   Energy consumption

The huge energy consumption required is a serious drawback in manufacturing refiner pulp. It has been estimated that only a small fraction of the electrical energy supplied is utilized to create well-refined pulp fibres, Htun et al. [35]. The majority of the energy is converted to heat without affecting pulp properties. The energy in manufacturing refiner pulp is about 2000 kWh/ton. In general, more energy is required to produce pulp with higher quality. The increasing quality demands have therefore led to higher energy consumption.

The total energy consumption in refining can be divided into the energy used to separate the wood chips into fibres and fibre bundles (the initial defibration phase), E_s, and the energy used to refine the fibres for development of fibre properties (the

fibrillation phase), E_d. Marton et al. [58] found that E_s corresponds to between 9-34 % of the total energy consumption in producing a spruce TMP at a freeness of 150 ml CSF. Based on refining experiments, Marton et al. [58] determined a theoretical value of the separation energy E_s at 15 kWh/ton. This theoretical value only constitutes a small fraction of the corresponding experimentally determined values for E_s, indicating an excessive waste of energy in the fibre separation phase. According to Atalla and Wahren [4] an upper limit of the theoretical separation energy is 23 kWh/ton. Several other studies concerning theoretically determined energy values for fibre separation and fibre development, and concerning the energy efficiency in mechanical pulping, have been presented, indicating a large energy saving potential, e. g. Atack et al. [2], Lamb [54] and Leider and Nissan, [56].

Many efforts have been made to decrease the energy consumption. For instance, changes of the plate design, e. g. Miles and May [60] and Sabourin et al. [74], adjustments of the disc speed, e. g. Sundholm et al. [81], Münster and Dahlquist [61] and Sabourin et al. [74], or changes of the refining temperature, e. g. Hägglund and Höglund [38] and Höglund et al. [40], have been tested. Different types of mechanical loading on the wood chips as a pre-treatment has also been investigated, for instance axial compression by Frazier and Williams [14] and screw press pre-treatment by Murton [62], Johansson et al. [42]. Some improvements concerning the energy efficiency and/or the pulp quality have been found, but no major breakthrough in energy reduction has yet been made. The most energy efficient systems today work at a low plate gap, which means that the fibres are treated more intensely and some inefficient mild loadings are avoided, Höglund [39].

In [40] Höglund et al. present a new two-stage refiner mechanical pulping system. The system is based on the fact that the final pulp properties are mainly established during primary refining, and that conditions during secondary refining are therefore of less importance in determining the final pulp quality. Accordingly, secondary refining is carried out at a temperature well above the softening temperature of the lignin, so as to take advantage of the lower fracture strength of the wood structure at such temperatures. This allows the energy consumption in producing news quality pulp to be reduced by about 20 %. The pulp quality, except for certain minor exceptions, is equivalent to that of the reference pulp. If the primary refining were likewise carried out at a temperature above the softening temperature of lignin, however, this would lead to higher energy consumption and to relatively poor optical properties. This is related to difficulties that exist in creating fine material suitable in quality from fibres that were initially separated in the lignin-rich middle lamella [40].

Höglund and Wilhelmsson [41] conclude that initial treatment at high frequencies and temperatures well below the softening temperature of lignin is beneficial for energy consumption and for optical properties, whereas low frequencies and high temperatures are unfavourable.

2.3.6 Concluding remarks

Conditions present during initial defibration appear to be crucial for both the quality of the pulp and the total consumption of energy, even though only a minor part of the

total energy supplied is consumed during initial defibration. Fracture initiation at the beginning of the process appears to largely control the further fracturing of the wood structure. This is the reason why the present study focuses on the initial conversion of wood into fibres rather than being concerned with the transformation of individual fibres into suitable fibre bundles through further treatment. It is essential to be able to control the initial defibration so that breakdown occurs in the best possible way through an optimized combination of loading mode, loading rate and temperature. This provides the conditions necessary for the saving of energy during subsequent treatment and also for achieving a better quality of pulp.

Chapter 3

Experimental Work

3.1 Introduction

The experimental work performed within this project is presented in this chapter. The main objective of the experiments has been to increase knowledge about the mechanical behavior of wood, in particular about properties of relevance and interest for mechanical pulping applications. The experimental results are also to be used for computer simulations of initial defibration processes. Only properties perpendicular to the grain were studied. Three different types of tests are dealt with, see Figure 3.1. The combined compression and shear tests, described in Section 3.2, concern the behavior of wood when loaded in radial compression and shear. The stable tensile tests, Section 3.3, deal with fracturing properties of wood; the influence of the loading rate on these properties was particularly investigated. The chip shearing tests, Section 3.4, illustrate the complex behavior of wood when loaded perpendicular to the grain under loading conditions similar to those found during refining. Optical equipment was used during the chip shearing tests and the compression and shear tests to obtain pictures of the deformed specimens. All tests were carried out on spruce (Picea abies). In the case of the chip shearing tests and the compression tests, both dry and wet samples were tested, whereas the tensile tests were performed on wood in wet condition only.
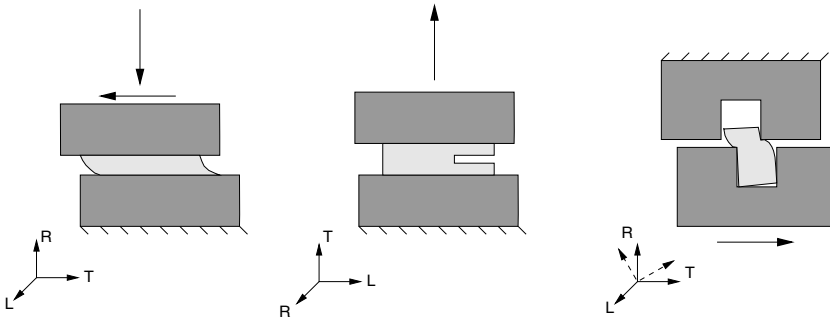

Figure 3.1: Different types of test considered. Left: combined compression and shear tests. Middle: stable tensile tests. Right: chip shearing tests. R, T and L denote the radial, tangential and longitudinal directions, respectively.

3.2 Combined Radial Compression and Shear

3.2.1 General remarks

In mechanical refining the wooden material is compressed between the refiner bars. In order to get good paper quality it is essential that the pulp fibres are collapsed. This makes the behavior of wood loaded by compression perpendicular to the grain of particular interest. The compressive behavior (perpendicular to the grain) of wood has been studied in several investigations, e.g. [28], [83], [84] and [86]. It has been shown that a great deal of energy is needed in order to achieve collapsed fibres by repeated compressive loading. Microscopic studies have indicated a combined compressive and shear loading to be advantageous in order to achieve a more well-defined collapse of the fibres than that obtained for pure compression, e. g. [80]. It is also possible that the energy required to collapse the fibres is lower for combined compression and shear. It is therefore interesting to study whether the combined loading is more energy efficient than the pure compression mode.

In addition, control of mechanical behavior and properties is needed in order to be able to perform realistic numerical simulations of wood disintegration. As is shown in Section 3.4, compressive behavior is of great importance for the overall response of wooden material. Tests involving combined compression and shear loading were thus performed, the specimens being loaded in radial compression and shear loading in the tangential direction. Several cases of combined loading as well as cases of pure compression and pure shear loading were considered. Tests were performed on both dry and wet samples.

The present study involves compressive loading perpendicular to the grain only. Axial compression of wood fibers and the resulting fibre damage and their influence on pulp properties has been studied by Hartler in e. g. [21] and [22].

3.2.2 Specimens and test setup

The specimen geometry is shown in Figure 3.2. Most tests were carried out using specimens with dimensions of approximately $2{\times}6{\times}10$ mm^3 in the radial, tangential and longitudinal directions, respectively. For some tests, specimens having a tangential width of 10 mm were used instead, the dimensions in the other direction being unchanged. The variations in dimensions were less than 6 %. The specimens were prepared with a middle layer of earlywood and with layers of latewood on the upper and lower parts. Approximately half of the specimens' thickness consisted of earlywood. The cross sections of the specimens to be photographed were cut with a razor blade in order to improve the image quality. All specimens were taken from an approximately one-hundred-year-old spruce cut in southern Sweden (Gyvik, Småland). The specimens were taken at chest height from the living tree at annual ring numbers 33, 43-44 and 52-53 counted from the pith. The wooden material had an average density of 450 kg/m^3. During the period of time between sample preparation and testing, the specimens were kept under stable climate conditions at either 60% RH and 20°C, or 95-100% RH and 20°C, corresponding to a moisture content of approximately 12% and

28% respectively. The specimens with an approximate moisture content of 12% will be referred to in this work as dry specimens, and those with the higher moisture content as wet specimens.
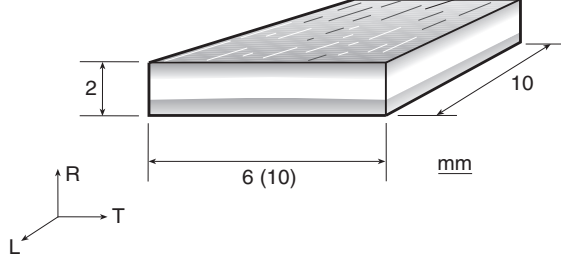

Figure 3.2: Dimensions and fibre orientation of tested specimens, where R, T and L denote the radial, tangential and longitudinal directions, respectively.

The loading mode is defined by the angle ξ

$$\xi = arctan\left(\frac{u_h}{u_v}\right) \tag{3.1}$$

where u_h is the prescribed horizontal displacement and u_v is the prescribed vertical displacement. Five cases were considered, namely ξ=0, 22.5, 45, 67.5 and 90°. Pure compression corresponds to ξ=0° and pure shearing to ξ=90°. At ξ=22.5° the horizontal displacement is about 41 % of the vertical one, at ξ=45° the horizontal and vertical displacements are equal and at ξ=67.5° the horizontal is about 2.4 times larger than the vertical. For the case of ξ=0, 22.5 and 45° the specimens were loaded up to $u_v = 1.0$ mm (corresponding to an average compressive strain of about 50 %), and then they were unloaded. For ξ=67.5 and 90° the maximum deformation was set to $u_h = 1.0$ mm (i.e. a shear strain of 50 %).

The tests were performed using a biaxial electromechanical testing machine. The load was measured using a load cell calibrated for 2.5 kN, and a LVDT transducer was used to measure the deformations. The tests were displacement controlled and the loading rate in the direction involving the largest displacement was set to 0.002 mm/s (the loading rate in the other direction was governed by the angle ξ). The loading rates at unloading were set to ten times higher than at loading. For the loading modes that involved horizontal displacements (shear loading), the specimens were bonded by gluing to the testing machine in order to prevent slipping. A fast-curing cyanoacrylate adhesive was used. For the pure compressive loading no adhesive was used.

In total, 12 test series were carried out. The conditions for the different test series are summarized in Table 3.1. In addition to the main test program consisting of the test series Ad-Ed and Aw-Ew, results from an earlier investigation involving pure radial compression are also given, referred to as test series Fd and Fw. The test conditions for these tests differed from those of series Ad-Ed and Aw-Ew mainly in three respects: the specimen had a different tangential width (10 mm instead of 6 mm); the wooden

material was not taken from the same annual rings (although from the same tree) and
no unloading was considered. For most test series, 5 successful tests were achieved.
For the wet specimens loaded in pure shear (test series Ew) no successful tests were
obtained, however. All 5 tests carried out were rejected. The total number of tests
carried out is 66, and the number of successful tests is 57. The reason for rejection was
in most cases failure in the adhesive layer, but in one case trouble with the test data
registration occurred (test series Fw).

Table 3.1: Test conditions for the different test series.

Test series	Dimension R,T,L [mm³]	Annual ring no.	Moisture content [%]	Loading mode, ξ [°]	Loading rate		Number of tests succ./tot.
					Vert. [mm/s]	Horiz. [mm/s]	
Ad	2×6×10	33	12	0	0.00200	0	5/5
Bd	2×6×10	33	12	22.5	0.00200	0.00083	5/5
Cd	2×6×10	33	12	45.0	0.00200	0.00200	5/5
Dd	2×6×10	33	12	67.5	0.00083	0.00200	5/7
Ed	2×6×10	33	12	90.0	0	0.00200	5/7
Aw	2×6×10	33	28	0	0.00200	0	5/5
Bw	2×6×10	33	28	22.5	0.00200	0.00083	5/5
Cw	2×6×10	33	28	45.0	0.00200	0.00200	5/5
Dw	2×6×10	33	28	67.5	0.00083	0.00200	6/6
Ew	2×6×10	33	28	90.0	0	0.00200	0/4
Fd	2×10×10	43-44, 52-53	12	0	0.00200	0	6/6
Fw	2×10×10	43-44, 52-53	28	0	0.00200	0	5/6

During the tests, series of photographs were taken showing the deformation of the
specimens, the forces and displacements being recorded at the same time. The optical
equipment employed is shown in Figure 3.3. It consists of a CCD camera with different
fixed-focus objectives, together with lighting equipment, a positioning table, a video
monitor and a computer outfitted with a frame-grabber board. The pictures taken were
stored in the computer. A frame-grabber board to which the analogue monochrome
camera (739×575 pixels) was attached was employed. The camera head unit and the
objective, together with fibre light guides, were mounted on top of a positioning table
which is manually adjustable in three directions. Three different camera objectives were
employed. For test series Ad-Ed and Aw-Ew two objectives were used, one capturing
objects of 5×6.5 mm² and the other 0.8×1.0 mm², the first one giving an overall view
of the specimen behavior and the latter providing a magnification making it possible
to observe the behavior of the microstructure. For each of these test series, both the

5 mm and the 0.8 mm objective were utilized. For test series Fd and Fw an objective capturing pictures of 1.5×1.4 mm^2 was used.

In addition to the twelve test series considered, some preliminary tests were performed using image analysis. The objective was to get a better perception of the variation in properties within the growth ring. Results from this type of test will also be given.
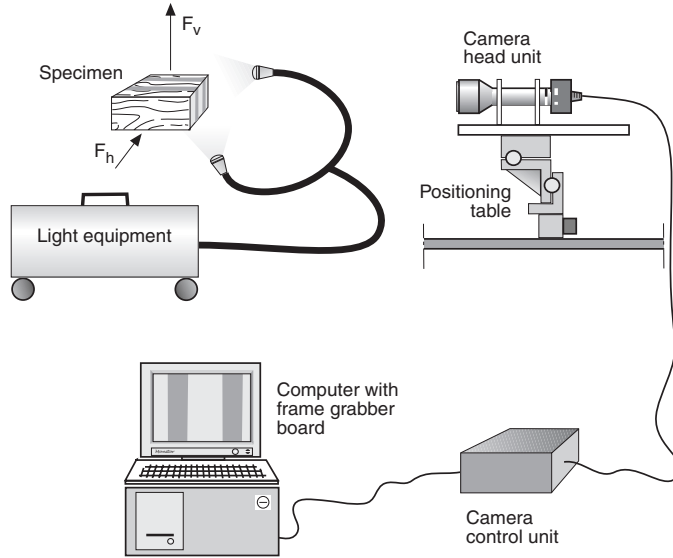
Figure 3.3: Optical equipment used for photographing the behavior of the specimens during loading.

3.2.3 Results

Typical deformation processes for dry specimens loaded in pure compression are shown in Figures 3.4 and 3.5. Figure 3.4 shows the overall deformation process of the specimen. The top picture shows the undeformed specimen, the next three showing the specimen subjected to a strain of 10, 20, and 40 %, respectively (all strain values presented being evaluated as deformation per total initial length of the specimens). In Figure 3.5 the deformation process is shown at a greater level of magnification. (Please note that the specimen depicted in this figure is not the same as in Figure 3.4; both are taken from test series Ad, however.) The photographs here include about 1.0 mm of the specimen height and 0.8 mm of its width, located in the lower part of the specimen (in its mid region) with the abrupt transition between earlywood and latewood being captured. The undeformed state is shown to the left, the two middle pictures showing the deformation of the cell structure at average strain values of 6 % and 10 % and the photograph to the right showing the response at a strain of about 30 %. Up to a strain of approximately 2 % the specimens behaved linearly. When the deformation

was increased further, a failure zone containing localized deformations began to develop. This failure zone started in the first cell rows of the earlywood and developed successively toward the latewood. It developed through collapse of the cell structure, the earlywood cells gradually being crushed. In the third picture in Figure 3.4, the strain was increased to 20 %, the failure zone expanded so as to include about 10 cell rows of the earlywood. Finally, in the fourth photograph, all the earlywood cells have collapsed and the entire earlywood zone is densified, resulting in a considerably higher stress value. From the photographs it can be seen that the cells within the failure zone appear to be totally collapsed, whereas the cells outside this zone seem to be intact.

The deformation processes for combined compression and shear loading at $\xi=22.5°$ and 45° were similar to those for pure compression, see Figure 3.6 showing the deformations at $\xi=45°$ for dry specimens (the pictures to the right do not refer to the same specimen as those to the left). Also in these cases the deformations were strongly localized. The failure zones being developed were initiated at the first rows of the earlywood, then expanding throughout the specimens until all earlywood layers were densified. The cells outside the failure zones were still almost undeformed. At $\xi=67.5°$ the deformations seemed to be slightly more evenly distributed, even though failure zones with localized deformations were developed. The cells outside these zones were, however, more deformed than previously, see Figure 3.7. Furthermore, it seemed as if the cell collapses for the combined modes are more well-defined than for pure compression, all cells being collapsed in a similar manner.

For pure shear loading successful tests were obtained in the dry condition only (in wet condition failure in the adhesive layers occurred in all tests). For the dry specimens shear fracture occurred at the lower transition between the latewood and the earlywood as shown in Figure 3.8. The shear fracture was in all cases developed at a shear strain of about 10-12 %.
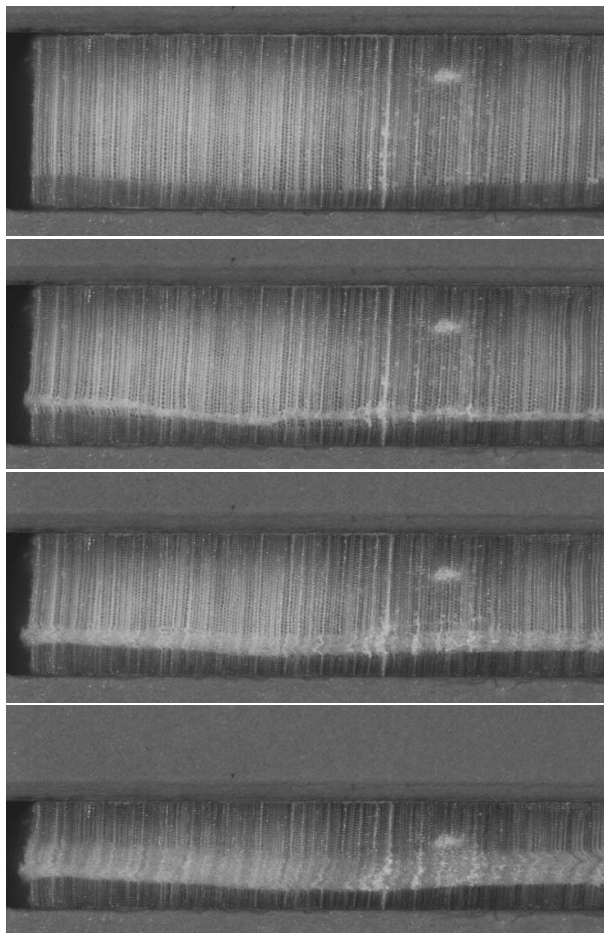
Figure 3.4: Deformation of a dry specimen loaded in pure radial compression. From top to bottom: undeformed, average strain of 10 %, 20 % and 40 %.
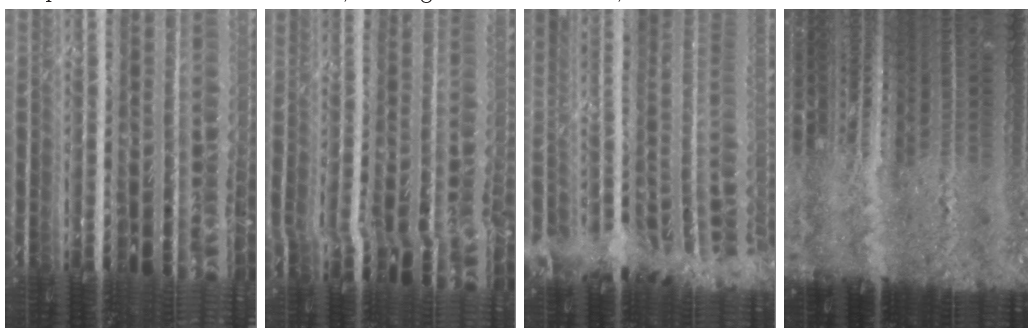
Figure 3.5: Deformation of a dry specimen loaded in pure radial compression. From left to right: undeformed, average strain of 6 %, 10 % and 30 %.
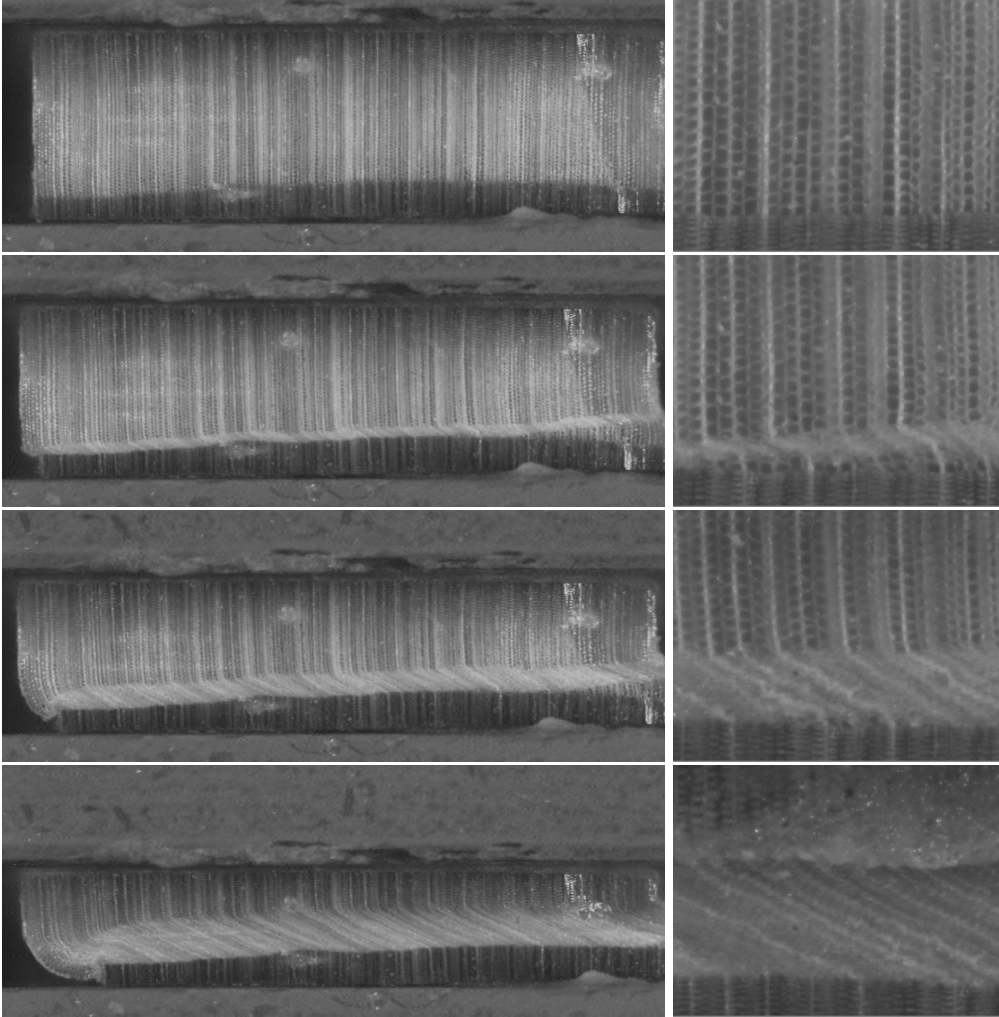
Figure 3.6: Deformation of a dry specimen loaded in combined compression and shear at ξ=45°. From top to bottom: undeformed, average strain of 10 %, 20 % and 40 %. The pictures to the right do not refer to the same specimen as those to the left.
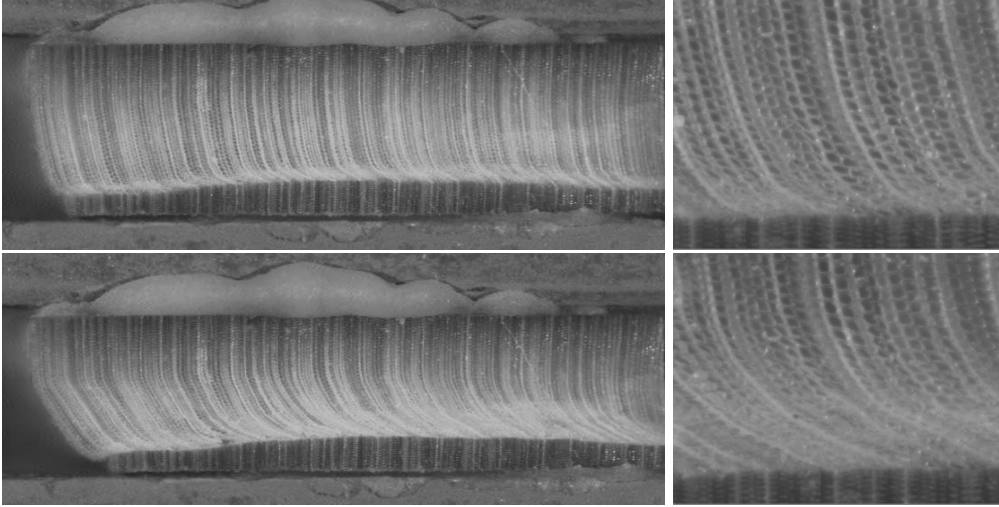
Figure 3.7: Deformation of a dry specimen loaded in combined compression and shear at ξ=67.5°. Top: shear strain of 20 % and normal strain equal to about 8 %. Lower: shear strain of 40 % and normal strain equal to about 17 %. The pictures to the right do not refer to the same specimen as those to the left.
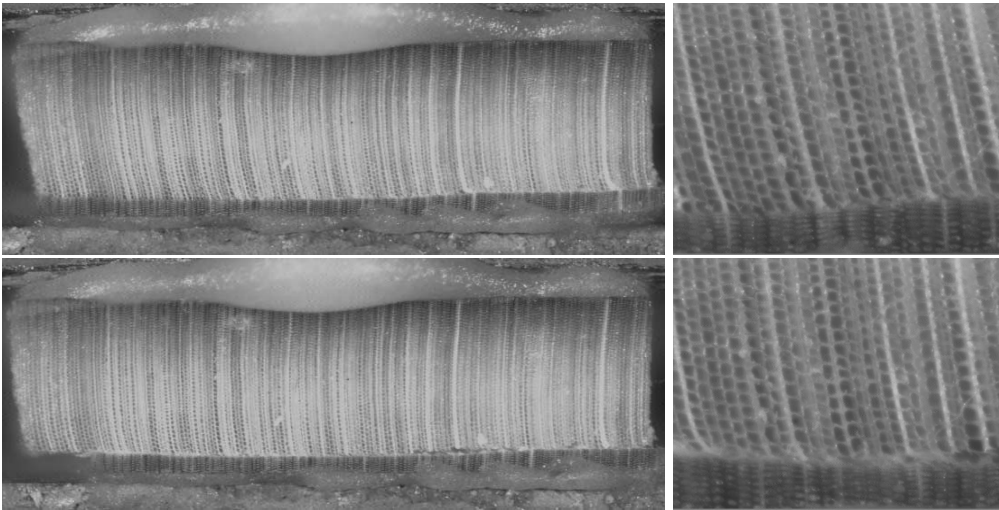
Figure 3.8: Deformation of a dry specimen loaded in pure shear. Top: shear strain of 11 %. Lower: shear strain of 40 %. The pictures to the right do not refer to the same specimen as those to the left.

In most of the specimens the failure zone started to develop in the first cell rows of the earlywood as is shown in Figures 3.4-3.7. This seems natural since these cells are, normally, the weakest ones, having the thinnest cell walls and the thickest lumens. In some of the specimens of test series Fd and Fw (3 of the 11), however, the cell collapse started in the middle of the earlywood. This behavior is illustrated in Figure 3.9. The first picture shows the undeformed specimen, the second shows the specimen when the failure zone had just started to develop and the third picture shows how the failure zone continued to expand. After the failure zone was initiated, somewhere in the middle of the earlywood zone, it first expanded initially to include the first part of the earlywood, expanding then towards the transition zone until all the earlywood cells had collapsed.
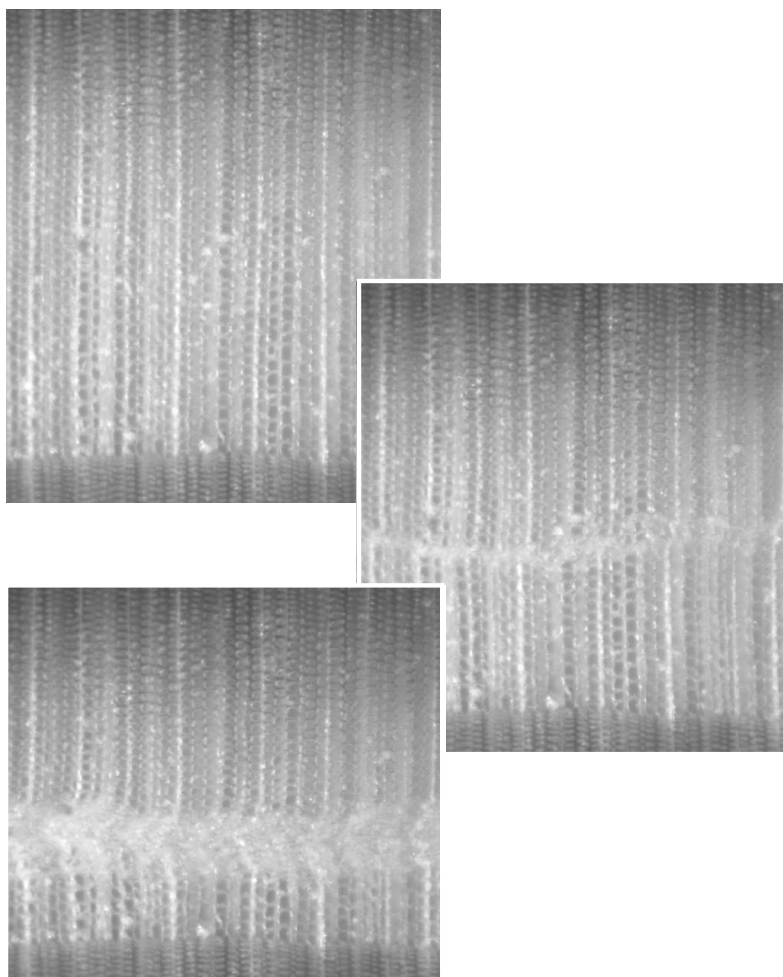
Figure 3.9: Cell collapse starting in the middle of the earlywood zone. Specimen from test series Fd.

The reason for failure starting in the middle of the earlywood zone and not in the first cell rows of earlywood in these specimens might be that there was some kind of weakening in the middle of the earlywood which then initiated the failure. The weakening could be due to some external damage to the cell structure or could be the result of special growth conditions. Another explanation could be that initiation of the failure zone is related to the action of the ray cells. These can be considered as columns or tubes oriented in the radial direction within the cell structure. Although the relatively stiff latewood cells provide support to the ray cells sideways, the ray cells may buckle in the weaker earlywood zone when the structure is loaded in compression. This buckling may result in cell collapse occurring in the middle of the earlywood zone instead of in a more natural way in the first, and normally weakest, cell rows.

The photographs of the deformed specimens revealed no significant differences in behavior between the dry and the wet samples. Differences between the dry and wet specimens could be observed, however, in the stress-strain curves that were recorded. Stress-strain curves for the different test series are given in Figures 3.10-3.12 (note the different scales in the diagrams). The solid curves show the response for the dry specimens and the dashed for the wet ones. The normal stress was evaluated by dividing the vertical force by the original cross section area of the specimens, and the shear stress was obtained similarly from the recorded horizontal force. The strain values were evaluated by dividing the displacements by the initial height of the specimens. It should be noted that since almost all the deformation occurs in the earlywood, the strain values would be considerably higher if they were determined for a pure earlywood layer separately. The curves given are hand-drawn mean value curves for each test series. The complete set of curves for each series (together with the mean value curves) are given in Appendix A. The curves there show filtered response, the filtering being made using the MATLAB signal processing toolbox [51] (Butterworth filtering). Typical unfiltered response together with the corresponding filtered curves are shown in Figure A.1 in the Appendix. As can be seen in the Appendix, there is fairly good agreement between the results of the various tests within the different test series except for a few differences in the stress values.

For the cases of pure compression and combined loading with ξ=22.5-45°, the compression stress-strain curve can be characterized by an initial linear region, followed by a plateau region in which stress only increases slightly, and finally a densification region with more rapidly increasing stress. The plateau stress is slightly lower for the case of pure compression than for the combined modes. In pure compression the value is about 4 MPa for the dry specimens and 2 MPa for the wet ones whereas the corresponding values in the combined modes are about 5 MPa and 2.5 MPa, respectively. For the combined loading modes, particularly for the dry specimens, there is a characteristic initial drop in yield stress, however. (This feature was also seen in a few of the dry specimens loaded in pure compression.) It can also be seen that for the case of ξ=45° there is almost no increase in stress at the plateau region, the stress after the initial drop being approximately constant up to a strain of about 30 %. In general, the compression stress values for the wet specimens are about half (or slightly more) of those for the dry specimens, throughout the response. The initial stiffness is also clearly lower for the wet specimens than for the dry ones.

Figure 3.10: Stress-strain curves for test series Ad-Cd and Aw-Cw. The curves shown are mean-value curves. Solid lines show results for dry specimens (Ad-Cd) and dashed lines for wet specimens (Aw-Cw). Top: Ad and Aw. Middle: Bd and Bw. Lower: Cd and Cw.

Figure 3.11: Stress-strain curves for test series Dd-Ed and Dw. The curves shown are mean-value curves. Solid lines show results for dry specimens (Dd-Ed) and dashed lines for wet specimens (Dw). Top: Dd and Dw. Lower: Ed.
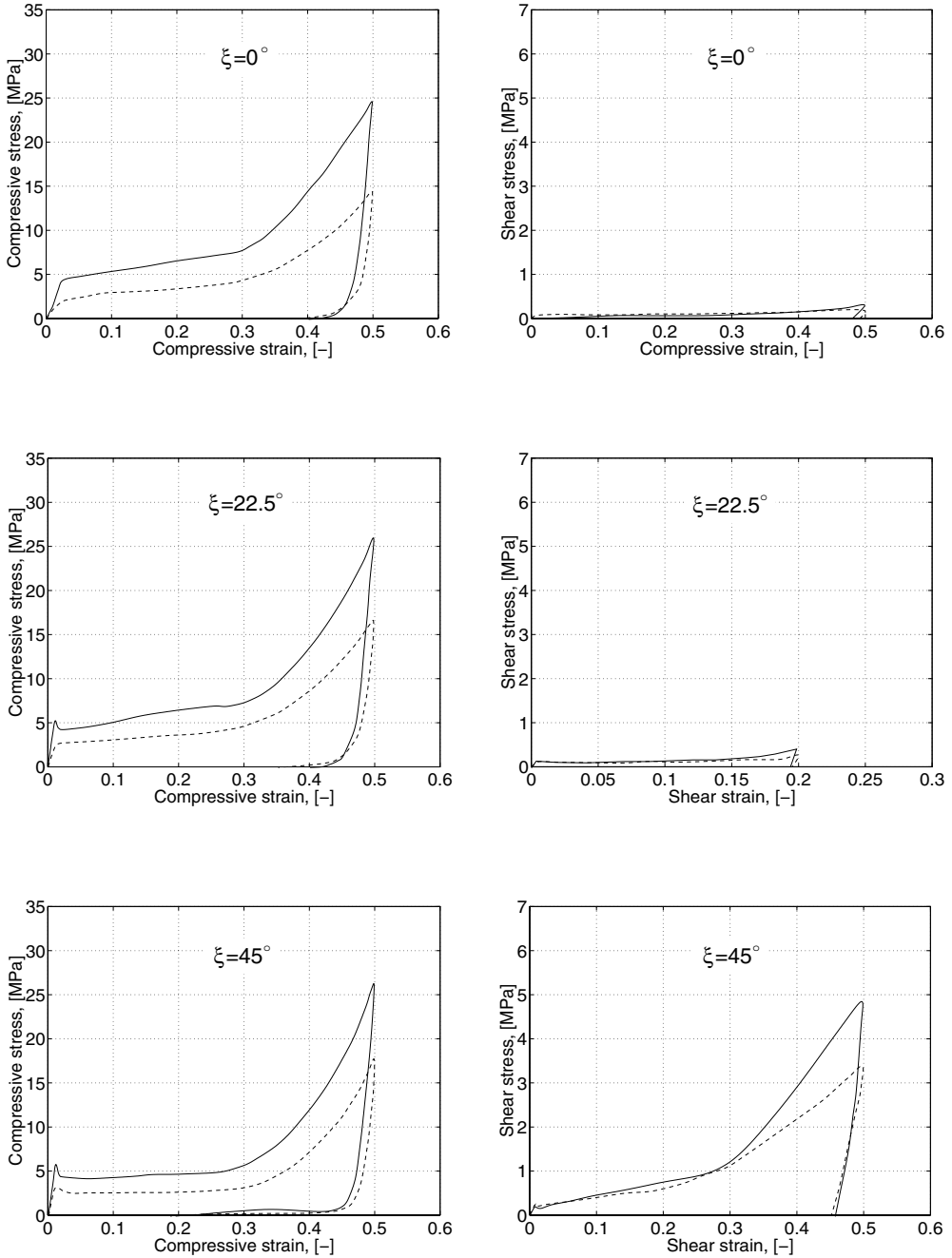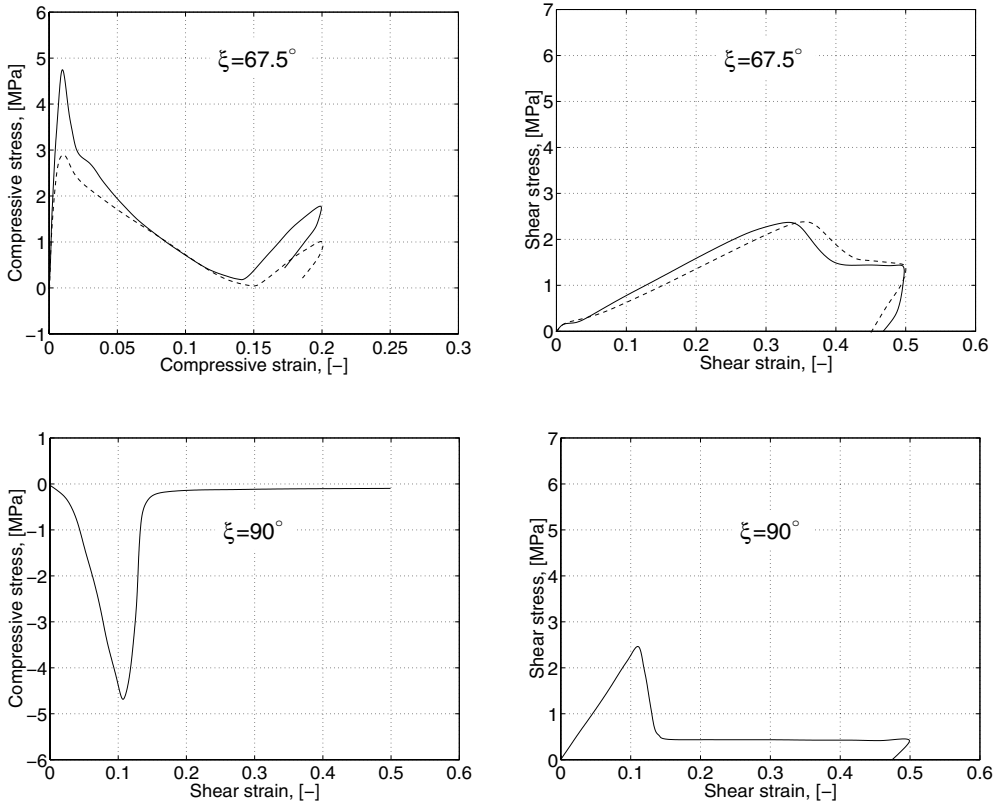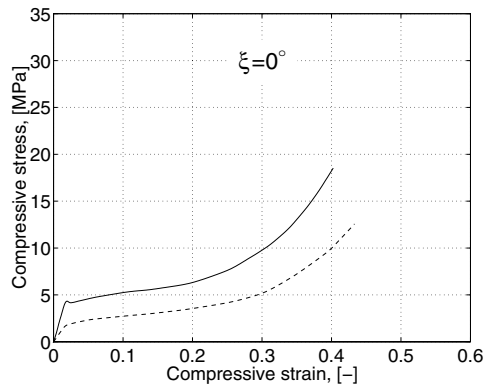

Figure 3.12: Stress-strain curves for test series Fd and Fw. The curves shown are mean-value curves. The solid line shows results for dry specimens (Fd) and the dashed line for wet specimens (Fw).

In comparing the responses of series Ad and Aw with those of the Fd and Fw series one can see that the results are very similar except that the densification region starts at a slightly lower deformation for the F series. This is probably due to the fact that the specimens in these series contained a larger amount of latewood than those of the A series.

The shear stress is very low and insignificant both for the case of pure compression and for ξ=22.5°. For ξ=45° the shear stress values are considerably higher, although they are still much lower than the compression stress values. The shape of the shear stress-strain curve for ξ=45° is similar to the compression stress-strain curve. The shear stress for the wet specimens is approximately the same as for the dry specimens, up to a strain of about 30 %. Thereafter the shear stress increases more rapidly for the dry than for the wet specimens.

At ξ=67.5° the responses differ significantly from those of the lower values of ξ. The initial yield stress, both for the wet and the dry specimens, is about the same as for the lower values of ξ. After the initial linear region the compression stress decreases consistently up to a strain of about 15 %, the stress here being almost zero. Thereafter the stress increases again. The shear stress increases almost linearly up to a shear strain of about 30 %. The shear stress there is about 2.5 MPa for both the dry and the wet specimens. For a further increase in deformation the shear stress decreases somewhat. This may be due to shear fracture, probably at the lower transition between the earlywood and the latewood. In pure shear, a tensile stress is developed with a maximum value of approximately 4.5 Mpa at a shear strain of about 10-12 %. At this point, shear fracture is developed at the transition zone between the earlywood and the latewood and the tensile stress then decreases rapidly. The shear stress increases linearly up to 10-12 % strain with a maximum value of about 2.5 MPa. The very low shear modulus of about 25 Mpa in rolling shear is apparent from the diagram.

As can be seen from the unloading paths, most of the deformation is inelastic. In all cases, the stresses initially decrease rapidly with low springbacks at unloading. For pure compression the strains at zero stresses are about 35-40 %. For the combined loading modes this strain is slightly lower, especially for the case of ξ=45°.

The influence of the shear deformation on the energy consumption is of significant interest. One of the goals of these test series was to elucidate if the combined loading modes are more energy consuming than that of pure radial compression. The energy absorbed at three different strain levels is given in Table 3.2 for some of the test series. The strain levels considered are those of 20 %, 40 % and the complete loading cycles.

The unloading for test series Ad-Cd, Aw-Cw was to occur at a compressive strain of 50 %. Due to small discrepancies in specimen lengths, unloading generally did not occur at this exact strain value, as can be seen from the diagrams in Appendix A. The influence on the results due to these discrepancies was rather small, but it explains the relatively larger spread in results for the complete loading cycles than for lower deformation levels. Gaps between the specimens and the loading machine were present in two cases for the pure compression loading (one in series Ad and one in Aw). This resulted in unloading occurring at a strain of about 45 % only, clearly affecting the results when evaluating the energy consumption for the complete loading cycle. The values indicated by * in Table 3.2 show the results obtained when these tests are

neglected. Furthermore, one test in series Cd had to be interrupted at a strain slightly lower than 50 % due to the capacity of the load cell being reached. The unloading path in this test was therefore not being captured. The values indicated by ** are the results when this test was neglected.

The combined loading modes are generally slightly more energy consuming than pure compression. Only in a few cases did combined loading require less energy than that of pure compression, and in these cases the reduction in energy consumption is small.

Table 3.2: Energy absorption at different strain levels (* one test neglected due to unloading at a too low strain, ** one test neglected due to unloading not being captured).

Test series	Absorbed energy [kJ/m³]					
	comp. strain of 20 %		comp. strain of 40 %		complete loading cycle	
	mean	s.d.	mean	s. d.	mean	s. d.
Ad	981.4	123.3	2776.8	271.4	3903.8, 4064.1*	627.4, 594.1*
Bd	986.4	45.7	2667.8	121.1	4408.4	501.1
Cd	940.2	62.1	2571.9	402.2	4139.4, 3901.3**	704.3, 532.3**
Dd	977.9	122.7	-	-	-	-
Aw	539.8	20.6	1492.4	74.8	2207.1, 2258.9*	172.0, 146.9*
Bw	628.7	32.8	1701.1	98.6	2630.2	229.4
Cw	630.8	32.3	1657.5	56.9	2662.8	156.2
Dw	858.1	62.3	-	-	-	-

In order to get information about the variation of properties within the growth ring, image analysis may be utilized. Some preliminary tests were made using this approach. The loading mode considered was that of pure compression. An example of a specimen used is shown in Figure 3.13, the specimen being supplied with dots. By following the movements of these dots, much additional information may be obtained. An example of results obtained is given in Figure 3.14. The diagram shows stress-strain curves for some different regions of the specimen. The numbers 1-4 refer to the points indicated in Figure 3.13. Clear differences between the curves can be seen, a significant variation in mechanical properties within the growth ring being present.
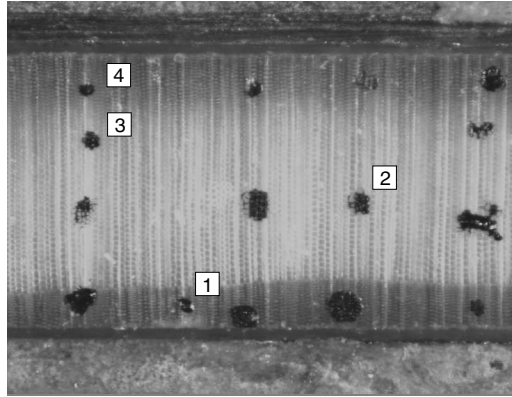
Figure 3.13: Example of specimen used in tests with image analysis.
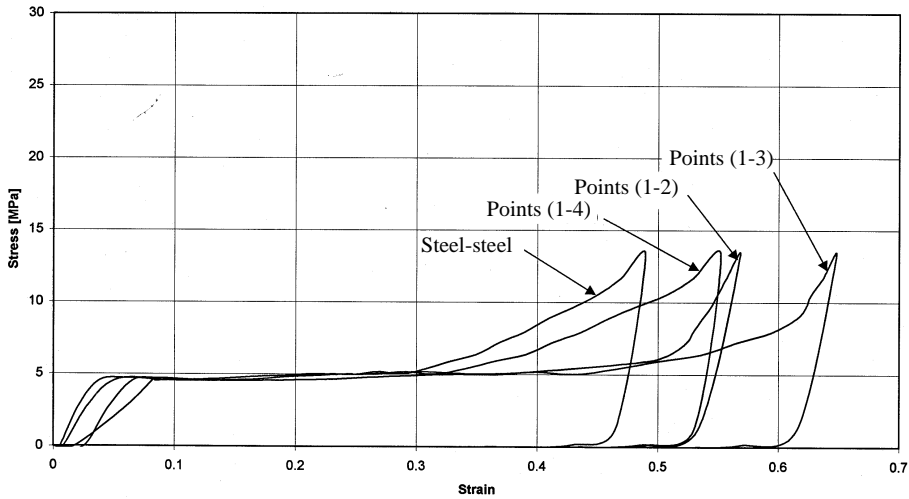
Figure 3.14: Examples of stress-strain curves for different regions of the growth ring obtained by use of image analysis. The numbers 1-4 refer to the dots on the specimen, see Figure 3.13.

3.2.4   Concluding remarks

The experimental work presented in this section was carried out in order to determine the mechanical behavior of wood when loaded in combined radial compression and rolling shear as well as in pure radial compression and pure rolling shear. The loading mode is defined by the angle ξ. Five cases were considered, namely $\xi=0$, 22.5, 45, 67.5 and 90° where $\xi=0°$ corresponds to pure compression and $\xi=90°$ to pure shear loading. At $\xi=45°$ the shear strain and normal strains are equal. Wood in both dry and wet

condition was tested, having a moisture content of 12% and of 28%, respectively. All tests were carried out at room temperature. No successful tests were obtained in the wet condition for the case of pure shear loading due to failure in the adhesive layer. For all the other cases considered, at least five successful tests were obtained. The results from the tests allow the following conclusions to be drawn:

- *Failure zones containing localized deformations develop when wood is loaded by compression in the radial direction.*
  The failure zones develop through collapse of the cell structure due to cell wall buckling processes, the earlywood cells gradually being crushed. Even when the cells within these zones have totally collapsed, the cells outside appear to be almost intact. For $\xi=67.5°$ it seems as if the deformations are not as localized into the failure zone as is the case for the lower values of ξ.

- *Normally the first cells to collapse are those formed early in the season close to the latewood cells.*
  These cells are normally the weakest, having the thinnest cell walls and the thickest lumens and thereby the lowest buckling force. However, in a few cases the initial collapse started in the middle of the earlywood zone. The reason for this might be related to buckling of the ray cells, special growth conditions or some external damage of the cell structure.

- *The influence of shear deformation on the compression stress-strain curve is relatively small up to $\xi=45°$. At $\xi=67.5°$ the response differs considerably from that of pure compression.*
  At $\xi=22.5°$ the compressive response is almost identical to that of pure compression and the shear stress is insignificant. The main difference at $\xi=45°$ is that the plateau region is flatter with almost no increase in stress and that the shear stresses are greater, although still considerably lower than the normal compressive stress. The initial yield stress was found to be somewhat higher for the combined modes than for pure compression. For the dry specimens, a small initial drop in the stress plateau was found for the combined modes (for the case of $\xi=45°$ this feature was also seen for the wet specimens although not as pronounced as for the dry ones). The initial yield stress is about the same at $\xi=67.5°$ as for the lower values of ξ but the stress then decreases to nearly zero at a strain of about 15 %, whereafter the stress increases again.

- *Pure shear loading results in shear fracture along the transition between earlywood and latewood.*
  The shear failure occurred at a shear strain of about 10-12 %. The average maximum shear stress was found to be about 2.5 MPa (dry specimens).

- *The rolling shear modulus is very low.*
  These tests indicate the modulus in rolling shear to be as low as about 20-30 MPa.

- *The combined compression and shear loading modes require about the same energy as that of pure compression.*

Up to a given compressive strain, the energy absorbed for the combined loading modes was, in most cases, found to be somewhat higher than for pure compression. The cell collapse for the combined modes seemed to be more well-defined than for pure radial compression, however, with all cells being collapsed in a similar manner.

- *Differences in the stress-strain relations between dry and wet specimens can be observed.*
  The dry and the wet specimens were similar in their general behavior, but clear differences in their initial stiffness and their plateau stress could be observed. Both the initial stiffness and the plateau stress were about 50 % lower for the wet specimens than for the dry ones. These differences mainly concern the compressive stress-strain relations, while the differences in shear stresses were smaller. The energy absorbed at a given compressive strain for the wet specimens was, in general, equal to about 60 % of that for the corresponding dry ones. For the case of $\xi=67.5°$ and a compressive strain of 20 %, the energy absorbed for the wet specimens was almost equal to that for the dry ones.

- *Stress-strain relations for different regions of the growth ring differ.*
  By the use of image analysis much additional information may be obtained. For instance, variations in properties within the specimen may be determined. Some preliminary tests that were carried out utilizing image analysis showed a variation in the stress-strain relations for different regions of the growth ring. The loading mode considered was that of pure compression.

3.3 Stable Tensile Tests

3.3.1 General remarks

Mechanical pulping aims at creating fractures in the wood so that the fibres will be separated. Knowledge about the fracture mechanical properties of wood is therefore essential for understanding defibration processes and also to be able to perform realistic computer simulations of wood disintegration. The aim of the investigation presented in this section was to determine the tensile strength, the modulus of elasticity and the fracturing properties of wood in wet condition (moisture content of about 30 %) for loading perpendicular to the grain, and the dependence of these properties on the loading rate. For the corresponding properties of dry wood (moisture content of about 12 %) reference is made to studies carried out earlier [8, 63]. The tests performed were displacement-controlled tensile tests, the specimens being loaded in the tangential direction. All tests were performed on spruce.

3.3.2 Determination of fracturing properties by tensile tests

Since the fracturing properties of wood were determined by tensile tests, these tests must be stable. It was also necessary to measure the complete load-displacement curve, including the descending path. The particular problem in measuring such a curve is obtaining stability in the test. In order for stability to be achieved, the testing equipment and the design of the specimen need to be appropriate. A background for this need is described in the following.

Consider a hypothetical experiment in which a specimen is loaded in pure tension. Assume that the testing machine and the grip arrangements are infinitely stiff. As the load is applied to the specimen, it will initially behave elastically. When the stress reaches the tensile strength of the material, a damage zone containing localized deformations may develop. If the deformation is further increased, the load carried by the specimen decreases and the material outside the damage zone is unloaded, see Figure 3.15a. The total deformation of the specimen Δl is assumed to be given by

$$\Delta l = l\epsilon + \delta, \tag{3.2}$$

where $l\epsilon$ is the deformation of the material outside the fracture zone and δ is the softening deformation of the fracture zone, Figure 3.15a. If the specimen is too long (and accordingly too weak), the unloading recovery is greater than the softening deformations in the fracture zone, implying that the total deformation decreases during unloading. Since this is usually not possible even when the test is displacement controlled, a sudden and unstable failure usually occurs, see Figure 3.15b. More generally, the strain energy stored in the specimen as the test is carried out is greater when the specimen is longer. If the strain energy becomes too great a sudden failure will occur, Gustafsson [18]. Thus, even for an infinitely stiff testing machine, there is a maximum length of the specimen which cannot be exceeded if stable tensile tests are to be performed. This critical length, l_c, depends on the modulus of elasticity, the fracture

energy and the tensile strength of the material. Representative values for spruce per-
pendicular to the grain correspond to a critical length in the range of 5-10 mm, see
Boström [8].

In the hypothetical experiment described above, the testing machine and the grip
arrangements were assumed to be infinitely stiff, something that obviously is not the
case in a real test. The stiffness of the surrounding of the fracture zone depends not only
on the stiffness of the specimen itself but also on the stiffness of the grip arrangements
and of the testing machine. Thus, in order to obtain stable tests, the testing equipment
and the design of the specimen must be appropriate. The dimensions of the specimen
should be small, the grip arrangements should be made sufficiently stiff and a stiff
testing machine should be used in order to facilitate recording of the complete load-
displacement curve. Not only the axial stiffness of the testing machine needs to be great
enough, but also the rotational stiffness, in order to avoid instability due to rotation [8].
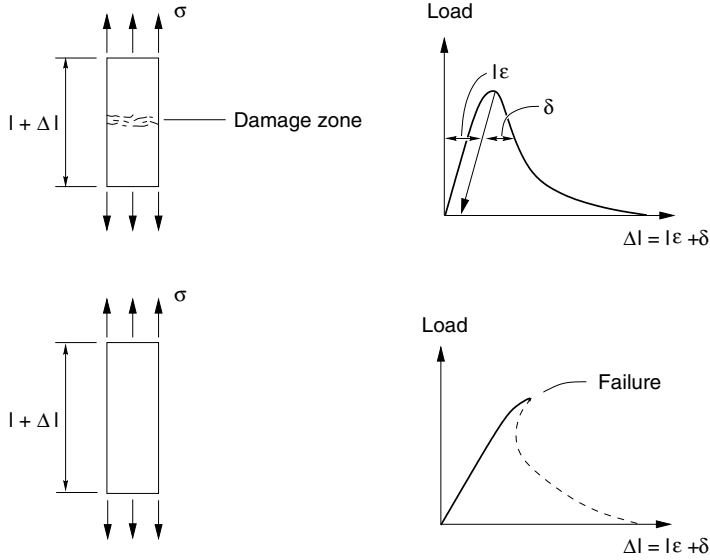
Figure 3.15: Characteristic load-displacement curves. Top: Stable tensile test. Lower:
Unstable tensile test.

The fracture energy G_F, defined as the energy needed to bring a unit area of
the material to complete fracture, is an important parameter in characterizing the
fracturing properties of a material. It is also an important measure in connection with
defibration processes aiming at decomposing the material. G_F is evaluated as the area
below the $\sigma - \Delta l$ curve, see Figure 3.16. The inelastic response of the material outside
the fracture zone is thus assumed to be negligible.

3.3.3   Specimens and test setup

The tests were carried out to determine the tensile strength, the modulus of elasticity
and the fracture mechanical properties of wood in green condition and the dependence
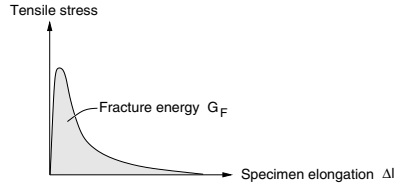
Figure 3.16: Evaluation of the fracture energy G_F.

of these properties on the loading rate. Displacement controlled tensile tests were employed, the specimens being loaded in the tangential direction. The specimens were taken from an approximately 100-year-old tree, at a location in the stem about 40 years from the pith; the ring width was about 1 mm. The wooden material had a density of 475 kg/m^3. Directly after the tree was cut, a 1.6 m long log was wrapped in plastic during transportation, and thereafter stored in 80% RH at 6°C.

A number of 15 mm thick slices were sawn from the log. Each slice was further divided into 3 mm thick strips from which the specimens were prepared, see Figure 3.17. A notch was cut in each specimen in order to obtain a well-defined fracture zone. Each notch was 0.5 mm wide and 5 mm long. Ten specimens were prepared from each slice of the log. In addition to these, special specimens were taken in order to measure the moisture content. To prevent drying, all specimens not used during the preparation period were kept in a climate box.
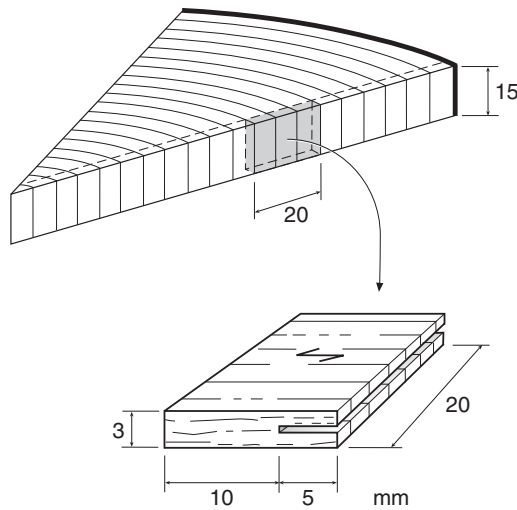

Figure 3.17: Preparation and geometry of the specimens.

Two solid steel cylinders were mounted in the hydraulic grips of the testing machine, (a MTS 810 "closed loop" machine). The specimen in question was placed between the

two cylinders, bonded to them by a fast-curing cyanoacrylate adhesive and cured for approximately 10 minutes at a constant compression of about 0.4 MPa. The test was run immediately thereafter. During testing, the load and the elongation were recorded. The load was measured using a load cell calibrated for 10 kN. The deformation was measured using a clip-gauge mounted between the free surfaces of the steel cylinders. The test setup, including a mounted specimen, is shown in Figure 3.18.
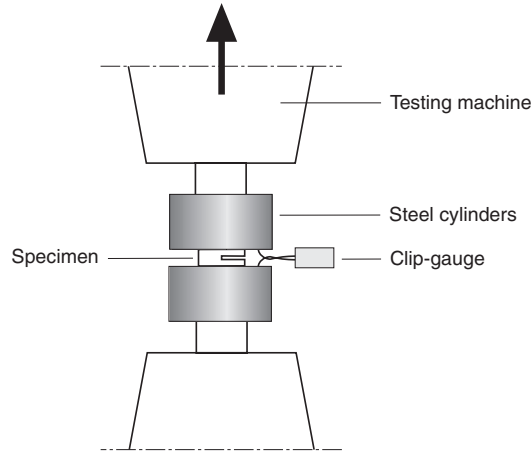
Figure 3.18: Schematic diagram of the test setup for tensile tests.

The test conditions for the different test series involved in the investigation are summarized in Table 3.3. The main part of the test program consisted of the series A1-A5. Tests were performed for loading rates that varied between 0.001 to 10 mm/s. The aim was to achieve 5 successful tests for each loading rate, which meant a total of 25 successful tests. To accomplish this, 37 tests needed to be performed, since 12 tests were rejected. The major reason for rejection was failure of the adhesive layer, although some problems in registering the test data also occurred. The maximum stress during the test involved a displacement of approximately 0.05 mm; taking only 0.005 s for the fastest loading. High demands were thus placed on the speed of the test data registration program. The program used was able to record 1000 test data per second.

In addition to the series A1-A5, tests were performed in order to investigate whether the stiffness properties of the glue had an influence on the evaluation of the modulus of elasticity. The specimens used for these tests were similar to those used in the A-series, although they were not notched. Two specimen thicknesses were investigated: 3 mm (series B1) and 6 mm (series B2). The loading rate in these tests was set to 0.1 mm/s.

Table 3.3: Test conditions for the different test series.

Test series	Loading rate [mm/s]	Specimen thickness [mm]	Moisture content [%]	Number of tests successful/total
A1	0.001	3	33	5/5
A2	0.01	3	33	5/6
A3	0.1	3	28	5/9
A4	1.0	3	31	5/9
A5	10	3	40	5/8
B1	0.1	3	30	4/5
B2	0.1	6	30	5/5

3.3.4 Results

The results for test series A1-A5 are shown in Figures 3.19-3.22. The complete stress-displacement curves for the different loading rates are given in Figure 3.19. A comparison of the mean-value curves obtained for the various loading rates is also shown. The fracture energy, tensile strength and modulus of elasticity for the different loading rates are shown in Figures 3.20-3.22, respectively.

No significant difference in results between the two specimen thicknesses considered in series B1 and B2 was found. The average tangential modulus of elasticity for the B1 series was found to be 302 MPa, whereas the result for the thicker specimens in series B2 was 323 MPa. The difference is small as compared to the spread in results within the test series (the standard deviation was 56 and 62 MPa for the two series, respectively). The influence of the glue stiffness on the results when evaluating the modulus of elasticity can thus be regarded as small.

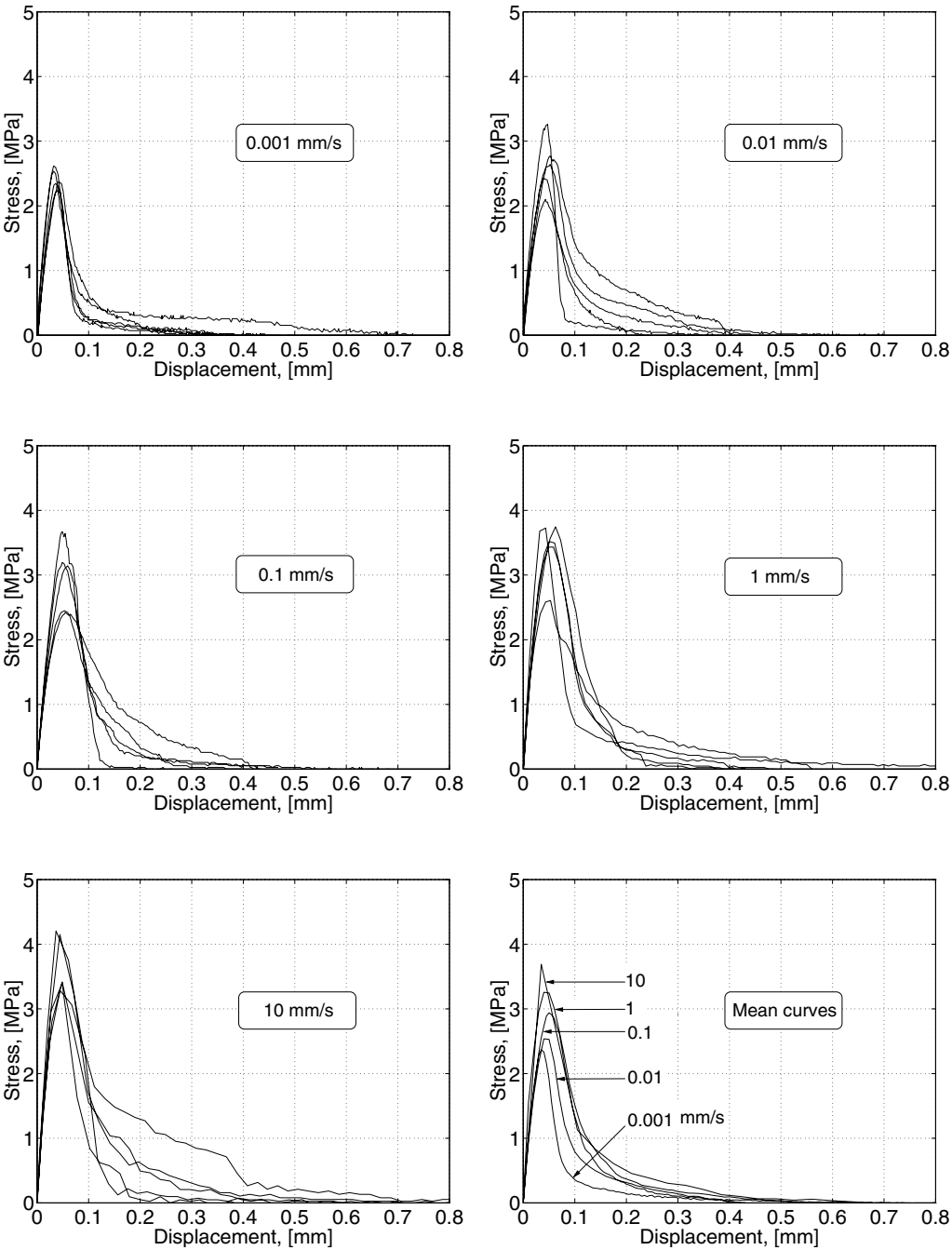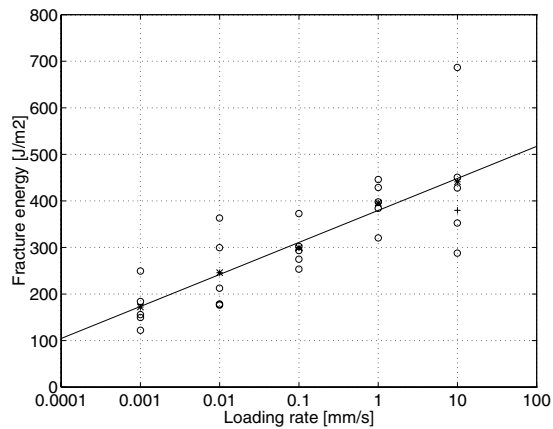Figure 3.19: Stress-displacement curves for different loading rates.

Figure 3.20: Fracture energy for different loading rates (*=average values and +=average values based on 4 tests). Note the logarithmic scale on the horizontal axis.
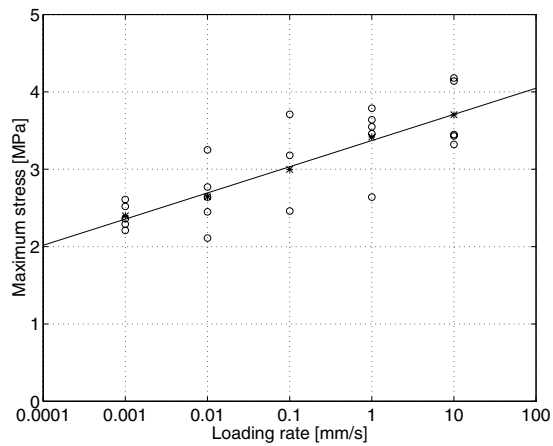

Figure 3.21: Tensile strength for different loading rates (*=average values). Note the logarithmic scale on the horizontal axis.
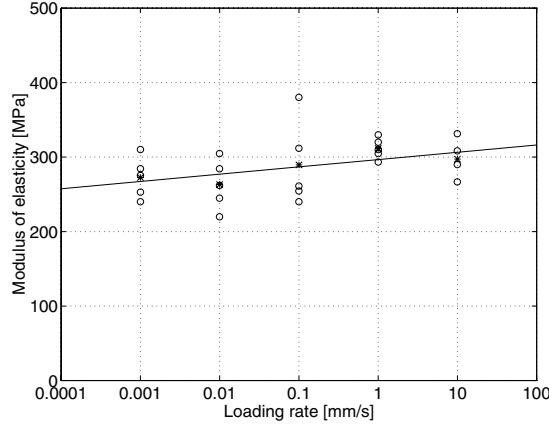
Figure 3.22: Modulus of elasticity for different loading rates (*=average values). Note the logarithmic scale on the horizontal axis.

3.3.5   Concluding remarks

The experiments presented constitute an introductory study to determine fracturing properties needed for numerical simulation of defibration processes. It would be desirable to supplement the investigation by further tests carried out with higher loading rates, with other material orientations and with specimens being taken from different annual rings. In addition, similar tests should also be performed for shearing-mode (Mode II) and mixed-mode fracture, since these play a significant role in the defibration process.

A total of 25 successful tensile tests were performed. The conclusions that can be drawn on the basis of these tests can be summarized as follows:

- *Fracture energy increases as loading rates increase.*
  The fracture energy ranged from about 170 J/m² to 440 J/m² in the loading rate interval studied, (0.001-10 mm/s). There was one value in the test series for the loading rate of 10 mm/s which differed very much from the others (due to the development of double cracks), see Figures 3.19 and 3.20. Disregarding this value, the average fracture energy for this test series was found to be 380 J/m². This indicates that, at a loading rate larger than 10 mm/s, the fracture energy is nearly constant.

- *Tensile strength increases as loading rates increase.*
  The tensile strength increased by about 10-15 % when the loading rate was increased by a factor of ten.

- *Modulus of elasticity increases slightly as loading rates increase.*
  This property is less rate-dependent than the fracture energy and the strength.

3.4 Chip Shearing Tests

3.4.1 General remarks

The chip shearing tests were performed in order to obtain a better understanding of the defibration process, especially with respect to the mechanical behavior of wood loaded perpendicular to the grain. The influence of the specimen orientation versus loading direction, and the influence of the earlywood and latewood configuration within the specimen on the deformation and fracturing process, were investigated. The tests performed also indicate the complex loading conditions present in initial defibration processes. Furthermore, the tests serve as examples used in numerical simulations (Chapter 6). Optical equipment was used to photograph the specimens during testing so as to reveal deformations and fracturing of the material. The forces and displacements involved were also recorded. The test setup and sample dimensions were chosen in light of the geometry typical of refiner segments, the loading conditions being made to resemble those present in the initial defibration process. A major difference between the testing conditions in the present study and those found in an actual refiner concerns the loading rate. The tests performed were carried out for a very low loading rate whereas the wood material in a refiner is subjected to much higher loading rates. Tests were performed on both dry and wet samples.

3.4.2 Specimens and test setup

The test setup is shown schematically in Figure 3.23. The specimen is placed between two steel plates, the test being run by moving the lower plate horizontally while the upper one remains fixed. The specimen is thus subjected to a shear loading resembling the loading on the wood chips in a refiner caused by the two rotating discs. In designing the steel plates, account was taken of the geometry of disc segments where the initial defibration occurs. A countersink of 4.0×4.0 mm^2 for both plates and a gap of 0.1 mm were selected, see Figure 3.24. In addition, tests were also performed using a somewhat different test setup, in which the right-angled upper steel plate was replaced by a knife, see Figure 3.25, with a angle of 30° and with a angle knife-wood or clearance angle of 2°.
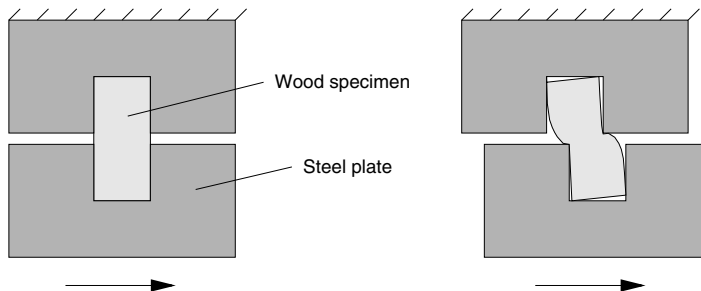
Figure 3.23: Schematic view of test setup.
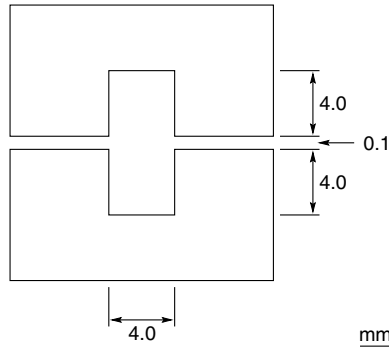
Figure 3.24: Geometry of main loading device, used in the major part of the test program.
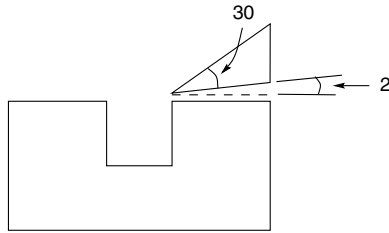
Figure 3.25: Geometry of knife used as loading device in some of the tests.

The tests were performed using a biaxial electromechanical testing machine. The two steel plates were mounted on the gripping device of the testing machine. A biaxial load cell was used to measure the horizontal and vertical forces, LVDT transducers mounted on the gripping device being used to record the displacements. The tests were controlled with respect to the horizontal displacement of the lower steel plate.

A major difference between the conditions in these tests and those in a refiner was, as mentioned, the loading rate. Due to the high velocity of the rotating discs in a refiner, the chips there are subjected to a very high loading rate, one of as much as 100 m/s. The test results presented here, in contrast, involved the very low loading rate of 0.02 mm/s.

During the tests, sequences of photographs were taken showing the deformations and the fracturing of the specimens. The forces in horizontal and vertical directions were recorded at the same time. The optical equipment used is described in Subsection 3.2.2 and is shown in Figure 3.3. Three different camera objectives were used in the investigation, for producing images of objects with heights of 2.5, 5.0 and 10 mm, respectively. The width of each picture was 1.3 times that of its height. Most of the tests were performed using the 10 mm objective, since this objective can capture the deformation of the entire specimen throughout the failure process. For some specimens, the 5 mm objective was employed, whereas in some other tests the 2.5 mm objective

was used in order to discern the response of the specimens in greater detail. The latter objective provided a magnification making it possible to see the cell structure.

The main part of the test program consisted of fourteen test series, referred to as series Ad, ..., Gd, Aw, ..., Gw. For these test series, two different specimen heights were used, 8.1 mm and 5.0 mm, see Figure 3.26. All specimens had a width of 4 mm and a depth of 10 mm. Note that the terms *depth* (away from the observer), *height* (in vertical direction) and *width* (left to right) are used here to clarify the alignment of the samples in the test apparatus, as shown in the figures that follow. For the 5 mm high specimens, 4 different orientations of the wooden material in relation to the direction of loading were tested, defined by the angle θ between the radial direction and the loading direction. The four orientations tested were: 0°, 45°, 90° and 135°. The orientations $\theta=0°$, 90° correspond to loading in the radial and tangential direction, respectively, and $\theta=45°$, 135° correspond to directions of loading diagonal to the growth rings. For the 90° orientation, i.e. loading in the tangential direction, two different configurations were tested, one with earlywood at the upper part of the specimen and one with latewood. All in all, six different specimen configurations were examined and for all cases, tests were performed using both dry and wet samples.
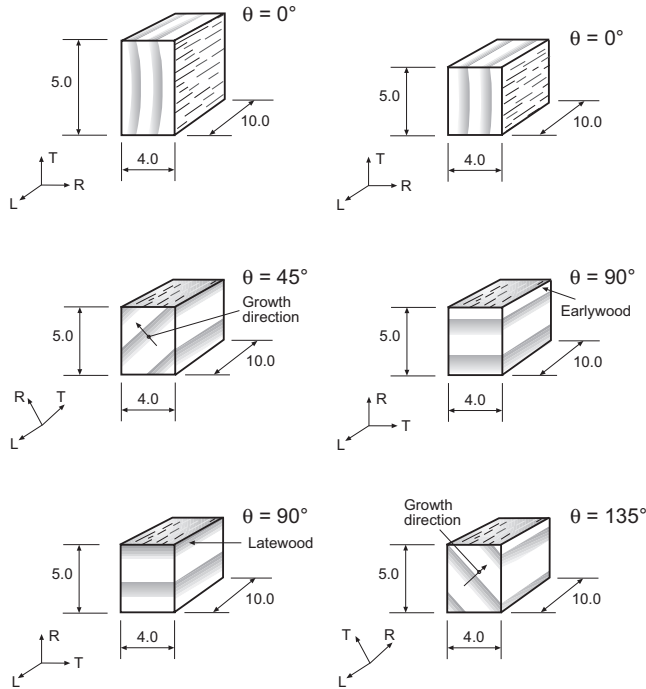

Figure 3.26: Geometry of specimens used for test series A-G. R, T and L denote the radial, tangential and longitudinal directions, respectively.

During the period between sample preparation and testing, the specimens were kept under stable climate conditions at either 60% RH and 20°C, or 95% RH and 20°C,

corresponding to a moisture content of approximately 12% and 28%, respectively. The specimens with the lower moisture content, series Ad, ..., Gd, will be referred to as dry specimens and those with the higher moisture content, series Aw, ..., Gw, as wet specimens. Test series Ad-Fd and Aw-Fw were performed using the loading device shown in Figure 3.24, whereas series Gd and Gw were carried out using the loading device in Figure 3.25. The test conditions for the fourteen test series are summarized in Table 3.4. The specimens within each series were prepared so as to be as similar as possible not only in their dimensions but also in the location and thickness of the earlywood and latewood zones. The specimens were cut to shape using a razor blade and were further sandpapered in order to get as good a fit between the steel plates as possible; the surface exposed to the camera was finished with fine grade sandpaper in order to get a good image with a clear differentiation of the earlywood and the latewood.

Table 3.4: Test conditions for the different test series. The orientation of the specimen is defined by the angle between the radial direction and the loading direction. The superscripts e, l denote that the upper part of the specimen consists of earlywood and latewood, respectively.

Test series	Specimen height [mm]	Specimen orient. [°]	Moisture content [%]	Angle of loading device surface [°]	Number of tests successful/total
Ad	8.1	0	12	90	8/16
Bd	5.0	0	12	90	8/12
Cd	5.0	45	12	90	4/5
Dd	5.0	90^e	12	90	5/6
Ed	5.0	90^l	12	90	5/6
Fd	5.0	135	12	90	6/6
Aw	8.1	0	28	90	6/9
Bw	5.0	0	28	90	6/6
Cw	5.0	45	28	90	5/5
Dw	5.0	90^e	28	90	6/6
Ew	5.0	90^l	28	90	4/12
Fw	5.0	135	28	90	6/6
Gd	5.0	90^e	12	30	6/6
Gw	5.0	90^e	28	30	6/6

After testing, all specimens were examined visually in order to verify that the deformation and crack pattern captured by the camera was representative throughout the depth of the specimen. The number of successful tests for the different test series

ranges between 4 and 8; for most series 6 successful tests were achieved. The total number of tests carried out is 107, of which 81 tests were successful and 26 tests were rejected. Several tests were rejected due to too large differences in their earlywood and latewood configuration as compared with the rest of the specimens. Another cause for rejection was the difficulty in preparing the specimens of correct dimensions which, in some cases, resulted in too large gaps between the specimens and the steel plates. Furthermore, some tests were discarded due to problems with test data registration.

In addition to the fourteen test series, a number of additional tests were carried out choosing other specimen geometries and using the 5 mm or the 2.5 mm objective instead of the 10 mm objective that was employed in the test series.

The wood material used for these tests was the same as for the compression tests presented in Section 3.2. All the specimens were thus taken from a spruce tree cut in southern Sweden (Gyvik, Småland). The specimens were taken at chest height from the tree, at annual ring numbers 43-44 and 52-53 counted from the pith, and the wooden material had an average density of 450 kg/m^3 and a growth ring width of about 2.0 mm.

3.4.3 Results

The results from the fourteen test series will be presented first. The general behavior of the material, differences between dry and wet samples, differences due to specimen orientation and differences between the two loading conditions will be discussed. Thereafter, results from some additional tests will be presented and discussed.

Test series A-D

The failure processes of a representative specimen in each test series are shown in Figures 3.27-3.33. A sequence of 5 pictures is presented for each test series showing the course of deformation and fracture in the specimens, together with the recorded load-displacement curves. The pictures are linked to points in the load-displacement curves by the numbers 1-5. For each test series, the first picture shows the undeformed specimen, pictures 2-5 showing the specimen subjected to a shearing displacement of 1.0, 2.0, 2.5 and 3.5 mm, respectively (except for the case of test series Bd and Bw for which pictures 2-5 show the specimen at a shearing displacement of 0.5, 1.0, 1.5 and 2.5 mm, respectively). The load-displacement diagrams show the recorded horizontal (solid lines) and vertical forces (dashed lines) as functions of the horizontal displacement of the lower steel plate. A different scale on the vertical axis of the diagrams in Figure 3.33 (series Gd and Gw) is used as compared to the diagrams in Figures 3.27 to 3.32.

In order to illustrate the differences in results within the test series, all the specimens of test series Bd and Bw are shown in Figures 3.34 and 3.35, respectively, when subjected to a shearing displacement of 3 mm.

Load-displacement curves for the different test series are given in Figures 3.36-3.38. The diagrams show hand-drawn mean-value curves for each test series; the solid lines represent horizontal forces and the dashed lines represent vertical forces as functions

of the horizontal displacement of the lower steel plate. Figure 3.36 shows the results
for test series Ad-Fd with dry specimens and Figure 3.37 shows the results for the
corresponding series Aw-Fw with wet specimens. In Figure 3.38 the load-displacement
curves for test series Gd and Gw are given. Note the different scale on the vertical axis
in Figure 3.38 as compared to that in Figures 3.36 and 3.37. The force displacement
curves for all tests within each test series are given in Appendix A. In these diagrams the
corresponding hand-drawn mean-value curves are also shown (dashed lines). In general,
about 250 samplings of forces were made during testing, except for the case of test series
Ad, Bd and some of the tests in series Aw and Bw for which only about 50 samplings
were made. For the tests with the higher number of sampling points, the curves given in
the Appendix, as well as those of Figures 3.27-3.33, show filtered response, whereas raw
data are presented for the tests with the lower number of sampling points. The filtering
of the recorded load signals was made using the Matlab signal processing toolbox [51]
(Butterworth filtering). Typical load signals recorded from a test together with the
corresponding filtered response are given in Figure A.7 in Appendix A.

The results in the form of maximum forces and energy consumption for the different
test series are given in Table 3.5. Since there is no vertical movement of the lower steel
plate, only the horizontal force contributes to the energy consumption, which is thereby
given by the area below the horizontal force displacement curve. It is, for all cases,
evaluated at a shearing displacement of 4 mm, although the horizontal force was not
equal to zero at this stage of deformation for several of the test series.
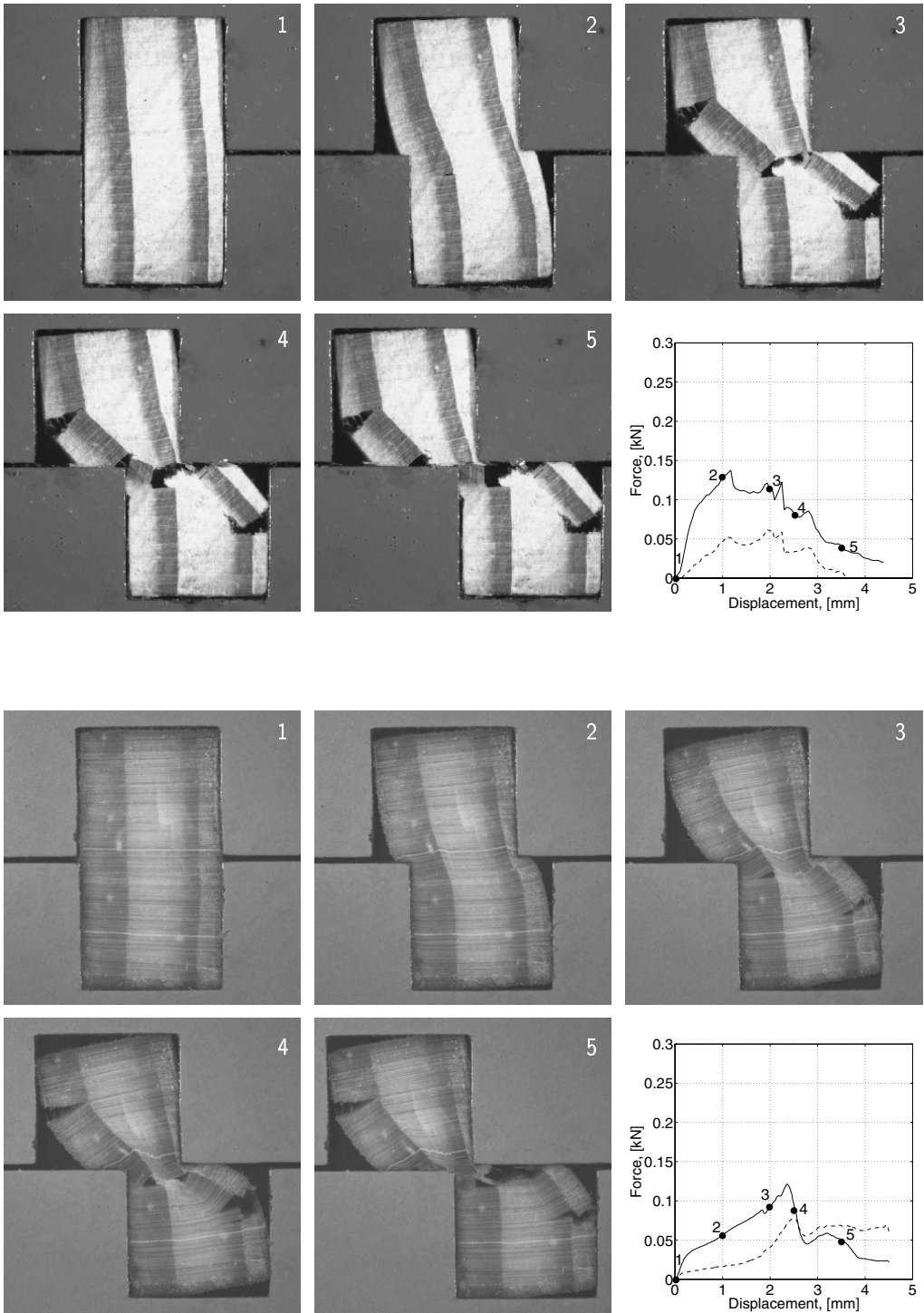
Figure 3.27: Illustration of the failure process of a typical dry specimen in test series Ad (top) and wet specimen in test series Aw (lower).
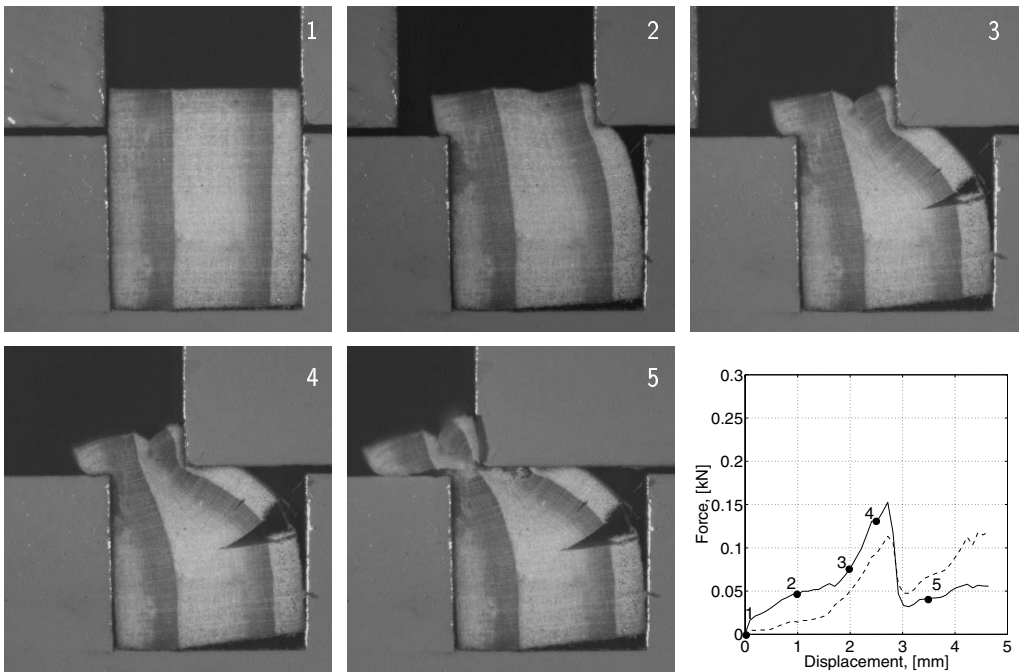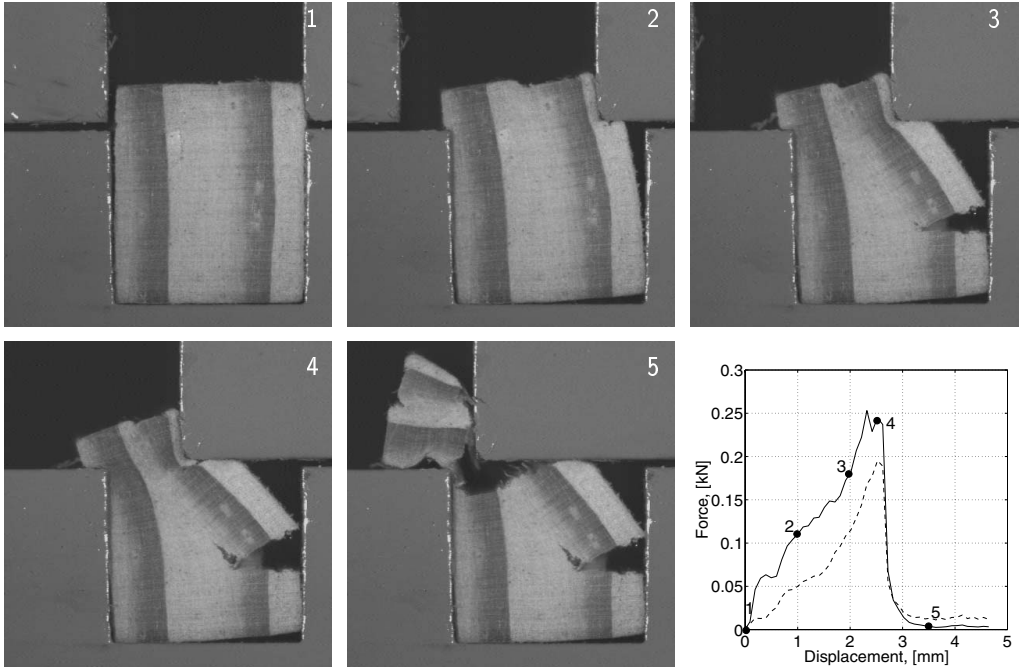
Figure 3.28: Illustration of the failure process of a typical dry specimen in test series Bd (top) and wet specimen in test series Bw (lower).
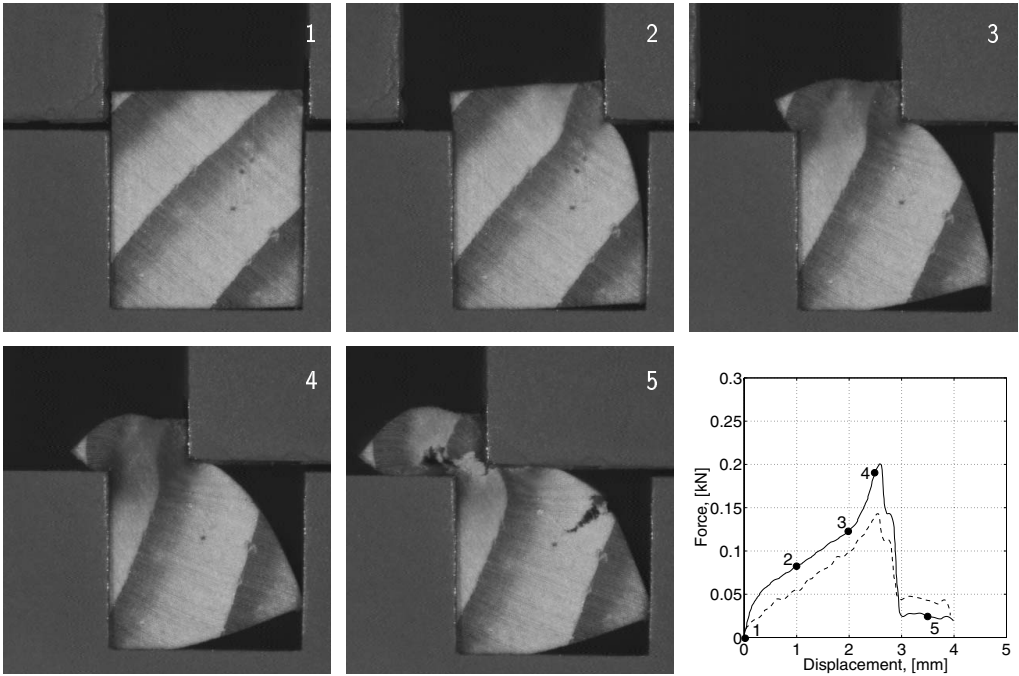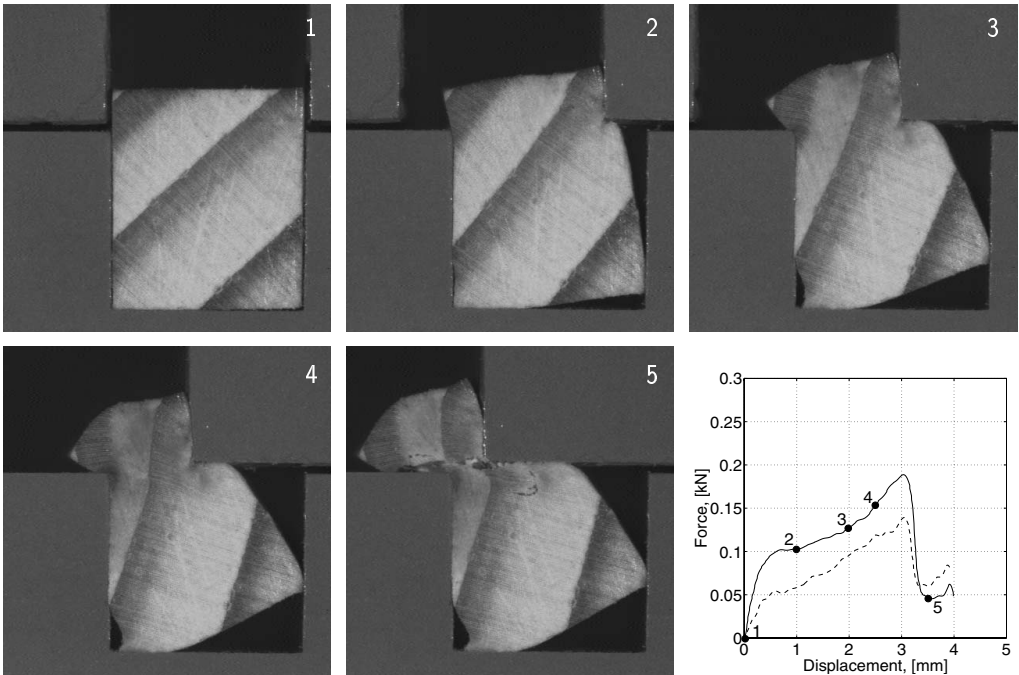
Figure 3.29: Illustration of the failure process of a typical dry specimen in test series Cd (top) and wet specimen in test series Cw (lower).
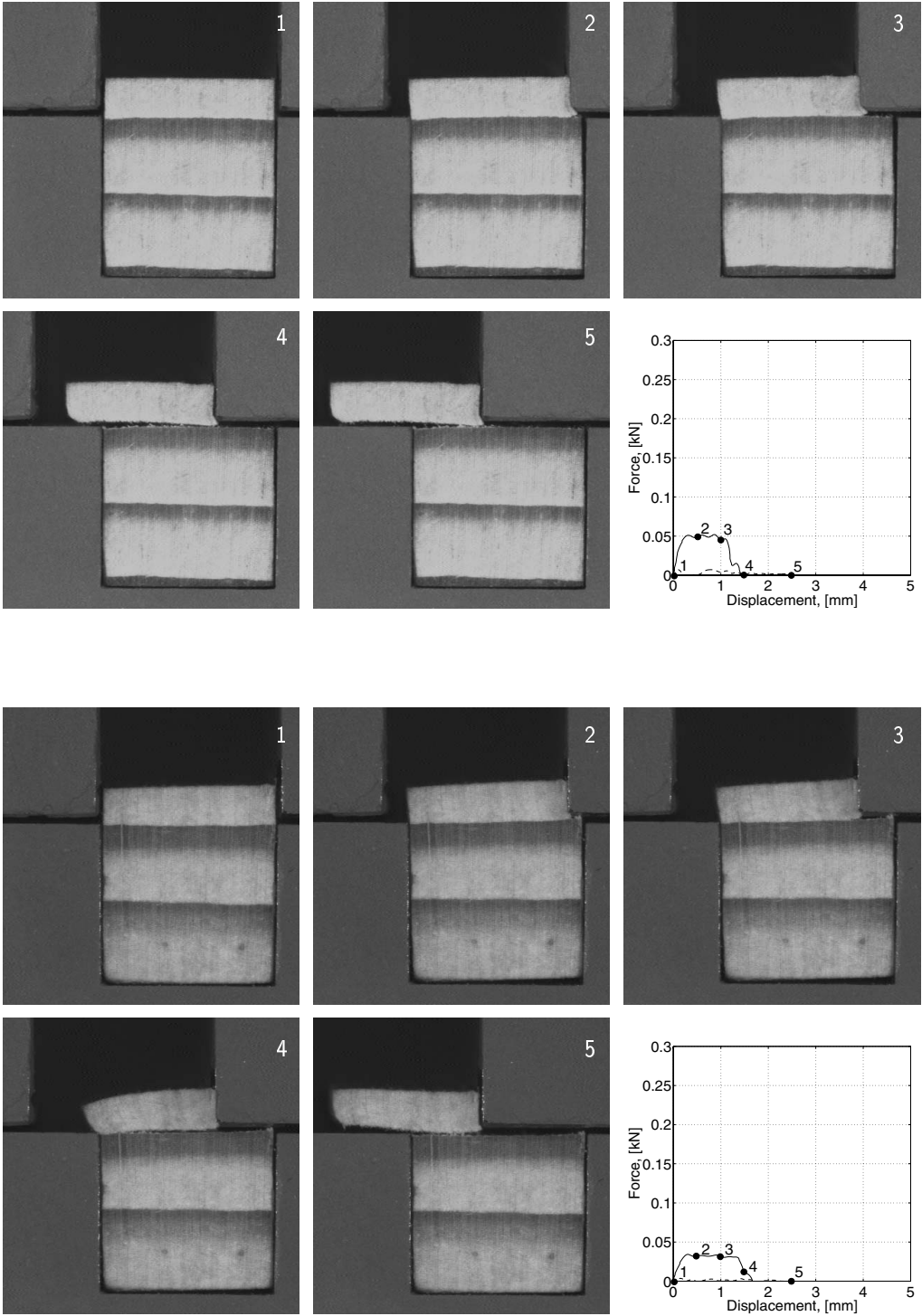
Figure 3.30: Illustration of the failure process of a typical dry specimen in test series Dd (top) and wet specimen in test series Dw (lower).
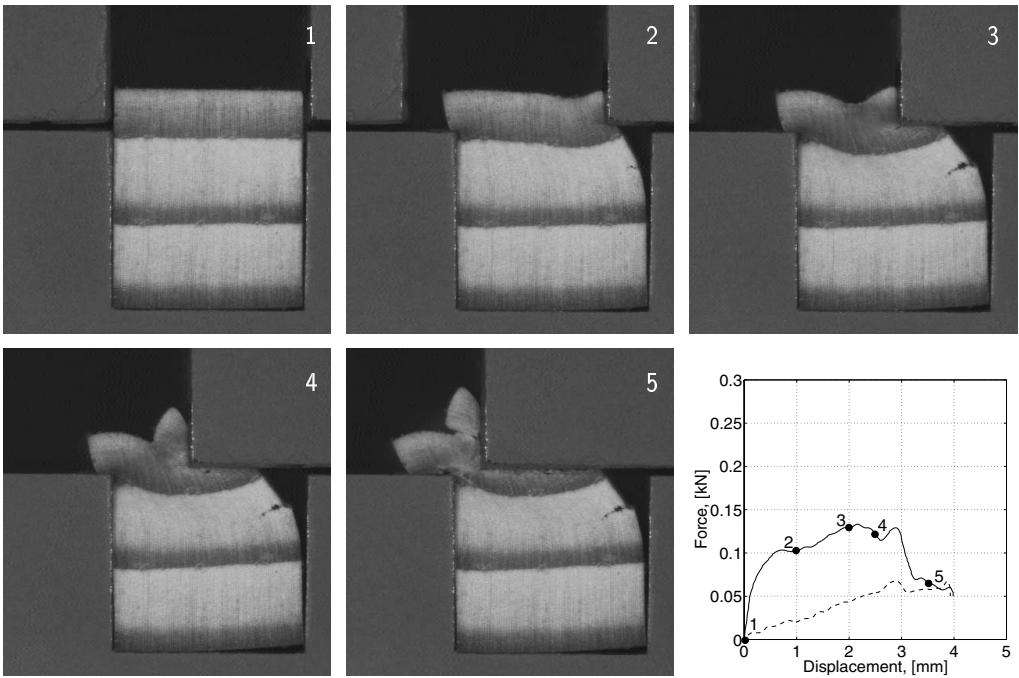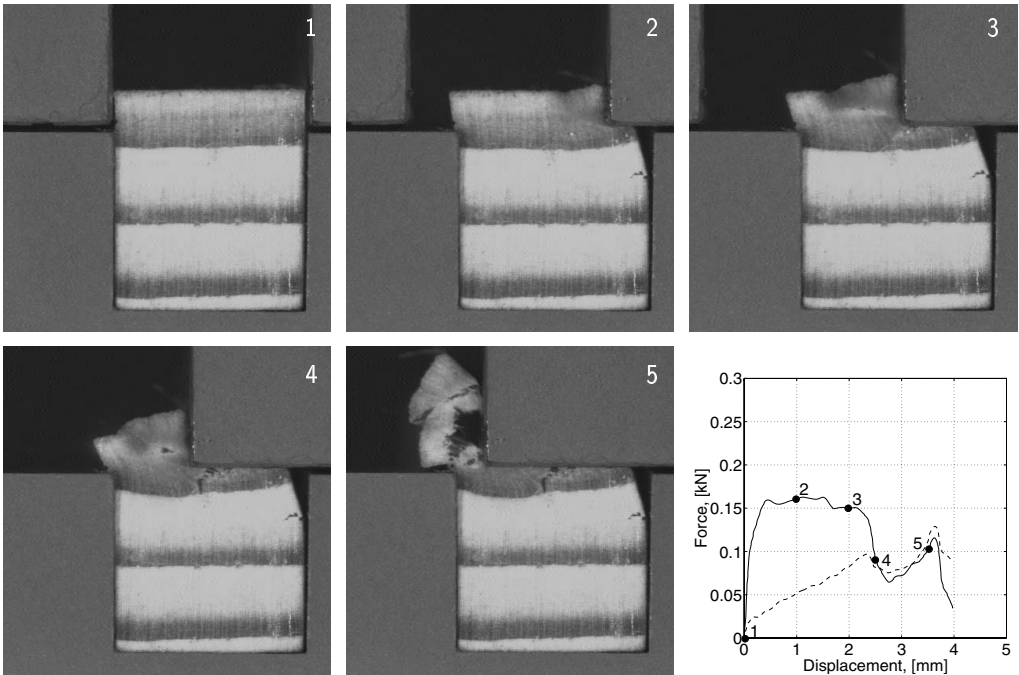
Figure 3.31: Illustration of the failure process of a typical dry specimen in test series Ed (top) and wet specimen in test series Ew (lower).
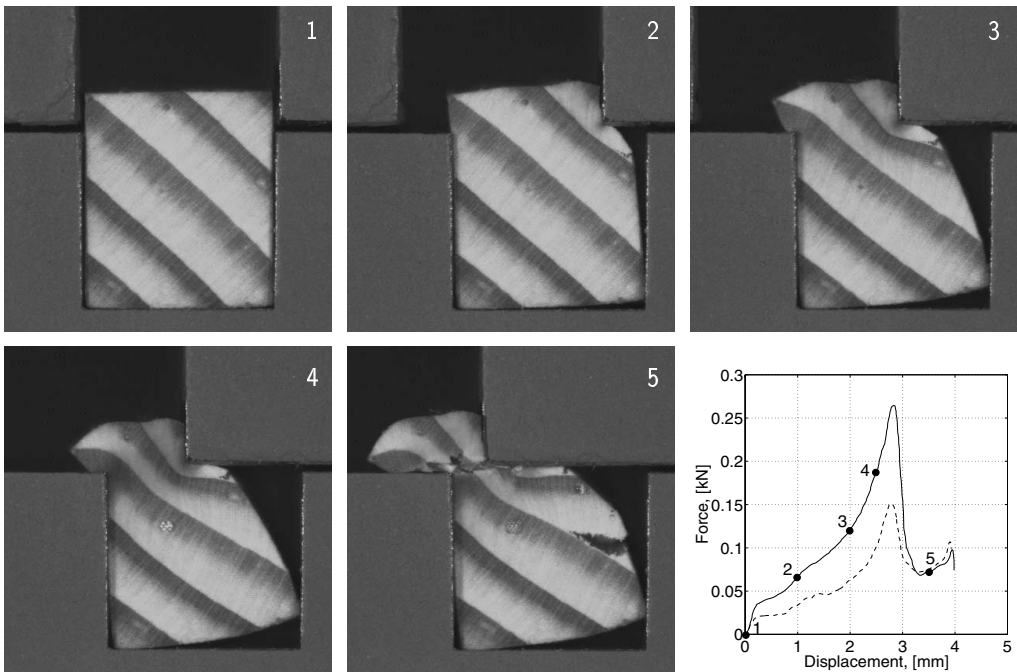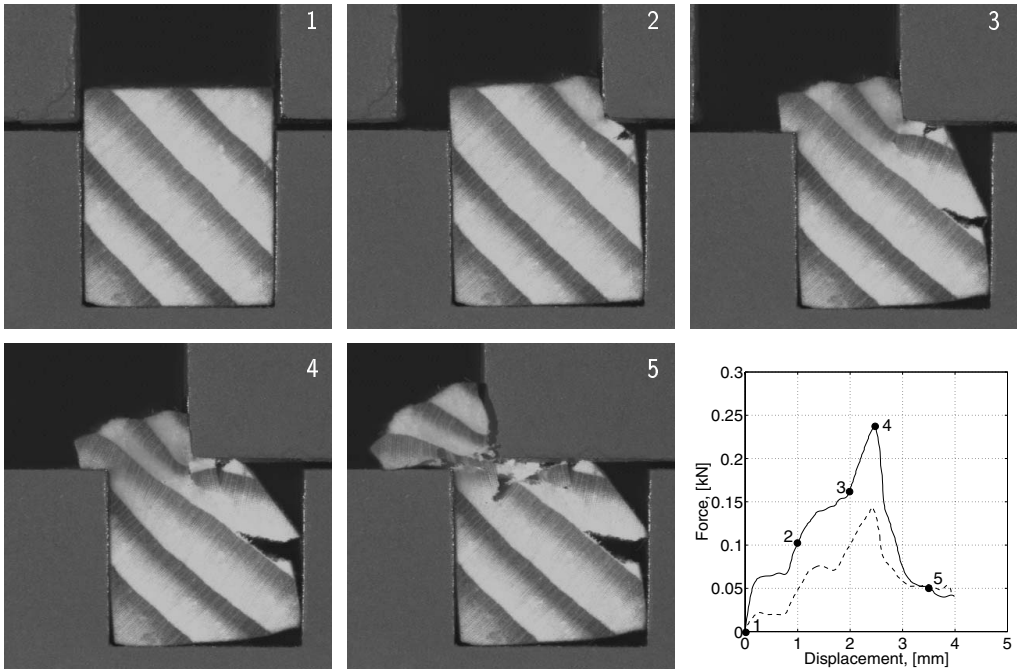
Figure 3.32: Illustration of the failure process of a typical dry specimen in test series Fd (top) and wet specimen in test series Fw (lower).
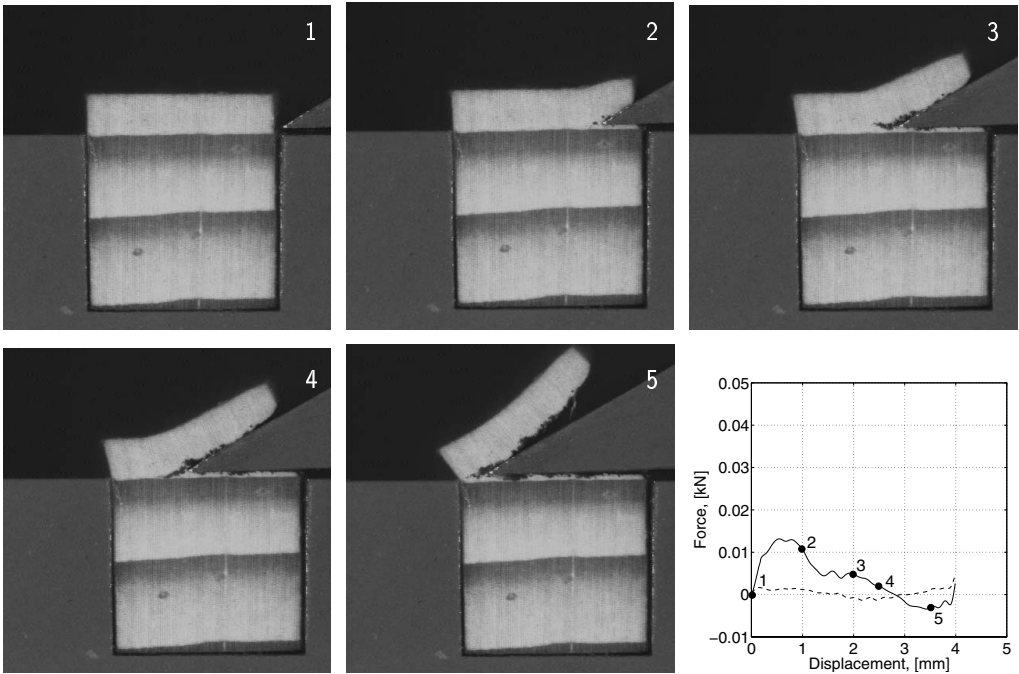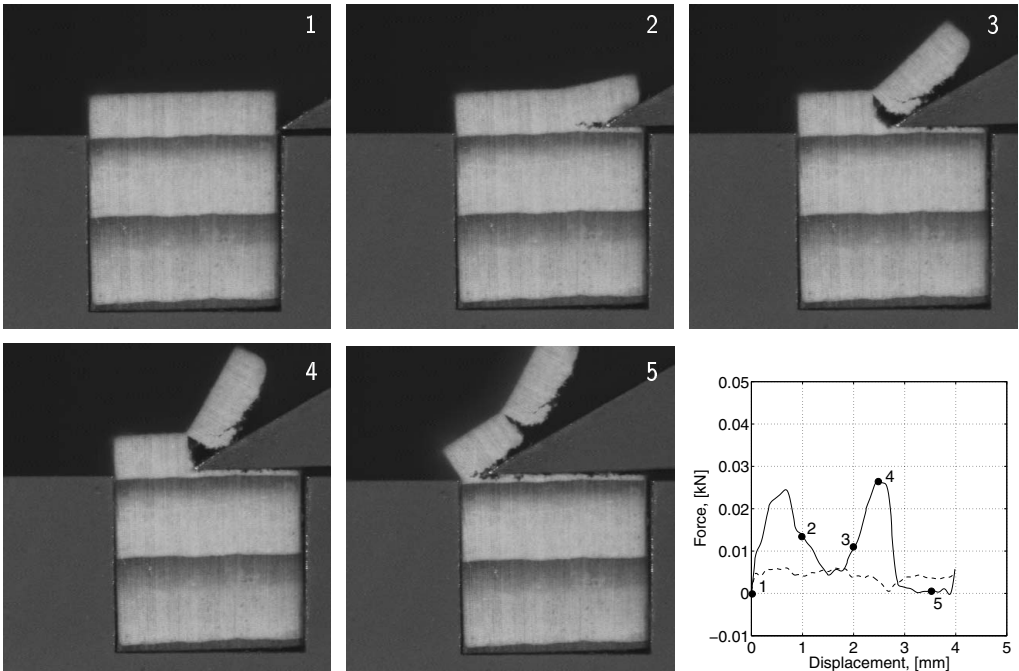
Figure 3.33: Illustration of the failure process of a typical dry specimen in test series Gd (top) and wet specimen in test series Gw (lower).
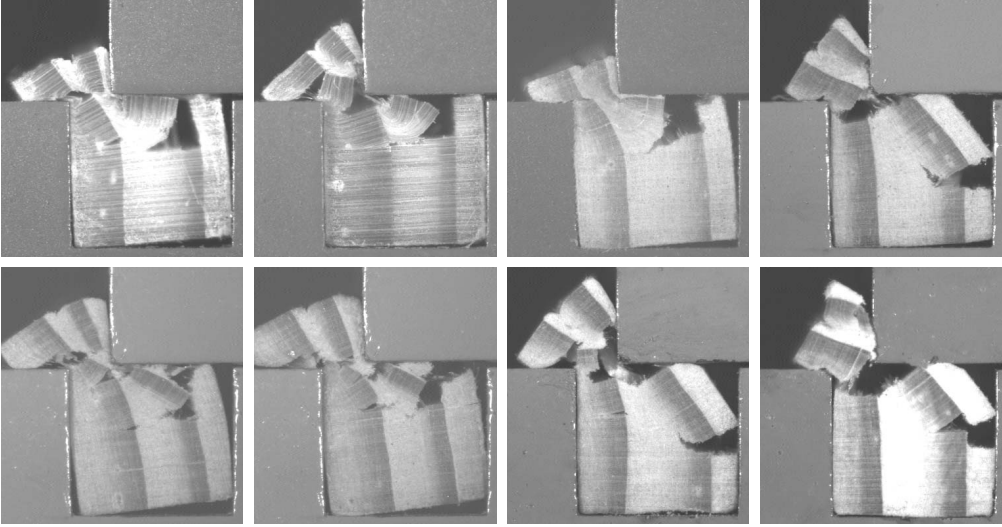
Figure 3.34: Deformation and fracturing of all 8 dry specimens in test series Bd. The specimens are subjected to a shearing displacement of 3 mm.
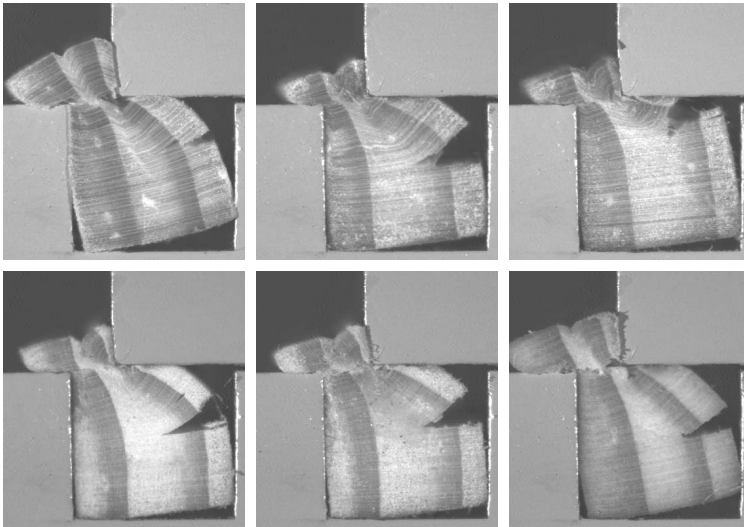
Figure 3.35: Deformation and fracturing of all 6 wet specimens in test series Bw. The specimens are subjected to a shearing displacement of 3 mm.
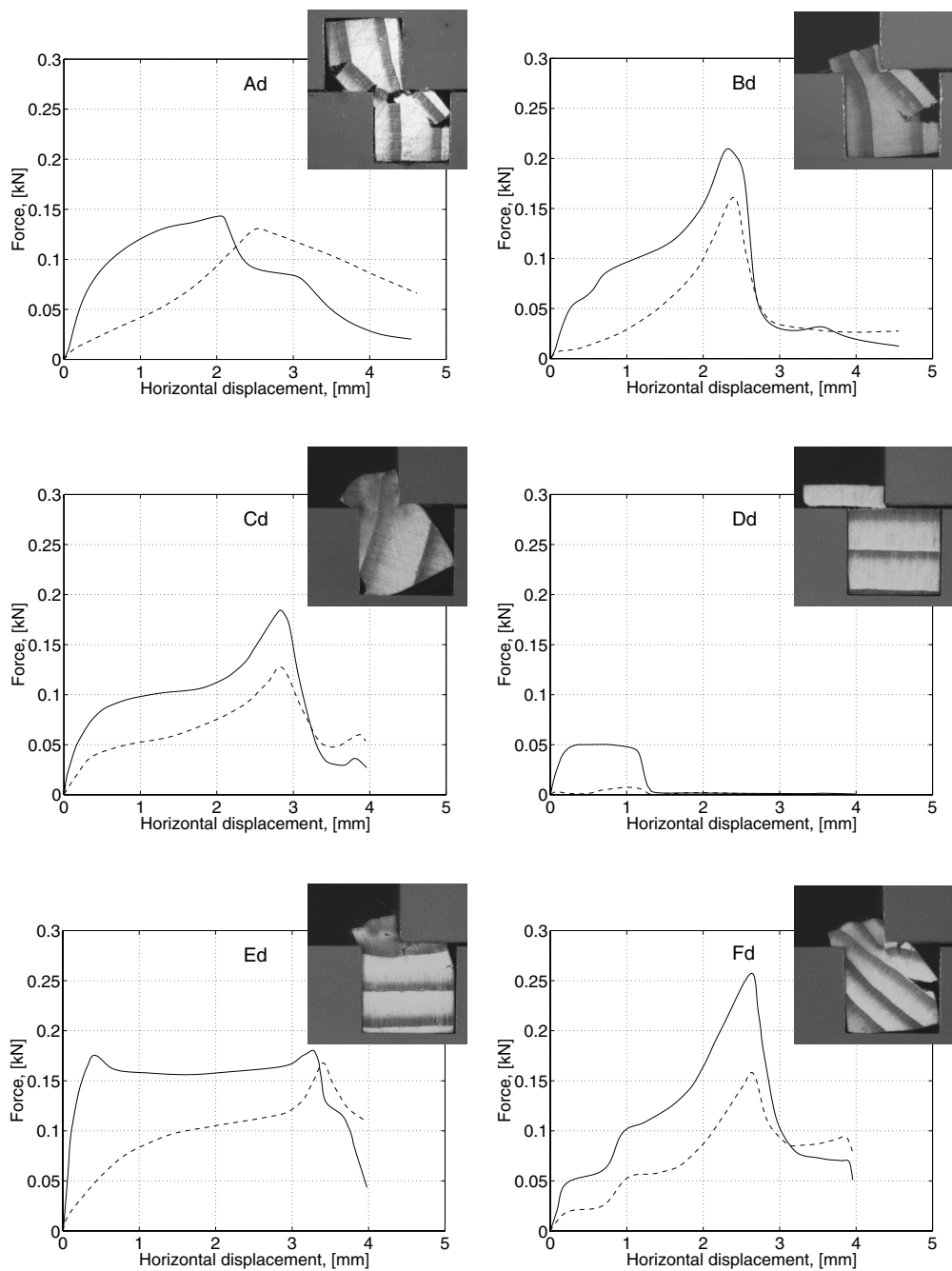
Figure 3.36: Load-displacement curves for test series Ad-Fd (dry specimens). The curves shown are mean-value curves for each test series; solid lines show horizontal forces and dashed lines show vertical forces.
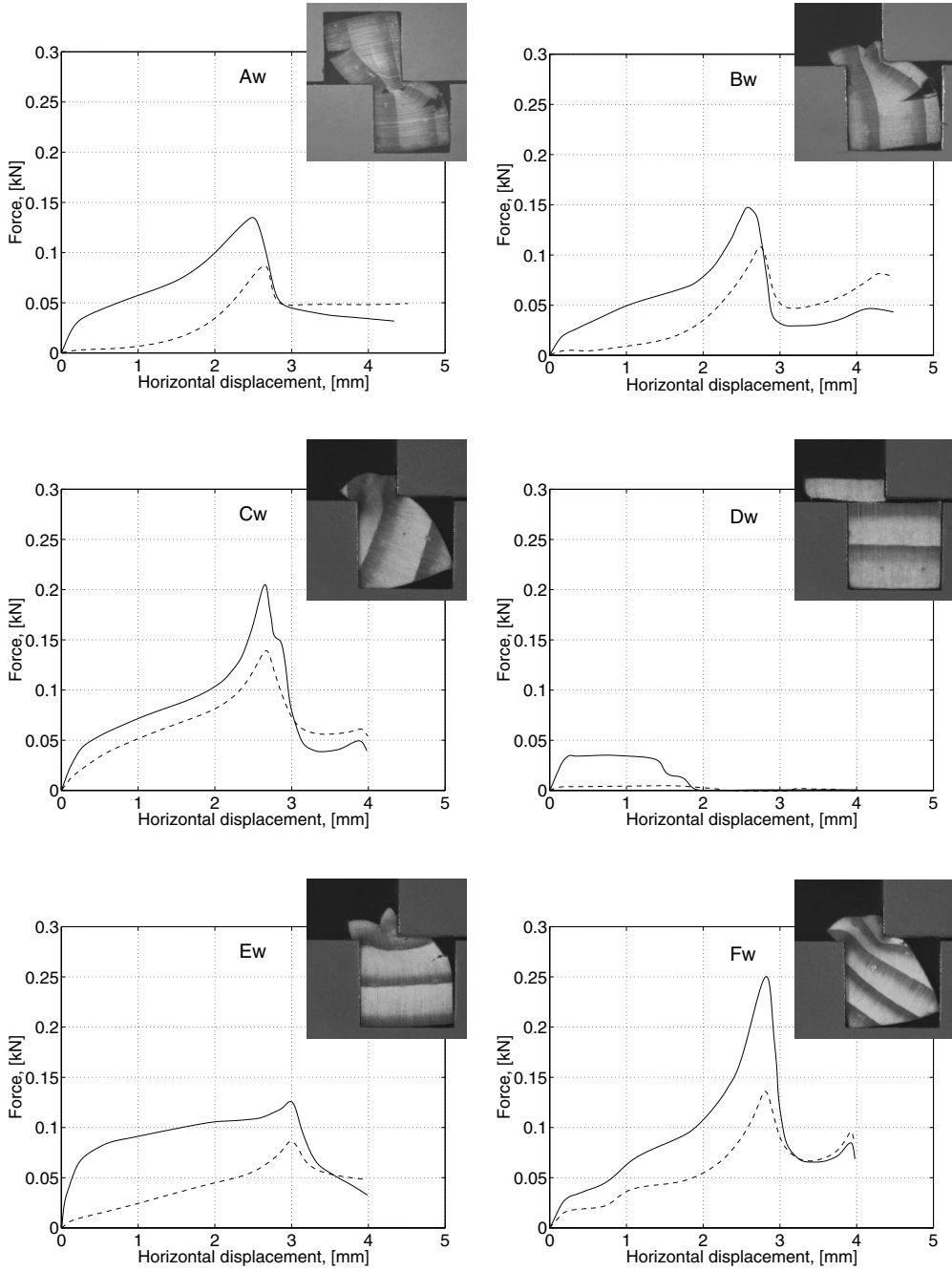
Figure 3.37: Load-displacement curves for test series Aw-Fw (wet specimens). The curves shown are mean-value curves for each test series; solid lines show horizontal forces and dashed lines show vertical forces.
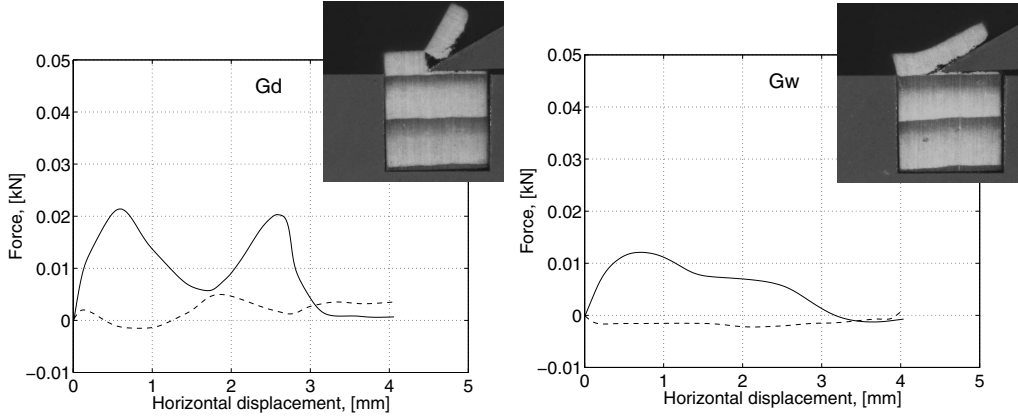
Figure 3.38: Load-displacement curves for test series Gd (left) and Gw (right). The curves shown are mean-value curves for each test series; solid lines show horizontal forces and dashed lines show vertical forces.

Table 3.5: Summary of results from the chip shearing tests.

Test series	Specimen orient. [°]	Maximum Vert. Force [N]		Maximum Horiz. Force [N]		Energy [mJ]		Number of tests
		mean	s. d.	mean	s. d.	mean	s. d.	
Ad	0	131.4	36.4	159.0	18.2	375.4	40.7	8
Bd	0	158.6	36.4	208.5	23.1	347.1	45.5	8
Cd	45	127.0	13.4	185.7	14.1	372.0	46.1	4
Dd	90^e	7.1	2.7	50.0	7.0	51.1	2.3	5
Ed	90^l	168.0	28.6	190.4	30.0	575.7	72.2	5
Fd	135	158.3	21.2	258.6	27.9	460.9	57.3	6
Aw	0	87.3	37.4	136.8	14.4	246.3	22.1	6
Bw	0	108.7	11.2	147.1	8.7	223.1	16.5	6
Cw	45	141.3	7.6	204.9	10.2	321.8	45.2	5
Dw	90^e	7.7	4.3	35.7	2.3	47.4	4.0	6
Ew	90^l	95.1	26.4	124.2	20.2	339.7	10.8	4
Fw	135	138.4	11.6	251.6	20.6	364.9	29.7	6
Gd	90^e	5.3	5.3	22.3	3.2	33.6	19.1	6
Gw	90^e	2.8	1.3	13.6	2.8	23.1	7.0	6

From the pictures in Figures 3.27-3.32, it can be seen that the mechanical behavior of the specimens is very complex. The behavior of the material is characterized by the development of cracks and by large volumetric changes occurring when the earlywood is subjected to compression. It can also be clearly seen that the properties of the latewood are very different from those of the earlywood, the latewood being very much stiffer.

By examining the failure processes shown in Figures 3.27-3.32, the load-displacement relations given in Figures 3.36-3.37 and the results summarized in Table 3.5, it can be concluded that the specimen orientation and its earlywood-latewood configuration have great influence on the failure process, on the load-displacement relations and, above all, on the energy consumption. For the 8 mm high specimens of tests series Ad and Aw, which were loaded in the radial direction, several cracks were formed and complex crack patterns were developed. The cracking mainly occurred in the tangential direction. The earlywood close to the edges and in the middle of the specimens was partly compressed substantially. For the specimens in test series Bd and Bw, two main cracks developed. First, a tensile crack appeared at a shear displacement of about 1 mm and then a fatal crack at a displacement of about 2.5 mm, running through the complete width of the specimen. For the dry specimens the fatal crack was dominated by the opening mode, whereas for the wet specimens it was dominated by shear. The behavior of the specimens in series Cd, Cw, Fd and Fw was somewhat similar to that of the Bd and Bw series with, in general, two main cracks developed. The shapes of the load-displacement curves for these series were also similar. The tests series deviating the most from the others are Dd and Dw, in which the specimens were loaded in the tangential direction and had an upper part of earlywood. For this setup, a neat shear fracture occurred in the earlywood along the abrupt earlywood-latewood transition, where the material below the fracture zone was practically undeformed. The shear forces in these tests were considerably lower than those of the other test series. It is interesting to compare this response with that of the specimens in test series Ed and Ew, which were also loaded in the tangential direction but with latewood at the top of the specimen. The latewood is much stiffer than the earlywood and provides greater resistance to deformation and cracking, and considerably larger forces were needed for failure. The failure mode was more of a peeling type than the neat shear fracture of the specimens in series Dd and Dw. For the dry specimens the energy consumption ranged between 51-576 J, and for the wet specimens between 47-356 J. For both the dry and the wet specimens the minimum energy consumption was found for the D series. The maximum energy consumption was found for series Ed and Fw. It is interesting to note that the minimum and the maximum energy consumptions, for the case of the dry specimens, were both obtained for loading in the tangential direction, the large difference in energy consumption being due to the different earlywood-latewood configuration between the two series only. A very large difference between the corresponding series with wet specimens loaded in the tangential direction was also found (series Dw and Ew).

It can be concluded that the wet specimens behaved somewhat differently than the dry specimens. The failure processes were similar for the wet and for the corresponding dry test series, but the dry specimens were in general more brittle than the wet ones,

which could be deformed more without cracking. Differences between the dry and the wet specimens in terms of load deformation curves could also be observed. The shape of the curves were similar, but the initial stiffness was lower for the wet specimens than for the dry, and the horizontal and the vertical forces at a given shear displacement were, in general, lower for the wet specimens than for the corresponding dry ones, with the exception of test series Cw (the vertical force of series Dw is also slightly higher than that of Dd). The energy consumption was consistently lower for the wet specimens than for the corresponding dry ones, 30-35% lower for series Aw, Bw, Ew and Gw, about 20 % lower for series Fw and about 10 % for test series Cw and Dw.

Comparing the behavior of the specimens within the different test series indicates that, although certain variations in the location of cracks can be seen, the overall behavior and the failure processes were similar. This can be seen in examining Figure 3.34 showing test series Bd, and Figure 3.35 showing test series Bw. In these figures all the specimens within the two test series, when subjected to a shearing displacement of 3 mm, are shown. In general, the variations within the test series were found to be smaller for the wet specimens than for the dry ones. From the load-displacement diagrams in Appendix A it can be seen that there is relatively good agreement between the results within the various test series. Although there are variations between the curves, their shape is in general similar. It can also be seen that the variations are smaller for the test series involving wet specimens than for the dry ones. The greatest variations could be observed at the end of the tests, especially in connection with the vertical force. The reason for these discrepancies is that, in some of the tests, small pieces of wood were squeezed within the small gap between the two steel plates. The forces were affected by the amount of material that was squeezed. This may also explain the oscillations in the vertical force recorded near the end of some of the tests. The smallest variations were found for test series Dd and Dw, for which the results within the series were very similar regarding both the failure process and the load-displacement relations.

By comparing the results from test series Gd, Gw with those from Cd and Cw, it can be concluded that the loading mode has a great influence on the failure process as well as on the energy consumption. The energy consumption is about 35 % lower for series Gd as compared to Cd and about 50 % lower for Gw as compared to Dw. The failure processes for test series Gd and Gw were considerably more dominated by opening mode fracture than those for test series Cd and Cw, and the knife loading did not produce such a clean smooth fracture surface as that for series Cd and Cw. It can also be seen that the knife loading setup results in less inelastic compressive deformations (cell collapses) in the earlywood than the setup with a right-angled support. Clear differences between the dry and wet specimens for the knife loading setup could be seen. The fracture surface was in general smoother for the wet specimens than for the dry ones. For most of the dry specimens (5 of 6) a tensile crack at the knife-edge, perpendicular to the knife, was developed at a shearing displacement of about 1.5 mm. The horizontal load-displacement curves for the dry specimens had two clear peaks, at about 0.5 mm and 2.5 mm displacement. For the wet specimens the cut-off part was in all cases intact and the load-displacement curves smoother with a peak at about 0.5-1.0 mm displacement.

Additional tests

In addition to the main test series, additional tests involving specimens having other earlywood-latewood configurations were carried out. In Figure 3.39, two different specimens are shown, both tested in the dry condition. The specimens were subjected to the same relative shearing displacement, 0.8 mm. They differ with respect to the location of the earlywood and latewood. The pictures were taken using the 5 mm objective. The differences in mechanical properties between earlywood and latewood are clearly illustrated, the stiffness of the latewood being much greater than that of the earlywood. It can also be seen that, when the earlywood is subjected to compression, this results in large deformations and large volumetric changes.
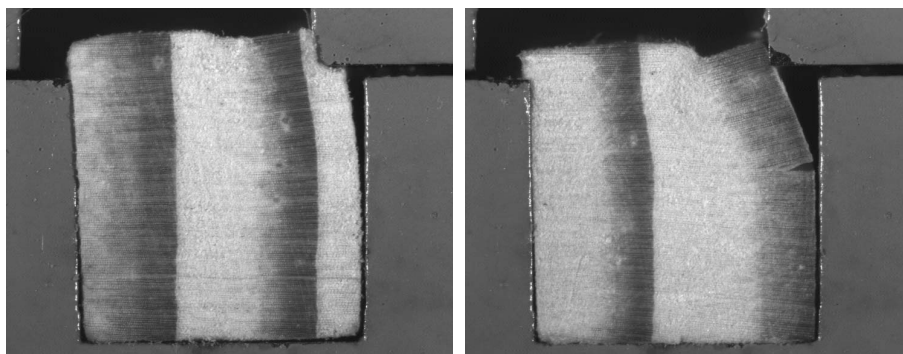
Figure 3.39: Illustration of the difference in mechanical properties between earlywood and latewood. The specimens were tested in dry condition.

When the 2.5 mm objective was used, the cell structure became visible. In Figure 3.40, four pictures are shown taken with this objective of a specimen tested in dry condition. The small inset picture, showing a complete specimen, is from a test of a similar specimen using a 10 mm objective. The area covered by the 2.5 mm objective is indicated by the dashed lines. In the first picture (upper left), the specimen is subjected to a shearing displacement of 1.1 mm. As can be seen, the deformations within the earlywood zone are not distributed uniformly. Three failure zones of collapsed earlywood cells have developed, but the cells between these zones appear to be intact. When the deformation was further increased, as shown in the next picture (lower left), additional earlywood cells have collapsed and a crack has been initiated in the right latewood zone in the radial direction. The third picture (upper right) shows the specimen at a shearing displacement of 1.5 mm. At this point, two major cracks oriented radially have developed; both appear to run between adjacent cell rows. This suggests that the bonds between the cells are crucial to the formation of cracks in latewood. A similar phenomenon has also been observed by Stefansson [80]. The crack formation and growth within the earlywood is more diffuse than that of the latewood. The further crack growth can be seen in the last picture (lower right) in which the specimen is shown at a shearing displacement of 2.2 mm. Note the deformation of the

ray cell at the bottom of the pictures, which clearly indicates the collapse of the cell structure.

The results shown in Figure 3.40 clearly indicate that much knowledge might be obtained by experimental observations and modelling on a micro level, which will be further treated in Chapter 7.
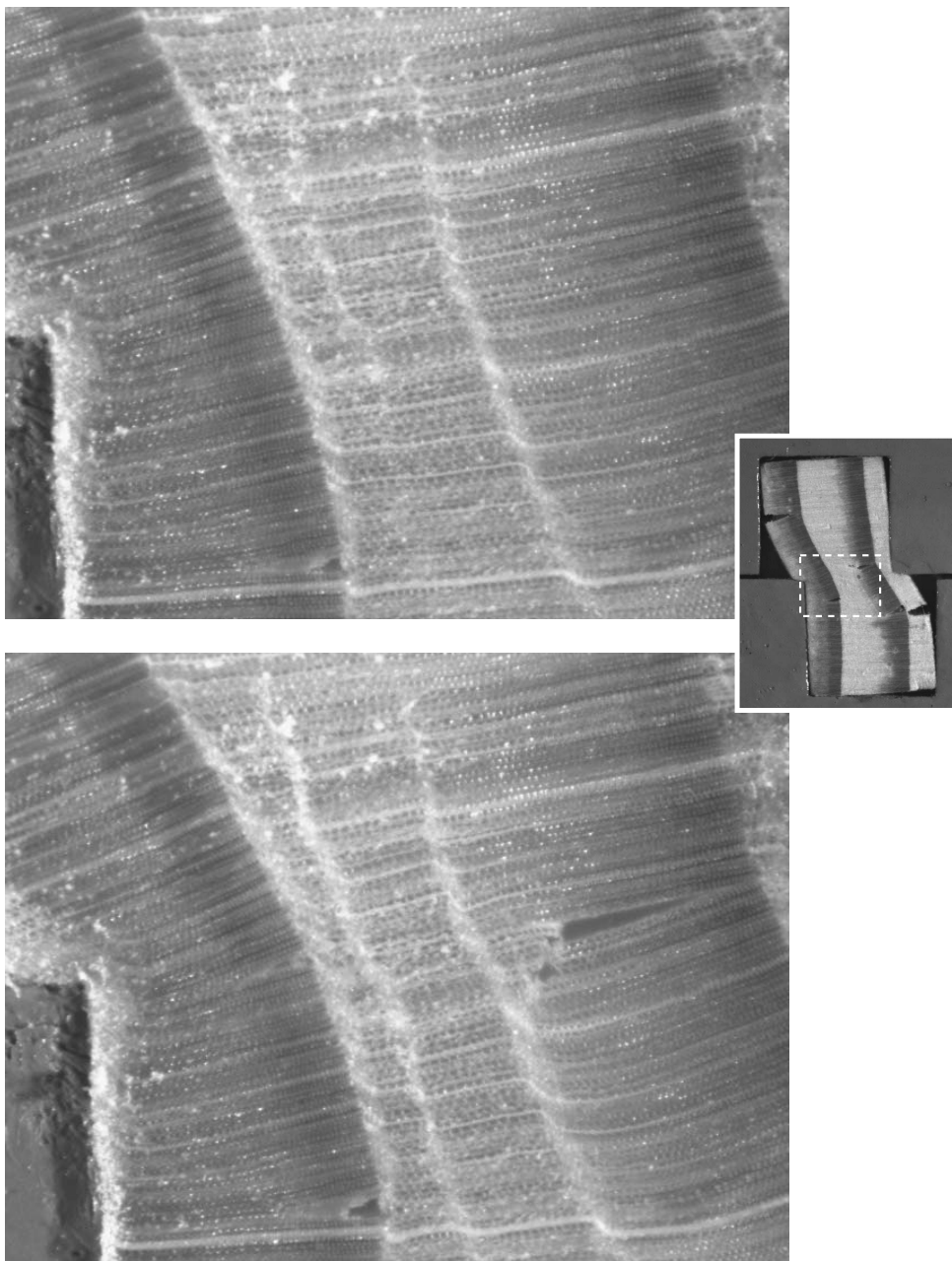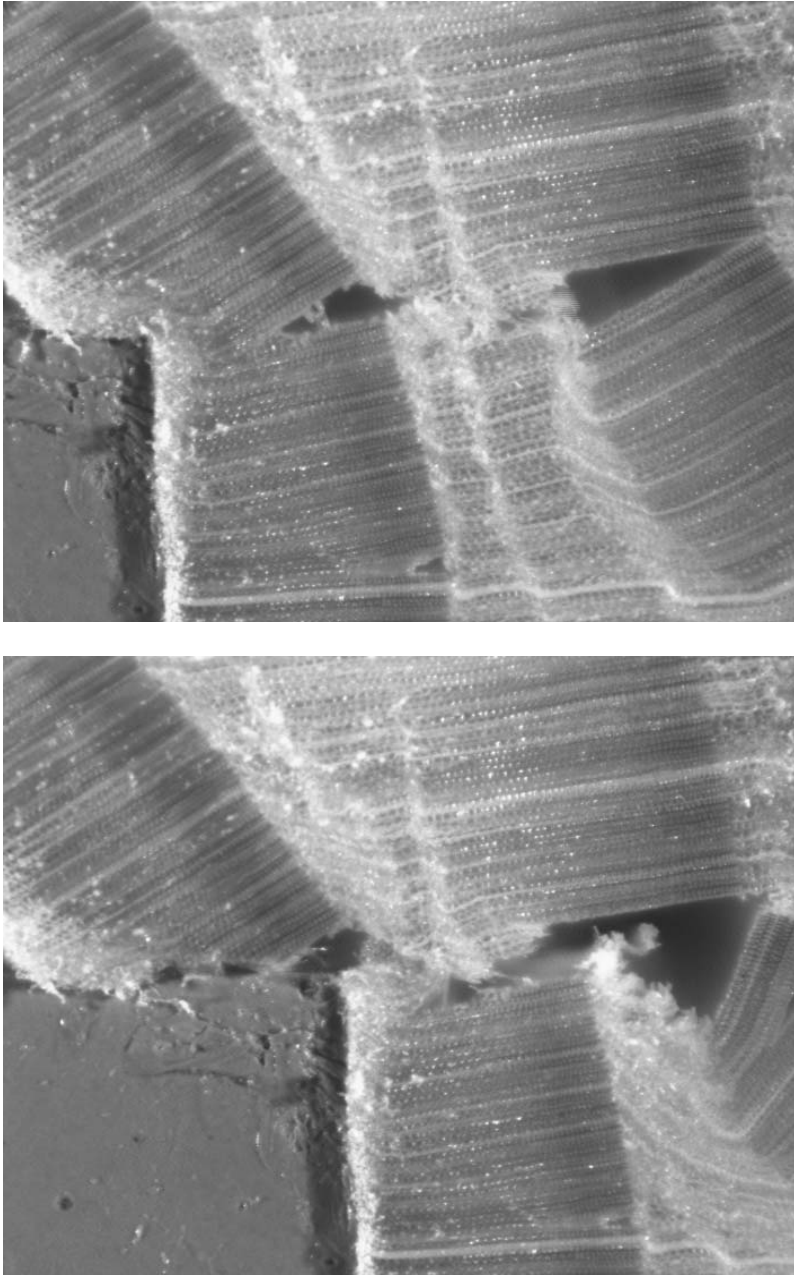
Figure 3.40: Localized deformations in the earlywood and cracking of the latewood. The small picture in the middle, taken from a test of a similar specimen, shows the area covered by the 2.5 mm objective. The specimen was tested in dry condition.

3.4.4 Concluding remarks

The tests presented in this section were carried out in order to gain a better understanding of the mechanical behavior of wood loaded perpendicular to the grain under conditions similar to those during refining. Specifically, the influence of the material orientation versus loading direction, the influence of the earlywood and latewood configuration within the specimens, and the effect of the loading mode on the failure process were studied. The tests also illustrate the complex loading conditions present during the initial defibration. The test setup and the dimensions of the samples were chosen to be similar to refiner segments. Optical equipment was used to obtain photographs of the specimens, showing the deformation and fracturing of the material. Tests were performed on wood in both a dry and a wet condition (with a moisture content of 12% and 28%, respectively). All tests were carried out at room temperature. It should be noted that in the refining process the wood material is subjected to very high loading rates, whereas the tests performed were carried out at a very low loading rate.

The tests provided valuable information concerning the mechanical behavior of wood that can be used for further analysis of initial defibration processes. The following conclusions can be drawn on the basis of the results of the tests performed:

- *The mechanical behavior of wood loaded perpendicular to the grain is very complex and involves both cracking and large volumetric changes.*
  The behavior of the material is characterized by the development of cracks in cases where the earlywood or the latewood is subjected to tension and/or shearing, and of large volumetric changes in cases where the earlywood is subjected to compression.

- *The mechanical properties of latewood differ markedly from those of earlywood; account should be taken of these differences in studying initial defibration processes.*
  These differences are usually not considered when wood is studied on a larger scale, but for the applications in mind here account must be taken of the different early- and latewood properties if the material behavior is to be understood.

- *Several zones of localized deformations may develop when earlywood is subjected to compression perpendicular to the grain.*
  Whereas the cells may be totally collapsed within these zones, the cells outside them appear to be nearly intact.

- *The specimen orientation and configuration has a great impact on the failure mode, the load-displacement relations and the energy consumption.*
  Very large differences concerning the deformation and fracture process, the magnitude of the recorded forces as well as the energy consumption were found between the different specimen orientations and configurations. The differences were somewhat greater for the dry specimens than for the wet ones. For the dry specimens the energy consumption ranged between 51-576 J and for the wet specimens between 47-356 J. It is interesting to note that the minimum and the maximum energy consumptions were found for the same specimen orientation

(loading in the tangential direction). The differences depended only on the the early- and latewood configuration within the specimen.

- *The design of the loading equipment has a strong influence on the failure process and energy consumption.*
  The failure process was considerably more dominated by the opening fracture mode in the knife loading case than for the setup with a right-angled crushing surface. The knife loading setup resulted in considerably lesser deformations (and fewer collapsed cells) within the earlywood, and the energy consumption was about 40 % lower than the results obtained with the right-angled contacting surface.

- *Moisture content has a strong influence on the mechanical properties of wood.*
  The dry specimens were in general more brittle than the wet specimens, which could be deformed more without cracking. From the load deformation curves it could also be seen that the initial stiffness was greater for the dry specimens than for the wet ones. The maximum shear load (except for the case of test series Cw) was also significantly lower for the wet test series than for the corresponding dry ones. Also the energy consumption was consistently lower for the test series with wet specimens than for the corresponding dry ones.

- *Cracks in the latewood seem to run between adjacent cell rows.*
  Observations made on the dry specimens clearly indicated that cracks oriented perpendicular to the tangential direction in the latewood run between adjacent cell rows rather than across the cell walls, which suggests that the bonds between the latewood cells are crucial to the crack formation. In the earlywood, on the other hand, the crack propagation is more diffuse.

Chapter 4

Material Modelling

4.1 Introduction

When numerical analyses of initial defibration processes are to be performed, two main approaches may be applied in modelling the wooden material. One approach is to use continuum models based on smeared material properties. The other approach is to develop models of the cellular microstructure, the individual fibres being modelled. The latter approach is the more general one, providing a higher degree of resolution. It has the disadvantage, however, of giving rise to extremely large models that are difficult to handle using the computer resources available today, unless very small pieces of wood are studied. Although a continuum modelling approach allows the deformation and fracturing of larger wood pieces to be analysed, it does not permit the deformation and fracturing of the individual fibres to be studied. On the whole, the continuum approach appears to be the most suitable for simulating the initial breakdown of the wooden chips in the refiner. For later stages of the defibration process, modelling at the microstructural level is needed in order to analyse the deformation process of the individual fibres.

In this chapter, one continuum modelling approach and one microstructural modelling approach are presented and discussed. Both these approaches are useful in analysing and simulating different defibration processes and different types of mechanical pre-treatment. The influence of different loading modes, loading directions and loading rates on the deformation and fracturing processes of wood are also of interest. Numerical examples using these two main approaches are presented in Chapters 6 and 7, where comparisons with experimental results also are made.

4.2 Modelling at Macrostructural Level

4.2.1 Modelling approach

The most important conclusion to be drawn from the experimental investigation presented in Chapter 3 is that the inhomogeneity and anisotropy of the material should be taken into account in studying initial defibration processes. The tests clearly illustrate

the differences in mechanical properties between earlywood and latewood. If numerical simulations of initial defibration processes are to be successful, account must be taken of these differences. It is also shown in Chapter 3 that the mechanical behavior of wood loaded perpendicular to the grain can be very complex. Characteristics for the behavior of the material are the development of cracks and the large volumetric changes of earlywood when subjected to compression. In order to be able to perform proper simulation of initial defibration processes, the following material characteristics need to be taken into account:

- The inhomogeneity and anisotropy of the material.

- The nonlinear inelastic response of earlywood when subjected to compression perpendicular to the grain.

- The fracture mechanical behavior of the material.

The inhomogeneity of the material is taken into account by dividing the wood into zones of earlywood and latewood. The earlywood zones can be further subdivided in the radial direction into several layers that differ slightly in their stiffness and strength properties. By doing this, the strain localization arising when earlywood is subjected to high compression can, at least partly, be captured.

A crushable foam model is used to model the behavior of earlywood. Foams are characterized by their ability to deform volumetrically when subjected to compression, a deformation which is due to cell wall buckling processes in the microstructure, similar to the behavior observed in earlywood. A general description of the structure and properties of cellular solids such as foams is given by Gibson and Ashby in [16]. Due to the increasing structural use of foams for insulation, cushioning, and the absorbing of kinetic energy in case of impacts, various constitutive models have been developed, such as that described by de Souza Neta et al. [77]. The model employed in the present study is similar to the one described in [77] and based on non-associative compressible plasticity. The model is included in ABAQUS [24]. For the latewood, linear elastic behavior is assumed as long as no cracks are developed. The foam plasticity model could also be employed in the modelling of latewood if the inelastic response in compression of the latewood is to be taken into account. In the present study, on the other hand, the assumption of linear elasticity seems sufficiently accurate in modelling latewood.

Fracture of the material is taken into account by use of a fictitious crack model. The fracturing properties are projected onto distinct cracking surfaces by use of softening stress displacement relations. The model is implemented in the finite element simulations by introducing special crack elements between the standard solid elements. The constitutive modelling adopted can be summarized by the following:

- Dividing the wood into zones of earlywood and latewood

- Subdividing the earlywood into several layers in the radial direction

- Crushable foam plasticity model used for the earlywood

- Linear elastic behavior assumed for the latewood

- Fracturing modelled by means of a fictitious crack model

To develop material models reflecting all the characteristics of importance for the mechanical behavior of wood is a tremendous task. Therefore, various assumptions and simplifications must be made. One of the most important simplifications made in the present study is to assume isotropy. For the present applications, a plasticity model seems to be the most suitable choice for modelling the behavior of earlywood, whereas the latewood can be assumed to behave in a linear elastic way except for the cracking. In the case of linear elastic behavior, it is quite simple to account for orthotropy, but plasticity models for orthotropic materials are considerably more complex than those for isotropic materials. The most common orthotropic plasticity model used is based on the Hill yield criterion [26]. This criterion is a function of the stress deviator only, which means that yielding is independent of the hydrostatic stress. Taken together with the assumption of associated plastic flow, it implies that the plastic deformation is deviatoric, i.e. that there is no plastic volume change. This type of plasticity model is developed for metals, for which assumptions of plastic incompressibility and yielding independent on the pressure stress have been verified experimentally. These assumptions are, however, not reasonable for capturing the behavior of wood, since volumetric plastic changes are a key feature of the material behavior. The foam plasticity model adopted in the present study is not based on these assumptions. It has the disadvantage, on the other hand, of being based on isotropic behavior of the material. Wood is a highly anisotropic material. The largest differences in mechanical properties are between the longitudinal and transverse directions. There is also some directional dependence within the transverse plane. The stiffness ratio between the radial and the tangential directions is normally assumed to be about 1.5 and 2, see [7], [9] and [45]. This stiffness ratio is based, however, on conditions in which the material is considered as a continuum, in which the differences in properties between earlywood and latewood not are taken into account.

It should also be noted that the differences between the radial and tangential direction normally observed, only concerns the initial linear elastic part of the material behavior. In the present applications, in which earlywood is loaded far beyond the linear elastic response, these differences are probably not particularly important for the overall behavior of the material. In comparing the stress-strain curves for radial and tangential compression that Uhmeier et al. [84] obtained, it can be seen that the general appearance of the curves is similar, the differences consisting mainly in there being a slightly higher plateau stress in radial compression. This is probably due to reinforcement by the ray cells and to differences between the two directions in the structural arrangements of the wood fibres [66].

Since the out-of-plane properties do not influence the in-plane response decisively and the difference between the tangential and the radial directions is not significantly large, the use of on isotropic foam model may give quite reasonable results when analyzing wood loaded perpendicular to the grain. However, in order to be able to study arbitrary loading conditions and loading directions (not only perpendicular to

the grain), account should be taken of the anisotropy of the material. Models for orthotropic foams have been developed, for instance by Schreyer et al. [75]. This type of model might be used instead of the isotropic model adopted in this study.

In the following two sections the foam plasticity model and the fictitious crack model are presented and discussed.

4.2.2   Foam plasticity model

The model is well established, see e. g. [77] and [24], and has been developed for analysis of crushable foams which are used for impact absorption, particularly in the automotive industry. Concerning specific parts of the model, different alternatives exist for the choice of various parameters and the dependence on certain field variables. In the following, the model is presented as it is applied in the present investigation.

The behavior in the elastic region is assumed to be linear. The yield surface is defined in terms of the equivalent pressure stress p and the Mises equivalent stress q, defined as

$$p = -\frac{1}{3}\sigma_{kk} \tag{4.1}$$

$$q = \sqrt{\frac{3}{2}S_{ij}S_{ij}}, \tag{4.2}$$

where σ_{ij} are the components of the Cauchy stress tensor and S_{ij} are the deviatoric stress components given as

$$S_{ij} = \sigma_{ij} + pI_{ij}. \tag{4.3}$$

The yield surface is defined as

$$F = \sqrt{\left(\frac{p_t - p_c}{2} + p\right)^2 + \left(\frac{q}{M}\right)^2} - \frac{p_c + p_t}{2} = 0 \tag{4.4}$$

where p_t is the strength of the material in hydrostatic tension and $p_c = p_c\left(\epsilon_{vol}^{pl}\right)$ is the yield stress in hydrostatic compression as a function of volumetric plastic strain. The volumetric plastic strain is defined by

$$\epsilon_{vol}^{pl} = lnJ^{pl}, \tag{4.5}$$

where J^{pl} is the plastic part of the volume change

$$J = \frac{V}{V_0} = J^{el}J^{pl}, \tag{4.6}$$

and where J is the ratio of the current volume to original volume and J^{el} is the corresponding elastic part. M is a constant computed from the yield stress in uniaxial compression

$$M = \frac{\sigma_0}{\sqrt{p_t p_{c/0} - \frac{1}{3}\sigma_0\left(p_t - p_{c/0}\right) - \frac{1}{9}\sigma_0^2}}, \tag{4.7}$$

where σ_0 is the initial yield stress in uniaxial compression and $p_{c/0}$ is the initial value of p_c. The parameters p_t, p_c and σ_0 are all defined as positive numbers. Eq. (4.4) defines an elliptical surface in the $p-q$ plane intersecting the p-axis at $-p_t$ and p_c. The compressive strength, p_c, increases when the material is compacted, whereas p_t remains fixed throughout any plastic deformation process. The yield surface is illustrated in Figure 4.1. Uniaxial compression is represented in the $p-q$ plane as $p/q = 1/3$. In the deviatoric plane the yield surface is a circle, which implies that the yield stresses in triaxial tension and compression are equal.

The strength in hydrostatic tension p_t remains fixed, whereas the compressive strength p_c evolves as a result of compaction of the material. This is modelled by a piecewise linear function. For the present applications a tri-linear function was used.
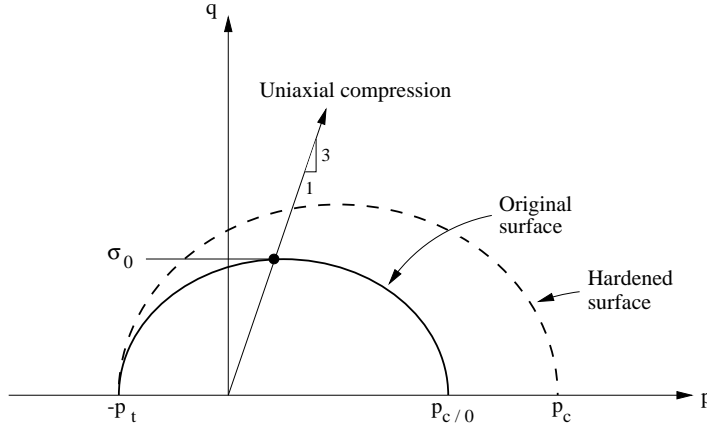
Figure 4.1: Yield surface in the $p-q$ plane for the crushable foam model.

Potential flow is assumed, the flow rule being written as

$$\Delta \epsilon_{ij}^{pl} = \Delta\lambda \frac{\partial h}{\partial \sigma_{ij}} \tag{4.8}$$

where $\Delta \boldsymbol{\epsilon^{pl}}$ is the plastic strain increment, $\Delta\lambda$ the plastic multiplier, and h the flow potential, given by

$$h = \sqrt{\frac{9}{2}p^2 + q^2}. \tag{4.9}$$

A geometrical representation of this flow potential is shown in Figure 4.2. The flow potential can be rewritten, using the definitions of the equivalent pressure stress and the Mises equivalent stress as given in Eq. (4.1) and (4.2), respectively:

$$h = \sqrt{\frac{9}{2}p^2 + \frac{3}{2}\left(S_{ij}S_{ij}\right)} = \sqrt{\frac{9}{2}p^2 + \frac{3}{2}\left(\sigma_{ij} + pI_{ij}\right)\left(\sigma_{ij} + pI_{ij}\right)}$$

$$= \sqrt{\frac{9}{2}p^2 + \frac{3}{2}\sigma_{ij}\sigma_{ij} + 3p\sigma_{ij}I_{ij} + \frac{3}{2}p^2 I_{ij}I_{ij}} \tag{4.10}$$

$$= \sqrt{\frac{9}{2}p^2 + \frac{3}{2}\sigma_{ij}\sigma_{ij} - 9p^2 + \frac{9}{2}p^2} = \sqrt{\frac{3}{2}\sigma_{ij}\sigma_{ij}}.$$

The plastic strain increment can now be expressed as

$$\Delta\epsilon_{ij}^{pl} = \Delta\lambda\frac{\partial h}{\partial\sigma_{ij}} = \Delta\lambda\frac{3}{2h}\sigma_{ij}. \tag{4.11}$$

The flow potential thus gives a direction of flow that is identical to the stress direction for radial paths. This means that loading in any principal direction causes no deformations in the other directions. Since the yield function is not used as the potential function, the plasticity is non-associated, resulting in a non-symmetrical material stiffness matrix.
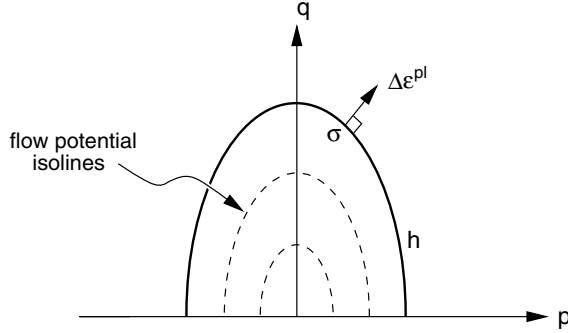
Figure 4.2: Plastic potential surface in the p-q plane for the foam plasticity model.

Foam materials often exhibit an increase in yield stress as strain rates increase. The strain rate dependence is assumed to be separable, the shape of the hardening curves at different strain rates being similar, according to

$$f^d = f^0\left(\epsilon_{vol}^{pl}\right) H_p\left(\dot{\epsilon}^{pl}\right), \tag{4.12}$$

where f^s is the static stress-strain behavior and H_p is the ratio of the yield stress at nonzero strain rate to the static yield stress. H_p is defined by a power law of the form

$$\dot{\epsilon}^{pl} = D(H_p - 1)^r \tag{4.13}$$

where D and r are material properties.

4.2.3 Fracture mechanics model

The nonlinear fracture mechanics model applied in this study corresponds to a Fictitious Crack Model (FCM), see Hillerborg [27], Gustafsson [18], Wernersson [87] and Petersson [68]. The model was implemented in the finite element simulations by introducing special crack elements. These crack elements are defined in a subroutine to the standard version of ABAQUS by use of the "UEL"-option. These crack elements are further discussed in Subsection 5.5.

The idea of FCM can be illustrated using a hypothetical experiment. A specimen without any crack is loaded in pure tension, as shown by Figure 4.3. Assume that the testing machine is very stiff and that the complete load-displacement curve for the specimen can be recorded. As the load is applied, the specimen initially behaves elastically. When the stress reaches the tensile strength of the material, a damage zone containing localized deformations may develop. If the deformation is increased further, the load carried by the specimen will decrease and the material outside the damage zone will be unloaded, as shown in Figure 4.3a. In modelling this behavior, the total deformation of the specimen, Δl, is assumed to be given by

$$\Delta l = l\epsilon + \delta \tag{4.14}$$

where $l\epsilon$ are the deformations of the material outside the fracture zone and δ is the distance between the separating surfaces in the fracture zone, Figure 4.3b. Note that δ is equal to zero until the fracture process zone starts to develop. The material properties of the fracture zone can now be separated from the material properties outside the fracture zone. The material behavior outside the fracture zone is described using a stress-strain relation ($\sigma - \epsilon$ relation), whereas the behavior of the fracture zone is described using a stress-displacement relation ($\sigma - \delta$ relation), Figure 4.3c and Figure 4.3d, respectively. The mechanical properties of the material are thus defined using two different types of relations; for the material outside the fracture process zone a stress - strain relation is employed and for the material within the fracture zone a relation between stress and displacement is used.

The fracturing properties given in the form of a softening stress relative displacement relation ($\sigma - \delta$ relation) are projected onto a fictitious crack surface. This surface is equivalent to an infinitely thin process zone, in which the relative displacement δ between the adjacent bounding surfaces of the zone is assumed to uniquely determine the stress in the fictitious process zone.

When testing for obtaining fracture mechanical properties, the softening deformation δ must be larger than the unloading recovery in order to establish stable performance during the complete test. More generally, this condition can be formulated in terms of energy, implying that more energy must be consumed in the crack opening process than the amount of elastic energy released during unloading. If this is not the case, a sudden failure will occur, as described in Section 3.3.

The above discussion concerns the pure opening mode (Mode I), corresponding to a relation between softening stress and relative displacements normal to the crack surface. Similarly, the concept can be applied to the pure shearing mode (Mode II), resulting in a relation between a softening shear stress and a relative shear displacement
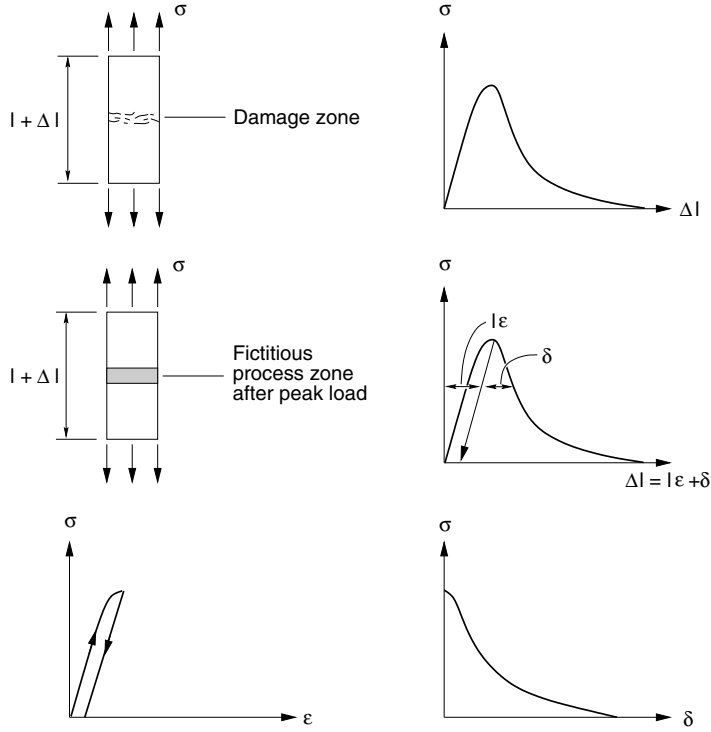
Figure 4.3: Characteristics of a fictitious crack model, illustrated for a specimen loaded in tension by displacement control, from [18]. Top: material behavior. Middle: model of the material behavior. Lower left: material properties outside the fracture zone. Lower right: material properties of the fracture zone.

parallel to the fracture surface. In addition to these pure modes, a mixed mode can be defined, involving stresses and displacements both normal and parallel to the fracture surface.

The fracture in the material is modelled by introducing two fictitious crack surfaces. The distance between these surfaces is initially zero. By introducing stresses and relative displacements between the surfaces, the fracturing can be modelled in a simple and well-defined way. The fracture mechanics model is to be used for applications involving large deformations. This means that the choice of stress measure by which the constitutive relations are formulated is very important. For instance, it can be seen from the experimental investigation (see for example Figure 3.27) that earlywood might be significantly compressed prior to cracking. This means that the fracture surface may be much smaller when cracking occurs than it was when defined in the undeformed configuration. Whether the stress measure is related to the undeformed or to the deformed configuration is thus important. The constitutive relations for the fracturing zone as presented in the following are formulated as forces per current area (true stress).

In the following, the tensile stress and the relative displacement normal to the fracture zone are denoted by σ_n and δ_n, respectively, and the shear stress and relative shear displacement by σ_s and δ_s. The fracturing properties for the pure opening mode, Mode I, and the pure shearing mode, Mode II, expressed as stress displacements relations, are approximated using bilinear curves, as shown in Figure 4.4. The tensile and shear strengths are denoted by f_t and f_s, respectively. The relative displacements for which the stresses are zero, i.e. at complete fracture, are denoted by δ_{n0}, δ_{s0} and the breakpoints on the curves are defined by σ_{n1}, δ_{n1} and σ_{s1}, δ_{s1}, respectively.
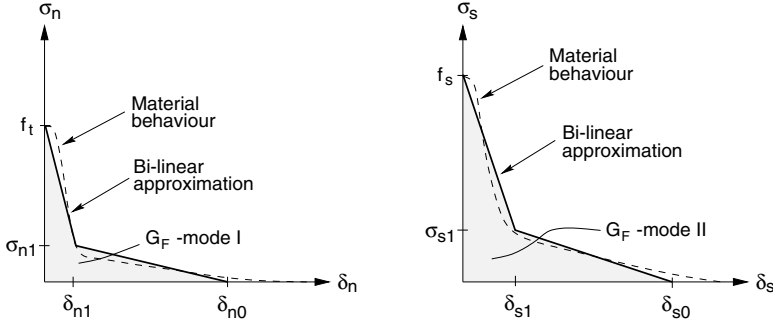
Figure 4.4: Approximation of fracturing properties using bilinear stress-displacement curves. Left: mode I. Right: mode II.

To be able to model a mixed mode fracture, there must be a coupling between the softening properties in tension and shearing. In this investigation, the stress components σ_n and σ_s are expressed as functions of the relative displacements δ_n and δ_s according to:

$$\sigma_n = \sigma_n \left(\delta_n, \delta_s \right) = \sigma_n \left(\delta_n \right) \left(1 - \frac{\delta_s}{\delta_{s0}} \right)^m \tag{4.15}$$

$$\sigma_s = \sigma_s \left(\delta_n, \delta_s \right) = \sigma_s \left(\delta_s \right) \left(1 - \frac{\delta_n}{\delta_{n0}} \right)^n, \tag{4.16}$$

where $\sigma_n(\delta_n)$ and $\sigma_s(\delta_s)$ denote the material description for the pure opening and the pure shearing mode, respectively, and where m, n are mixed mode coupling parameters. For $m = n = 0$ there is no coupling between the tensile and shearing behavior. Suitable values for m, n are in the range of 1-10. For $\delta_s = 0$, the shear stress is zero and the $\sigma_n(\delta_n, \delta_s)$ relation coincides with that of the pure opening mode. For $\delta_n = 0$, the tensile stress is zero and the $\sigma_s(\delta_n, \delta_s)$ relation coincides with that of the shearing mode, see Figure 4.4. When, however, $\delta_s > 0$ and $\delta_n > 0$ we have mixed mode fracturing, and the tensile (shearing) capacity is gradually reduced for increasing shearing (normal) deformation. This coupling for mixed mode fracturing is illustrated in Figure 4.5. Two examples of stress displacement relations for mixed mode loading are shown in Figure 4.6. In the figure, the tensile stress is plotted as a function of the relative normal and shear displacement for two different values of the coupling parameter m.

Figure 4.5: The coupling between tensile and shearing softening properties, illustrated for $m = n = 2$.

Figure 4.6: Examples of stress displacement relations for mixed mode fracturing. Tensile stress as a function of the relative normal and shear displacement for $m = 2$ and $m = 5$, respectively.
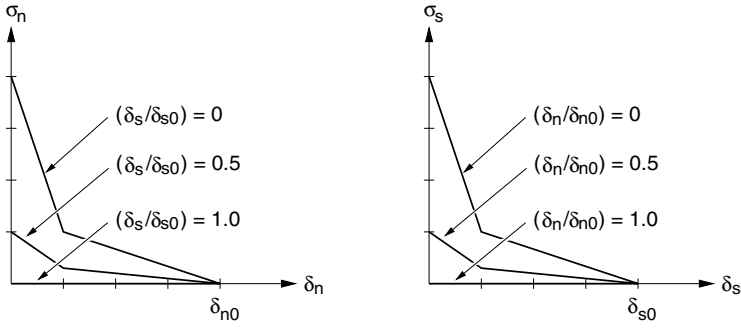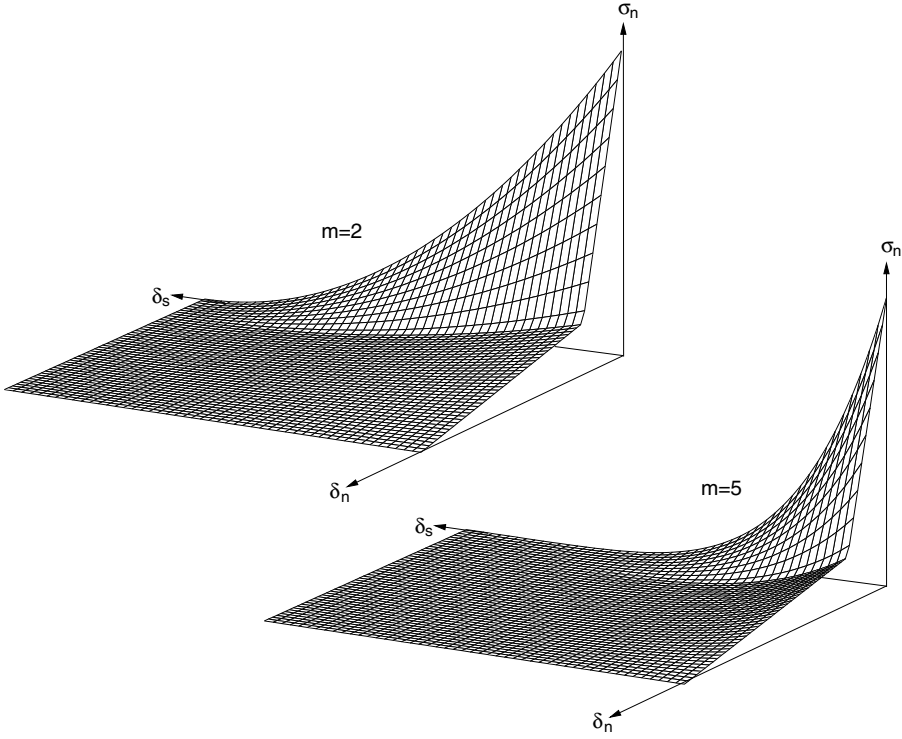
For compression perpendicular to the crack plane, a Coulomb friction model is used. This means that the shearing capacity is increased according to

$$\sigma_s = \sigma_s \left(\delta_s\right) \left(1 - \frac{\delta_n}{\delta_{n0}}\right)^n + \sigma_p \mu \tag{4.17}$$

where σ_p is the contact pressure at the fracture zone ($\sigma_p = -\sigma_n$) and μ is the coefficient of friction. The influence of friction on the shearing capacity is illustrated in Figure 4.7.
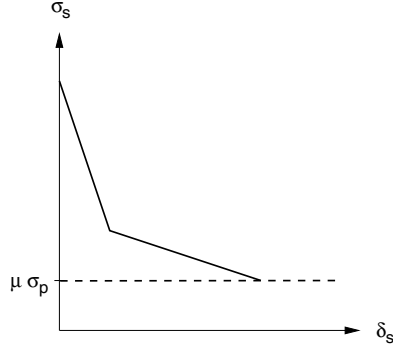
Figure 4.7: Increasing shear capacity due to friction.

Within the loading rate interval studied, the experimental investigation presented in Section 3.3 showed that the fracture energy and the maximum stress increase with increasing loading rate. The fracture energy and maximum stress varied approximately linearly with the logarithm of the loading rate. The increase in fracture energy with increasing loading rate was greater than that of the maximum stress except for the highest loading rate tested. The rate dependence of the fracturing properties is, in this study, modelled in a simple manner in terms of the initial stress rate (i.e. the stress rate prior to softening). It is assumed that the rate dependence is such that the shape of the softening curves for different loading rates is similar, cf. Figure 3.19. The uniaxial softening relations are then written as

$$\sigma_n = \sigma_n^0 \left(\delta_n, \delta_s\right) H_{fn} \tag{4.18}$$

$$\sigma_s = \sigma_s^0 \left(\delta_n, \delta_s, \sigma_p\right) H_{fs} \tag{4.19}$$

where σ_n^0, σ_s^0 are the uniaxial stress displacement relations for the reference loading rate and H_{fn}, H_{fs} are ratios of the softening stress at the current loading rate to the softening stress at the reference loading rate. H_{fn} is determined according to

$$H_{fn} = \left[1 + \frac{\Delta f_n}{f_n^0} \left(log\left(\frac{\dot{\sigma}_n}{\dot{\sigma}_n^0}\right)\right)\right] \tag{4.20}$$

where Δf_n is the increase in tensile strength when the loading rate is increased by a factor 10, f_n^0 is the tensile strength for the reference loading rate, $\dot{\sigma}_n$ is the current

stress rate (prior to softening) and $\dot{\sigma}_n^0$ is the corresponding stress rate for the reference loading rate. H_{fs} is defined in a similar manner as H_{fn}. The effect of the loading rate on fracturing behavior is illustrated in Figure 4.8.
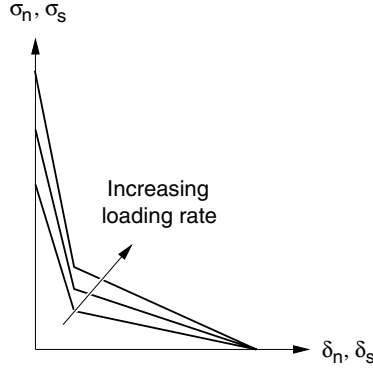
Figure 4.8: Change of uniaxial softening properties with increasing loading rate.

One of the most important parameters for characterizing fracture-mechanical properties is the fracture energy G_F, defined as the energy needed to bring a unit area of the material to complete fracture. For the pure opening mode, the fracture energy corresponds to the area under the $\sigma_n - \delta_n$ curve. Thus

$$G_F = \int_0^{\delta_{n0}} \sigma_n \left(\delta_n \right) d\delta_n \tag{4.21}$$

and similarly for pure shearing mode. For mixed mode fracture, the magnitude of G_F is the sum of the contributions from the two modes according to

$$G_F = \int_\Gamma \left(\sigma_n \left(\delta_n, \delta_s \right) d\delta_n + \sigma_s \left(\delta_n, \delta_s \right) d\delta_s \right) \tag{4.22}$$

where Γ is the deformation path resulting in complete separation of the material. The fracture energies for pure opening and pure shear modes are given as input data to the model. The mixed mode fracture energy is governed by these energy values, the magnitude of the coupling parameters m, n and the loading path. The influence of the radial loading direction and the magnitude of the coupling parameters on the fracture energy is illustrated in Figure 4.9 for equal values of m and n. It is assumed that tensile and shear softening begin at the same time. The radial loading path is expressed in terms of a mixed mode angle defined as

$$\psi = arctan \left(\frac{\delta_n}{\delta_s} \right). \tag{4.23}$$

The input data for the case illustrated are defined in Figure 4.9. The values are representative for spruce loaded in tension perpendicular to the grain and in longitudinal shear. The fracture energy for the pure opening mode is 400 J/m^2 and for the shearing mode 1000 J/m^2. For the case of $m = n = 0$, i.e. with no coupling between the two
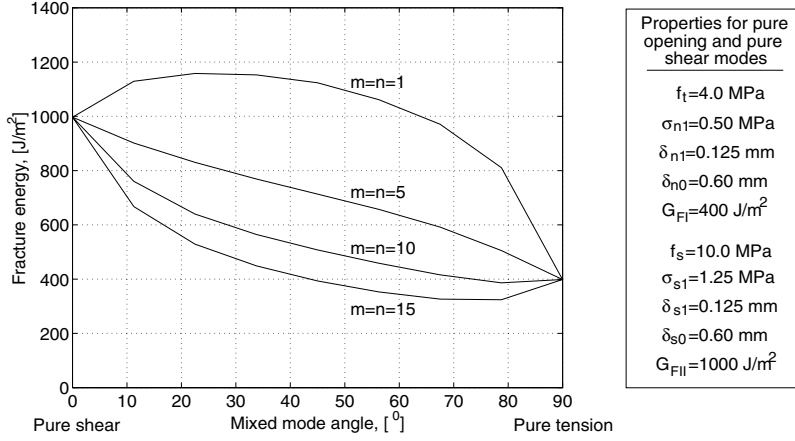
Figure 4.9: Fracture energy at radial loading paths.

modes, the fracture energy would be the sum of the uniaxial fracture energies irrespective of the loading direction. For $m = n = 1$ the mixed mode fracture energy exceeds that of the pure shear mode for some loading directions. For $m = n = 5$ the fracture energy varies approximately linearly between the uniaxial values. For higher values of m and n the fracture energy decreases more rapidly from that of the pure shear mode and may go below that of the pure opening mode. According to experimental data [20] suitable values of m and n for the case studied would be in the range of about 10. The fracture energy predicted by the model is (except for the case where m and n are set to zero) dependent on the loading path, i.e. on how a certain deformation state is reached. For combined compression and shear the fracture energy increases linearly with the compressive stress and the slope of the curve is equal to the coefficient of friction μ, Figure 4.10.
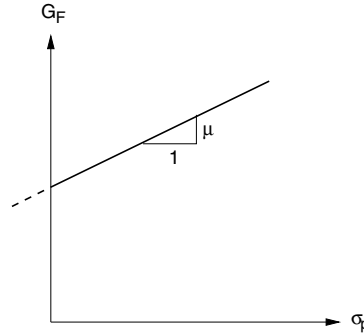
Figure 4.10: Fracture energy as a function of compressive stress.

If the crack width does not increase monotonically, crack closure may occur. For the applications in mind here, involving complex loading conditions and deformation patterns, crack closure can take place and must therefore be taken into account. In

the present model, it has simply been assumed that the crack closing path reverts to the origin. This behavior is illustrated in Figure 4.11.
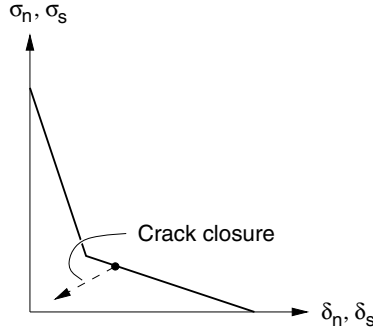
Figure 4.11: Illustration of crack closure.

The fracture mechanics model presented in this subsection was implemented in the finite element simulations by introducing special crack elements. This is discussed further in Section 5.5.

4.3   Modelling at Microstructural Level

4.3.1   General remarks

In contrast to the continuum approach discussed previously, a modelling of the cellular microstructure enables the deformation and fracturing of the individual cells to be simulated. This approach gives rise to very large computer models, however, permitting only small pieces of wood to be analysed. One method that might be used to overcome this problem, at least to some extent, is to assume periodic structures and to apply cyclic boundary conditions. This method was used in the present study.

An interesting aspect concerning the constitutive modelling is that the strong nonlinearities in mechanical response observed at the macroscopic level for compressive loading perpendicular to the grain are largely related to geometrical effects at the microstructural level when the cells are buckling and collapsing. At the continuum level, complex material models are needed in order for these nonlinearities to be taken into account. The constitutive models for the cell wall material when modelling at the microstructural level do not need to be so complex, however, in order for realistic results to be obtained. The material modelling for the cell wall material adopted in this work is based on linear anisotropic elasticity in combination with nonlinear fracture mechanics in order for microcracking of the cells to be captured. Nonlinear behavior in compression (plasticity) for the cell wall material is considered for the ray cells only.

In modelling the cellular structure, two main approaches may be distinguished [66]. One approach is to model real structures that are obtained from micrographs. The other approach is to generate a fictitious cell structure with properties representative of those of real structures. In this study the latter alternative is chosen. This approach

makes it simple to automatically generate a complete model, thus making it much easier to investigate the influence of various parameters of interest on the response and behavior of the structure. Furthermore, with this approach it is easy to generate structures that are periodic which, in combination with cyclic boundary conditions, is a clear advantage if larger structures are to be analysed. In a real cell structure model it might be difficult to apply cyclic boundary conditions as the cell walls at opposing boundaries will not be exactly equal. The model adopted to create the cellular microstructure was suggested by Persson [66]. It involves an irregular hexagonal cell shape and is based on micrographs and microstructural measurements.

4.3.2 Structural model

The model adopted to generate the wooden microstructure will only be outlined briefly. For more details reference is made to [66]. The length of the tracheids (longitudinal direction) is very large as compared to their cross-sectional dimensions. In the model the length of the tracheids is assumed to be infinite, the influence of the end caps of the tracheids thus being neglected. Furthermore, the small pits of the cell walls are omitted in the modelling. An irregular hexagonal cell shape is assumed, Figure 4.12. The radial width w_r, the tangential widths w_{t1} and w_{t2}, the cell wall thickness t and the irregularity parameter e are introduced. The parameter e determines the irregularity of the cell structure. For $e = 0.5$ a regular cell structure is obtained. The ratio of the tangential widths w_{t1} and w_{t2} determines the angle between the adjacent cell walls. For $w_{t1} = w_{t2}$ a quadratic cell shape is obtained. The tangential widths and the value of the irregularity parameter are assumed to be constant over the growth ring. The cell wall thickness and the radial cell width, on the other hand, vary over the growth ring. Constant width values are assumed for the earlywood and latewood regions, while in the transition region the radial cell width varies between the widths of the earlywood and the latewood.

The density of the cell can be determined by calculating the total area occupied by the cell, A_t, and the cell wall area A_w as

$$\rho_c = \frac{A_w}{A_t}\rho_0 \qquad (4.24)$$

where ρ_0 is the cell wall bulk density. As seen in Figure 2.5, the density over a growth ring varies considerably. To model this variation, the growth ring is divided into three regions: earlywood, transitionwood and latewood. In the earlywood region the density is assumed to have a slight linear increase. In the transitionwood the density is assumed to increase quadratically, and in the latewood the density is assumed to increase linearly. The breakpoints on the density curve are denoted by ρ_1 - ρ_4. The width of the latewood region l_l is set to 0.20 mm and the width of the transitionwood region l_t is assumed to represent 20 % of the total growth ring width [66]. The width of the earlywood region l_e can then be determined by subtracting the latewood and transitionwood widths from the total growth ring width.

The cell structure is modelled by assuming that the growth ring width l_r is known. The average density ρ_r can then be determined according to
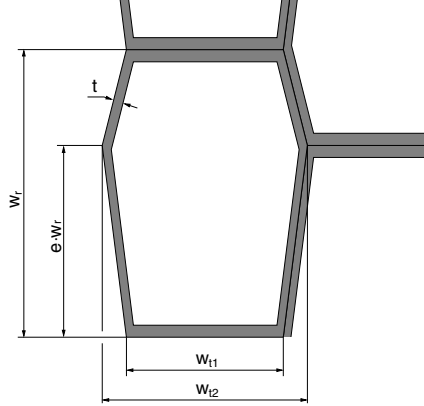
Figure 4.12: Assumed geometry of hexagonal cell from Persson [66].

$$\rho_r = \rho_e \frac{l_e}{l_r} + \rho_t \frac{l_t}{l_r} + \rho_l \frac{l_l}{l_r}. \tag{4.25}$$

The radial cell width w_r is assumed to be constant within the earlywood and the latewood. Within the transitionwood w_r is assumed to decrease linearly from that of the earlywood to that of the latewood. By knowing the radial width of each region and the radial cell widths, the number of cells in each region can be calculated.

By selecting a value of ρ_1 and by considering the assumptions concerning the variation in density within the different regions, the values of ρ_2, ρ_3 and ρ_4 can be computed allowing the complete density function over the growth ring to be established. The density of each cell ρ_c can then be determined. The cell wall thickness is then calculated by using Eq. (4.24) and the cell structure of the growth ring is established. The steps involved in generating the cell structure can be summarized by

- Selecting the growth ring width l_r.

- Selecting other values of the basic geometry and density variables needed.

- Calculating the widths of the earlywood l_e and transitionwood l_t.

- Determining the number of cells in the radial direction of each region.

- Determining the density functions for the three regions.

- Calculating the cell wall thickness of each cell in the growth ring using Eq. (4.24).
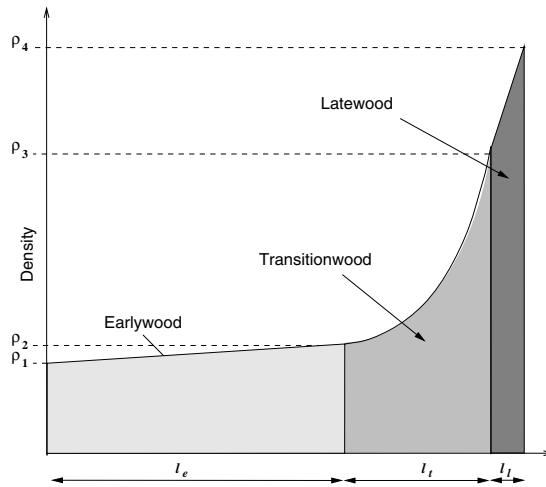
Figure 4.13: Assumed variation in density over a growth ring [66].

In addition to tracheid cells the cell structure also comprises radially oriented cells (ray cells), which are of importance for the mechanical behavior of the cell structure. The ray cells are incorporated in the model by introducing an equivalent cell wall layer at each side of the generated structure (half a ray cell at each side). The width of the ray cell layer was set to 1.5 μm. The parameters needed to define the cell structure and the values assumed in this study are given in Table 4.1. The geometric values are chosen on the basis of microstructural measurements and of micrographs, see [66].

Examples of cell structures generated by the model are shown in Figure 4.14. The picture at the top shows the structure generated when assuming an average density of the growth ring of 550 kg/m^3, and the lower one corresponds to an average density of 400 kg/m^3. At a density of 550 kg/m^3 the number of cells in the radial direction of the growth ring is equal to 27, whereas at a density of 450 kg/m^3 the number of cells is increased to 42. In the examples shown the number of cells between two ray cells was set to four.

4.3.3   Constitutive modelling of the cell wall material

The cell wall consists of four layers. In addition, there is the inter-cellular layer of lignin, the middle lamella, holding the fibres together, see Figure 2.3. The various layers differ in their thickness, chemical composition and microfibril orientation. The cell wall is modelled in a simplified manner through dividing it into two main layers, one representing the middle lamella together with the primary wall and the S1 layer, and the other representing the S2 layer together with the S3 layer. The reason for not considering all the individual cell wall layers separately is primarily to keep down the size of the models without losing much accuracy. The elastic stiffness parameters for the different layers are determined from stiffness values of the basic elements of the cell

Table 4.1: Adopted geometry and density parameters needed to define the cell structure. The values are chosen in agreement with those used by Persson [66]. The radial cell width w_r is assumed to be constant in the earlywood and the latewood and to vary linearly in the transitionwood.

Parameter	Assumed value	Remark
w_{t1}	25 μm	-
w_{t2}	27 μm	-
w_r	35 μm	earlywood
w_r	35-16 μm	transitionwood
w_r	16 μm	latewood
e	0.65	-
w_{ray}	1.5 μm	-
l_t	$0.20 l_r$ mm	20% of total ring length
l_l	0.20 mm	-
ρ_0	1500 kg/m^3	-
ρ_1	260 kg/m^3	-
ρ_e	300 kg/m^3	-
ρ_l	450 kg/m^3	-
ρ_t	1000 kg/m^3	-
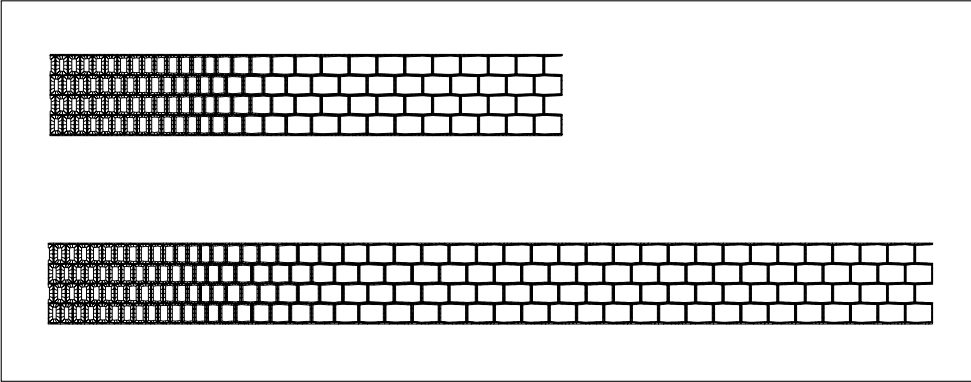
Figure 4.14: Examples of growth ring structures generated by the model. Top: Average density of 550 kg/m^3 and a growth ring width of 0.8 mm. Lower: Average density of 450 kg/m^3 and a growth ring width of 1.2 mm.

walls (the so-called microfibrils) as reported by Persson [66]. These stiffness values of the microfibrils were obtained from the properties of the basic chemical constituents (the cellulose, the hemicellulose and the lignin) and by using a homogenization method. Depending on the assumed shape and composition of the microfibril model (different models have been suggested in the literature, for example by Fengel [13] and Preston [70]), either an orthotropic or a transversely isotropic material is obtained. The stiffness values adopted for the microfibrils are expressed in terms of a local microfibril coordinate system. In order to orient the local coordinate system of the microfibrils to the global coordinate system of the overall structural model, two transformations are needed. First, a transformation of the principal directions of the microfibril to the cell wall coordinate system is made, according to the microfibrillar angle of the cell wall layer considered (a constant microfibril angle for each layer is assumed, possible variations within the layers not being considered). The second transformation is made to align the cell wall layers to the global directions of the hexagonal cells, see Figure 4.15. Transformations of the constitutive matrices are made according to Eq. (2.7).
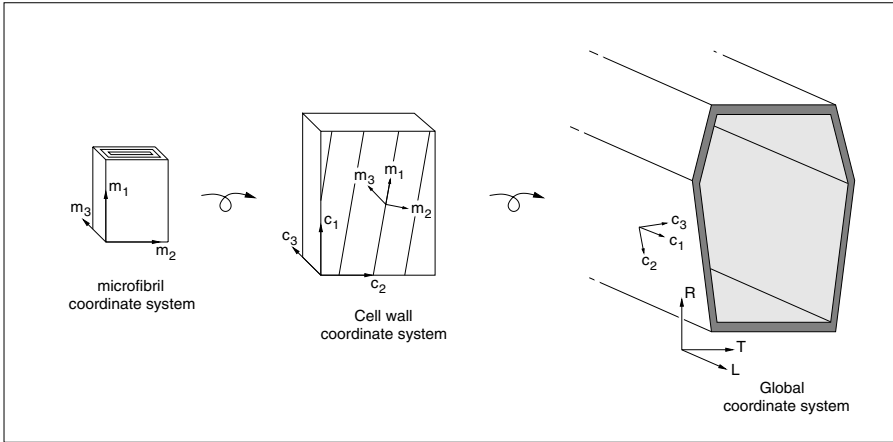
Figure 4.15: Transformations needed to orient the local microfibril coordinate system to a common global coordinate system.

Microscopic investigations have shown microcracking to occur frequently for compressive loading perpendicular to the grain [80]. By the present modelling, fracturing at the cell corners can be considered, see Figure 4.16, but delamination of the cell wall layers is not taken into account. The fictitious crack model of Section 4.2.3 was employed to capture the fracturing of the cell wall material.

Nonlinear effects in compression for the cell wall material are taken into account for the ray cells only. This is done by adopting the orthotropic yield criterion proposed by Hill [26]. When the axes of the 123-coordinate system coincide with the axes of orthotropy, the Hill yield criterion is given by
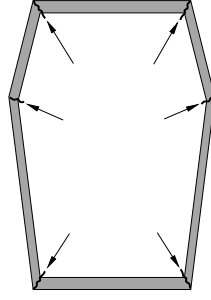
Figure 4.16: Zones of possible microcracking can be considered in the modelling.

$$f\left(\boldsymbol{\sigma}\right) = a_1\left(\sigma_{22} - \sigma_{33}\right)^2 + a_2\left(\sigma_{33} - \sigma_{11}\right)^2 + a_3\left(\sigma_{11} - \sigma_{22}\right)^2$$

$$+ a_4\sigma_{23}^2 + a_5\sigma_{13}^2 + a_6\sigma_{12}^2 - \sigma_{ref}^2 = 0, \tag{4.26}$$

where $\boldsymbol{\sigma}$ is the Cauchy stress tensor and the material parameters $a_1 - a_6$ are expressed as

$$
\begin{aligned}
a_1 &= \frac{\sigma_{ref}^2}{2}\left(\frac{1}{\sigma_{22y}^2} + \frac{1}{\sigma_{33y}^2} - \frac{1}{\sigma_{11y}^2}\right) & a_4 &= \frac{\sigma_{ref}^2}{\sigma_{23y}^2} \\
a_2 &= \frac{\sigma_{ref}^2}{2}\left(\frac{1}{\sigma_{33y}^2} + \frac{1}{\sigma_{11y}^2} - \frac{1}{\sigma_{22y}^2}\right) & a_5 &= \frac{\sigma_{ref}^2}{\sigma_{13y}^2} \\
a_1 &= \frac{\sigma_{ref}^2}{2}\left(\frac{1}{\sigma_{11y}^2} + \frac{1}{\sigma_{22y}^2} - \frac{1}{\sigma_{33y}^2}\right) & a_6 &= \frac{\sigma_{ref}^2}{\sigma_{12y}^2}
\end{aligned}
\tag{4.27}
$$

where σ_{ijy} are the yield stresses with respect to the orthotropic directions i and j and σ_{ref} is a reference stress. The Hill yield criterion is an extended form of von Mises' criterion for isotropic materials. When the parameters $a_1 - a_6$ satisfy

$$6a_1 = 6a_2 = 6a_3 = a_4 = a_5 = a_6, \tag{4.28}$$

Eq. (4.26) reduces to the von Mises criterion.

For compressive and shear loading, very large deformations occur locally resulting in cell walls coming into contact with each other and interacting as the cells collapse. Due to the strong localization occurring for compressive loading perpendicular to the grain, this phenomenon becomes of importance already at rather low average (macroscopic) strains. It is therefore of great importance to take this into account in the modelling. In each cell lumen, contact conditions are introduced controlling the contact and preventing the cell walls from penetrating each other. A Coulomb friction model is employed for the contacting surfaces.

Numerical examples simulating the behavior of wooden cell structures when loaded perpendicular to the grain using the modelling approach outlined are presented in

Chapter 7. The influence of different constititive assumptions on the response is illustrated, and a comparison is made with the observed behavior of real structures.

Chapter 5

Numerical Procedure

5.1 Introduction

In the next two chapters, numerical simulations related to initial defibration processes are presented. In the simulations performed both nonlinear material behavior and geometric nonlinearity were taken into account. The simulations were carried out using the general purpose finite element code ABAQUS [24]. The present chapter provides a background to the computer simulations, and of the theory involved in the simulations will be presented. The finite element equations, the technique used when solving them, and the solid element formulation employed by the program in dealing with problems exhibiting both geometric and material nonlinearity will be outlined. The fracture mechanics model presented in Section 4.2.3 was applied in the finite element simulations by introducing special crack elements. The formulation used for these crack element is also discussed. The aim is not to provide a complete description of the theory and the numerical algorithms involved, but rather to describe the general procedure used in establishing and solving the finite element equations. For a more comprehensive description, reference is made to [24].

5.2 Finite Element Equations

The finite element method is a numerical approach allowing partial differential equations to be solved approximately. The basics of the finite element method and its application to various types of problems are dealt with, for example, in Ottosen and Petersson [64] and in Zienkiewiecz and Taylor [89]. For a review of different formulations used in non-linear finite element analysis, see e.g. Bathe [6].

The formulation is based on a Lagrangian description of motion, according to which the path of a material point is followed through the various configurations of the body, every position being defined in relation to a reference configuration. The relation between the current and the referential coordinates for any point is given by

$$x_i = X_i + u_i \qquad i = 1, 2, 3, \tag{5.1}$$

where x_i are current (spatial) coordinates, X_i are referential (material) coordinates which remain fixed for a particular material point and u_i are the components of the

displacement vector. The current position and, thereby, the displacements are expressed in terms of the coordinates of the referential position.

The finite element equations are derived from the equations of motion given by

$$\frac{\partial \sigma_{11}}{\partial x_1} + \frac{\partial \sigma_{21}}{\partial x_2} + \frac{\partial \sigma_{31}}{\partial x_3} + b_1 = \rho \ddot{u}_1$$

$$\frac{\partial \sigma_{12}}{\partial x_1} + \frac{\partial \sigma_{22}}{\partial x_2} + \frac{\partial \sigma_{32}}{\partial x_3} + b_2 = \rho \ddot{u}_2$$

$$\frac{\partial \sigma_{13}}{\partial x_1} + \frac{\partial \sigma_{23}}{\partial x_2} + \frac{\partial \sigma_{33}}{\partial x_3} + b_3 = \rho \ddot{u}_3$$

or expressed in a compact form (summation over repeated indices) as

$$\frac{\partial \sigma_{ji}}{\partial x_j} + b_i = \rho \ddot{u}_i \qquad i = 1, 2, 3, \tag{5.2}$$

where σ_{ij} are components of Cauchy's stress tensor, b_i represent body forces per unit of current volume, $\ddot{u}_i$ are the accelerations and ρ is the current density of the material. The tractions, t_i, acting on the surface S surrounding the body are given by

$$t_i = \sigma_{ji} n_j. \tag{5.3}$$

In order to develop the finite element formulation, the three equilibrium equations represented by Eq. (5.2) are replaced by an equivalent "weak form". This weak form is a single scalar equation over the entire body. The weak form is obtained by multiplying the differential equations by arbitrary weight functions v_i and integrating over the volume V occupied by the body. Taking the scalar product of Eq. (5.2) with respect to the weight functions v_i results in a single scalar equation

$$\int_V v_i \frac{\partial \sigma_{ji}}{\partial x_j} \, dV + \int_V v_i b_i \, dV = \int_V \rho v_i \ddot{u}_i \, dV. \tag{5.4}$$

An integration by parts using the Green-Gauss theorem is performed on the first term on the left-hand side, resulting in

$$\int_V v_i \frac{\partial \sigma_{ji}}{\partial x_j} \, dV = \int_S v_i \sigma_{ji} n_j \, dS - \int_V \frac{\partial v_i}{\partial x_j} \sigma_{ji} \, dV. \tag{5.5}$$

Inserting Eq. (5.5) into Eq. (5.4) and using Eq. (5.3) yields the weak form of the equations of motion

$$\int_S v_i t_i \, dS + \int_V v_i b_i \, dV = \int_V \frac{\partial v_i}{\partial x_j} \sigma_{ji} \, dV + \int_V \rho v_i \ddot{u}_i \, dV. \tag{5.6}$$

The terms on the right-hand side of Eq. (5.6) can be replaced by integrals over the reference volume, giving

$$\int_{V_0} \rho_o v_i \ddot{u}_i \, dV_0 + \int_{V_0} \frac{\partial v_i}{\partial x_j} \tau_{ji} \, dV_0 = \int_S v_i t_i \, dS + \int_V v_i b_i \, dV \tag{5.7}$$

where ρ_0 is the density referred to the reference volume and τ_{ij} are components of the Kirchhoff stress tensor defined by

$$\tau_{ij} = \frac{dV}{dV_0}\sigma_{ij}. \tag{5.8}$$

The finite element equations are obtained by introducing approximations of the displacement vector and the acceleration vector and by choosing the weight functions appropriately. The displacements and the accelerations are approximated by

$$u_i = N_{ik}a_k \tag{5.9}$$

$$\ddot{u}_i = N_{ik}\ddot{a}_k \tag{5.10}$$

where N_{ik} ($i = 1, 2, 3;\ k = 1, 2, 3...$ total number of degrees of freedom in the problem) are time-independent interpolation functions and a_k and $\ddot{a}_k$ are nodal displacements and accelerations, respectively. In accordance with the Galerkin method, the weight functions are selected as

$$v_i = N_{il}c_l. \tag{5.11}$$

where c_l are components of an arbitrary vector. The gradient of the weight functions can now be expressed as

$$\frac{\partial v_i}{\partial x_j} = c_l\,\frac{\partial N_{il}}{\partial x_j}. \tag{5.12}$$

Inserting Eqs. (5.9)-(5.12) into Eq. (5.7) yields

$$c_l\left(\int_{V_0}\rho_0 N_{il}N_{ik}\ddot{a}_k\ dV_0 + \int_{V_0}\frac{\partial N_{il}}{\partial x_j}\tau_{ji}\ dV_0\right) = c_l\left(\int_S N_{il}t_i\ dS + \int_V N_{il}b_i\ dV\right). \tag{5.13}$$

This equation should hold for all values of c_l, which means that we get a system of nonlinear equilibrium equations

$$\left(\int_{V_0}\rho_0 N_{il}N_{ik}\ dV_0\right)\ddot{a}_k + \int_{V_0}\frac{\partial N_{il}}{\partial x_j}\tau_{ji}\ dV_0 = \int_S N_{il}t_i\ dS + \int_V N_{il}b_i\ dV. \tag{5.14}$$

This system of equations is the basic finite element formulation of the problem. Eq. (5.14) can be expressed in the more compact form

$$M_{lk}\ddot{a}_k + P_l^{int} - P_l^{ext} = 0 \qquad l = 1, 2, 3... \tag{5.15}$$

where M_{lk} are the components of the mass matrix, P_l^{int} the internal forces and P_l^{ext} the external forces as defined by

$$M_{lk} = \int_{V_0}\rho_0 N_{il}N_{ik}\ dV_0 \tag{5.16}$$

$$P_l^{int} = \int_{V_0}\frac{\partial N_{il}}{\partial x_j}\tau_{ji}\ dV_0 \tag{5.17}$$

$$P_l^{ext} = \int_S N_{il}t_i\ dS + \int_V N_{il}b_i\ dV. \tag{5.18}$$

The definition of the mass matrix above is the consistent mass matrix. However, for the first-order elements, a lumped diagonal mass matrix is employed by the computer code.

In the description that follows, it is convenient to use matrix notation, Eq. (5.15) then being written as

$$\mathbf{M\ddot{a}} + \mathbf{P}^{int} - \mathbf{P}^{ext} = \mathbf{0}. \tag{5.19}$$

For static problems, the set of finite element equations given by Eq. (5.19) reduces to

$$\mathbf{P}^{int} - \mathbf{P}^{ext} = \mathbf{0}. \tag{5.20}$$

5.3   Solution Technique

An implicit operator defined by Hilber, Hughes and Taylor [25] is used for the time integration. For this operator, the equilibrium equations, Eq. (5.19), are replaced by a balance of inertia forces at the end of the time step and a weighted average of the static forces at the beginning and end of the time step

$$\mathbf{M\ddot{a}}_{n+1} + (1+\alpha)\left(\mathbf{P}^{int}_{n+1} - \mathbf{P}^{ext}_{n+1}\right) - \alpha\left(\mathbf{P}^{int}_{n} - \mathbf{P}^{ext}_{n}\right) = \mathbf{0}, \tag{5.21}$$

where the subscripts n and $n+1$ refer to time t_n and t_{n+1}, respectively. The displacement and velocity integration procedure is defined by Newmark's algorithm:

$$\mathbf{a}_{n+1} = \mathbf{a}_n + \Delta t \dot{\mathbf{a}}_n + \Delta t^2 \left(\left(\frac{1}{2} - \beta\right)\ddot{\mathbf{a}}_n + \beta\ddot{\mathbf{a}}_{n+1}\right) \tag{5.22}$$

$$\dot{\mathbf{a}}_{n+1} = \dot{\mathbf{a}}_n + \Delta t \left((1-\gamma)\ddot{\mathbf{a}}_n + \gamma\ddot{\mathbf{a}}_{n+1}\right) \tag{5.23}$$

where Δt is the time increment, i.e.

$$\Delta t = t_{n+1} - t_n, \tag{5.24}$$

and

$$\beta = \frac{1}{4}\left(1-\alpha\right)^2 \qquad \gamma = \frac{1}{2} - \alpha \qquad -\frac{1}{3} \le \alpha \le 0. \tag{5.25}$$

The parameter α controls the amount of numerical damping. When $\alpha = 0$ there is no damping (corresponding to the trapezoidal rule), whereas significant damping is available when $\alpha = -\frac{1}{3}$. The default value for the numerical damping is $\alpha = -0.05$.

The residual or out-of-balance forces at t_{n+1} are defined as

$$\mathbf{G}_{n+1} = -\mathbf{M\ddot{a}}_{n+1} + (1+\alpha)\left(\mathbf{P}^{ext}_{n+1} - \mathbf{P}^{int}_{n+1}\right) - \alpha\left(\mathbf{P}^{ext}_{n} - \mathbf{P}^{int}_{n}\right) \tag{5.26}$$

The aim is to find the solution of

$$\mathbf{G}_{n+1} = \mathbf{0} \tag{5.27}$$

By using Eq. (5.22), the system of equations can be solved. Eq. (5.27), may be written in the form of an equation for the displacement vector $\mathbf{a}_{n+1}$,

$$\mathbf{G}_{n+1} = \mathbf{G}\left(\mathbf{a}_{n+1}\right) = \mathbf{0}, \tag{5.28}$$

where

$$\mathbf{G}\left(\mathbf{a}_{n+1}\right) = -\mathbf{M}\left[\frac{1}{\beta\Delta t^2}\left(\mathbf{a}_{n+1} - \mathbf{a}_n\right) - \frac{1}{\beta\Delta t}\dot{\mathbf{a}}_n + \left(1 - \frac{1}{2\beta}\right)\ddot{\mathbf{a}}_n\right]$$
$$+ (1+\alpha)\left(\mathbf{P}_{n+1}^{ext} - \mathbf{P}_{n+1}^{int}\right) - \alpha\left(\mathbf{P}_n^{ext} - \mathbf{P}_n^{int}\right). \tag{5.29}$$

Due to the non-linearity of Eq. (5.28), the equation system is solved in an iterative manner. This is done using the Newton Raphson method. The principle of this method is to start with an initial prediction of the response and then, by successive iterations, improving the initial prediction until equilibrium is reasonably well satisfied. Eq. (5.28) can to the first order be approximated as

$$\mathbf{G}\left(\mathbf{a}_{n+1}^{i+1}\right) \approx \mathbf{G}\left(\mathbf{a}_{n+1}^i\right) + \left(\frac{\partial\mathbf{G}}{\partial\mathbf{a}}\right)_{n+1}^i \Delta\mathbf{a}_n^i = \mathbf{0} \tag{5.30}$$

where i is the iteration counter starting from

$$\mathbf{a}_{n+1}^1 = \mathbf{a}_n. \tag{5.31}$$

The iterative correction is found, through Eq. (5.30), to be

$$\Delta\mathbf{a}_n^i = \left(\hat{\mathbf{K}}^i\right)^{-1}\mathbf{G}^i{}_{n+1} \tag{5.32}$$

where

$$-\frac{\partial\mathbf{G}}{\partial\mathbf{a}} = \hat{\mathbf{K}} \tag{5.33}$$

is the Jacobian matrix. A series of successive iterations gives

$$\mathbf{a}_{n+1}^{i+1} = \mathbf{a}_{n+1}^i + \Delta\mathbf{a}_n^i. \tag{5.34}$$

The principle of the process is shown for a one-degree-of-freedom system in Figure 5.1. The criterion used for stopping the iterations is based on all the entries in both $\mathbf{G}$ and $\Delta\mathbf{a}$ being sufficiently small.

The Jacobian matrix $\hat{\mathbf{K}}$ used in the Newton Raphson scheme is derived by differentiating Eq. (5.29) with respect to $\mathbf{a}_{n+1}$ and consists of several terms

$$-\left(\frac{\partial\mathbf{G}}{\partial\mathbf{a}_{n+1}}\right) = \hat{\mathbf{K}}_{n+1} = \frac{1}{\beta\Delta t^2}\mathbf{M} + (1+\alpha)\frac{\partial\mathbf{P}^{int}}{\partial\mathbf{a}_{n+1}} - (1+\alpha)\frac{\partial\mathbf{P}^{ext}}{\partial\mathbf{a}_{n+1}}. \tag{5.35}$$

$\partial\mathbf{P}^{int}/\partial\mathbf{a}_{n+1}$, representing the variation of internal forces with displacement, is generally referred to as the tangent stiffness matrix $\mathbf{K}$. It is derived by differentiating Eq. (5.17) with respect to $\mathbf{a}$. In component form it becomes

$$K_{lk} = \int_{V_0}\frac{\partial N_{il}}{\partial x_j}\frac{\partial\tau_{ji}}{\partial a_k}\,dV_0 + \int_{V_0}\frac{\partial}{\partial a_k}\left(\frac{\partial N_{il}}{\partial x_j}\right)\tau_{ji}\,dV_0 \tag{5.36}$$
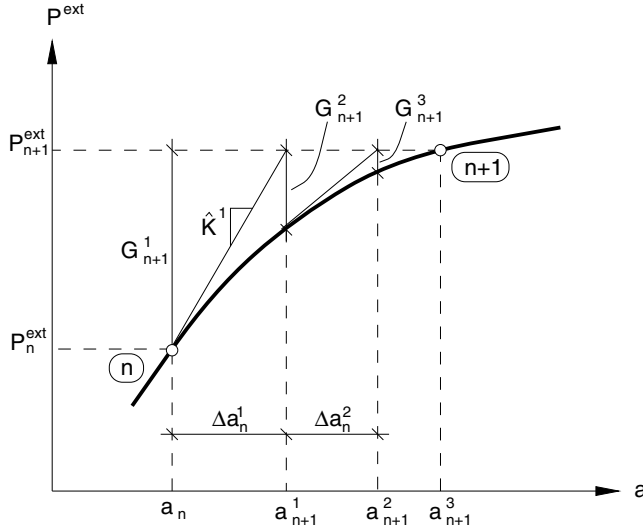
Figure 5.1: The Newton Raphson method illustrated for a one-degree-of-freedom system.

where the first term corresponds to the usual small displacement stiffness matrix, except for the fact that the term $\partial N_{il}/\partial x_j$ is a function of displacement, and where the second term is the initial stress matrix.

$\partial \mathbf{P}^{ext}/\partial \mathbf{a}_{n+1}$, describing the dependence of the external forces upon the geometry, is generally referred to as the load stiffness or load correction matrix $\mathbf{K}_{load}$. It can be derived from Eq. (5.18). Using these definitions, the Jacobian matrix can be written as

$$\hat{\mathbf{K}} = \frac{1}{\beta \Delta t^2} \mathbf{M} + (1 + \alpha)\, \mathbf{K} - (1 + \alpha)\, \mathbf{K}_{load}. \tag{5.37}$$

The solution of the corresponding static problems is also given by Eq. (5.30) to (5.34). The residual forces at the increment $n + 1$ are then defined as the difference between the external and the internal forces. Accordingly,

$$\mathbf{G}_{n+1} = \mathbf{P}_{n+1}^{ext} - \mathbf{P}_{n+1}^{int}, \tag{5.38}$$

the Jacobian matrix reducing to

$$\hat{\mathbf{K}} = \mathbf{K} - \mathbf{K}_{load}. \tag{5.39}$$

For a review of different techniques of solving dynamic and static nonlinear problems, see e.g. Zienkiewicz and Taylor [90] or Owen and Hinton [65].

5.4   Solid Element Formulation

A description of the formulation for solid elements when used for geometrically nonlinear analysis at finite strains will be given in this subsection. The description is

restricted to materials having some kind of inelastic behavior. For such materials the constitutive relations are established in rate form, whereas for elastic materials at finite strain, such as rubber-like materials or elastomeric foams, the constitutive behavior is defined as a total stress-total strain relationship.

It should be emphasized that the type of rate formulation used here, based on hypo-elasticity, satisfies the objectivity principle only if the elastic stiffness tensor is isotropic. Strictly, this means that such formulations, which are implemented in many commercial finite element codes, exclude anisotropic elasticity. For details on this subject and for a discussion of different large strain plasticity theories, see e.g. Ristinmaa and Ottosen [72].

The stress measure appearing in the equilibrium equations is the Kirchhoff stress $\boldsymbol{\tau}$. This is also the stress measure used to develop constitutive relations for solid elements in ABAQUS. Since the constitutive relations are established in rate form, the rate of Kirchhoff stress used in these constitutive equations needs to be defined. Since the Kirchhoff stress components are associated with spatial directions in the current configuration, the material time rate of Kirchhoff stress $\dot{\boldsymbol{\tau}}$ is not suitable as such a stress rate measure. Instead, use is made of the co-rotational (or Jaumann) rate of Kirchhoff stress as the stress rate when constitutive relations for solid elements are established. For further reading on different stress rates, see e.g. Malvern [57]. The Jaumann rate of Kirchhoff stress $\hat{\boldsymbol{\tau}}$ is defined as

$$\hat{\boldsymbol{\tau}} = \dot{\boldsymbol{\tau}} - \mathbf{W}\boldsymbol{\tau} + \boldsymbol{\tau}\mathbf{W}, \tag{5.40}$$

where $\dot{\boldsymbol{\tau}}$ is the material time rate of Kirchhoff stress and the last two terms on the right side correspond to the rate caused by pure rigid body spin. The spin tensor $\mathbf{W}$ is defined as the antisymmetric part of the spatial velocity gradient. Accordingly,

$$\mathbf{W} = asym\left(\frac{\partial \dot{\mathbf{u}}}{\partial \mathbf{x}}\right) = \frac{1}{2}\left(\frac{\partial \dot{\mathbf{u}}}{\partial \mathbf{x}} - \left[\frac{\partial \dot{\mathbf{u}}}{\partial \mathbf{x}}\right]^T\right), \tag{5.41}$$

or in component form

$$W_{ij} = \frac{1}{2}\left(\frac{\partial \dot{u}_i}{\partial x_j} - \frac{\partial \dot{u}_j}{\partial x_i}\right). \tag{5.42}$$

The symmetric part of the velocity gradient is called the rate of deformation tensor

$$\mathbf{D} = sym\left(\frac{\partial \dot{\mathbf{u}}}{\partial \mathbf{x}}\right) = \frac{1}{2}\left(\frac{\partial \dot{\mathbf{u}}}{\partial \mathbf{x}} + \left[\frac{\partial \dot{\mathbf{u}}}{\partial \mathbf{x}}\right]^T\right). \tag{5.43}$$

The velocity gradient can then be written as

$$\mathbf{L} = \mathbf{W} + \mathbf{D}. \tag{5.44}$$

The spin tensor measures the angular velocity of the principal axis of the rate of deformation. The rate of deformation tensor is the strain rate measure which is work-conjugate to the Kirchhoff stress. The constitutive equations thus relate the Jaumann

rate of Kirchhoff stress $\hat{\boldsymbol{\tau}}$ to the rate of deformation $\mathbf{D}$. The constitutive equations may then be assumed to be of the form

$$\hat{\boldsymbol{\tau}} = \mathbf{CD} \tag{5.45}$$

or in component form

$$\hat{\tau}_{ij} = C_{ijkl} D_{kl}, \tag{5.46}$$

where $\mathbf{C}$ is the Jacobian matrix of the constitutive model.

In the one-dimensional case, a corresponding strain rate measure $\dot{\epsilon}$ can be integrated to a total strain measure which is the logarithmic strain

$$\epsilon_{log} = \int_{l_0}^{l} \frac{dl}{l} = ln\left(\frac{l}{l_0}\right) = ln\left(1 + e\right) \tag{5.47}$$

where e is the nominal or engineering strain. This identifies $\dot{\epsilon}$ as the rate of logarithmic strain. This identification also applies in the multi-dimensional case if the principal axes of straining remain fixed during the deformation. In the general case, the strain rate measure $\mathbf{D}$, however, is not integrable into a total strain measure, cf. the disussion by Malvern [57].

The strain increment $\Delta\mathbf{D}$ from increment n to $n + 1$ is defined by

$$\Delta\mathbf{D} = \int_{t_n}^{t_{n+1}} \mathbf{D}\left(r\right) dr \tag{5.48}$$

and may be constructed by integrating the strain rate approximately over the increment by using the central difference algorithm, as suggested by Hughes [36]. This algorithm defines the strain increment as

$$\Delta\epsilon = \Delta\mathbf{D} = sym\left(\frac{\partial\Delta\mathbf{u}}{\partial\mathbf{x}_{n+\frac{1}{2}}}\right) \tag{5.49}$$

where $\Delta\mathbf{u}$ is the displacement increment and $\mathbf{x}_{n+\frac{1}{2}}$ is the midpoint configuration. Accordingly,

$$\Delta\mathbf{u} = \mathbf{x}_{n+1} - \mathbf{x}_n \tag{5.50}$$

$$\mathbf{x}_{n+\frac{1}{2}} = \frac{1}{2}\left(\mathbf{x}_n + \mathbf{x}_{n+1}\right). \tag{5.51}$$

The total strain at configuration $n + 1$ is constructed using a method suggested by Hughes and Winget [37], giving

$$\epsilon_{n+1} = \Delta\mathbf{R}\epsilon_n\Delta\mathbf{R}^T + \Delta\mathbf{D} \tag{5.52}$$

where the first term accounts for rotational effects during the increment and the second term is the approximate strain increment. $\Delta\mathbf{R}$ is the rotation in the increment defined as

$$\Delta\mathbf{R} = \left(\mathbf{I} - \frac{1}{2}\Delta\mathbf{W}\right)^{-1}\left(\mathbf{I} + \frac{1}{2}\Delta\mathbf{W}\right) \tag{5.53}$$

where $\mathbf{I}$ is the identity tensor and $\Delta\mathbf{W}$ is the central difference integration of the spin:

$$\Delta\mathbf{W} = asym\left(\frac{\partial\Delta\mathbf{u}}{\partial\mathbf{x}_{n+\frac{1}{2}}}\right). \tag{5.54}$$

The total stress at configuration $n+1$ is calculated as

$$\boldsymbol{\tau}_{n+1} = \Delta\mathbf{R}\boldsymbol{\tau}_n\Delta\mathbf{R}^T + \Delta\hat{\boldsymbol{\tau}}, \tag{5.55}$$

where the first term accounts for rotational effects and the second term represents the material response during the increment. The second term is determined from the constitutive equations, Eq. (5.45), as

$$\Delta\hat{\boldsymbol{\tau}} = \mathbf{C}\Delta\mathbf{D}. \tag{5.56}$$

The formulae for calculating the total strains and stresses, see Eqs. (5.52) and (5.55), satisfy the criterion of incremental objectivity, which is a discrete analogue of the objectivity of the governing constitutive theory and precludes the generation of spurious stresses in rigid motions. An alternative to the use of the approximate rotation increment $\Delta\mathbf{R}$ as defined in Eq. (5.53) would be to apply the rotation increment obtained from the polar decomposition theorem. This would lead to more complex operations, however [37].

To form the Jacobian matrix used in the Newton Raphson method, the variation in stress with respect to the nodal variables is needed. This is obtained by differentiating Eq. (5.55), giving

$$\begin{aligned}\frac{\partial\boldsymbol{\tau}_{n+1}}{\partial\mathbf{a}} &= \frac{\partial\Delta\mathbf{R}}{\partial\mathbf{a}}\boldsymbol{\tau}_n\Delta\mathbf{R}^T + \Delta\mathbf{R}\boldsymbol{\tau}_n\frac{\partial\Delta\mathbf{R}^T}{\partial\mathbf{a}} + \mathbf{C}\frac{\partial\Delta\mathbf{D}}{\partial\mathbf{a}} \\[2mm] &= \frac{\partial\Delta\mathbf{R}}{\partial\mathbf{a}}\Delta\mathbf{R}^T\left(\boldsymbol{\tau}_{n+1} - \mathbf{C}\Delta\mathbf{D}\right) \\[2mm] &\quad + \left(\boldsymbol{\tau}_{n+1} - \mathbf{C}\Delta\mathbf{D}\right)\Delta\mathbf{R}\frac{\partial\Delta\mathbf{R}^T}{\partial\mathbf{a}} + \mathbf{C}\frac{\partial\Delta\mathbf{D}}{\partial\mathbf{a}}.\end{aligned} \tag{5.57}$$

Use of this expression leads to the exact Jacobian for the Hughes-Winget integration operator [37]. In ABAQUS, however, a simpler expression for this variation is used, yielding an approximate expression for the Jacobian matrix.

For inelastic material models, such as plasticity models, it is assumed that there is an additive relationship between the elastic and the inelastic (plastic) strain rates, i.e. that

$$\dot{\boldsymbol{\epsilon}} = \dot{\boldsymbol{\epsilon}}^{el} + \dot{\boldsymbol{\epsilon}}^{pl} \tag{5.58}$$

where $\dot{\boldsymbol{\epsilon}}$ is the total strain rate, $\dot{\boldsymbol{\epsilon}}^{el}$ is the elastic strain rate and $\dot{\boldsymbol{\epsilon}}^{pl}$ is the plastic strain rate. This strain rate decomposition is consistent when the elastic strains are infinitesimal and when the strain rate measure used is the rate of deformation [24]. In incremental form this yields

$$\Delta\boldsymbol{\epsilon} = \Delta\boldsymbol{\epsilon}^{el} + \Delta\boldsymbol{\epsilon}^{pl} \tag{5.59}$$

where $\Delta\boldsymbol{\epsilon}$ is defined by Eq. (5.49). The integration of the material equations is based on the backward Euler method to meet the consistency condition. For further information on the integration of plasticity models, see for example Krenk [52].

5.5   Crack Element Formulation

The fracture mechanics model presented in Subsection 4.2.3 was implemented in the finite element simulations by introducing special crack elements between the standard solid elements, see Figure 5.2. These crack elements connect adjacent nodes at the boundaries of the solid elements. The width of the crack elements is initially zero, which means that the nodes of neighbouring solid elements initially coincide. The crack elements were formulated as 4-noded elements.
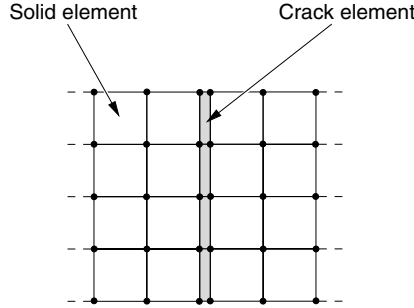

Figure 5.2: Finite element implementation of the crack elements.

The crack elements, which represent fictitious crack surfaces, behave according to the constitutive relations given in Subsection 4.2.3, except for a slight modification concerning the initial stiffness of the elements. Theoretically, the initial stiffness should be infinitely high since the elements are not supposed to "open" until the tensile or shear strength is reached. However, for numerical reasons, this stiffness should not be too high compared with the other terms in the global stiffness matrix. The initial stiffness was set at 1000 times higher than the slope of the first softening branch, see Figure 5.3. When the tensile or shear strength of the material is reached, these crack elements express the softening behavior of the material.

The crack element was implemented as a subroutine to the standard version of ABAQUS, [24], using the "UEL" option. The uniaxial characteristics, i.e. the properties for the pure opening and pure shearing mode, respectively, the values of the mixed mode coupling parameters m, n and the value of the coefficient of friction μ are given as input data for the elements.

The subroutine is called each time element calculations are required. Estimates of displacements and displacement increments at the end of each increment are supplied as inputs to the subroutine. The requested output from the routine is the contributions of the user element to the out-of-balance (or residual) force vector $\mathbf{G}$ and the Jacobian matrix $\hat{\mathbf{K}}$ of the overall system of equations. Since no body forces are associated with the elements, the out-of-balance force vector is given by the vector of internal forces $\mathbf{P}^{int}$ as

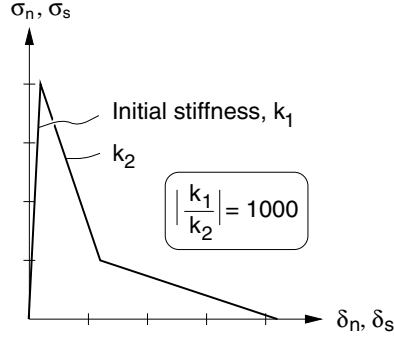$$\mathbf{G}_{n+1} = -\mathbf{P}^{int}_{n+1} \tag{5.60}$$

Figure 5.3: Modified softening stress-relative displacement curve used for the crack elements.

and the Jacobian matrix is determined from the tangent stiffness matrix $\mathbf{K}$ as

$$\hat{\mathbf{K}} = \mathbf{K} \tag{5.61}$$

according to Eq. (5.27) and Eq. (5.37), respectively.

The crack elements are used for finite deformation applications, which may result in non-negligible rotations of the crack elements compared to their orientation in the initial configuration. In order to take this into account, a local rotating coordinate system was introduced. In the following, a barred variable indicates that the variable is referred to this local coordinate system. The current orientation of the local coordinate system is determined from the current orientation of the crack element boundaries (see Figure 5.4) as

$$\bar{\varphi} = \frac{\varphi_a + \varphi_b}{2} \tag{5.62}$$

where $\bar{\varphi}$, φ_a and φ_b are defined in the figure.

With the orientation $\bar{\varphi}$ determined, a transformation matrix $\mathbf{B}$ can be constructed. This matrix is orthogonal, i.e.

$$\mathbf{B}^T \mathbf{B} = \mathbf{I}. \tag{5.63}$$

The nodal displacements $\mathbf{a}$ can now be referred to the local coordinate system through

$$\bar{\mathbf{a}} = \mathbf{B}\mathbf{a}. \tag{5.64}$$

The vector of internal forces (referred to the local system) is determined on the basis of the constitutive relations, i.e. the stress-relative displacement curves. This force vector is then transformed back to the global coordinate system by

$$\mathbf{P}^{int} = \mathbf{B}^T \bar{\mathbf{P}}^{int}. \tag{5.65}$$

The tangent stiffness matrix in the global coordinate system is defined as

$$\mathbf{K} = \frac{\partial \mathbf{P}^{int}}{\partial \mathbf{a}}. \tag{5.66}$$
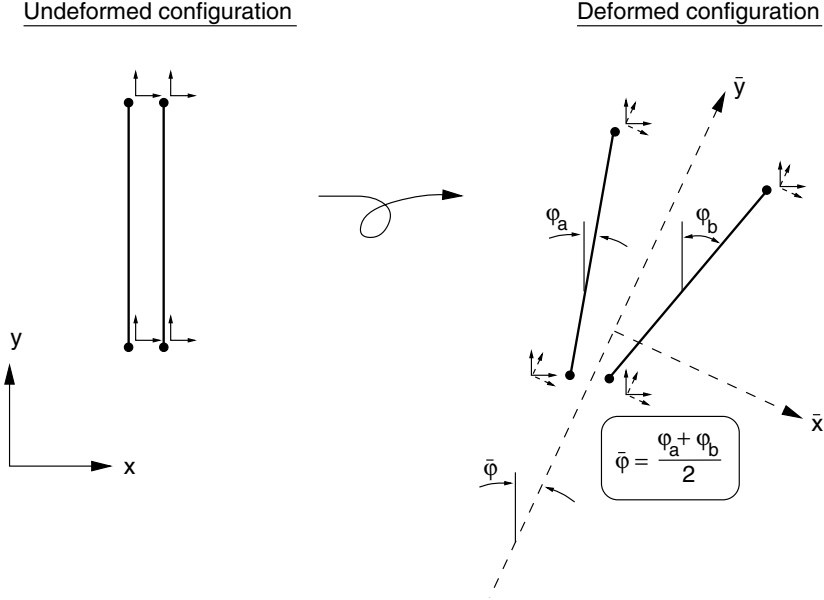
Figure 5.4: Local rotating coordinate system for a crack element.

By use of Eqs. (5.64) and (5.65) and the chain rule of differentiation, Eq. (5.66) can be rewritten as

$$\mathbf{K} = \frac{\partial \left(\mathbf{B}^T \bar{\mathbf{P}}^{int} \right)}{\partial \mathbf{a}} = \frac{\partial \mathbf{B}^T}{\partial \mathbf{a}} \bar{\mathbf{P}}^{int} + \mathbf{B}^T \frac{\partial \bar{\mathbf{P}}^{int}}{\partial \mathbf{a}}$$
$$= \frac{\partial \mathbf{B}^T}{\partial \mathbf{a}} \bar{\mathbf{P}}^{int} + \mathbf{B}^T \frac{\partial \bar{\mathbf{P}}^{int}}{\partial \bar{\mathbf{a}}} \mathbf{B}.$$

(5.67)

An approximation of the tangent stiffness matrix can be obtained by neglecting the term containing the derivative of the transformation matrix $\mathbf{B}$ with respect to the nodal displacements. This results in the simpler expression

$$\mathbf{K} \approx \mathbf{B}^T \frac{\partial \bar{\mathbf{P}}^{int}}{\partial \bar{\mathbf{a}}} \mathbf{B} = \mathbf{B}^T \bar{\mathbf{K}} \mathbf{B}.$$

(5.68)

The tangent stiffness matrix in the local system $\bar{\mathbf{K}} = \partial \bar{\mathbf{P}}^{int}/\partial \bar{\mathbf{a}}$ is determined from the slope of the stress-relative displacement curves. This matrix is then transformed to the global system by Eq. (5.68).

Chapter 6

Numerical Examples - Continuum Modelling

6.1   Introduction

This chapter deals with numerical simulation of wood disintegration based on the continuum material modelling approach presented in Section 4.2. The basis for the simulations is the chip shearing tests presented in Section 3.4. Numerical simulations of several of the test series, including both dry and wet conditions, are presented and compared with the experimental results. The adopted material parameters are discussed and the finite element modelling technique described. The influence of the choice of material data on the results was also studied, results obtained when using properties different from those of the reference values being presented and compared. Simulations of the combined radial compression and shear tests, Section 3.2, were also performed. This was done in order to check the appropriateness of the material modelling approach and the adopted material properties.

There are several industrial applications aiming at disintegrating wooden materials using knife-cutting processes. Examples are wood chipping, veneer cutting and lumber slicing. Knife-loading processes might therefore be of special interest to study, and results obtained from simulations can illustrate the influence of the knife design on the fracturing process and the cutting forces can be determined.

Since the wooden material in the mechanical pulping processes (and in many wood machining processes) is subjected to very high loading rates, the influence of the loading rate on the failure process and on the energy consumption is of great interest. The influence of the loading rate on the deformation and fracturing processes was therefore studied. Results from simulations made with various loading rates, up to 50 m/s, are presented. The conditions assumed in these simulations are, with the exception of the loading rate, similar to those used in the chip shearing tests.

The commercial FE code ABAQUS [24] was used for all simulations. The finite element formulation and the solution technique used by the program were outlined in Chapter 5.

6.2   Mechanical Properties

The material data presented in this section are the reference values that were used generally in the simulations throughout this chapter. In a few cases, however, slightly modified material data were adopted. This was done in order to overcome numerical problems in some of the simulations of the chip shearing tests, see Section 6.4.3. Furthermore, in order to study the influence of the choice of material properties on the response, simulations were performed using material data differing from the reference values presented below. This parameter study is discussed further in Subsection 6.4.4. The rate-dependent effects assumed in the study of the influence of the loading rate on the failure process are treated in Section 6.6.

For the numerical simulations, elastic, plastic and fracture mechanical properties are needed. Furthermore, these properties must be defined for earlywood and latewood separately, since the differences in mechanical behavior between these two types of wood have to be taken into account. In addition to the distinction between earlywood and latewood, a variation in properties is also assumed to be present in the radial direction within the earlywood zone. This zone is divided into five equally thick layers which differ slightly in their stiffness and strength properties. These layers are referred to as earlywood 1-5, earlywood 1 being the weakest layer representing the material formed in early spring, and earlywood 5 being the strongest layer, representing the transition zone, see Figure 6.1. The specimens used for the chip shearing tests had a growth ring width of about 1.8-2.1 mm. In the simulations, the growth ring width was set to 2.0 mm, the width of the earlywood region to 1.4 mm (each earlywood layer having a thickness of 0.28 mm), and the width of the latewood was set to 0.6 mm (the transition region being included in the latewood zone). The growth rings of the specimens used in the combined radial compression and shear tests were generally slightly smaller than those of the chip shearing specimens. In the simulations of the combined compression and shear tests, the width of the earlywood region was set to 1.5 mm (each layer having a thickness of 0.25 mm) and the width of the upper and lower latewood regions was set to 0.375 mm.
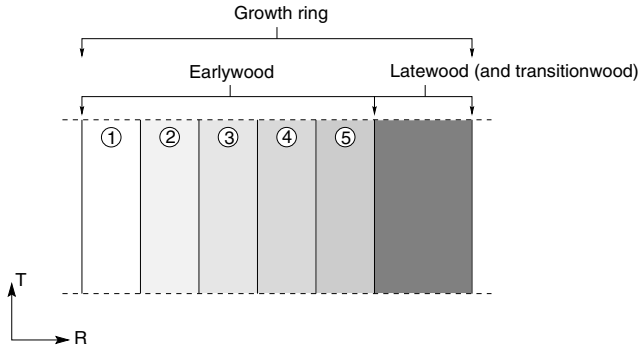

Figure 6.1: Subdivision of the growth ring zone into layers. T and R denote the tangential and radial directions, respectively.

In the experimental studies, Section 3.4 and 3.2, tests were performed on wood under both dry and wet conditions (moisture contents of 12% and 28%, respectively). Numerical simulations were performed for wood in both conditions. The reference values of the elastic and the plastic material parameters adopted for the dry and the wet condition are summarized in Table 6.1. Since both the earlywood layers and the latewood zone are modelled as being isotropic, the elastic behavior is defined by the modulus of elasticity E and Poisson's ratio ν. The plastic parameters that need to be specified are the strength in hydrostatic tension p_t, the initial yield stress in uniaxial compression σ_0, the initial yield stress in hydrostatic compression $p_{c/0}$ and the hardening parameters, defined by expressing the yield stress in hydrostatic compression p_c as a function of the volumetric plastic strain ϵ_{vol}^{pl}. The parameters p_t, σ_0, $p_{c/0}$, p_c and ϵ_{vol}^{pl} are defined in Subsection 4.2.2.

Table 6.1: Adopted elastic and plastic properties of wood in dry and wet condition corresponding to moisture contents of 12 % and 28 %, respectively. E.w. denotes earlywood and L.w. denotes latewood.

Wood layer	Elastic parameters		Plastic parameters					
						Hardening parameters $p_c\left(\epsilon_{vol}^{pl}\right)$ [MPa(-)]		
	E [MPa]	ν [-]	p_t [MPa]	σ_0 [MPa]	$p_{c/0}$ [MPa]			
Dry.								
E.w. 1	200	0.20	1.80	3.60	1.80	2.20(1.05)	10.20(1.50)	90.20(2.00)
E.w. 2	225	0.20	2.00	4.00	2.00	2.60(1.00)	11.60(1.40)	95.60(1.90)
E.w. 3	250	0.20	2.40	4.80	2.40	3.20(0.95)	13.20(1.30)	101.20(1.80)
E.w. 4	275	0.20	3.00	6.00	3.00	4.00(0.90)	15.00(1.20)	107.00(1.70)
E.w. 5	300	0.20	3.80	7.60	3.80	5.00(0.85)	17.00(1.10)	113.00(1.60)
L.w.	1000	0.20	-	-	-	-	-	-
Wet.								
E.w. 1	80	0.20	1.08	2.16	1.08	1.32(1.05)	6.12(1.50)	54.12(2.00)
E.w. 2	90	0.20	1.20	2.40	1.20	1.56(1.00)	6.96(1.40)	57.36(1.90)
E.w. 3	100	0.20	1.44	2.88	1.44	1.92(0.95)	7.92(1.30)	60.72(1.80)
E.w. 4	110	0.20	1.80	3.60	1.80	2.40(0.90)	9.00(1.20)	64.20(1.70)
E.w. 5	120	0.20	2.28	4.56	2.28	3.00(0.85)	10.20(1.10)	67.80(1.60)
L.w.	400	0.20	-	-	-	-	-	-

In dry condition, the modulus of elasticity was assumed to range from 200 up to 300 MPa within the earlywood, whereas a considerably higher value, 1000 MPa, was assumed for the latewood. In wet condition, the elastic stiffnesses were set to 40 % of those of the dry condition, i. e 80-120 MPa within the earlywood and 400 MPa for the latewood.

The values of the plastic parameters were chosen in view of results from radial compression tests. How reasonable the selected material parameters are will be investigated in the next section, where the combined compression and shear tests of Section 3.2 are simulated.

The hardening was modelled by piecewise linear curves. For the wet condition, the stress values were set to 60 % of those assumed for the dry condition. The plateau stress σ_0 ranges for the dry condition from 3.60 MPa for the weakest layer (earlywood 1) up to 7.6 MPa for the strongest (earlywood 5). The corresponding values for the wet condition are 2.16 MPa and 4.56 MPa, respectively. The response in the form of stress-strain curves for the five earlywood layers loaded in uniaxial compression is shown in Figure 6.2 for both the dry and the wet condition. In the diagrams, the strain is defined as being nominal strain, i.e. as change in length per initial length, the numbers 1-5 referring to the five different layers. The average stress response for the complete earlywood zone when compressed in the radial direction is shown in Figures 6.3.
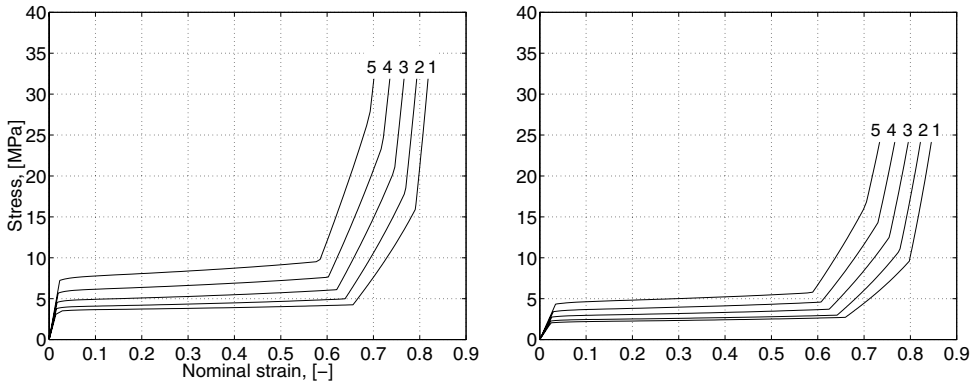

Figure 6.2: Stress-strain curves for the five earlywood layers when loaded in uniaxial compression. Left: wood in dry condition (12 % m.c.). Right: wood in wet condition (28 % m.c.).

When the tensile and/or shearing strength of the material is reached, the fracturing or softening behavior of the material is captured by the crack elements. The values selected for the plastic parameters assign the solid elements higher yield stresses in tension and in shearing than the strength values used for the crack elements. This prevents inelastic response in tension and in shearing prior to cracking.

The fracture occurring will normally be a mixed mode fracture, involving both the opening and the forward shear mode (rolling shear). The fracture mechanical properties for the pure opening and pure shearing modes, the values of the mixed mode parameters m, n and the coefficient of friction μ affecting the fracturing behavior in combined compression and shear are given as input to the crack elements. The properties used in the simulations are given in Table 6.2. A small variation of the properties was assumed to be present within the earlywood zone. The shape of the curves adopted for uniaxial tension has an initial rapid decrease in stress followed by
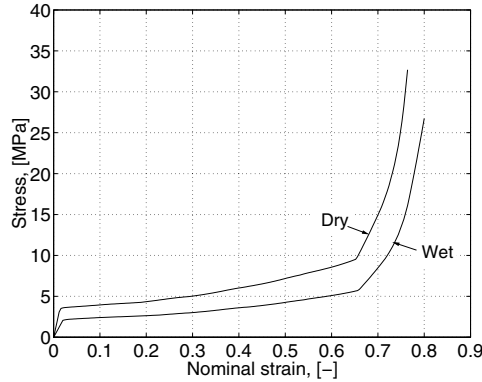
Figure 6.3: Average response of the earlywood zone when loaded uniaxially in compression in the radial direction.

a region of considerably slower decrease. The input for these curves is based on the results from the tensile tests reported in Section 3.3 and from other investigations of tangential tensile fracture of spruce, as reported by Boström [8], Wernersson [87] and Olejniczak [63]. In Table 6.2 f_t and f_s denote the tensile and shear strength, respectively, σ_{n1}, δ_{n1} and σ_{s1}, δ_{s1} define the breakpoints on the bi-linear curves, δ_{n0}, δ_{s0} are the displacement values for which the crack is fully developed and G_F denotes the fracture energy.

The strength in rolling shear was set equal to the tensile strength, whereas the fracture energy was assumed to be somewhat higher. The tensile strength, shear strength and fracture energy for the latewood were assumed to be twice as high as the values used for the strongest earlywood layer. The strength values and the fracture energies for the case of the wet condition were set equal to 70 % of the corresponding values assumed for the dry condition.

The values adopted for the dry condition result in an average tensile strength in the tangential direction of approximately 4.4 MPa and a fracture energy of 440 Nm/m^2. These values are in accordance with experimental results from investigations involving stable tensile tests on spruce performed at low loading rates and at low moisture contents. Boström [8] reports a tangential tensile strength of 4.0 MPa and a fracture energy of 460 Nm/m^2 at a moisture content of 13 % and with an average density of 470 kg/m^3. Wernersson [87] reports a strength of 4.8 MPa and a fracture energy of 475 N/m^2 at a moisture content of 11 % and with a density of 570 kg/m^3. Olejniczak [63] studied the influence of the specimen geometry and the effect of the loading rate, for loading rates varying between 0.00001-0.1 mm/s, on the fracture mechanical properties on spruce in tangential tensile fracture and has reported strength values in the range of 2.88-4.16 MPa and fracture energies between 203-385 Nm/m^2. The mean density of the material was 492 kg/m^3 and the moisture content was 14 %. For the wet condition the adopted values result in an average tangential tensile strength of about 3.1 MPa and a fracture energy of 310 Nm/m^2. These values are in close agreement with the results from the stable tensile tests as presented in Section 3.3 for the case of a loading

Table 6.2: Adopted fracture mechanical properties of wood in dry and wet condition corresponding to moisture contents of 12 % and 28 %, respectively. E.w. denotes earlywood and L.w. denotes latewood.

Wood layer	Opening mode					Shearing mode (rolling shear)				
	f_t [MPa]	σ_{n1} [MPa]	δ_{n1} [mm]	δ_{n0} [mm]	G_F [J/m^2]	f_s [MPa]	σ_{s1} [MPa]	δ_{s1} [mm]	δ_{s0} [mm]	G_F [J/m^2]
Dry										
E.w. 1	2.40	0.30	0.125	0.60	240	2.40	1.20	0.125	0.25	300
E.w. 2	2.80	0.35	0.125	0.60	280	2.80	1.40	0.125	0.25	350
E.w. 3	3.20	0.40	0.125	0.60	320	3.20	1.60	0.125	0.25	400
E.w. 4	3.60	0.45	0.125	0.60	360	3.60	1.80	0.125	0.25	450
E.w. 5	4.00	0.50	0.125	0.60	400	4.00	2.00	0.125	0.25	500
L.w.	8.00	1.00	0.125	0.60	800	8.00	4.00	0.125	0.25	1000
Wet.										
E.w. 1	1.68	0.21	0.125	0.60	168	1.68	0.84	0.125	0.25	210
E.w. 2	1.96	0.245	0.125	0.60	196	1.96	0.98	0.125	0.25	245
E.w. 3	2.24	0.28	0.125	0.60	224	2.24	1.12	0.125	0.25	280
E.w. 4	2.52	0.315	0.125	0.60	252	2.52	1.26	0.125	0.25	315
E.w. 5	2.80	0.35	0.125	0.60	280	2.80	1.40	0.125	0.25	350
L.w.	5.60	0.70	0.125	0.60	560	5.60	2.80	0.125	0.25	700

rate of 0.1 mm/s, which should be representative considering the loading rate at which the chip shearing tests were carried out. The shape of the curves adopted is also in agreement with the experimental results. The values of the coupling parameters for mixed mode fracture were chosen to m=n=5 which, for the case of different radial loading paths, results in an approximately linear relation between the fracture energy in rolling shear and tension. The coefficient of friction at the fracture zones was set to 0.5.

When the mechanical properties of wood are determined, it is generally considered as a homogeneous material and the differences between earlywood and latewood are not considered. Not much experimental work has been carried out to determine the mechanical properties of these two types of wood separately or, more generally, to determine the variation of properties within the growth ring. Such experiments must be given a high priority in the future. Due to the lack of experimental data, it is difficult to verify the adopted material data in any other way than in an average sense.

6.3 Simulations of Combined Radial Compression and Shear Tests

6.3.1 General remarks

As has been shown, the mechanical behavior of wood loaded perpendicular to the grain is very complex with large deformations, localization phenomena and highly nonlinear response occurring. In order for numerical simulations of wood disintegration to be successful, these material characteristics need to be captured appropriately. In Section 3.2 a study concerning the behavior in combined radial compression and shear was presented. By simulating these tests, the adequacy of the material modelling approach can be evaluated for these important loading modes. In particular, the performance of the foam plasticity model and the suitability of the material data related to it are tested. In the following, simulations of the different test series involved in the experimental study are presented and compared with the experimental results.

6.3.2 Finite element modelling

Due to the very low loading rates involved in the tests, static conditions were assumed in the simulations. The problem was treated as a two-dimensional one. First-order solid elements were employed, 3-noded linear triangular elements for the earlywood and 4-noded bilinear quadrilaterals for the latewood. The triangular elements were used as they are not so sensitive to large distortions. The model consisted of about 2800 elements and involved 3200 degrees of freedom. The lower boundary of the specimen was restrained from moving, whereas the displacements of the nodes at the upper boundary were prescribed according to the loading mode in the particular test being considered. The finite element model used is shown in Figure 6.4, the subdivision of the earlywood zone into five layers being indicated, earlywood 1 being the weakest layer and 5 the strongest. The width of each earlywood layer was set to 0.25 mm and the width of the two latewood zones to 0.375 mm each. For the loading modes considered, fracture of the specimen may occur (as was the case in the experiments for the pure shear loading and probably also for the mixed loading at ξ=67.5°). Crack elements were introduced at the lower transition between the earlywood and the latewood, this region constituting the weakest part of the specimen. The fracturing properties were set equal to those of the earlywood layer as defined in Table 6.2.

6.3.3 Results

Due to extreme element distortion at the left boundary, the complete deformation process could not be simulated for the case of ξ=45°. It was possible to trace the response up to average strains of about 30 % only, for which locally very large distortions occurred. This problem may be avoided by using a more optimal mesh (with smaller elements in the critical region) or with a remeshing technique. For all the other cases, the complete deformation processes could be simulated. The simulated deformation
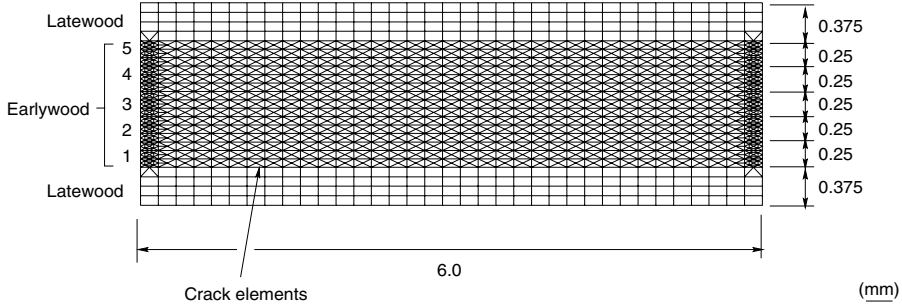
Figure 6.4: Finite element model used in simulations of compression and shear tests.

process for pure compression is shown in Figure 6.5. The top picture shows the undeformed specimen, the next three show the specimen at a strain of 10, 20 and 40 %, respectively. The pictures shown concern the dry condition, but the deformation process for the wet specimen was completely analogous. At a strain of 10 % the earlywood 1 layer is compressed considerably, the earlywood 2 layer has just entered its plateau region, whereas layers 3-5 are still behaving elastically, with negligible deformations. At a strain of 20 % the only earlywood layers behaving elastically are layers 4 and 5. Finally, when the strain is increased to 40 % all the layers are deformed considerably, the deformations in the latewood being insignificant, however. The strain localization arising when wood is loaded in compression perpendicular to the grain is thus captured to some extent by the modelling employed (compare Figure 6.5 with Figure 3.4). Also for the combined loading modes at $\xi=22.5°$ and $\xi=45°$ the predicted deformations are in reasonably good agreement with the experiments. The simulated deformation process for the case of $\xi=45°$ is shown in Figure 6.6. By comparing with Figure 3.6 it can be seen that there is a good agreement with the experiments, the failure zone being initiated at the lower transition zone except for the right edge of the specimen at which the failure starts a little higher. In the simulation, a tensile crack was developed at the right edge of the specimen, but it did not propagate much.

The behavior for pure shear loading is shown in Figure 6.7. Shear fracture occurred at the lower transition zone just as in the experiments, but the failure occurred at a lower shear deformation.
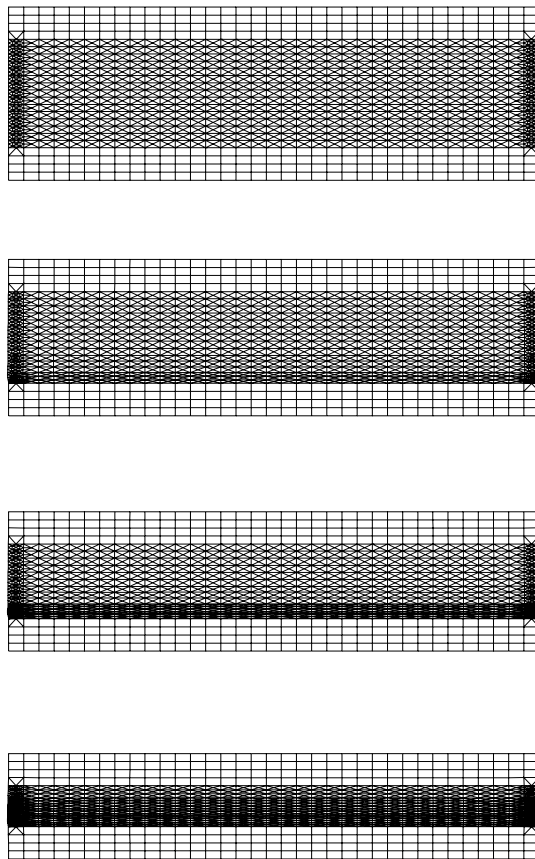
Figure 6.5: Simulation of the deformation process of a dry specimen loaded in pure radial compression (test series Ad). From top to bottom: undeformed, average strain of 10 %, 20 % and 40 %.
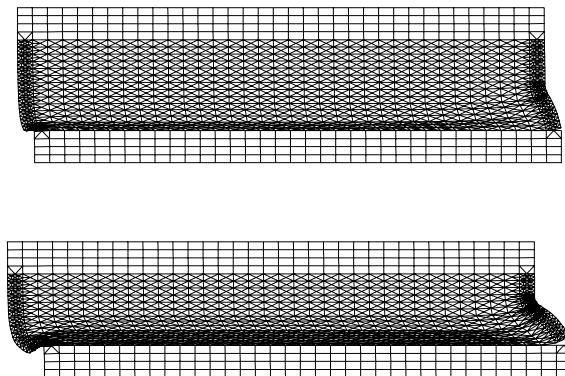
Figure 6.6: Simulation of the deformation process of a dry specimen loaded in combined compression and shear at ξ=45° (test series Cd). Top: average strain of 10 %. Lower: average strain of 20 %.
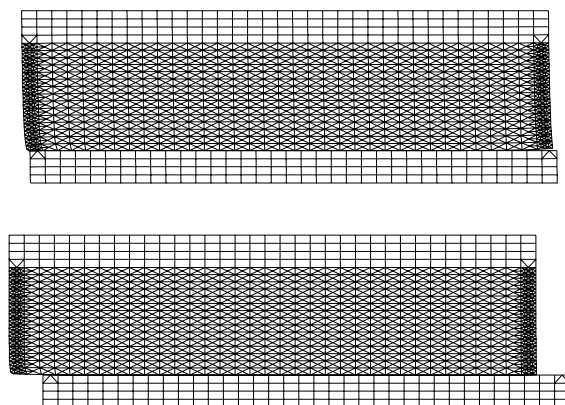

Figure 6.7: Simulation of the deformation process of a dry specimen loaded in pure shear (test series Ed). Top: average strain of 5 %. Lower: average strain of 20 %.

The stress-strain curves obtained from the simulations of the different test series are given in Figures 6.8 and 6.9. For comparison, see the corresponding experimental results given in Figures 3.10-3.11. The diagrams to the left show the normal stress and the diagrams to the right show shear stress. For pure compression and pure shear, only one diagram is given, the shear stress being close to zero in the first case whereas the normal stress is very low (less than 0.1 MPa) for pure shear. As can be seen, there is reasonably good agreement between the simulated response and the experiments for the case of pure radial compression and for combined compression and shear up to $\xi=45°$. The overall shape of the curves and the stress plateau values are in a relatively good agreement with the experimental results. The discrepancies found are more related to the choice of material data than to the overall performance of the foam model. With a more optimal choice of material data, the discrepancies present may be reduced significantly. The influence of the shear deformation on the compressive stress-strain curves obtained from the simulations being small, just as in the experiments. At $\xi=22.5°$ the compressive stress-strain response is practically identical to that of pure compression, which was also the case in the experimental study. At $\xi=45°$ the stresses at the plateau region are somewhat lower than for pure compression and $\xi=22.5°$, also in agreement with the experimental results. The initial stress peak found in many of the experiments for $\xi=22.5°$ and $\xi=45°$ is not captured, however. The shear stresses are overestimated in the simulations, although still being considerably lower than the vertical (compressive) stress. The relation between the response in the dry and the wet condition is similar to that found in the experiments.

For the case of $\xi=67.5°$, and for pure shear loading, there are clear discrepancies between the simulations and the experimental results, concerning both the compressive and the shear stress-strain relations, the shear stiffness being considerably too high in both cases. For pure shear loading, a rather high tensile stress was developed in the experiments, but this was not the case in the simulations, where instead a very small compressive stress was present. The shear strength value assumed for the earlywood 1 layer seems to be appropriate, however, since the maximum shear stress value predicted for the pure shear loading is in good agreement with the experimental results. A much better agreement concerning the response for the case of $\xi=67.5°$ and in pure shear is obtained by reducing the assumed elastic stiffness. This is shown in Figure 6.10. The diagram shows the shear stress-strain response for the case of pure shear loading when assuming the default elastic stiffness, together with the response obtained when assuming an elastic stiffness of only one fifth of the reference values. The reduction stiffness was made for all layers (both earlywood and latewood). The agreement between the simulation and the experiments concerning the normal stress is not improved, however. The tensile stress obtained in the experiments for pure shear is still not captured by the model. The reduction in elastic stiffness greatly improves the response concerning the shear forces but results in an unrealistic normal stiffness. This is the dilemma encountered when using an isotropic model.
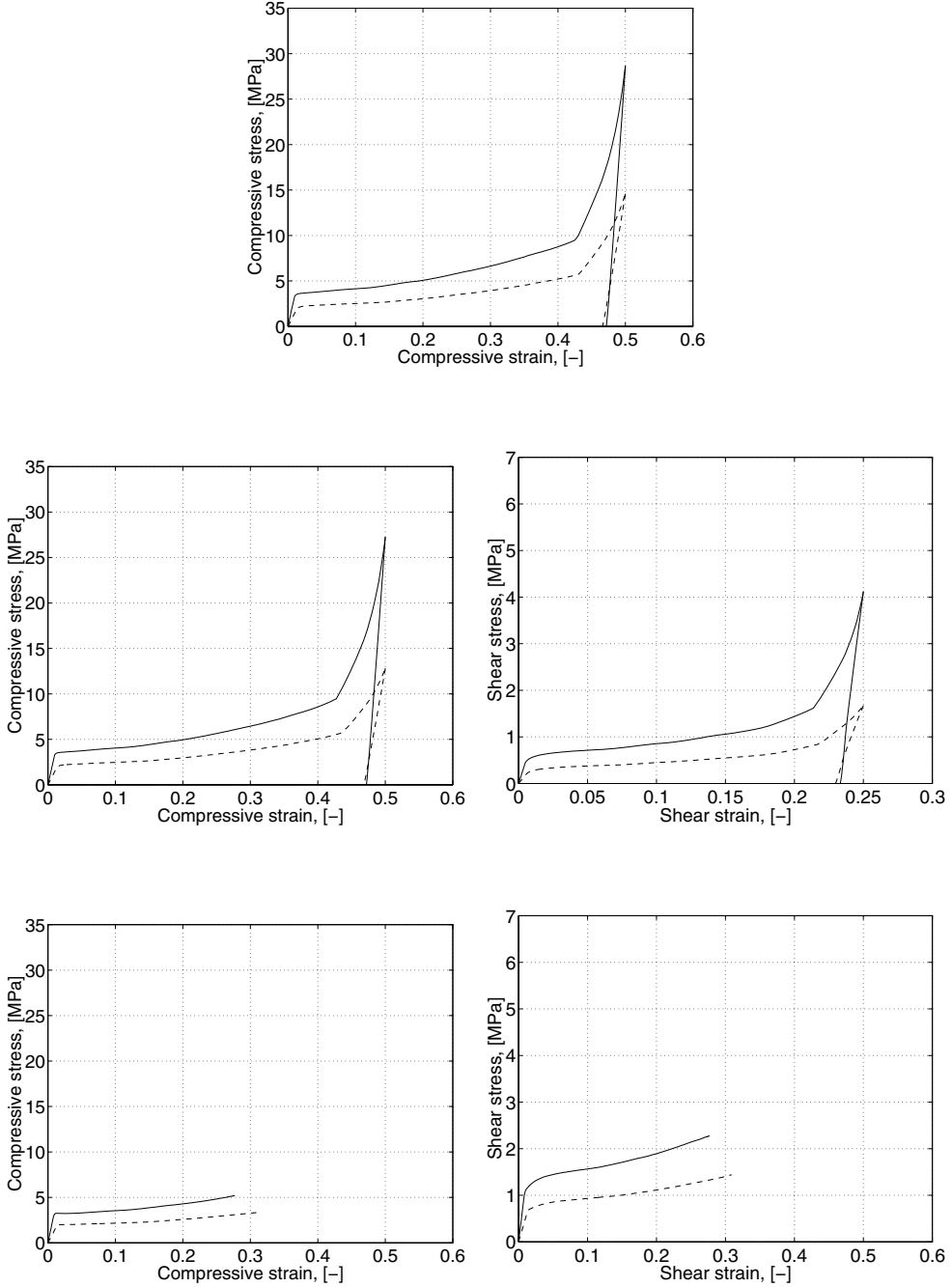
Figure 6.8: Simulated stress-strain curves for the combined compression and shear tests. Solid lines show results for specimens in dry condition and dashed curves for the wet condition. Top: test series Ad and Aw (pure compression). Middle: test series Bd and Bw (mixed loading at ξ=22.5°). Lower: test series Cd and Cw (mixed loading at ξ=45°).
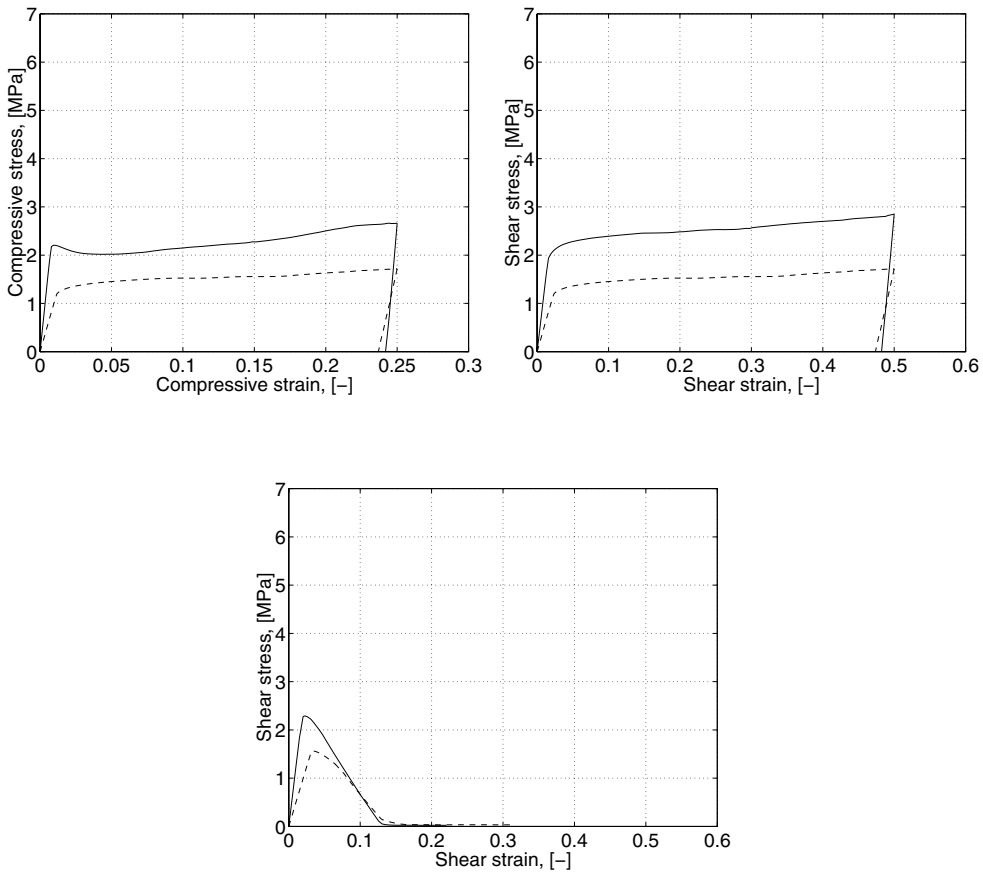
Figure 6.9: Simulated stress-strain curves for the combined compression and shear tests. Solid lines show results for specimens in dry condition and dashed curves for the wet condition. Top: test series Dd and Dw (mixed loading at ξ=67.5°). Lower: test series Ed and Ew (pure shear).

The influence of boundary effects due to the specimen design on the stress-strain curves obtained may be estimated by simulations. If cyclic boundary conditions are applied, connecting the left and the right boundary of the specimen, the response of an infinitely wide specimen is simulated. Cyclic boundary conditions in this case means that the displacements of the nodes at the left boundary are set equal to those of the corresponding nodes at the right boundary. The deformation of a specimen loaded at ξ=45° is shown in Figure 6.11. It can be seen by comparing Figure 6.11 with Figure 6.6 that the deformation pattern differs from that of the 6 mm wide specimen at the specimen edges. It can be concluded, however, that the effects of specimen width on the stress-strain curves obtained are very small. This can be seen in Figure 6.12, showing the normal stress-strain response for an infinitely wide specimen (solid curves) and the curve obtained for the 6 mm wide specimen. In both cases mixed loading
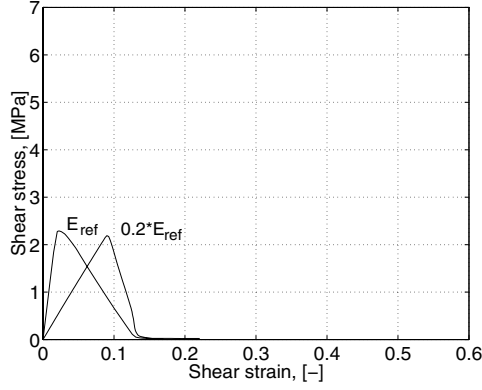
Figure 6.10: Influence of Young's modulus on the response in pure shear loading. Material data for wood in dry condition. E_{ref} refers to the reference values of the modulus of elasticity defined in Table 6.1.

at $\xi=45°$ and material data for wood in dry condition were assumed. The differences in stress-strain response between the infinitely wide specimen and the 6 mm wide specimen were found to be very small for all loading cases considered.
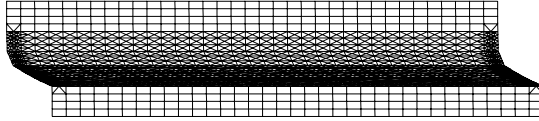

Figure 6.11: Deformation of an infinitely wide specimen loaded at $\xi=45°$. The specimen is shown at an average strain of 30 %.

To summarize, it can be concluded that the modelling employed predicts the behavior for pure compression as well as for combined compression and shear up to $\xi=45°$ reasonably well. The normal stress-strain relations obtained are similar to those obtained in the experiments; the differences are mainly related to the choice of material parameters and to the choice of an isotropic model. The shear stresses are overestimated although still being low in comparison with the normal stresses. The responses for $\xi=67.5°$ and for pure shear are not so well captured by the modelling employed, concerning both the normal and the shear stress-strain relations. The results indicate that the shear fracturing properties for the earlywood 1 layer seem to be appropriate, though.

It should be emphasized that the material data given in Section 6.2 and adopted for all simulations throughout this chapter were selected prior to the combined compression
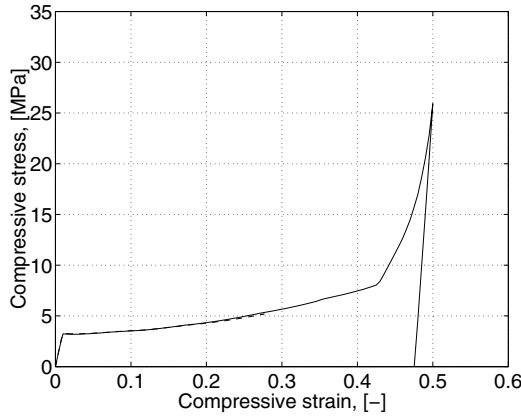
Figure 6.12: Normal stress-strain response for an infinitely wide specimen (solid curve) as compared to that of the 6 mm wide specimen (dashed curve).

and shear tests were carried out. They do therefore not represent the optimal choices for achieving the best possible agreement with the experiments presented in Section 3.2. A better fit may be obtained by choosing slightly different yield stress values as the densification in the simulations starts at a slightly too high strain and the stiffness is too high.

The fact that the very low modulus in rolling shear in relation to the normal stiffness is not captured by the modelling is more crucial, however. Due to the foam plasticity model being isotropic, the shear modulus is governed by the modulus of elasticity and Poisson's ratio. The shear stiffness is considerably overestimated with the present choice of material data. This is the reason for the overall poor agreement concerning the shear-dominated loading modes and the fact that the shear stresses generally are being overestimated for all loading modes.

A significant improvement concerning the prediction of the shear stress-strain relations was obtained by decreasing the moduli of elasticity drastically (down to one fifth of the reference values). Such low values of Young's modulus give rise to unrealistic normal stiffness, however. It should also be emphasized that the modulus of elasticity perpendicular to the grain may, due the extremely low modulus in rolling shear, be very low depending on the annual ring orientation. This was illustrated in Figure 2.4. The choice of the elastic stiffness using an isotropic model is thus not trivial. It is a balance between obtaining a low modulus in rolling shear and obtaining a suitable normal stiffness. The optimal choice of the stiffness values depends on the type of problem considered. For the problems dealt with in the following, the stiffness values adopted seem reasonable, however.

6.4 Simulations of Chip Shearing Tests

6.4.1 General remarks

Simulations of the behavior of the specimens in tests series Ad, Aw, Bd, Bw, Dd, Dw, Fd, Fw, Gd and Gw of the chip shearing tests were performed. Simulations were thus made for both the dry and the wet condition, for different specimen heights, orientations and the different loading conditions applied in the experimental study.

In general, the material data presented in Section 6.2 was used for all the cases studied. A few exceptions were made, however. Firstly, in the simulations of test series Ad, Aw, Bd and Bw slightly modified material data were used (as compared with those given in Table 6.1 for the earlywood 1-3 layers) for the elements near the right edge of the upper rigid surface. Somewhat lower values were used for the volumetric plastic strain ϵ_{vol}^{pl} when defining the hardening of these elements. This modification was made for numerical reasons, so as to prevent excessive distortion of these elements. Furthermore, in a few cases, slightly higher values of δ_{n1}, δ_{s1} and δ_{s0} compared to the values in Table 6.2 were used in defining the softening behavior of the material. This was done to decrease the negative stiffness of the crack elements, in order to obtain sufficient stability in the calculations to be able to pass certain critical stages in the solutions.

6.4.2 Finite element modelling

The problem was analysed as a two-dimensional static problem under plane strain conditions. First-order solid elements were employed, 4-noded bilinear quadrilateral elements for the latewood zones and 3-noded linear triangular elements for the earlywood. The tests indicated large deformations occuring in the earlywood. Triangular elements were thus used for the earlywood zones since these elements are not as sensitive to distortion. Crack elements were introduced between the solid elements at locations where large tensile and/or large shearing stresses occurred. When the strength of the material was reached, these elements captured the softening behavior of the material as described earlier.

The two steel plates in the tests were modelled as rigid surfaces. Interface elements were used to describe the contact forces between the rigid surfaces and the wood specimen. A Coulomb friction model was employed, the coefficient of friction between the steel plates and the specimen being set to 0.25. A perfect fit of the specimens between the steel plates was assumed. The gap between the steel plates was set to 0.1 mm, just as in the experiments. For numerical reasons, the sharp edges of the steel plates were smoothed.

A finite element model used in the simulations is shown in Figure 6.13.

6.4.3 Results

The results from the simulations are presented and discussed in the following. Firstly the simulations of the 8 mm high specimens of test series Ad and Aw are dealt with,
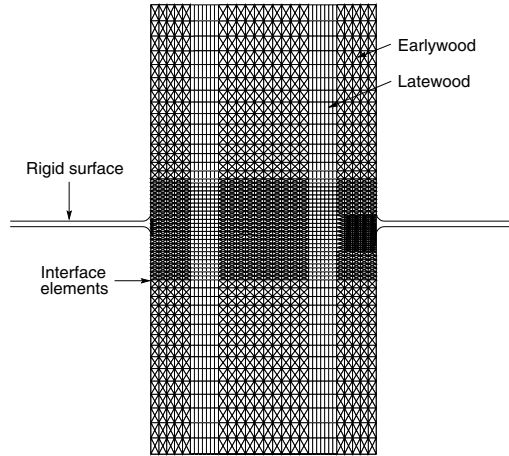
Figure 6.13: Example of finite element model used in the simulations.

thereafter the 5 mm high specimens of the B and D series and finally the simulations of the specimens subjected to the knife-loading setup (series Gd and Gw). A comparison of the results of the simulations with the experimental results is given in Section 6.4.5.

Test series Ad and Aw

The specimen geometry and the earlywood-latewood configuration used in the simulations are given in Figure 6.14, and can be considered to be representative for the specimens used in test series Ad and Aw. The earlywood zone was, as described earlier, divided into five equally thick layers, the location of these layers being indicated by the numbers 1-5 in the figure. The figure also shows the finite element mesh adopted for the simulations. The finite element model involved about 5500 solid elements and 3200 nodes.

The simulated deformation and fracturing processes for tests series Ad and Aw are given in Figure 6.15. In the figure, sequences of five pictures showing the course of deformation and fracturing in the specimens together with the corresponding load-displacement curves obtained are given. The upper part of the figure shows the response for the dry specimen and the lower part the corresponding response for the wet one. The pictures are linked to the load-displacement curves by the numbering 1-5. The solid lines in the load-displacement diagrams show the horizontal force and the dashed ones the vertical force.

The simulated behavior of the wet specimen was rather similar to that of the dry one. The differences mainly consisted of lower force values involved for the wet specimen, and fracturing occurring at somewhat larger shear displacements, and the maximum load (point of global softening of the specimen) being reached at a somewhat later stage for the wet than for the dry specimen. The response of the specimens could be predicted up to a shearing displacement of about 2.0 mm (1.9 mm for the dry and 2.1 mm for the wet specimen). The maximum horizontal force was reached at a shear-
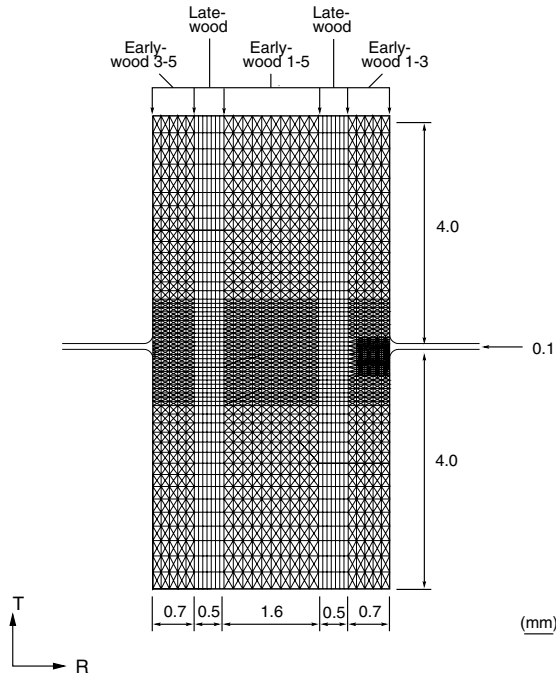
Figure 6.14: Specimen geometry and earlywood-latewood configuration used in the simulation of test series Ad and Aw.

ing displacement of approximately 1.7 mm for the dry specimen and about 2 mm for the wet one. Thereafter the load decreased rapidly until the end of the analysis.

The energy needed to break the specimen consists of elastic energy, plastic dissipation, frictional work and fracture energy. Since it was not possible to simulate the complete failure processes, the complete energy consumption could not be evaluated. At the points at which the maximum loads were reached (at a shearing displacement of about 1.7 mm for the dry and 2.0 mm for the wet specimen), approximately 250 mJ and 165 mJ was consumed for the dry and the wet specimen, respectively. The main part, about 80 %, was due to plastic dissipation, approximately 10 % being consumed in the fracturing processes and elastic energy and frictional work constituting the rest.
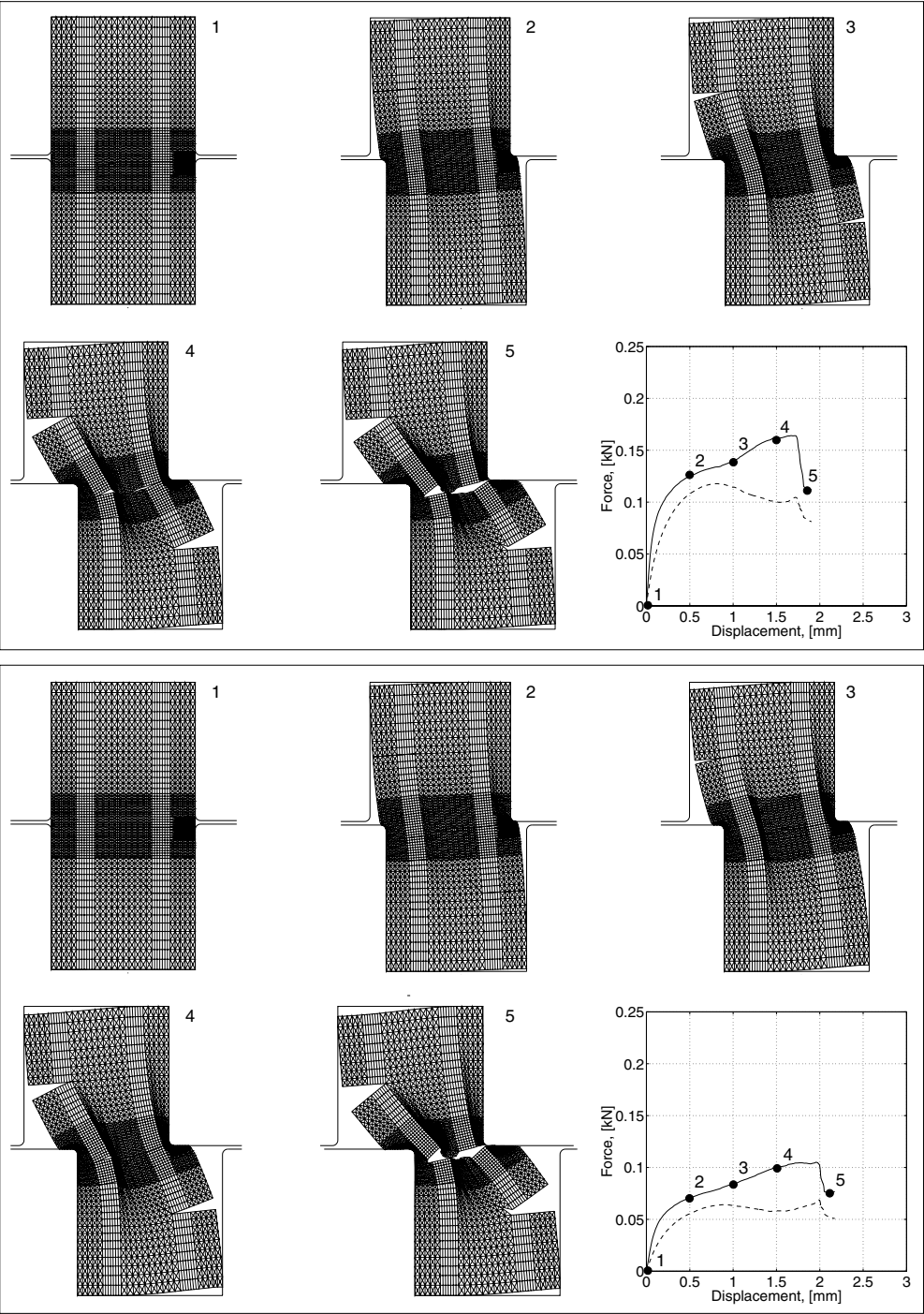
Figure 6.15: Simulated deformation and fracture processes of test series Ad (top) and Aw (lower). Solid lines show the horizontal forces and the dashed lines show vertical forces.

Test series Bd and Bw

The specimen geometry and the earlywood-latewood configuration used in the simulations are shown in Figure 6.16. The finite element model involved 3200 solid elements and 2400 nodes, the mesh density being similar to that of the model used in simulating the Ad and Aw test series. The simulated deformation and fracturing processes for the two test series are given in Figure 6.17. Just as for the case of the simulation of series Ad and Aw, it was not possible to capture the entire failure processes for these specimens due to numerical instability problems. However, for both cases the main course of deformation, including a major part of the global softening, was captured. The response was traced up to a shear displacement of 1.9 mm for the dry and 2.5 mm for the wet specimen. The maximum load was reached at a shear displacement of 1.85 mm and 2.0 mm for the dry and the wet specimen, respectively. Just as for the simulation of the 8 mm high specimens, the simulated behavior of the dry and the wet specimen was similar, the differences consisting of lower forces involved for the wet specimen and fracturing generally occurring at somewhat larger shear displacements.

Since the complete failure processes of the specimens could not be simulated, the total energy needed to break them could not be evaluated. At the end of the analyses, the major part (more than 80 %) of the energy supplied was consumed due to plastic dissipation, fracture energy constituting about one tenth, elastic energy and frictional work constituting the rest.
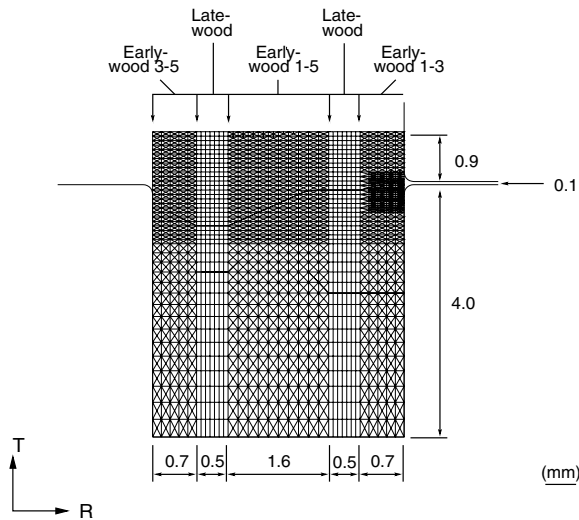

Figure 6.16: Specimen geometry and earlywood-latewood configuration used in the simulation of test series Bd and Bw.
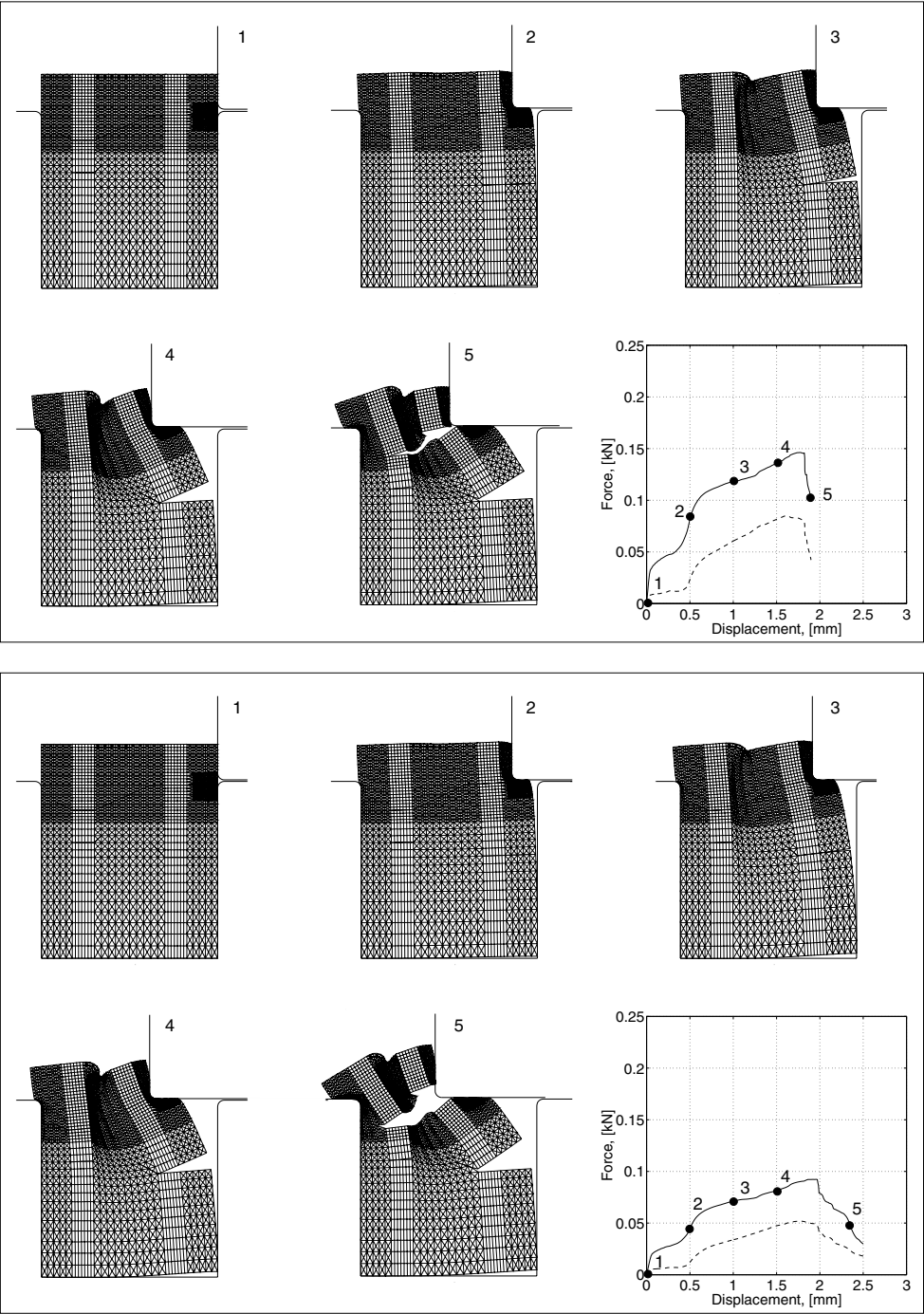
Figure 6.17: Simulated deformation and fracture processes of test series Bd (top) and Bw (lower). Solid lines show the horizontal forces and dashed lines show the vertical forces.

Test series Dd and Dw

Figure 6.16 shows the adopted specimen geometry, the earlywood-latewood configuration and the finite element model adopted in the simulations. In the model 4600 solid elements were used, the total number of nodes equal to 3100. The simulated deformation and fracturing processes for the two test series are given in Figure 6.19. For both the dry and the wet specimens it was possible to simulate the complete failure processes. The simulated behavior of the dry and the wet specimen was similar with almost pure shear fracture along the transition between the earlywood and the latewood, and with large compressive deformations in the earlywood near the upper rigid surface. The deformations of the material below the fracture zone were negligible. The differences between the wet and the dry specimen consisted of the calculated forces for the wet specimen being consistently lower (maximum horizontal force about 40 % lower), global softening occurring at a larger shear displacement (1.5 mm compared to 1.3 mm) and the fracturing involving slightly more of the opening mode for the wet than for the dry specimen.

The total energy consumption predicted for the dry (wet) specimen was equal to 75.4 (49.6) mJ. The energy due to plastic deformations constituted the main part of the total energy consumption, about 86 (85) %, fracture energy about 13 (13) %, elastic energy and energy due to frictional work constituting approximately 1 (2) % of the total energy consumption.
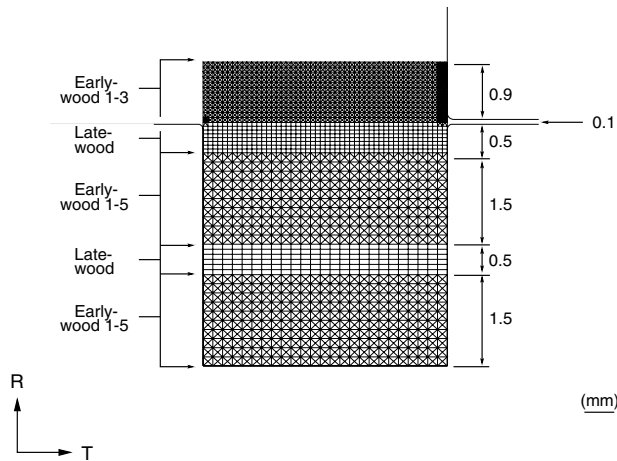

Figure 6.18: Specimen geometry and earlywood-latewood configuration used in the simulation of test series Dd and Dw.
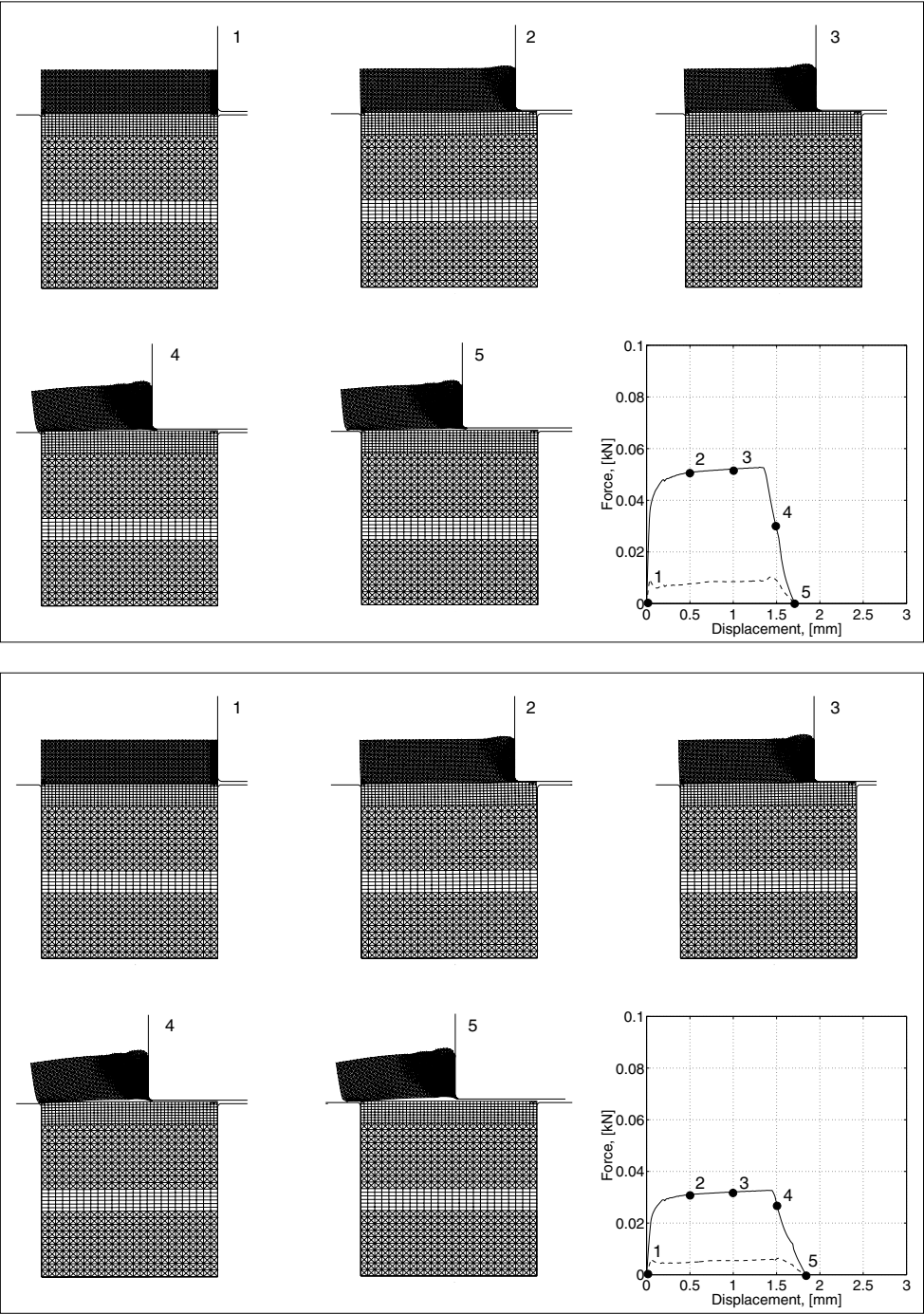
Figure 6.19: Simulated deformation and fracture processes of test series Dd (top) and Dw (lower). Solid lines show the horizontal forces and dashed lines show the vertical forces.

Test series Gd and Gw

The specimen geometry and earlywood-latewood configuration assumed were similar to that adopted in the simulation of series Dd and Dw. A similar finite element model was also used, with the exception of the upper steel plate now being shaped as a knife and that the mesh was refined at the fracture zone. The knife was modelled using two rigid surfaces with their edges crossing in order to prevent elements from slipping over the edge of the knife. The knife angle was, just as in the experiments, set to 30° and the clearance angle to 2°. The finite element model is shown in Figure 6.20.
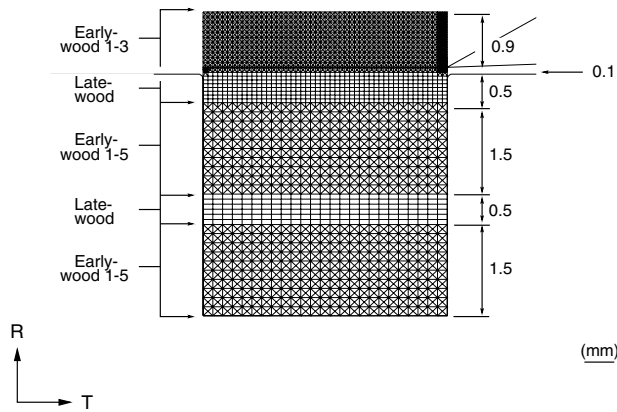

Figure 6.20: Specimen geometry and earlywood-latewood configuration used in the simulation of test series Gd and Gw.

For both the dry and the wet specimens it was possible to simulate the complete failure processes, Figure 6.21. The simulated failure process for the wet specimen was similar to that of the dry one, the differences mainly consisting of lower forces for the wet than for the dry (about 40 % lower). In both cases the cut-off part was broken into two pieces, the force-displacement curves thereby having two clear peaks (at about 0.5 mm and 2.0 mm, respectively).

The small oscillations in forces are related to the contact conditions near the edge of the knife, especially to the lower side of the knife, and are due to the contact between rigid surfaces (representing the knife) and the solid elements (representing the contacting wood) being checked at the nodes only and not along the entire contact boundary. The oscillations are thus strongly influenced by the fineness of the mesh at the edge of the knife (i.e. at the fracture zone). A coarse mesh results in large oscillations whereas a fine mesh gives rise to smaller variations. This is shown in Figure 6.22 in which the response obtained by using the reference mesh is compared to that obtained using a coarser mesh with the element size at the fracture zone doubled as compared to the reference mesh.
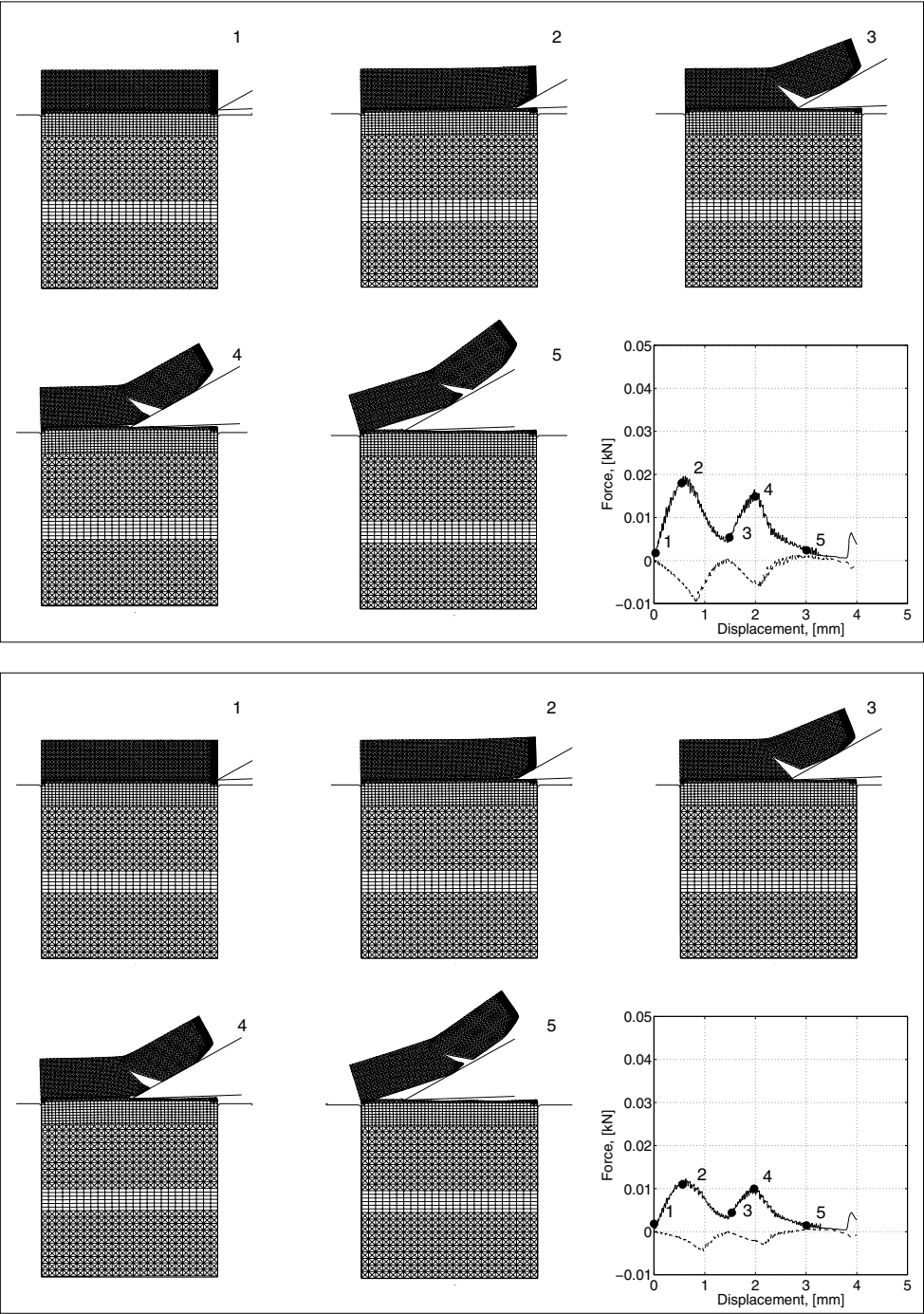
Figure 6.21: Simulated deformation and fracture processes of test series Gd (top) and Gw (lower). Solid lines show the horizontal force and dashed lines show the vertical forces.
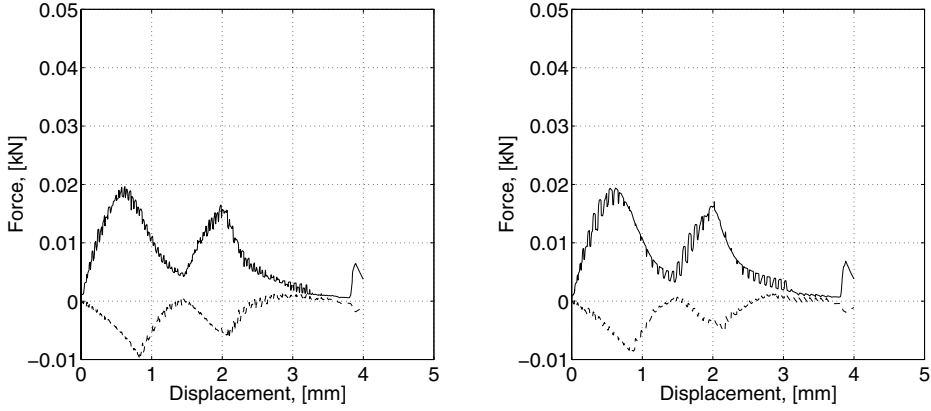
Figure 6.22: Influence of mesh fineness on the results in simulating test series Gd. Left: reference mesh. Right: coarse mesh (element size at the fracture zone doubled as compared to the reference mesh). Solid lines show the horizontal forces and dashed lines show the vertical forces.

The total energy consumption predicted for the dry (wet) specimen was equal to 26.8 (20.4) mJ. The main part of the energy supplied was consumed by frictional work, 45 (40) %, fracture energy equal to 33 (32) %, plastic dissipation equal to 22 (27) % and elastic energy constituting less than 1 (1) %.

6.4.4   Influence of variations in material data

In order to illustrate the influence of the choice of material data on the results, simulations were performed using modified values as compared to the adopted reference values presented previously. The cases studied were those of test series Bd, Dd and Gd and the properties considered were the elastic stiffnesses, the plastic properties of the earlywood, the fracture mechanical properties and the coefficient of friction between the steel plate and the wood specimen. The influence of the elastic stiffness was studied by changing the modulus of elasticity for all the different wood layers as well as by changing the modulus of elasticity for the latewood only. The influence of the plastic properties was studied by changing the initial yield stress $p_{c/0}$ and the values of p_c at the specified plastic volumetric strains, the relative change of $p_{c/0}$ being equal to that of p_c and the properties for all the earlywood layers being changed simultaneously. The effect of the fracture mechanical properties was investigated by varying the tensile and shear strengths and the stress values f_t, f_s, σ_{n1} and σ_{s1}, keeping the values of the relative displacements δ_{n1}, δ_{n0}, δ_{ns} and δ_{s0} unchanged. This results in a relative change of the fracture energy of the same amount as the change of the strength and stress values. A variation of the coefficient of friction μ in the fracture zones (affecting the softening behavior in combined shear and compression) was also investigated. The influence of variations of the fracture mechanical properties was studied in an overall sense by changing the properties in all the wood layers simultaneously.

The influences of the different parameter variations considered on the horizontal

force-displacement relations in simulating test series Bd, Dd and Gd are shown in Figures 6.23-6.25. The solid lines in the diagrams show the response obtained by assuming properties different from those of the reference material properties, and the dashed curves show the response using the reference material data. Generally, for variations of the elastic stiffnesses and the friction coefficients, the responses obtained by using 40 % lower and higher values than the reference values are shown. For the cases concerning the variations of plastic properties of the earlywood and the fracture mechanical properties (fracture energy), the results obtained by using 20 % lower and higher values are given. In some cases, additional results are given in order to more clearly illustrate the dependence on the parameters in question. For series Dd and Gd it was in most cases possible to simulate the complete failure processes. For those cases where this was not possible (numerical problems probably due to instability, severe element distortion or contact problems) the probable further response is indicated by dotted curves. For the sake of clarity, the curves for the Gd series (see Figure 6.25) were smoothed (compare with the curves in Figures 6.21 and 6.22).

The influence of variations in the elastic stiffness on the response is in all cases very small, especially when considering the stiffness of the latewood only. The horizontal force, when using a lower (higher) elastic stiffness, is consistently slightly lower (higher) and the point of global softening, for series Bd and Dd, occurs at a somewhat higher (lower) shear displacement than that obtained using the original elastic stiffness values. The largest influence of the overall elastic stiffness was present for series Gd, but the effect of changing the elastic stiffness of the latewood only was negligible.

The yield stress variations of the earlywood have a great influence on the results. A 20 % increase of the yield stress ($p_{c/0}$ and p_c) as compared to the reference values results in about 20 % higher load values throughout the response, for both Bd and Dd. For test series Gd the influence of the plastic properties is not as significant as for series Bd and Dd, though still important. For series Bd and Dd an increase of the yield stress results in the maximum load (point of global softening) being reached at a lower shearing displacement, and lower values result in the maximum load being obtained at a later stage. For series Gd an increase (decrease) of the yield stress results in the two peak force values being higher (lower), whereas the force values in between the two peaks become lower (higher) as compared to the results using the reference data. The fracture mechanical properties are also of great importance, for series Bd and Dd mainly influencing when the point of global softening of the specimen is reached, whereas the effect on the load values prior to softening is small. The effect of lowering the fracture energy is greater than that of increasing it. Furthermore the effect is highly nonlinear, especially when considering the simulation of series Bd. For this case a decrease of the fracture energies for the pure opening and the pure shearing mode by 20 % results in global softening beginning already at a shearing displacement of about 0.75 mm instead of the 1.85 mm that was obtained using the reference material data. A decrease of 10 % only influences the results marginally, however. For series Gd an increase (decrease) of the fracture energy results in consistently higher (lower) load values throughout the response, the peak loads being obtained at the same shear displacement.
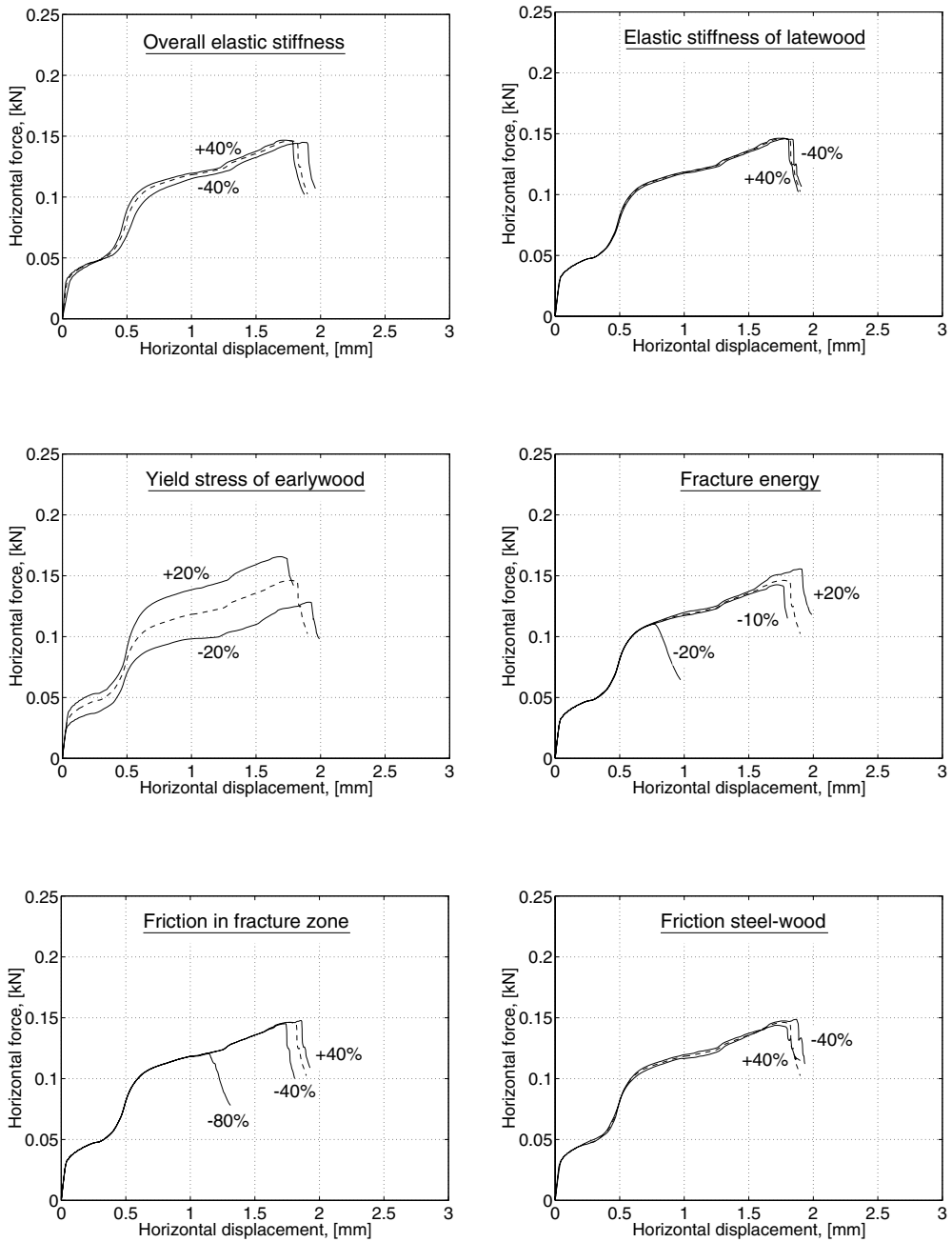
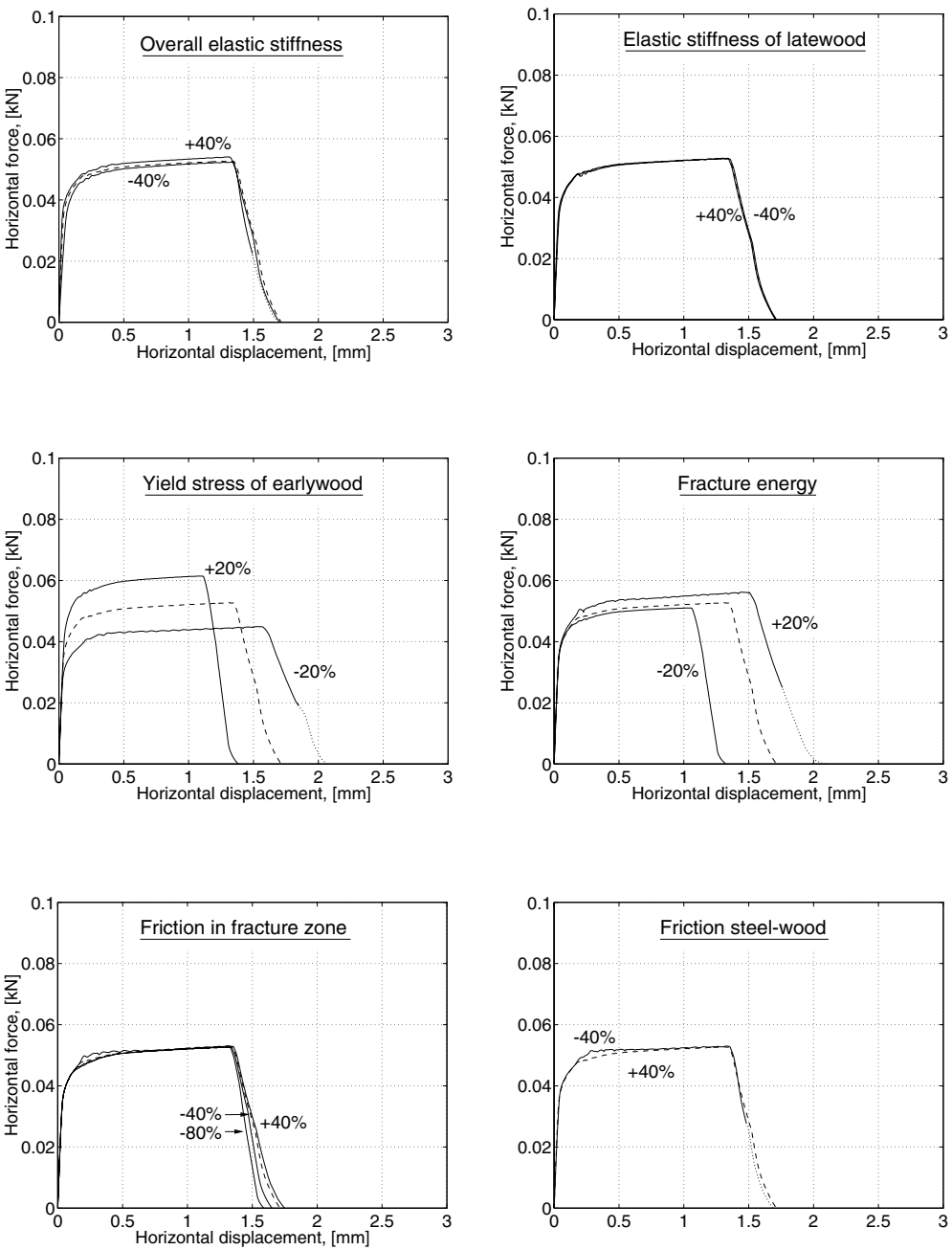Figure 6.23: Influence of variations of material properties for test series Bd.

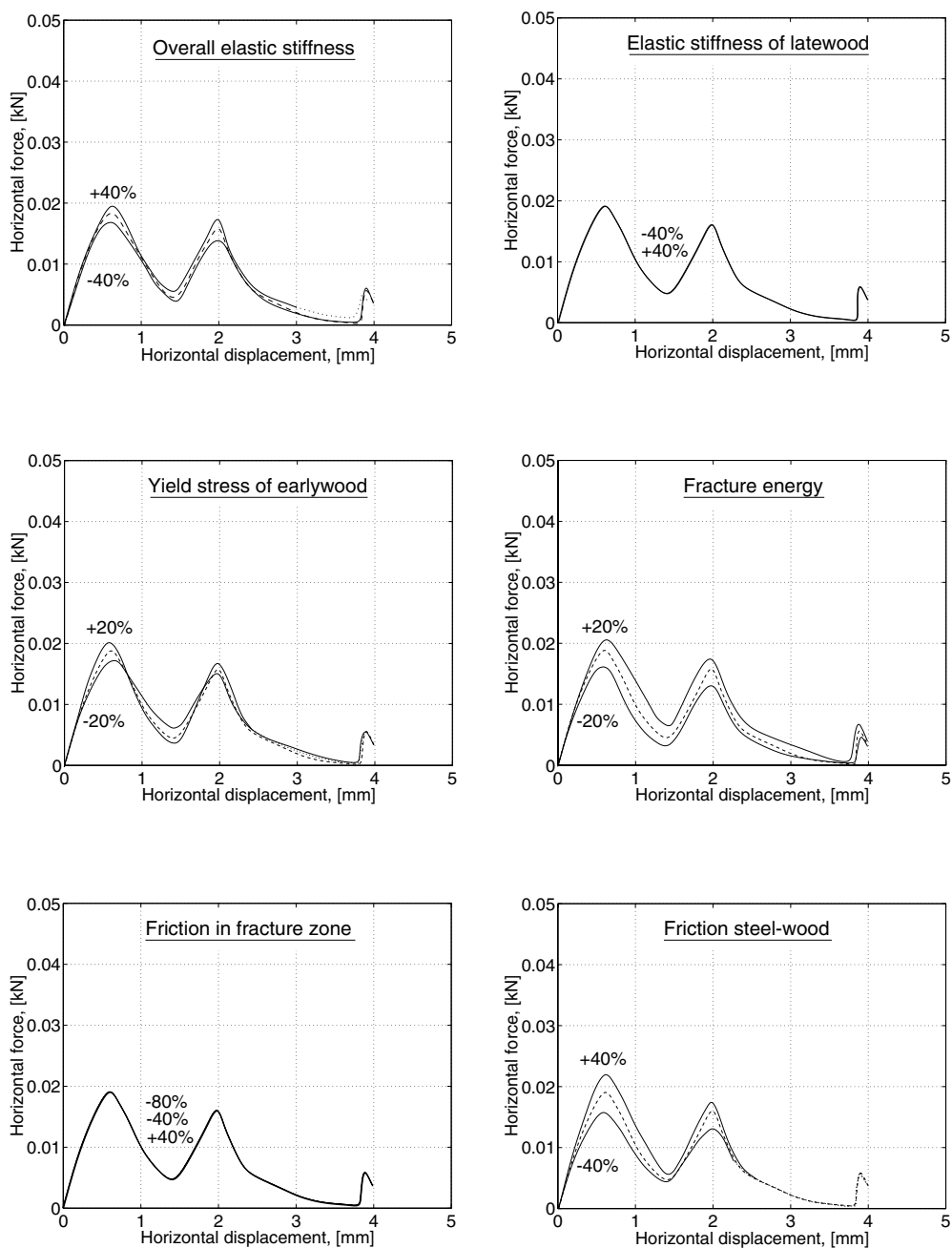Figure 6.24: Influence of variations of material properties for test series Dd.

Figure 6.25: Influence of variations of material properties for test series Gd.

The variations of the coefficient of friction μ, controlling the fracturing behavior in combined shear and compression, have for the case of series Bd a similar influence on the results as have the fracturing properties, although not as great and, furthermore, the effect on the load levels before softening is negligible. The effect of reducing μ with 40 % is relatively small, whereas a further reduction (80 %) results in softening occurring at a considerably lower shear displacement. The effect of μ on the results in simulating series Dd is small, mainly affecting the slope of the softening branch of the force-displacement curve. The influence of μ for series Gd is negligible, the load-displacement curves using the different values of μ are unchanged. The influence of the friction between the wood specimen and the steel plate is very small for series Bd and Dd, but for the case of series Gd it has a significant influence on the response. Higher values of the friction result in higher load values whereas a decrease of the coefficient of friction results in lower force values.

By plotting the corresponding diagrams for the vertical force, it can be concluded that the influences of the parameter variations are similar to those for the horizontal forces. The effect of the coefficient of friction between the steel and the wood is somewhat higher, although still rather small for the case of series Bd and Dd.

To summarize, it can be concluded that the influence of the variations of the material parameters considered is clearly dependent on the load case studied. The effect of changing the coefficient of friction between the steel plate and the wood specimens was negligible in simulating test series Bd and Dd, whereas it had a significant influence on the response in simulating series Gd. The coefficient of friction in the fracture zone (affecting the fracturing behavior in combined shear and compression) had a large influence on the results for series Bd, a small effect for series Dd whereas the effect was negligible for series Gd. It can further be concluded that the influence of the elastic stiffness was (for all cases studied) very small, whereas the plastic hardening properties of the earlywood and the fracturing properties had a large influence on the results for all the three cases studied.

6.4.5 Comparison with experimental results

The deformation and fracture processes predicted by the simulations are in good agreement with the experimental results both for the dry and the wet specimens. This is evident by comparing Figures 6.15-6.21 with the corresponding experimental results of Figures 3.27-3.33 or by studying Figures 6.26-6.29, in which the simulated deformation and fracture processes for some of the test series are compared with those of typical specimens from the corresponding test series. The location of the fracture zones predicted by the FE simulations and the large deformations within the earlywood appear to have been captured by the modelling employed. The simulated fracturing, for the A and B series, generally occurs at slightly lower shear displacement than found in the experiments, and the simulated fracturing of series Bw is too much dominated by the opening mode as compared to the experimental results. Another difference between the simulated failures and the experiments was found for the series with knife loading (Gd and Gw series). In the simulations the cut-off part, for both the dry and the wet specimens, was broken into two pieces, whereas in the experiments the cut-off part was intact for all the wet specimens.

Figure 6.26: Comparison of results from numerical simulation with experimental results. Deformation and fracturing of a specimen in test series Ad.

Figure 6.27: Comparison of results from numerical simulation with experimental results. Deformation and fracturing of a specimen in test series Bd.
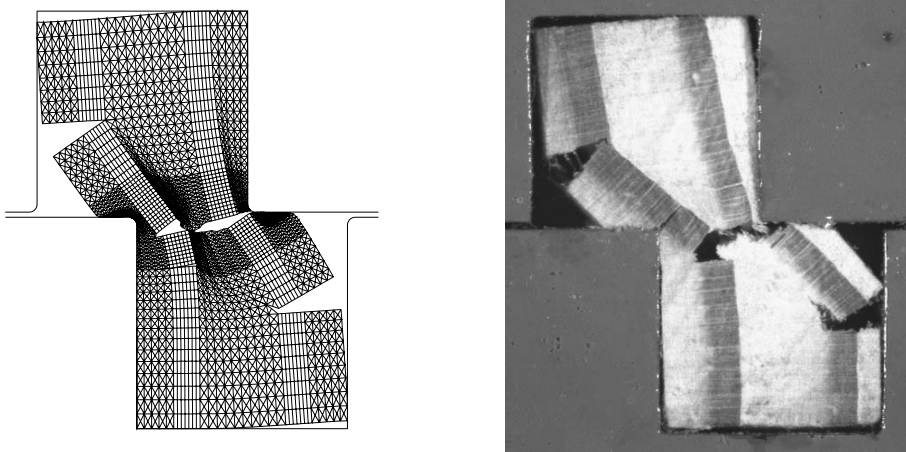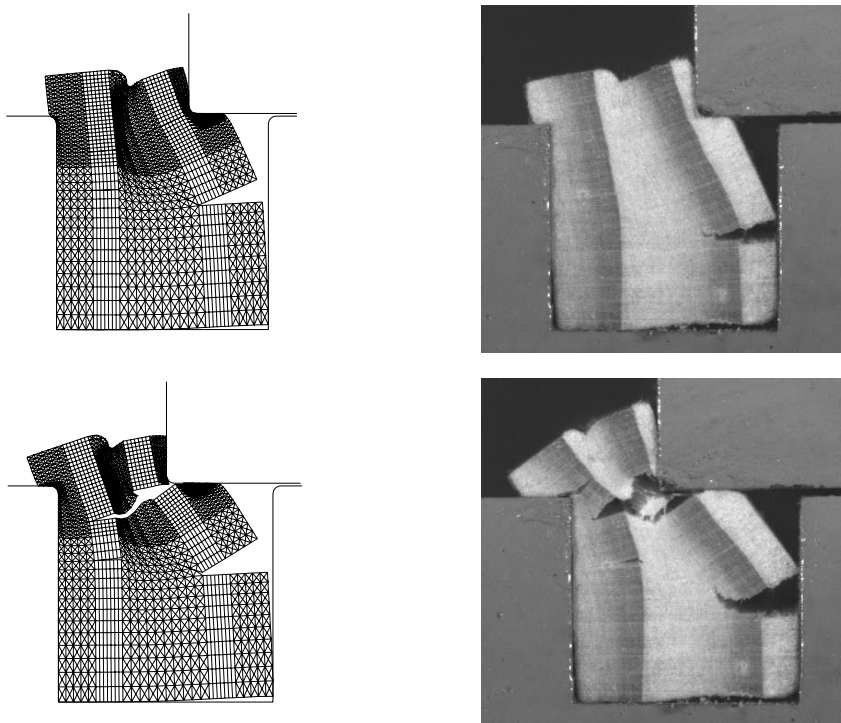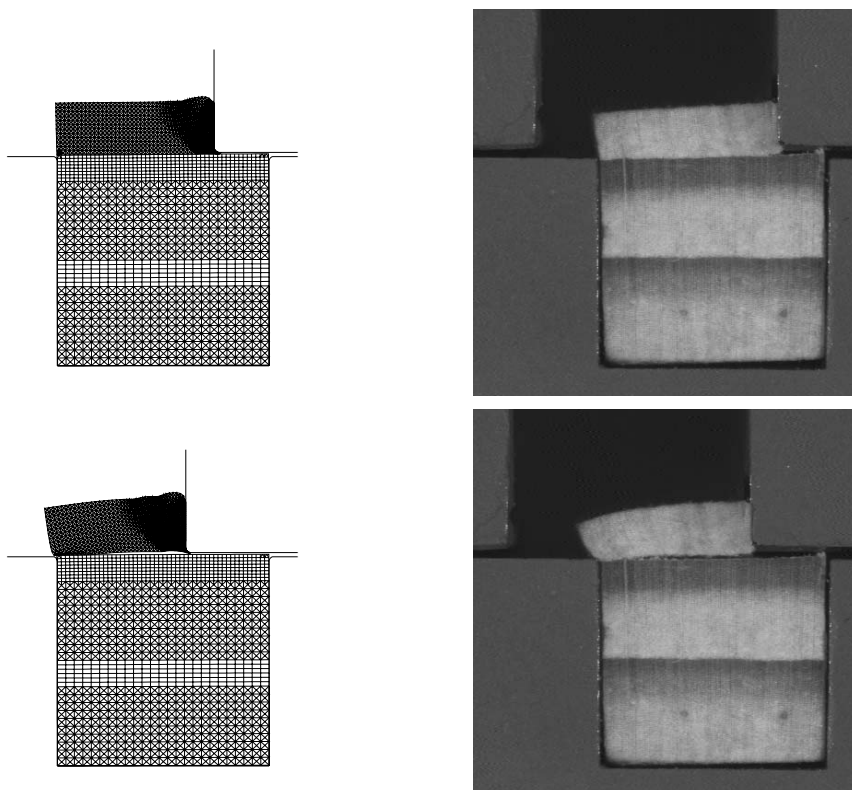
Figure 6.28: Comparison of results from numerical simulation with experimental results. Deformation and fracturing of a specimen in test series Dw.
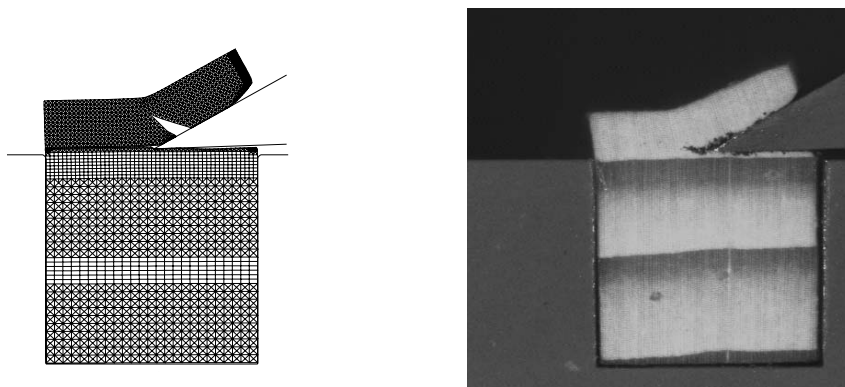

Figure 6.29: Comparison of results from numerical simulation with experimental results. Deformation and fracturing of a specimen in test series Gw.

In Figures 6.30-6.32 the calculated load-displacement curves are compared with those obtained from the experiments. Figure 6.30 shows the results for the dry specimens of test series Ad, Bd and Dd and Figure 6.31 shows the results from the corresponding wet series (Aw, Bw and Gw). Figure 6.32 shows the results for test series Gd and Gw. The dashed (and in some cases also dotted) curves in the diagrams show simulated response, whereas the solid lines show experimental results (hand-drawn mean-value curves). There is, generally, good agreement between the simulated response and the experimental results. In comparing the horizontal force-displacement curves from the simulations with the corresponding experimental curves, it can be seen that there is in all cases relatively good agreement concerning the shape of the curves. The overall stiffness is in general somewhat too high, however, and the maximum load for the A and B series is reached at a lower shearing displacement than found in the experimental results. These differences can be explained to some extent by the fact that in the simulations a perfect fit of the specimen between the steel plates was assumed, whereas small gaps between the specimen and the steel plates were present in most of the experiments, due to difficulties in preparing specimens of exactly correct dimensions. For numerical reasons, somewhat modified material data were used in the simulation of test series Ad, Bd, Aw and Bw for the elements in the right earlywood zone near the upper rigid surface. Using the modified material data, these elements were not as compressed as they would have been using the reference data. This contributes also to the differences found between the simulated response and the experimental results. It is also likely that the modulus of elasticity was set too high, considering the very low stiffness in rolling shear. In comparing the simulated responses with the experimental results it should also be emphasized that there is relatively large variation in the experimental results as can be seen from the diagrams in Appendix A. In some cases it was therefore difficult to determine representative average force-displacement curves. As can be seen from the diagrams there is a less good agreement between the simulations and the experiments concerning the vertical force of series Ad and Aw (8mm high specimens). This may partly be explained by the fact that a perfect fit of the specimens between the steel plates was assumed in the simulations. Due to difficulties in preparing the specimens to exact dimensions, small gaps between the specimens and the steel plates were probably present in most of the tests, especially for the 8 mm high specimens of test series Ad and Aw. If a small gap of only 0.08 mm (equal to one hundredth of the specimen height) is assumed in the vertical direction, the simulated vertical force displacement relations are changed drastically and the agreement between the simulated and the experimental response for test series Ad and Aw is improved considerably. This is shown by the dotted curves in Figure 6.30.

Figure 6.30: Comparison of results from numerical simulations with experimental results. Load-displacement curves for test series Ad, Bd and Dd. The solid lines are experimental results and the dashed lines are simulated response.
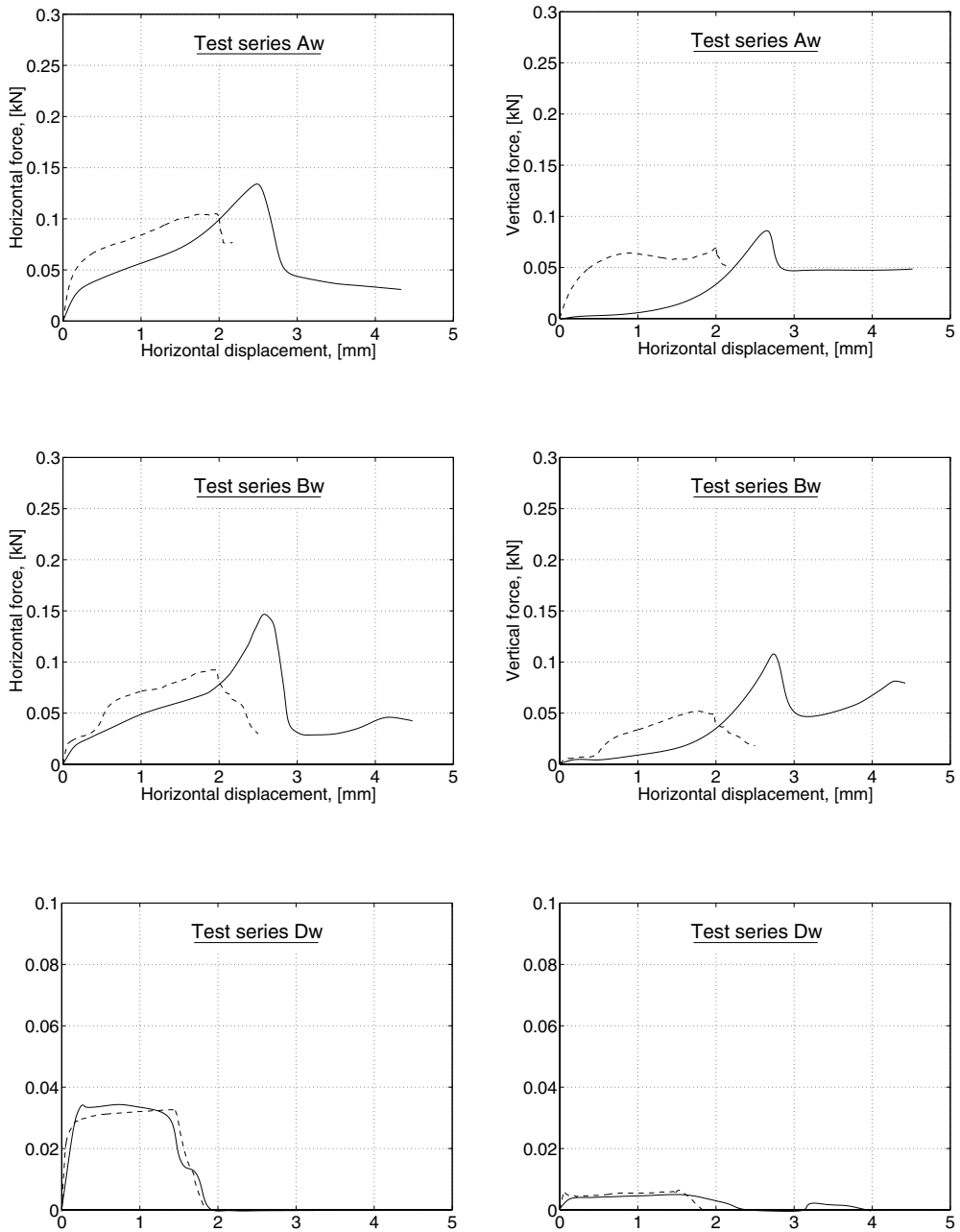
Figure 6.31: Comparison of results from numerical simulations with experimental results. Load-displacement curves for test series Aw, Bw and Ew. The solid lines are experimental results and the dashed lines are simulated response.
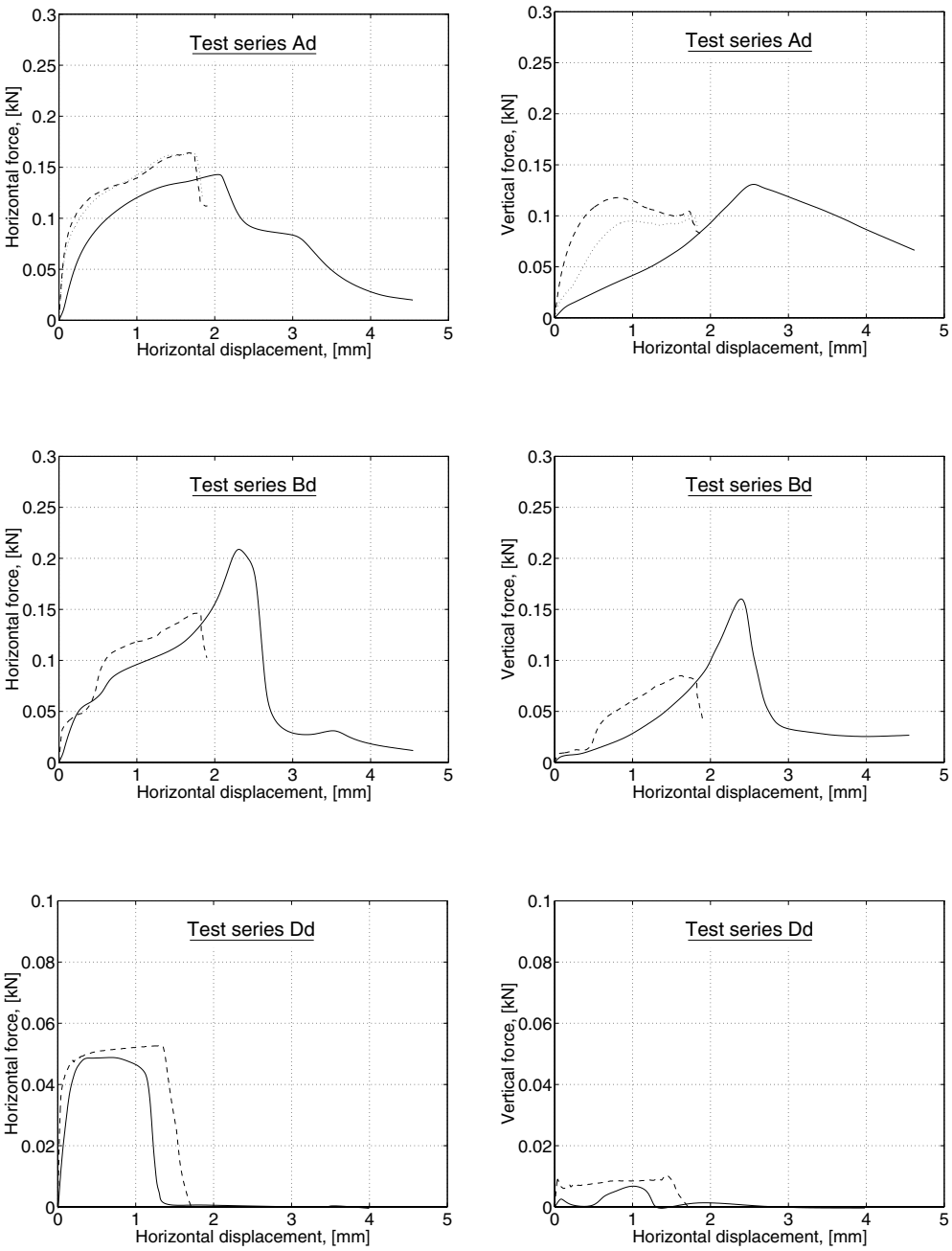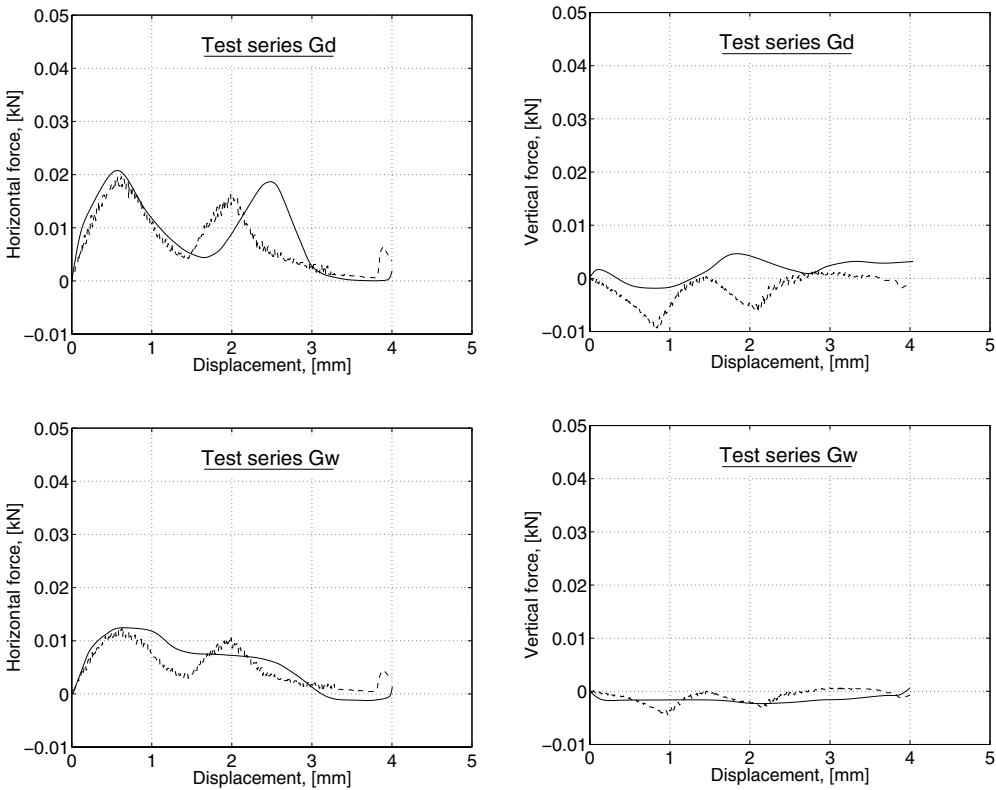
Figure 6.32: Comparison of results from numerical simulations with experimental results. Load-displacement curves for test series Gd and Gw. The solid lines are experimental results and the dashed lines are simulated response.

In comparing the results of the dry test series with those of the wet it can be concluded that the best agreement between the simulations and the experiment was found for the dry specimens in the A and B series, whereas the best agreement in simulating the D series was found for the wet specimen. From the experiments clear differences between the dry and the wet specimens were found, mainly consisting of a lower initial stiffness for the wet specimens. The wet specimens were deformed more without cracking and the forces were generally lower for the wet specimens. For the A, B and D series, the point of global softening for the wet specimens is reached at a slightly larger shear displacement as compared with the dry specimens. These differences were all captured in the simulations.

With the numerical technique applied it was not possible to simulate the complete failure processes for all the cases considered. A comparison between the energy consumption predicted by the simulations and the experimental results is therefore feasible only for the D and the G series. For these series, however, a very good agreement was

obtained, except for the case of test series Dd for which the energy consumption was overestimated significantly (about 47 %), see Table 6.3.

To sum up, a fairly good agreement between the simulations and the experiments, as regards both the deformation and fracture processes and the global load-displacement relations, was obtained using the material modelling approach adopted. The observed differences can be explained by the various assumptions made in the numerical modelling in order to simplify the analyses, especially the use of an isotropic material model. Due to lack of experimental data there are uncertainties concerning the material properties assumed. With better knowledge and modelling of these properties still better agreement between the simulations and the experiments may be obtained. It should also be emphasized when comparing the numerical results with the experimental that wood is a natural material with significant variations in properties, which results in a spread in experimental results.

Table 6.3: Comparison of calculated energy consumption with experimental results.

Test series	Experimental result [mJ]	Calculated result [mJ]
Dd	51.5	75.4
Dw	47.4	49.6
Gd	33.6	30.7
Gw	23.1	20.2

6.5 Influence of Knife Design in Wood Cutting

6.5.1 General remarks

There are several other industrial applications aimed at decomposing wooden material than defibration for mechanical pulps. Disintegration by use of knife cutting is employed in a number of industrial processes, for example wood chipping, veneer production and lumber slicing. Numerical simulations using the finite element method may be used to obtain better knowledge about these processes in order to optimize them. For instance, it might be interesting to find the most suitable knife design in order to obtain a better end-product quality, to avoid knife edge damage or to minimize the energy consumption. A good constitutive modelling of the wood is a key issue for obtaining realistic results in such numerical analyses. In this section some examples illustrating the influence of the knife design on the fracturing processes and on the cutting forces are presented.

In principle, the knife used in wood cutting is defined by the knife angle θ_1 and the angle knife-wood (clearance angle) θ_1 as shown in Figure 6.33. Typical values of these

angles are in the range of $\theta_1 = 15 - 25°$ and $\theta_2 = -1 - +1°$ [17]. In veneer cutting, stress concentrations in the wood arise at the regions indicated in Figure 6.34. One problem in veneer cutting is veneer cracking, which occurs when the tensile stresses in region 1 exceed the tensile strength of the wood.
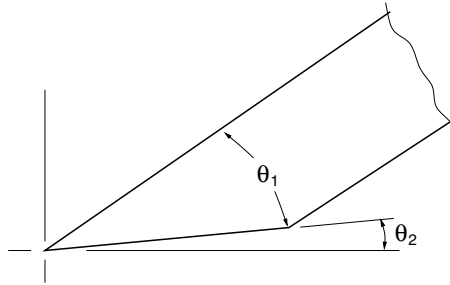
Figure 6.33: Definition of angles.
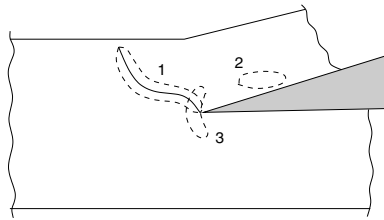
Figure 6.34: Stress concentrations in the wood in veneer cutting. Region 1: tensile stresses, region 2: shear stresses and region 3: fibre compression. From Koch [44]

6.5.2 Results

Naturally, the cutting process is influenced by the design of the knife. The deformation and fracturing of the wood as well as the cutting forces and the energy consumption are affected by the values of the angles θ_1 and θ_2. Figure 6.35 shows the response for various values of the knife angle θ_1; the angle knife-wood θ_2 is set to 2°. The top part of the figure shows the simulated fracturing using values of θ_1 of 15° (left), 30° (middle) and 45° (right), respectively. The pictures show the response at a horizontal displacement of about 3 mm. The diagrams in Figure 6.35 show cutting forces as function of the displacement; the left diagram shows the horizontal forces and the right diagram shows the vertical forces for various values of θ_1. The conditions assumed in the simulations (specimen geometry, material properties, boundary conditions etc.) were similar to those adopted in the simulation of test series Gw (except for the variation of angle θ_1). The material data refer to wood in wet condition and static loading conditions being assumed.
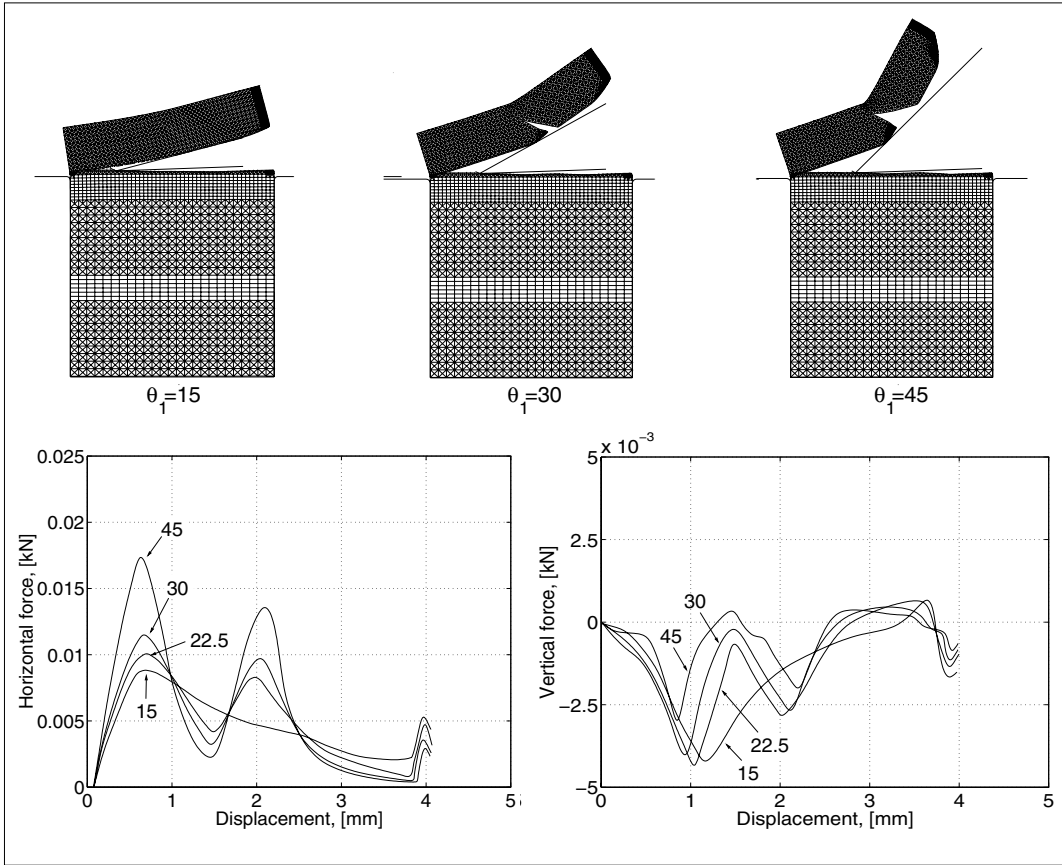
Figure 6.35: Influence of knife angle θ_1 on the cutting process ($\theta_2 = 2°$).

From the simulations it can be concluded that the horizontal cutting force, the energy consumption and the risk of cracking decrease with decreasing knife angle. The horizontal force for $\theta_1 = 15°$ is about half of that obtained for $\theta_1 = 45°$. For the case of $\theta_1 = 15°$ the cut-off part was intact, whereas it was broken into pieces for the higher values of θ_1 considered. The energy consumption ranged between 19.4-22.7 mJ, with the lowest value for $\theta_1 = 15°$. The increase in energy consumption for increasing values of θ_1 was mainly due to an increase of the fracture energy (due to the fracturing of the cut-off part), but also due to an increase of the plastic deformations.

The influence of the angle knife-wood θ_2 on the cutting process is illustrated in Figure 6.36 where the responses obtained assuming values of θ_2 of 0 and 2° are shown. In the calculations the knife angle was assumed to be 30°. As can be seen, the influence of the angle knife-wood on the horizontal force is small whereas the effect on the vertical force is much greater. The influence of θ_2 on the energy consumption is also small, with a slightly lower value for $\theta_2 = 2°$ than for $\theta_2 = 0°$.
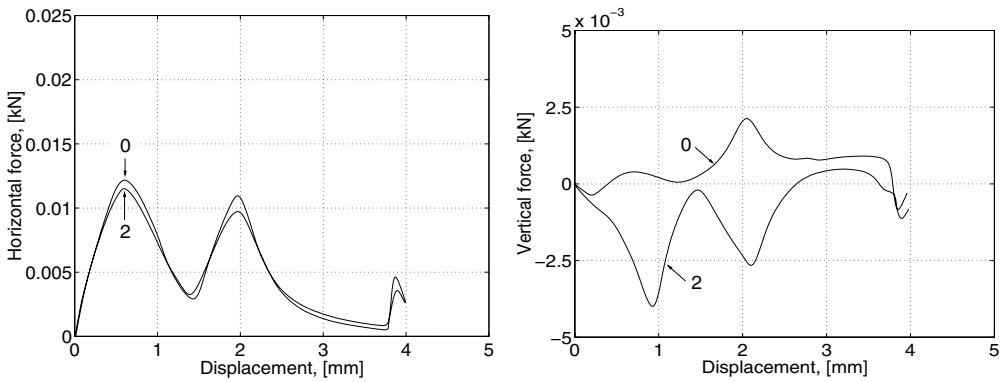
Figure 6.36: Influence of angle knife-wood θ_2 on the cutting process.

6.6 Influence of Loading Rate in Wood Disintegration

6.6.1 General remarks

In refining as well as in grinding, chipping and several other wood machining processes the wooden material is subjected to high loading rates. The effect of the loading rate on the fracturing and deformation processes of wood is therefore of great interest. In refining, the peripheral loading rate may be as high as 100 m/s, the loading rate near the inlet of the refiner, where the initial fibre separation occurs, being substantially lower, however.

The aim of the following section is to illustrate the influence of the loading rate in wood disintegration. The effects on the deformation process, the force-displacement relation and on the energy consumption are analysed. The B and D series of the chip shearing tests were chosen as the basis for the simulations, and loading rates between 0.01-50 m/s are considered.

6.6.2 Mechanical properties

The material properties adopted in the simulations are of course of greatest importance for the results. One of the main issues is the moisture content of the wood. The mechanical properties of wood are clearly dependent on the moisture content, stiffness and strength decreasing with increasing moisture content. In general, the mechanical properties are affected by the moisture content up to the point of fibre saturation. A further increase in moisture content, resulting in free lumen water, has no influence on the mechanical properties. This is true at low loading rates only, however. At high loading rates the material acts as a two-phase material, the free lumen water significantly affecting the overall behavior. The higher the loading rate, the more difficult for the lumen water to be squeezed out and the greater the effect of the lumen wa-

ter. It should also be emphasized that a high water content does not only influence by the internal lumen water pressure but also gives rise to different inertia forces due to changes in the density as compared to the density in the dry condition. Concerning the moisture content, two extreme cases may be distinguished: firstly, wood in dry condition with no major changes in the mechanical behavior as the loading rate increases; secondly, fully saturated wood (which is often the case in a refiner) with significant rate-dependent effects. Both these cases are considered. Results from simulations based on wood in dry condition as well as fully saturated wood are presented in the following. For wood in dry condition, the reference material data used in the simulations of the dry specimens in the previous section (as defined in Tables 6.1 and 6.2) were adopted with no rate effects being taken into account. The density was set to vary between 200-300 kg/m^3 in the earlywood (with the lowest value for the earlywood 1 layer) and to 1000 kg/m^3 in the latewood.

For the case of the wood fully saturated with water, the reference material data for the wet specimens as defined in Tables 6.2 and 6.1 were adopted together with rate-dependent effects for the plastic behavior of the earlywood as well as for the fracturing properties. Rate-dependent effects on the elastic properties (viscoelastic properties) were not taken into account, partly for reasons of simplicity, but also because the experimental results in Section 3.3 indicated that the tangential modulus of elasticity is not very rate-dependent. Furthermore, it was shown in Section 6.4.4 that the elastic properties only have a very small influence on the overall response at low loading rates. The strain rate behavior of the foam plasticity model is specified by the parameters D and r as defined in Section 4.2.2. These parameters were, for all the earlywood layers, set to $D = 60$ and $r = 1$. The response for the earlywood zone when loaded in radial compression at different strain rates is shown in Figure 6.37, the strain rate being defined as the rate of nominal strain. At a strain rate of 0.001 s^{-1} the response is similar to the static one. Increasing the strain rate to 10 s^{-1} results in the plateau stress being increased slightly (about 30 %) and a further increase to 100 s^{-1} results in the plateau stress being increased about 150 % and, finally, at a strain rate of 1000 s^{-1} the response is changed drastically, the material behaving almost elastically. According to Uhmeier et al. [84] the plateau stress values in radial compression of saturated wood were approximately doubled when the loading rate was increased from 0.0025 s^{-1} to 25 s^{-1}, whereas only a small increase occurred when changing the loading rate from 0.0025 s^{-1} to 0.25 s^{-1}. This is in agreement with the response obtained using the adopted material properties.

As was concluded in Section 3.3 the Mode I fracture mechanical properties are dependent on the loading rate; the fracture energy and the maximum stress were found to increase as the loading rate increases. The value of Δf_n (increase in maximum stress when the loading rate is increased by a factor of ten), for all the earlywood layers as well as for the latewood, was set to 0.35 MPa, which is in an overall sense in accordance with the experimental results. The corresponding value defining the rate dependent behavior in shear fracture Δf_s was also set to 0.35 MPa. The density of saturated wood is considerably higher than that of wood in dry condition and, furthermore, the difference in density between the earlywood and the latewood is much smaller. For the earlywood layers, the density was set to 1000 kg/m^3 and for the latewood to
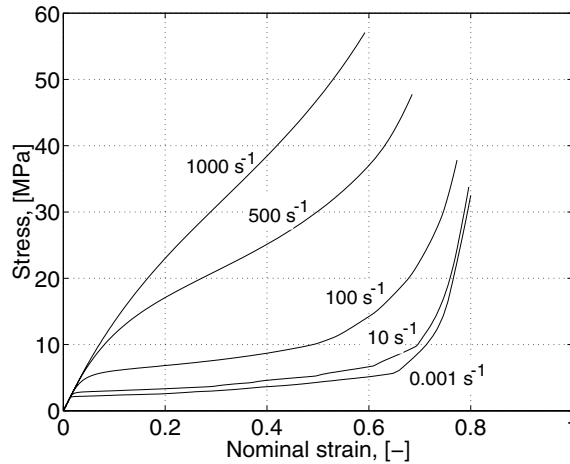
Figure 6.37: Stress-strain curves for radial compression of the earlywood zone at various strain rates.

1300 kg/m^3.

It should be emphasized that there are several uncertainties concerning the chosen material properties due to lack of experimental data. Some simplifications were also made in the modelling. Nevertheless, the key features of the material behavior are probably being captured. It is believed that the influence of the loading rate on the failure process can, by this approach, be predicted with reasonably accuracy.

6.6.3 Finite element modelling

The finite element modelling was similar to that adopted in Section 6.4, the same element meshes being used as in the simulation of the B and D test series (except for the location of the crack elements, due to fracturing in some cases occurring in a different manner as compared to the static simulations). The friction between the rigid surfaces and the wood specimen was as previously set to 0.25 and the gap between the steel plates to 0.1 mm. The upper steel plate was given a constant velocity in the horizontal direction and restrained from moving in the vertical direction. The lower steel plate was completely restrained from moving. For numerical reasons a softened contact relationship, in which the contact pressure is an exponential function of the clearance between the surfaces, was employed. The implicit time integration method, outlined in Section 5.3, was used with a small amount of numerical damping being assumed ($\alpha = -0.05$).

6.6.4 Results

Simulations were performed for loading rates of 0.01, 0.1, 1, 10, 25 and 50 m/s both for the case of wood in dry condition (no rate effects taken into account) and for saturated wood (with significant rate effects). The specimen configurations considered were those

of the B and D series of the chip shearing tests. For the dry condition, simulations were performed for the D type specimen, whereas in the saturated condition simulations were performed for both types of specimens. For the D type specimen the complete failure processes, at all loading rates considered, could be simulated both for the dry and the water saturated condition. For the B type specimen difficulties caused by material instability, severe distortion etc. made it impossible to capture the complete failure processes at some loading rates

For the case of wood in dry condition, the failure process for specimen configuration D is not much affected by the loading rate, and up to a loading rate of 1 m/s no significant changes in the deformation and fracturing process can be seen. Increasing the loading rate further results in global failure occurring at a larger shear displacement and in larger plastic deformations of the fractured part. The failure mode with shear fracture along the transition between the earlywood and the latewood is unchanged, however. At the highest loading rate, 50 m/s, the global failure occurs at a shear displacement 50 % greater than that of the lowest loading rates (0.01-1 m/s). In Figure 6.38 the deformed specimens are shown just before global softening and complete failure occurs for loading rates of 0.01, 1 and 50 m/s.

Figure 6.38: Influence of loading rate on the failure process for wood in dry condition. Specimen configuration according to the D series of the chip shearing tests. Left: loading rate of 0.01 m/s. Middle: loading rate of 1 m/s. Right: loading rate of 50 m/s.

The influence of the loading rate on the failure process for the case of saturated wood is shown in Figure 6.39 for specimen configuration B and in Figure 6.40 for the D configuration. The figures show the deformation and fracturing at loading rates of 0.01 (top), 1 (middle) and 50 (bottom) m/s. For each loading rate the pictures to the left show the specimen at the beginning of the process (at approximately 50 % of peak load), the pictures in the middle just before the major global softening begins (which in most cases is equal to the point of maximum load) and the pictures to the right show the specimen at the end of the failure process when the forces are approaching zero (or at the end of the simulation in those cases when the complete failure process could not be simulated). As can be seen in Figure 6.39 the failure process at the lowest loading

rate (0.01 m/s) for specimen configuration B is similar to that of the static one obtained in the simulation of test series Bw; compare with Figure 6.17. The failure process at higher loading rates is significantly different, however. The failure mode changes from opening mode dominated fracturing at low loading rates to shear dominated fracturing as the loading rate increases. For specimen configuration D, the failure mode with shear fracture along the transition zone is independent on the loading rate. The point of global softening and the plastic dissipation differ considerably, however.

The force-displacement diagrams for the different loading rates considered are given in Figures 6.41 and 6.42. Figure 6.41 shows the results for specimen configuration B and Figure 6.42 for the D configuration. In the figures, the upper diagrams show the results assuming wood in dry condition and the lower the results for wood in water saturated condition. The diagrams to the left in the figures show the horizontal forces and those to the right the vertical forces. For each of the four main cases the simulated static response is also given (the dashed curves in the diagrams). Note the differences in scale between the diagrams.

The influence of the loading rate on the load-displacement relations for the dry specimen is rather small. The effects of increasing the loading rate consist of the forces increasing and global softening occurring at larger shear displacements. These effects are significant, however, only at the highest loading rates. The maximum horizontal force at a loading rate of 50 m/s is about 20 % greater than that of the static response and the global softening occurring at a shear displacement of 2.1 mm as compared to 1.4 mm for the static simulation.

The responses for the saturated specimens are strongly influenced by the loading rate. For specimen configuration D, the response clearly deviates from the static one already at the low loading rate of 0.01 m/s, the shape of the curves being similar, however. For specimen configuration B the response at the lowest loading rate is very similar to the static one, although not identical. Increasing the loading rate up to 0.1, 1 or 10 m/s for specimen B and to 0.1 or 1 m/s for specimen D results in higher forces and global softening occurring at smaller shearing displacements. Further increases results in the points of global softening occurring at later stages, the forces still increasing, however. The maximum force at a loading rate of 50 m/s is about two or three times as high as that of the static response for the case of specimen configuration B and almost 6 times as high for configuration D.
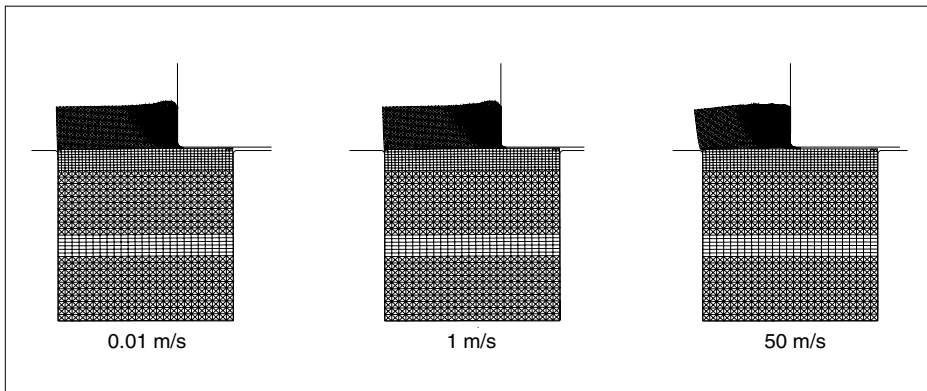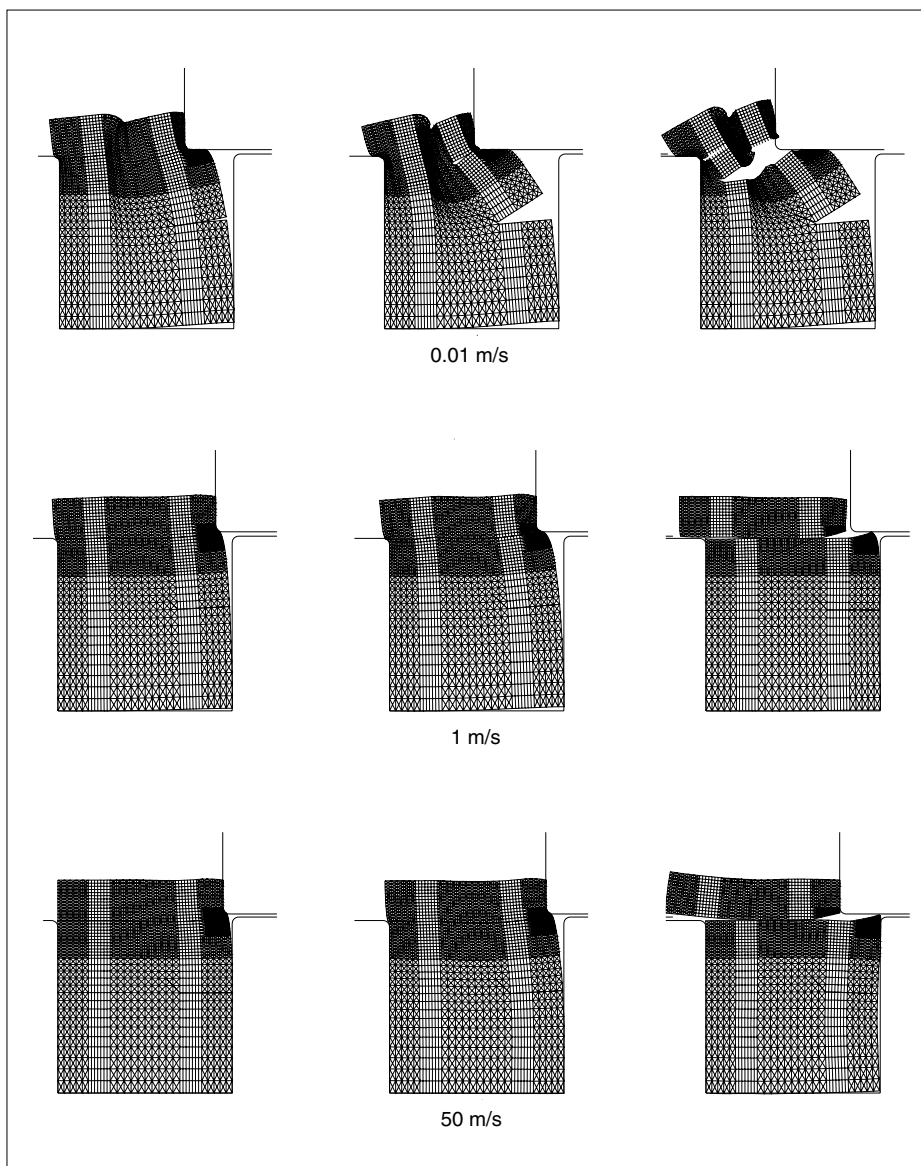
Figure 6.39: Influence of loading rate on the failure process for water saturated wood. Specimen configuration according to the B series of the chip shearing tests. Top: loading rate of 0.01 m/s. Middle: loading rate of 1 m/s. Lower: loading rate of 50 m/s.
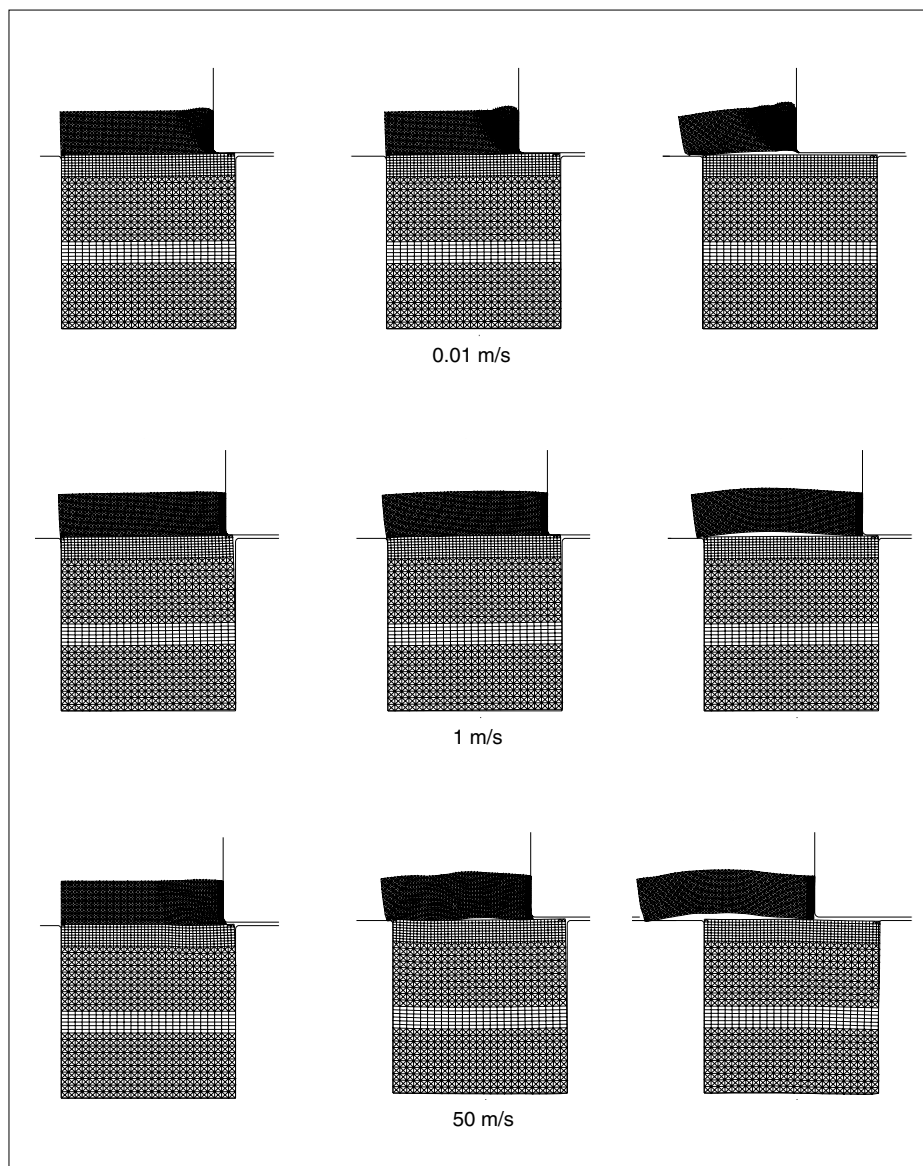
Figure 6.40: Influence of loading rate on the failure process for water saturated wood. Specimen configuration according to the D series of the chip shearing tests. Top: loading rate of 0.01 m/s. Middle: loading rate of 1 m/s. Lower: loading rate of 50 m/s.
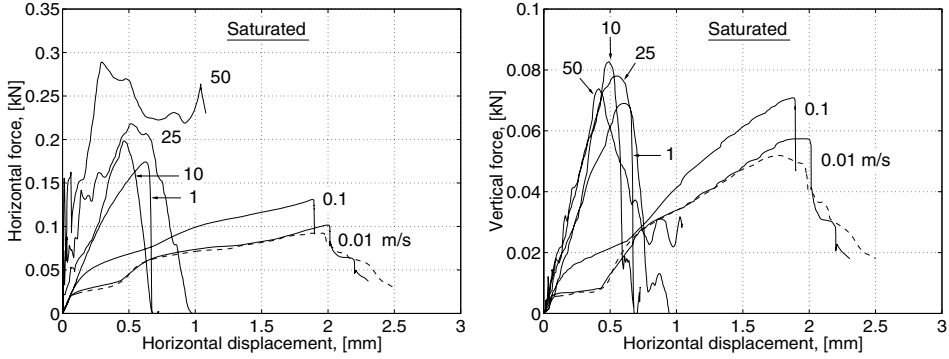
Figure 6.41: Influence of loading rate on the load-displacement relations for specimen configuration B. Material data for water saturated wood. The dashed curves show the simulated quasi-static response.
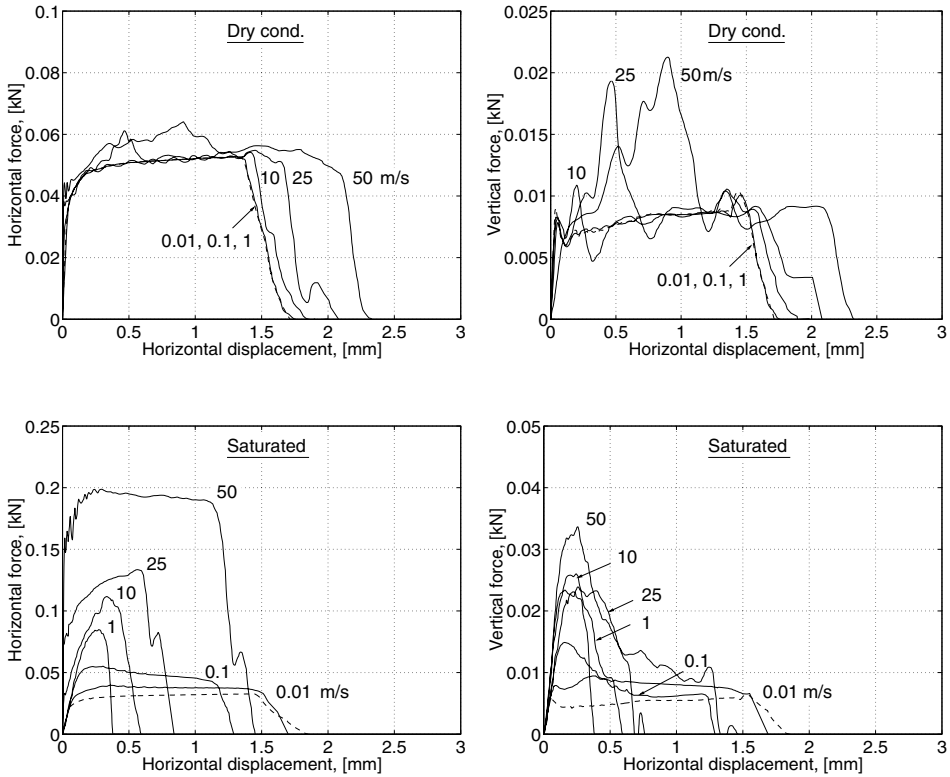
Figure 6.42: Influence of loading rate on the load-displacement relations for specimen configuration D. Top: wood in dry condition with no rate effects taken into account. Lower: water saturated wood. The dashed curves show the simulated quasi-static responses.

A very important aspect concerning the influence of the loading rate on the failure process is that of its effect on the energy consumption needed to break the specimen. The total energy can be divided into 5 parts: elastic energy, energy due to plastic deformations, energy consumed in frictional work, kinetic energy and energy consumed in the fracturing process. The magnitudes of these energy components (as well as the total energy consumption) for the different loading rates are given in Table 6.4. Results both for using the material properties for wood in dry condition and for using those of the saturated condition are shown. The values given in the table are, in most cases, evaluated at the end of the failure process when the horizontal force has approached zero. In those cases for which the complete failure processes could not be simulated (some of the loading rates for specimen configuration B), values evaluated at the end of the simulation are given instead. These values are indicated by the * superscript. Examples of the variation of the different energy components with time are shown in Figure 6.43. The diagrams given concern specimen configuration D and loading rates of 0.1 and 50 m/s. The upper diagrams concern wood in dry condition and the lower diagrams water saturated wood. The differences in scale should be noted in comparing the diagrams. As can be seen from the diagrams, the ratios between the different energy components vary considerably with time.

For the dry condition the energy consumption increases as the loading rate increases. The increase is not so large, however, and of importance for the highest loading rates only. The energy consumption at the highest loading rate considered (50 m/s) is about 60 % higher than that at the lowest loading rates. The increase is mainly due to increasing plastic dissipation and kinetic energy, but also due to an increase in frictional work.

The influence of the loading rate on the energy consumption for saturated wood is similar for the B and D specimen configurations. The total energy consumption is approximately unchanged when the loading rate is increased from 0.01 to 0.1 m/s. A slight increase for the B configuration due to an increase in plastic dissipation can be seen. For the D configuration the difference between the loading rates is less than 1 %; the small increase in fracture energy at 0.1 m/s is compensated for by the decrease in plastic dissipation. When the loading rate is increased to 1 m/s the total energy consumption reduces significantly for both specimen types, for the B configuration to less than half of that of the lower loading rates and for the D configuration down to about one third, although in both cases there is an increase in fracture energy. The decrease in total energy consumption for both specimen types is due to a dramatic decrease in plastic dissipation. When the loading rate is further increased the energy consumption increases, mainly due to an increase of the kinetic energy but also due to the increase in fracture energy. At the highest loading rate the kinetic energy for the D type specimen constitutes more than 80 % of the total energy consumption, whereas the energy consumed in the fracturing only constitutes 6 %. For the B type specimen the complete failure process at the highest loading rate could not be simulated, but at the end of the simulation almost 70 % of the total energy supplied was absorbed as kinetic energy.

Table 6.4: Influence of the loading rate on energy consumption.

| Loading rate [m/s]	Specim. config.	Moisture content	Elastic energy [mJ]	Plastic dissip. [mJ]	Frictional work [mJ]	Kinetic energy [mJ]	Fracture energy [mJ]	Total energy [mJ]
0.01	B	satur.	4.4*	124.5*	7.5*	0.0*	13.7*	**150.1***
0.1	B	satur.	10.5*	146.2*	3.1*	0.0*	9.6*	**169.4***
1	B	satur.	2.4	36.1	4.4	9.5	18.8	**71.2**
10	B	satur.	3.9	5.7	5.1	37.9	21.1	**73.7**
25	B	satur.	9.7	3.8	7.1	92.8	21.5	**134.9**
50	B	satur.	44.4*	4.0*	6.0*	155.5*	21.3*	**231.2***
0.01	D	dry	0.1	64.4	0.9	0.0	9.6	**75.0**
0.1	D	dry	0.1	64.5	0.9	0.0	9.6	**75.1**
1	D	dry	0.1	64.9	0.9	0.0	9.6	**75.5**
10	D	dry	0.2	68.2	0.9	0.7	9.5	**79.5**
25	D	dry	0.4	76.5	1.9	3.7	9.4	**91.9**
50	D	dry	0.4	93.9	4.6	12.1	9.1	**120.1**
0.01	D	satur.	0.6	47.8	1.7	0.0	6.7	**56.8**
0.1	D	satur.	0.5	46.7	1.9	0.0	7.9	**57.0**
1	D	satur.	0.2	5.3	1.9	2.0	12.4	**21.8**
10	D	satur.	2.0	1.9	3.7	21.0	14.5	**43.1**
25	D	satur.	7.9	2.8	6.6	50.3	15.4	**83.0**
50	D	satur.	7.0	5.1	12.0	203.8	15.0	**242.9**
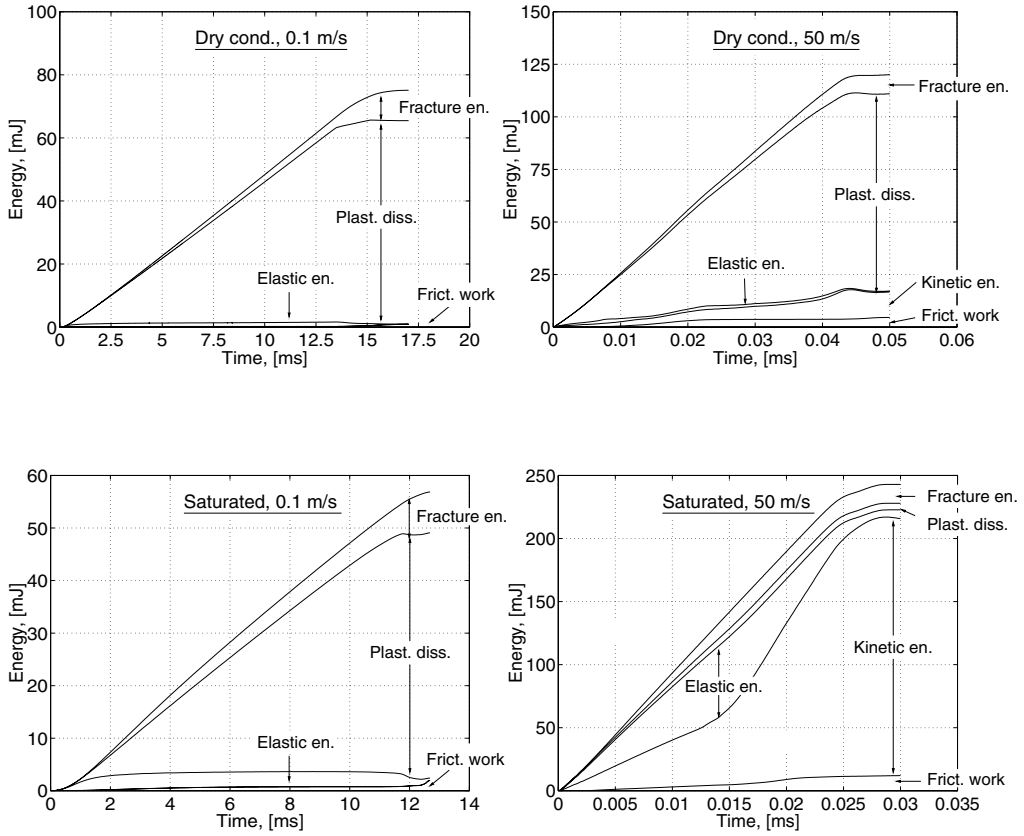
Figure 6.43: Energy versus time relations for specimen configuration D at loading rates of 0.1 and 50 m/s. Top: wood in dry condition with no rate effects taken into account. Lower: water saturated wood.

6.7   Concluding Remarks

In this chapter numerical simulations of wood disintegration were presented. The constitutive modelling is based on the continuum modelling approach outlined in Section 4.2. The aim of the simulations was to verify the modelling approach, to identify problems that can arise when simulations of this type are performed and to illustrate the influence of different parameters on the failure processes. The basis for the simulations was the chip shearing tests of Section 3.4. Numerical simulations of several of the test series were performed. Wood in both dry and wet condition was considered. The results from the simulations were compared with the experimental results. Simulations of the combined compression and shear tests (Section 3.2) were also performed, the reason for this mainly being to evaluate the performance of the modelling employed for the loading modes in question. It was concluded that the response in pure compression and in mixed loading up to $\xi=45°$ (average shear strain equal to average normal strain) is rather well predicted, the differences between the simulated response and the experimental results mainly related to the choice of material data and not to the modelling technique in general. The behavior for the shear dominated loading modes is not so well captured, however. This is related to the extremely low modulus in rolling shear (in relation to the modulus of elasticity) not being captured, due to the use of an isotropic model.

Numerical difficulties due to the large deformations, the complex material behavior (with possible material instability) and the contact conditions arise when simulations of this sort are performed. It was thus not possible with the numerical technique that was employed to fully simulate the behavior of all the specimens considered during the complete course of events. For all cases, the major part of the deformation and fracture processes that occurred could, however, be predicted.

It could be concluded that the overall deformation and fracture processes predicted by the simulations were in reasonably good agreement with the experimental results. Not only was the location of the fracture zones as predicted by the simulations in good agreement with the experimental results, but the large deformations within the earlywood zones were also captured with the modelling technique adopted. The discrepancies concerning the deformation and fracturing processes consist of the simulated fracturing for some of the test series occuring at a slightly lower shear displacement than found in the experiments, the simulated fracturing in one case too much dominated by the opening mode and the cut-off part in the simulation of the knife cutting test with wood in wet condition being broken in two pieces (whereas it was intact in the experiments). In comparing the load-displacement curves from the simulations with the experimental ones it can be seen that there is, for all cases, relatively good agreement concerning the shape of the curves. The differences mainly consist of the overall stiffness in general being somewhat too high and the maximum load in some cases being reached at a lower shear displacement than found in the experiments. For the cases for which the complete failure processes could be predicted, a comparison of the calculated energy consumption with the experimental results showed a good agreement.

The differences between the results from the simulations and the experimental re-

sults can to some extent be explained in terms of various assumptions being made in order to simplify the analyses. For instance, a perfect fit of the specimen between the steel plates was assumed in the simulations and somewhat modified material data were used for some elements in some of the simulations in order to prevent excessive distortion of these elements. Due to lack of experimental data there are still uncertainties concerning the adopted material properties. With better knowledge of the material properties a better agreement between simulations and experiments can be obtained.

A study of the influence of the choice of material properties on the response in simulating some of the test series was performed. Elastic, plastic and fracturing properties as well as the friction between the steel plates and the wood specimen were considered. It can be concluded that the elastic stiffness has a very small influence, whereas the plastic properties of the earlywood and the fracturing properties have a great influence on the response for all three cases studied. The coefficient of friction in the fracture zones (influencing the fracturing behavior in combined compression and shear) had a significant influence on the response for one of the cases considered, while its influence on the other two cases was small or negligible. The coefficient of friction between the steel and the wood was found to have a significant effect on the response for the knife-cutting case, whereas it had a small influence for the other two load cases.

The influence of the loading rate on the failure process, and especially on the energy consumption needed to break the specimen into two pieces, was investigated. Loading rates ranging from 0.01 m/s up to 50 m/s were considered. The mechanical properties of wood are, at low loading rates, affected by the moisture content up to the point of fibre saturation only. A further increase in moisture content does not influence the mechanical behavior. This is not the case at high loading rates, however. Free lumen water then significantly influences the compressive response of the material (a two-phase system). This is due to the difficulties of squeezing out the lumen water at high loading rates. Wood at high moisture contents (above the point of fibre saturation), especially fully saturated wood, thus shows significant rate effects. Concerning the moisture content of the wood two extreme cases were modelled. Wood in dry condition with no rate effects and water saturated wood with rate effects concerning the plastic properties of the earlywood and the fracture mechanical properties were taken into account. Two different specimen configurations were considered.

The influence of the loading rate on the failure process and on the energy consumption differed significantly between the case of the dry and the saturated wood. When assuming material properties for wood in dry condition (with no rate effects considered for the material) the effect of the loading rate was rather small. The forces increased somewhat and the point of global softening occurred at greater shear displacements as the loading rate increased. These effects were only of importance at the highest loading rates, however. The maximum force at a loading rate of 50 m/s was about 20 % higher than that obtained in the static analysis. The energy consumption also increased for increasing loading rates: the energy consumption at a loading rate of 50 m/s was about 60 % higher than that of the lowest loading rates, the increase mainly being due to an increase in plastic dissipation and kinetic energy but also due to an increase in the frictional work. The response for the case of the saturated wood was greatly influenced by the loading rate. The higher the loading rate, the higher the forces involved. At a

loading rate of 50 m/s the maximum shear forces were about three and six times as high as the corresponding static results for the two types of specimens considered.

The total energy consumption ranged between 71-231 mJ for specimen type B and between 22-243 mJ for type D. In both cases, the lowest values were obtained at loading rates of 1 m/s and the highest values at the highest loading rates. At low loading rates (0.01-0.1 m/s) the energy consumption was about 150 and 60 mJ, respectively. The reason for the decrease in energy consumption when increasing the loading rate to 1 m/s was due to a substantial decrease in plastic deformations, although the fracture energy and the kinetic energy were increased. The increase in energy consumption at the higher loading rates was mainly due to an increase in kinetic energy, the other energy components also increasing slightly. At the highest loading rate the kinetic energy constituted almost 70-85 % of the total energy consumption, whereas only a small portion (about 5-10 %) was consumed in the fracture process.

There are several industrial processes in which wooden material is disintegrated using knife cutting. Analyses aiming at illustrating the influence of the knife design on the cutting process were presented. The cutting forces (both the horizontal and the vertical force component), the energy consumption and the risk of fracturing of the cut-off part were found to decrease with decreasing knife angle. The influence of the angle knife-wood (or clearance angle) on the horizontal force (and thereby also on the energy consumption) was small, whereas it has a greater influence on the vertical force.

Material modelling is the key issue in performing realistic simulations. It was obvious from the experiments that account must be taken of differences between earlywood and latewood. Unfortunately, little experimental work has been carried out to determine the mechanical properties of these two wood types separately. More experimental work needs to be done in order to determine the elastic, plastic and fracture mechanical properties of earlywood and latewood separately. Especially the properties at high loading rates need to be better established in order to better understand the complex deformation and fracturing behavior at high loading rates.

Chapter 7

Numerical Examples - Microstructural Modelling

7.1   Introduction

Although the strongly nonlinear response of wood loaded perpendicular to the grain is largely related to geometric effects at the microstructural level, the constitutive modelling of the cell wall material is of great importance for capturing these nonlinearities and obtaining realistic results from numerical simulations. Some different constitutive assumptions for the cell wall material are applied in the following, ranging from the basic assumption of linear elasticity to more sophisticated approaches involving plastic behavior as well as microcracking. Numerical examples simulating the behavior of wooden cell structures loaded perpendicular to the grain using the different constitutive approaches are presented. The influence of the ray cells, the friction at contacting cell lumens, etc. are also studied. The loading cases considered are those of pure radial compression and combined compression and tangential shear of one growth ring. The simulations are made in accordance with the microstructural modelling approach presented in Section 4.3.

Modelling at the microstructural level often gives rise to very large models. In order to limit the model size, a rather high density of the growth ring was chosen (500 kg/m^3), implying a rather small growth ring width resulting in a low number of cells in the growth ring. Furthermore, the number of cells between two adjacent ray cells was set to four, even though measurements indicate the average number to be about six or seven [66].

The experimental results from the combined compression and shear tests of Section 3.2 are of great interest in evaluating the simulations performed. In comparison with the experiments it should be noted that the simulations were made assuming an average density of 500 kg/m^3, which results in a rather small growth ring width, whereas the experiments were performed on wood having a lower density and a considerably larger growth ring width. This means that higher yield stress values are to be expected, and that the densification region starts at a lower strain level in the simulations than in the experimental results. The optical equipment utilized in the experiments of Section 3.2 captured the overall behavior of the specimens, but it did
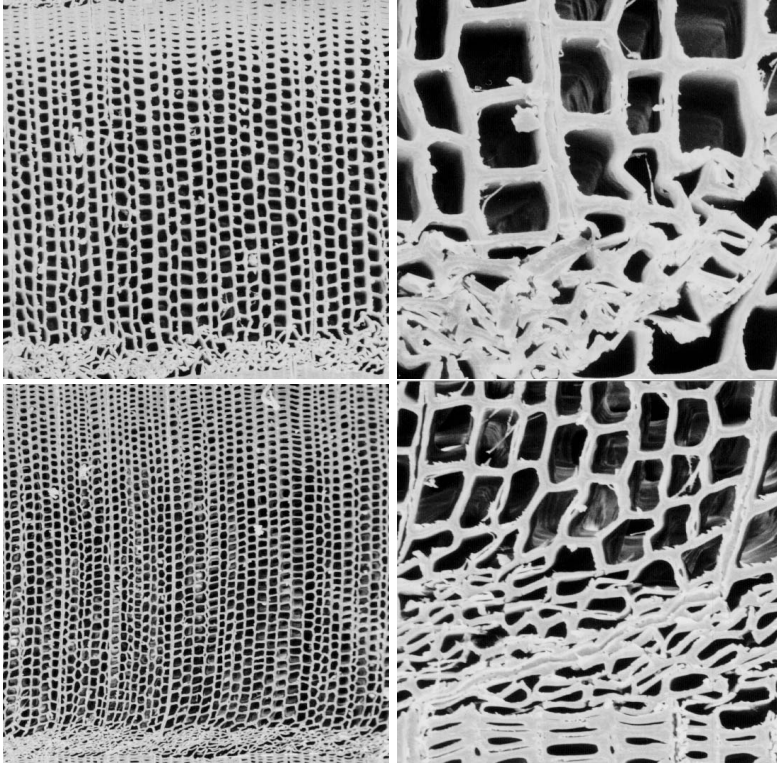
Figure 7.1: Cell structure deformations at radial compression (top) and combined radial compression and shear (lower) [80].

not give detailed information about the deformation and collapses of the individual fibres. For this reason some results from a study of the behavior of the cell structure with the aid of SEM micrographs are given in Figure 7.1. The study was performed on Norway spruce with low moisture content. The pictures show the deformations of the cell structure (at two levels of magnification) for pure radial compression and for combined compression and shear loading.

7.2   Mechanical Properties

The cell wall is divided into two main layers, one representing the middle lamella together with the primary wall and the S1 layer, the other one representing the S2 and S3 layer, as was outlined in Section 4.3. The elastic stiffness properties for these two layers are chosen according to the stiffness values of the microfibrils as reported by Persson [66]. They are given in Table 7.1.

The material properties of the microfibrils need to be transformed in order to orient the microfibrils to the global directions of the model. In these transformations the

Table 7.1: Adopted elastic stiffness properties for the cell wall layers. The values are expressed in terms of a local microfibril coordinate system where 1 denote the longitudinal direction of the microfibril, 2 the tangential direction of the microfibril and 3 the direction normal to the cell wall according to Figure 4.15. From [66].

Parameter	S2 and S3	ML+P+S1
E_1 [MPa]	68500	30500
E_2 [MPa]	11000	6400
E_3 [MPa]	9700	5700
G_{12} [MPa]	3600	2200
G_{13} [MPa]	3000	1900
G_{23} [MPa]	2850	1800
ν_{21} [-]	0.054	0.071
ν_{31} [-]	0.047	0.062
ν_{32} [-]	0.39	0.400

microfibril angle of the cell wall layer considered is needed. In the following examples the microfibril angle of the outer layer was set to 45°, and to 10° for the inner layer. The elastic stiffness of the ray cell material in the local microfibril coordinate system was set equal to that of the S2 layer.

Fracture mechanical properties for the cell wall material are not well known. Due to the lack of experimental data and for reasons of simplicity, several rather crude assumptions were made in the present modelling. Firstly, similar fracture properties were assumed irrespective of the in-plane orientation of the fracture zone. Secondly, the fracture properties for the outer and the inner cell wall layer were set equal. Furthermore, the softening stress-relative displacement relations adopted for the pure tensile and pure shear fracture modes were assumed to be linear. The tensile strength was set to 100 MPa, and the fracture energy in Mode I to 1500 J/m². The fracturing properties in shear were set equal to those in tension. The mixed mode coupling parameters m and n were set equal to 5, and the coefficient of friction in the fracture zone μ was set to zero, i. e. no increase in shear capacity for combined compression and shear was taken into account.

Plastic behavior of the ray cells was taken into account by using the Hill yield criterion [26]. The yield stress was set to 150 MPa in the axial direction of the ray cell (radial direction globally) and to 45 MPa in the transverse directions. Isotropic hardening was assumed, the plastic stiffness set to about one tenth of the elastic stiffness. For the tracheid cell material no plastic response was taken into account.

The material data adopted concerns wood in dry condition and in room temperature. No simulations were performed for wood in wet condition or at elevated temperatures.

Due to the lack of experimentally verified material data for wood in general and for the cell wall material in particular, there are clear uncertainties regarding the adopted cell wall material properties. The aim of the simulations was only to indicate the influence and importance of various assumptions made regarding the constitutive modelling. This aim can be met despite the fact that the material properties adopted are not necessarily the correct ones, and that some rather crude assumptions were being made in the modelling.

7.3   Finite Element Modelling

Static conditions were assumed and the problem was analysed as a two-dimensional one. In general, plane strain conditions were assumed. For comparison, a few analyses were performed assuming plane stress conditions. Second-order 8-node solid elements were used. These element show a much better performance in problems dominated by bending than first-order linear elements. The cell wall was divided into two layers of elements in the thickness direction: one element for the inner cell layer (S2 together with the S3 layer) and one element for the outer layer (middle lamella together with the primary wall and the S1 layer). In the radial direction six to eight elements were used per cell depending on the cell type (the larger number for the wider earlywood cells and the lower number for the latewood cells). In the tangential direction the number of elements in each cell was set to six. The total number of elements in the models depends on the number of cells assumed between the ray cells. For the case of four cells between the ray cells included the total number of elements is equal to about 7000 and the number of nodes to approximately 35000. Contact conditions were introduced within each cell lumen in order to prevent cell walls from penetrating each other as the cells collapse. Most of the simulations were carried out taking no friction into account. In order to investigate whether the coefficient of friction has any influence on the response predicted, a few analyses were carried out with friction included. A standard Coulomb friction model was applied.

Crack elements were introduced at the corners of the hexagonal cells in order for microcracking to be taken into account, as was outlined in Section 4.3.3. In connection with fracture mechanics analyses, the use of second-order solid elements may give rise to problems. Constraint equations were therefore applied at the zones where the crack elements are introduced, forcing the displacements of mid-node of the solid elements to be equal to the average values of the nearest corner nodes, thus inferring a linear variation in displacements there. The crack elements connect the corner nodes of the solid elements. It should be emphasized that cracks were not allowed to propagate completely through the cell walls. It would be desirable to increase the number of elements in each cell, in particular the number of crack elements across the cell walls. However, a relatively coarse element mesh was adopted in order to limit the size of the models.

Cyclic boundary conditions connecting the left and the right boundaries were applied (the displacements of the nodes at the left boundary were set equal to those of the corresponding right boundary), inferring the structure analysed to be infinitely wide.

For this modelling technique to be correct, the structure must be periodic, so that the element mesh at the left boundary exactly fits that of the right. The displacement of the nodes at the upper boundary was prescribed according to the loading mode considered, whereas the nodes at the lower boundary were restricted from moving. The notation for the loading mode introduced in Section 3.2 is adopted, with $\xi=0°$ denoting pure radial compression and $\xi=22.5°$ and $45°$ being combined modes involving both compression and shear. At $\xi=22.5°$ the horizontal displacement is equal to about 40 % of the vertical and at $\xi=45°$ the horizontal and vertical displacements are equal. In order to stabilize the solution for the case of pure compression, a small horizontal displacement (equal to one hundredth of the vertical displacement) was applied.

The finite element formulation and solution technique used are outlined in Chapter 5. It should be emphasized that the objectivity principle is violated when assuming material anisotropy in geometrically nonlinear analyses due to the constitutive relations being formulated as rate equations (hypo-elasticity). The effect of this inadequacy is difficult to estimate, however. The directional dependence is not so great (except for the ray cells) within the plane considered and, furthermore, the strains developed are relatively moderate. These conditions are probably beneficial, but the implications of this inadequacy should be investigated in future work.

Due to the character of this type of analysis, involving a great deal of contact interactions together with material softening behavior and strong geometric nonlinearities, numerical difficulties and convergence problems readily occurred in the simulations. An explicit integration scheme may represent a more optimal choice for this type of analysis. The microscale of the problem considered will infer extremely small time steps however, and furthermore, the implications of material softening behavior in explicit analyses is not obvious (the critical time step being undefined during softening).

7.4 Results

The simplest possible case to consider is that of pure linear elastic material behavior. At the structural level, a further simplification can be made by not considering the ray cells in the modelling. The simulated behavior for pure radial compression and combined compression and shear at $\xi=22.5°$ and $\xi=45°$ assuming elastic behavior and omitting the ray cells is shown in Figure 7.2. The pictures show the specimen at the undeformed state and at average normal strains of 5, 20 and 40 %. In these, as well as in all subsequent pictures of the cell structures, 8 cells in the tangential direction are included, irrespective of the number of cells included in the analysis in question.

In all three cases, the structure starts to behave nonlinear at strains of about 1 - 2 %. Thereafter, strain localization occurs with collapse of the weak earlywood cells at the bottom of the structure (thin cell walls and large radial width). The collapse then continues successively until all the earlywood cells are collapsed, which occurs at a strain of about 40 %. It can be seen that the strain localization is not as pronounced as in a real cell structure; compare with Figure 7.1.
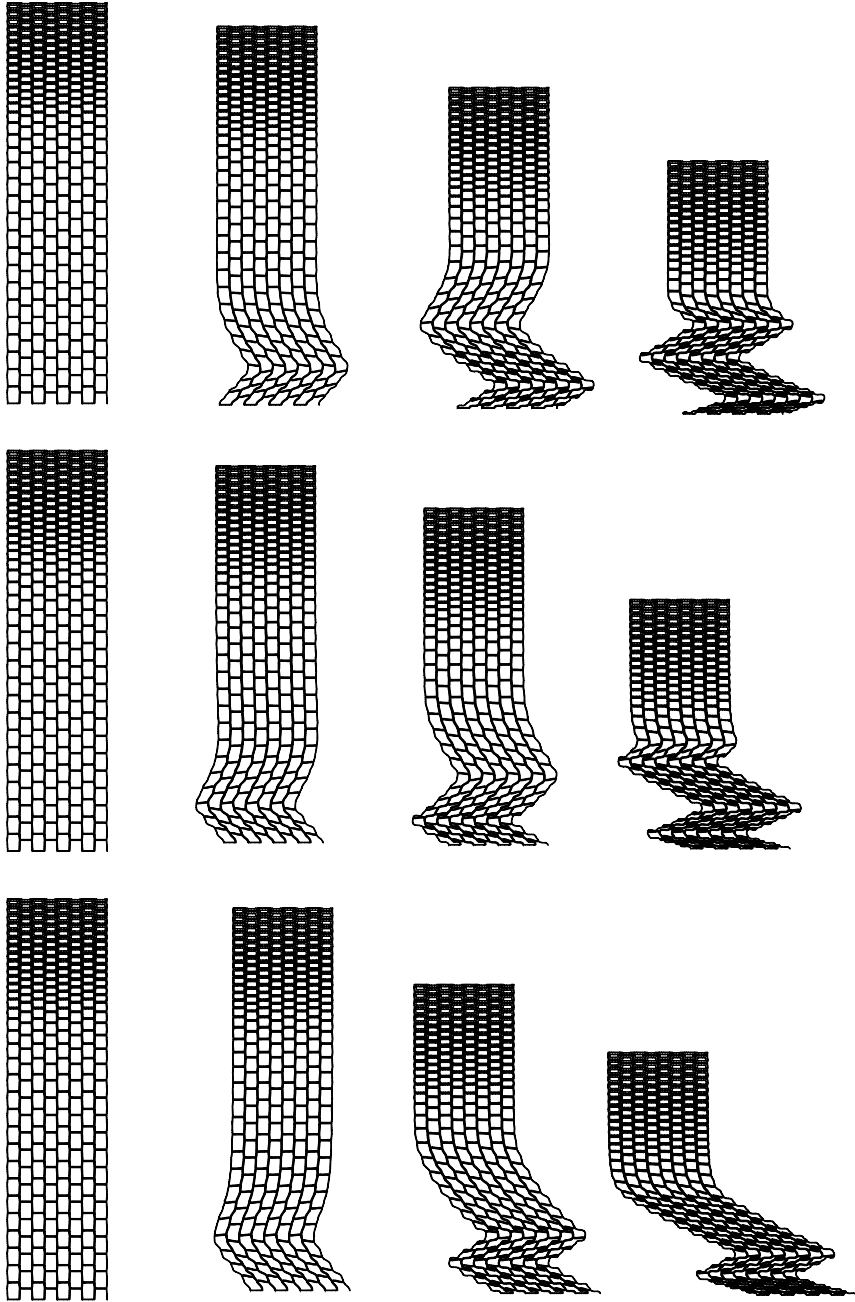
Figure 7.2: Deformation process assuming elastic material behavior and omitting the ray cells. From left to right: undeformed, average normal strain of 5 %, 20 % and 40 %, respectively. Top: pure radial compression. Middle: combined compression and shear at ξ=22.5°. Lower: combined compression and shear at ξ=45°.

The stress-strain curves for the three loading cases considered are given in Figure 7.3. The overall shape of the curves is in relatively good agreement with the results of the compression and shear experiments of Section 3.2, cf. Figure 3.10. The stiffness and stress values are generally too high as compared to the experimental results (the difference in density between the simulations and the experiments should be observed, however). It can be seen that the normal stress-strain curves are very similar for the three loading modes considered. Slightly lower compressive stress values were found for combined loading at $\xi=45°$, which is in good agreement with the experimental results. The shear stress values are also similar to those found in the experiments.
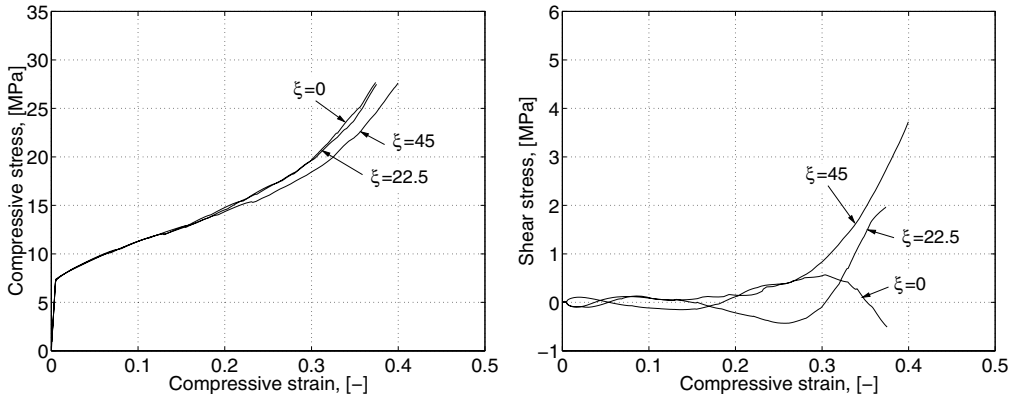

Figure 7.3: Compressive stress-strain curves obtained assuming elastic material behavior and omitting the ray cells. Left: Normal stress. Right: Shear stress.

With ray cells present in the model, the deformation pattern is changed. This can be seen in Figure 7.4 showing a specimen loaded at combined compression and shear at $\xi=22.5°$. The collapse of the cell structure is now less localized than without the ray cells. The stress-displacement relations are changed in the sense that the plateau stress values are increased, the shape of the curves being similar. As previously, the stress-strain curves for pure compression and the combined loading modes at $\xi=22.5°$ and $45°$ are very similar. The shear stresses when the ray cells are included are about the same as previously.

It can be concluded that the response predicted with the assumption of linear elastic behavior of the cell wall material shows clear similarities with experimental results. The overall cell structure deformations obtained, characterized by the cell collapses and strain localization, the shape of the stress-strain curves with a first linear region, a plateau region and finally a densification region, are all typical features of the behavior of real structures. There are naturally differences, mainly concerning the degree of localization, but it is surprising how well the structural response is captured by this very simple constitutive modelling. The unloading behavior when assuming purely elastic behavior is very different from the true response, however. It is seen from the unloading response in the diagrams of Figure 3.10 that the material behaves inelastically. A first approach to include inelastic behavior is to consider plastic response for the ray cells.
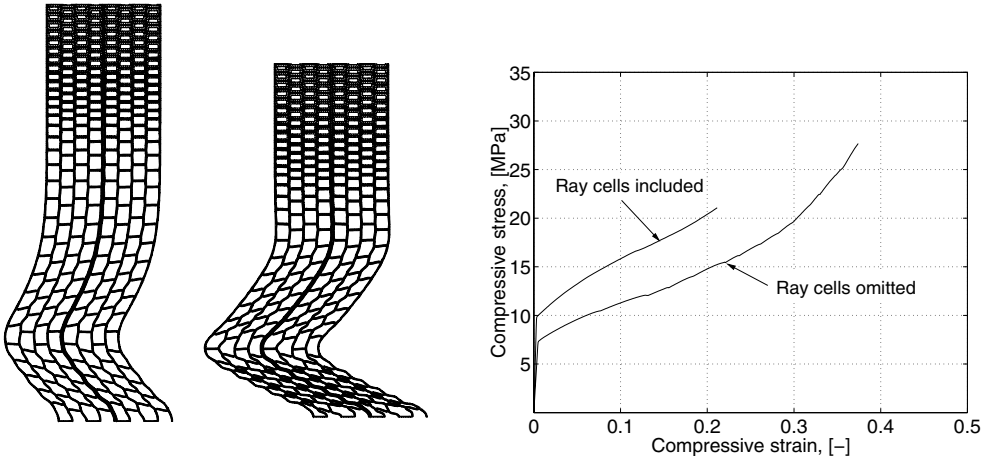
Figure 7.4: Deformations at an average normal strain of 5 % and 20 %, respectively, for combined radial compression and shear (ξ=22.5°) assuming elastic material behavior and with ray cells included in the model. Comparison between the stress-strain response with and without ray cells.

With this assumption, the localization phenomenon becomes more pronounced, cf. Figure 7.5 with 7.4. The plateau stress values will be lowered, with the plateau region being flatter, see Figure 7.6. The unloading response is still unrealistic, however.

Another approach for including inelastic material behavior in the modelling is to include microcracking as discussed previously. An example of the response obtained by this approach is given in Figure 7.7. The deformed cell structure at normal strains of 5 % and 20 % is shown together with a detailed view of the cell collapse and the microcracking. The loading mode is that of ξ=22.5°. The overall cell structure deformations are similar to the behavior obtained when including plastic behavior for the ray cells, the microcracking implying a more pronounced localization. The normal stress-strain curve differs from that obtained assuming pure elastic material, in that the plateau stress is consistently lower, the plateau region being flatter and an initial drop in yield stress occurring. These features all contribute to a better agreement with the real response.

The most sophisticated modelling approach considered in this study is combining the possibility of microcracking of the tracheid cells with elasto-plastic behavior of the ray cells. The deformation process for the cell structure obtained with this approach is for the case of combined loading at ξ=22.5° shown in Figure 7.8. As can be seen, this approach results in the most pronounced localization, closest to the real behavior of the cell structure of wood. Stress-strain curves obtained by this modelling approach are given in Figure 7.9. From these diagrams it can be seen that the response predicted is rather close to the experimental one during loading, whereas the response predicted for unloading still shows poor agreement with the real response. The curves for the
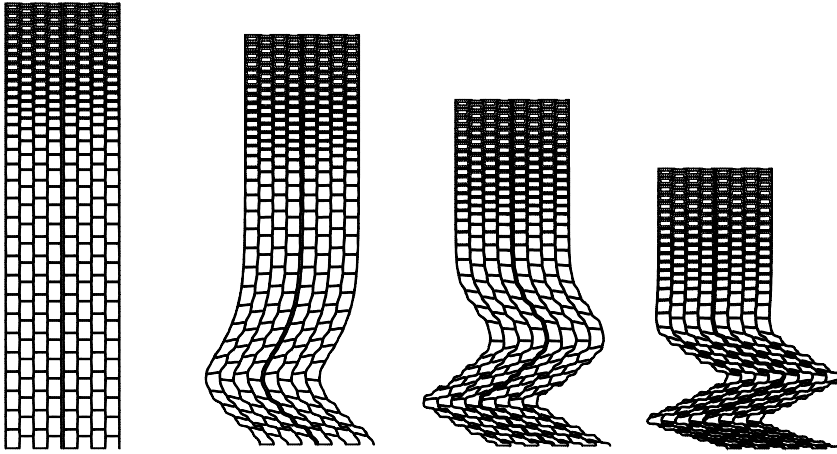
Figure 7.5: Deformation process for combined radial compression and shear at ξ=22.5° assuming elastic behavior for the tracheid cell material and elasto-plastic behavior for the ray cell material. From left to right: undeformed, average normal strain of 5 %, 20 % and 40 %, respectively.

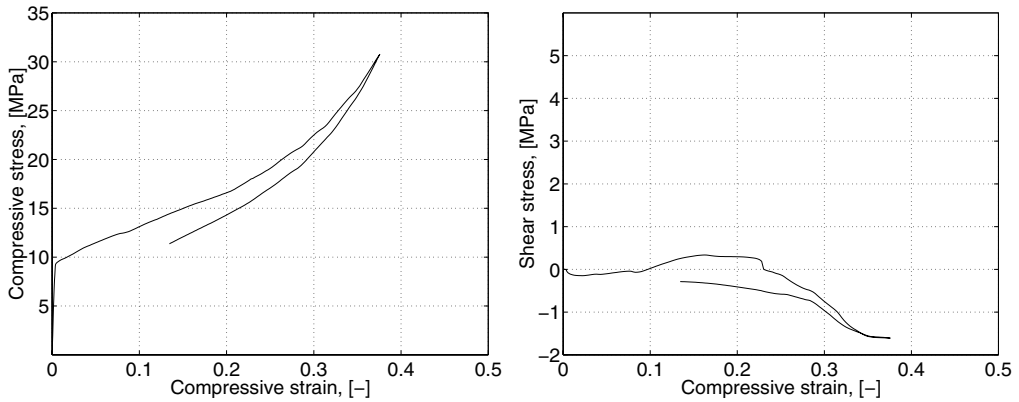Figure 7.6: Stress-strain curves for combined radial compression and shear at ξ=22.5° assuming elastic material behavior for the tracheid cell material and elasto-plastic behavior for the ray cell material.

different loading conditions are, as previously, very similar. The shear stresses were, for all cases, lower than 0.5 MPa in the strain interval considered.
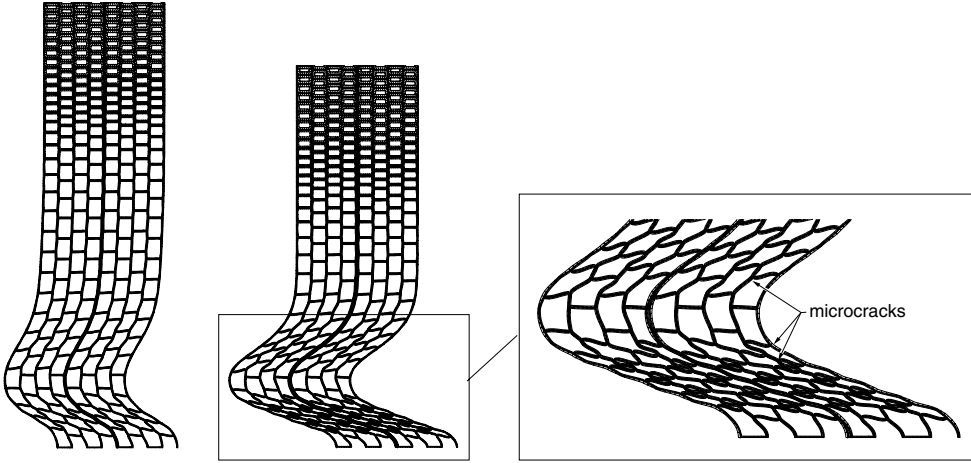
Figure 7.7: Cell structure deformations at strains of 5 % and 20 % when including microcracking in the modelling; the ray cells are assumed to behave elastically. The specimen was loaded in combined compression and shear at ξ=22.5°.

Figure 7.8: Deformation process for combined compression and shear at ξ=22.5° when including microcracking for the tracheid cells and elasto-plastic behavior for the ray cells. From left to right: undeformed, normal strain of 5 %, 20 % and 30 %, respectively

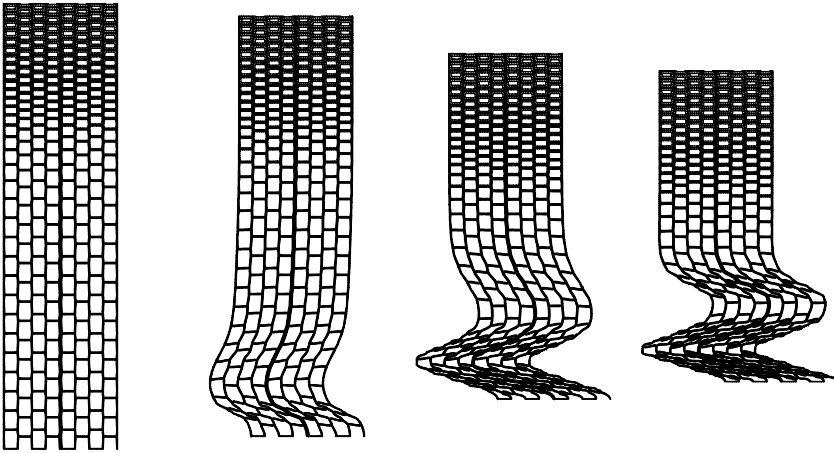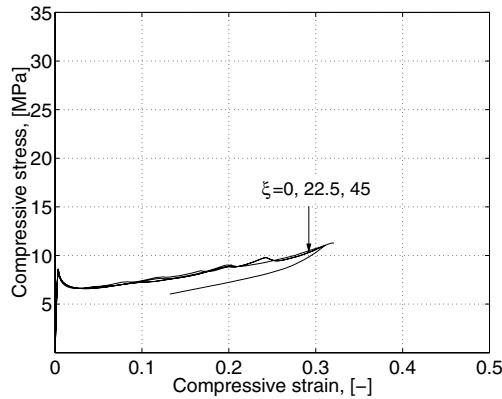Figure 7.9: Stress-strain curves obtained when including microcracking for the tracheid cells and elasto-plastic behavior for the ray cells.

A summary of the responses obtained by the different constitutive assumptions considered is given in Figure 7.10. In the figure, the deformed cell structures are shown at an average normal strain of about 5 % together with the corresponding stress-strain curves obtained. The loading mode considered is that of combined compression and shear at ξ=22.5°.

Clear differences between the different analyses can be seen concerning both the deformation of the cell structures and the stress-strain response obtained. The most realistic response is obtained when including microcracking and elasto-plastic behavior for the ray cells. The response in unloading, however, is unrealistic.

In the analyses presented so far, no friction was taken into account for the contact interaction in the cell lumens. The coefficient of friction does not seem to influence the response significantly, however. With the coefficient of friction set to 0.4, no difference could be seen as compared to the case with no friction assumed. The loading considered was that of combined loading at ξ=22.5°, and the material modelling considered included plastic response for the ray cells and microcracking of the tracheids. Nor was any change in response found for the extreme case of an infinitely high coefficient of friction (i. e. rough conditions with no slipping).

When assuming plane stress conditions, no differences could be seen regarding the cell structure deformations as compared to plane strain conditions. The only difference found was about 15 % lower plateau stress values than when assuming plane stress.

The influence on the normal stress-strain curve when changing the fracture energy can be seen in Figure 7.11. The variation in fracture energy was made by changing the softening displacement only, the strength values being constant. The lower the fracture energy, the lower the plateau stress values. The influence was not very large, however, and no distinct differences concerning the cell structure deformations could be seen.

1: Elastic behavior, no ray cells included.
2: Elastic behavior, ray calls included.
3: Elastic material behavior for tracheids, elasto-plastic behavior for ray cells.
4: Microcracking included for tracheids, elastic behavior for ray cells.
5: Microcracking included for tracheids, elasto-plastic behavior for ray cells.

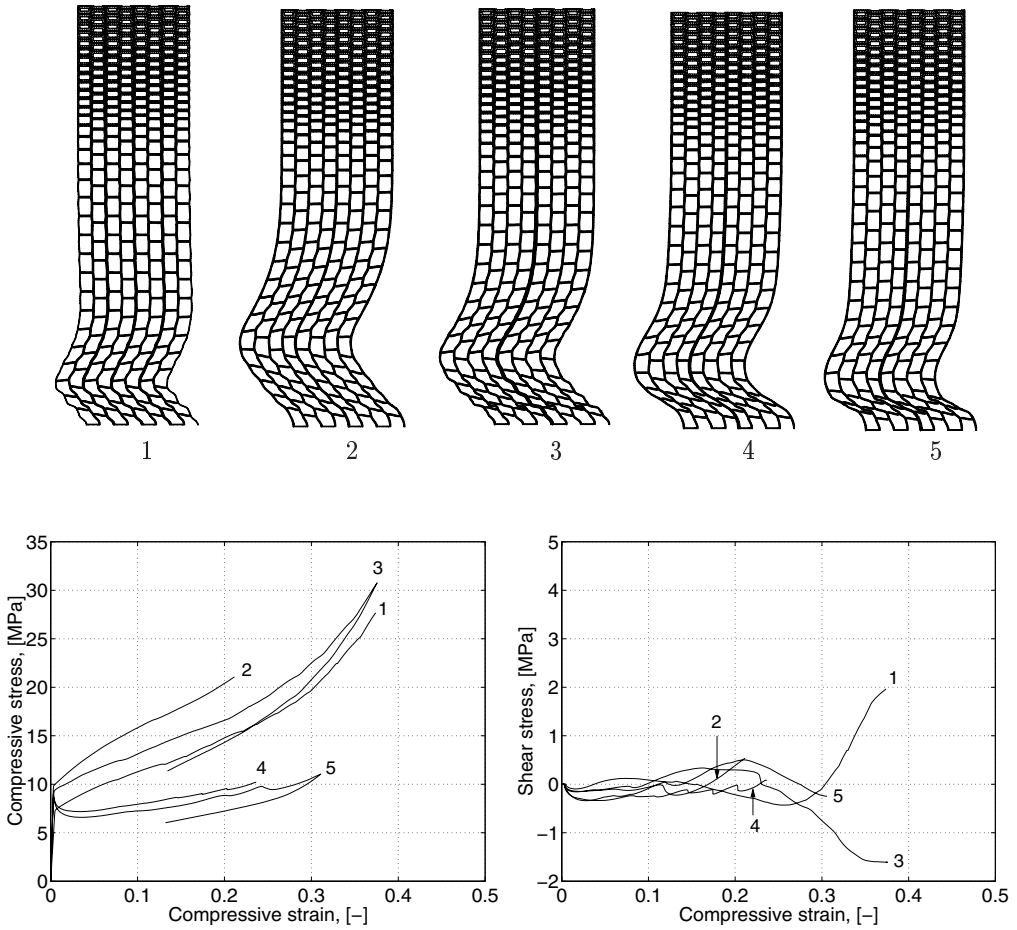Figure 7.10: Comparison of responses obtained by various constitutive modelling assumptions for combined loading at $\xi=22.5°$. Top: constitutive modelling assumptions. Middle: deformed cell structures. Lower: stress-strain curves.
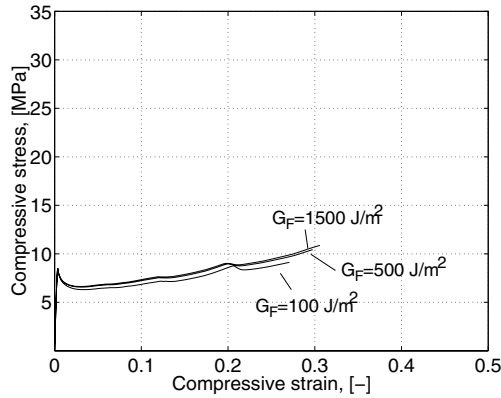
Figure 7.11: Comparison of response obtained by various values of the fracture energy. stress-strain curves for combined loading at ξ=22.5°.

7.5 Concluding Remarks

In this chapter the consequences of making different constitutive assumptions on the response in simulating the behavior of wood at the microstructural level when loaded perpendicular to the grain was investigated. Several rather crude assumptions and simplifications were made, and uncertainties concerning the material data, in particular the plastic and fracture mechanical properties, are present. It should be emphasized that the differences between the modelling approaches considered are strongly dependent on the material properties adopted. With other material data assumed, different results may be obtained. Nevertheless, some principal differences concerning the deformation processes and the stress-strain relations were illustrated for the different modelling techniques applied.

Even with the simple approach of assuming purely elastic behavior of the cell wall material, a response with clear similarities of the real behavior is obtained. The highly nonlinear response at the macrostructural level when loading wood in compression perpendicular to the grain is thus to a large extent related to geometrical effects at the microstructural level. The main divergence between the simulations and the real behavior of the wood microstructure when assuming elastic behavior concerns the degree of strain localization. In the real structure the deformations are strongly localized, the cell collapse occurs for one or a few cell rows at a time, whereas in the simulations the collapse is of a more global nature. When including the ray cells, the localization became less pronounced than was the case when neglecting them. It is obvious also from the unloading response that the material behaves inelastic, and in order to obtain more accurate predictions, inelastic material behavior needs to be taken into account. Plastic behavior of the ray cells as well as the microcracking of the tracheid cell were considered. With plastic behavior of the ray cells taken into account, more realistic results were obtained. The deformations were more localized and the plateau

region on the stress-strain curve became flatter. Similar behavior was observed when including the possibility of microcracking. The most accurate results were attained when combining plastic behavior of the ray cells with the possibility of microcracking of the tracheids. The agreement concerning the unloading response was, however, still poor. This is related to the adopted material properties, and better agreement may be achieved using different material data. The unloading behavior for the fracture mechanics model used, assuming the crack closing path to revert to the origin, certainly influences the unloading response as well. The results of the simulations also indicate the friction assumed in the cell lumen to have a small or negligible influence on the response.

The simulations presented were performed assuming fictitious periodic cell structures. It is possible that somewhat different results would be obtained using real cell structure models. Simulations of the behaviour of real structures should be performed and compared with results from microscopic investigations. This will enable a better possibility to verify constitutive assumptions in the modelling.

It is obvious that more experimental work needs to be carried out in order to better determine the mechanical properties of wood at the microstructural level. With precise material data available the numerical modelling can be further refined, verified and optimized, facilitating more accurate simulations of the microstuctural performance of wood.

Chapter 8

Concluding Remarks

8.1 Conclusions

The extremely large energy consumption required is a major drawback to the use of the defibration process in manufacturing mechanical pulp. Large amounts of energy could be saved if the mechanics of the defibration process were better understood. Numerical simulations by means of the finite element method represent a powerful tool that can be used to analyse different defibration methods. Numerical simulations of such processes require proper constitutive models, wood's being a very advanced material from a mechanical point of view. The thesis deals with various aspects of the constitutive modelling involved in simulating disintegration and defibration processes of wood. The major aim is to gain increased knowledge of material modelling approaches suitable for numerical simulations of this type as well as to acquire greater knowledge of the complex mechanical behaviour of wood and of the mechanics of initial defibration.

A substantial part of the present study concerns experimental work. Valuable information about the mechanical behaviour of wood, useful for further analysis of initial defibration processes, was provided by the experiments that were conducted. In the chip shearing tests, the deformation and fracture processes of wood chips subjected to various well-defined loading modes were studied. The test setup employed was chosen on the basis of the geometry of typical refiner segments. In particular, the influence of specimen orientation versus loading direction as well as the influence of the earlywood and latewood configuration of the specimens, were investigated. It was shown that the mechanical behaviour of wood loaded perpendicular to the grain is very complex. When earlywood is subjected to compression, its material behaviour is characterized by the development of cracks in combination with large volumetric changes. One of the most important observations made was that the mechanical properties of latewood differ markedly from those of earlywood. Latewood is much stiffer than earlywood, for which zones of localized deformations can develop when subjected to compression perpendicular to the grain. The failure zones develop through collapse of the cells structure due to cell wall buckling processes, which lead to the earlywood cells gradually being crushed.

It was concluded that specimen orientation and earlywood and latewood configuration have a strong influence on the failure mode and on energy consumption. The

energy needed to break the specimen may differ up to a factor of ten, depending on the specimen's orientation and configuration. In addition to use of the main loading device, adopted for the major part of the test programme, certain tests were performed using a knife loading setup instead. It was concluded that the design of the loading equipment strongly influences both the failure process and energy consumption.

The mechanical behaviour of wood loaded by radial compression and by rolling shear was investigated. In addition to pure radial compression and pure shear, three different types of combined loading were considered. In the different types of combined loading employed, the effect of shear deformation on the compressive response was found to be rather small, although the initial yield stress was somewhat higher and the plateau region flatter in the case of combined loading than of pure compression. The shear stresses were low throughout. The combination of compression and shear loading was found to require about the same energy as pure radial compression for achieving a given normal strain. The cell collapse which the different types of combined loading produced appeared to be more well-defined, however, than that which pure radial compression produced, all the cells being collapsed in a similar way in the former case.

It was likewise concluded that the moisture content has a strong influence on the mechanical properties of wood. In the chip shearing tests, dry specimens were found to be much more brittle than wet specimens; which could be deformed much more without cracking. The load displacement curves also indicated that the initial stiffness was much higher for the dry than for the wet specimens. The load capacity was also significantly lower for the wet specimens than for the dry. In the combined compression and shear tests, the general behaviour of the dry and of the wet specimens was found to be similar, although clear differences in initial stiffness and in plateau stress could be seen. Both the initial stiffness and the plateau stress were about 50 % lower for the wet specimens than for the dry ones.

From the results of the tensile tests it could be concluded that the fracture energy, the tensile strength and the modulus of elasticity increase as loading rates become higher. The fracture energy ranged from about 170 J/m² to 440 J/m² in the loading rate interval studied (0.001-10 mm/s). When the loading rate is increased by a factor of ten, the tensile strength increases by about 10-15 %. The modulus of elasticity is less rate-dependent than the fracture energy and tensile strength are, its increasing only slightly as the loading rates become higher.

Two main approaches may be applied in modelling the wooden material when numerical analyses of initial defibration processes are to be performed. One approach is to use continuum models based on smeared material properties. The other is to develop models of the cellular microstructure in which the individual fibres are modelled. The latter approach is the most general one, showing a higher degree of resolution. It has the disadvantage, however, of giving rise to extremely large models, difficult to handle with the computer resources available today unless very small pieces of wood are studied. Although a continuum modelling approach allows the deformation and fracturing of larger wood pieces to be analysed, it does not permit the deformation and fracturing of the individual fibres to be studied. The continuum approach is the most suitable one for simulating the initial breakdown of the wood chips in a refiner. At later stages of the defibration process, modelling at the microstructural level is needed

for analysing the deformation process of the individual fibres.

In the thesis, both continuum modelling and microstructural modelling are dealt with. Numerical simulations, related to initial defibration processes are presented, using each of these two approaches and comparisons are made with experimental results. The numerical simulations were performed using the finite element method. The procedure employed for the simulations is outlined, the finite element formulation, the solution technique and the implementation of a mixed-mode fracture mechanics model are described.

The continuum modelling approach involves use of a foam plasticity model and a fictitious crack model. The inhomogeneity of the material is taken into account by subdividing the growth ring into several layers, differing in their stiffness and strength properties. Several simulations of the chip shearing tests and the combined compression and shear tests were performed using this modelling approach. Comparing the results of the simulations with the experimental results, it was found that the deformation and fracture processes predicted by the simulations agreed closely with the experimental results. The location of the fracture zones and the large deformations of the earlywood zones were captured by the modelling employed. The differences between the results from the simulations and the experiments concern mainly the load displacement relations, and may to some extent be explained in terms of various assumptions that were made in order to simplify the analyses. The main problem of the modelling employed is the use of an isotropic plasticity model which implies that the extremely low modulus in rolling shear (in relation to the modulus of elasticity) cannot be captured.

A study of the effect which the choice of material properties has on the response was carried out. It was concluded that elastic stiffness has only a very small influence, whereas the plastic properties of the earlywood and the fracturing properties have a very strong influence on the response.

The effect of the loading rate on the failure process and on the energy consumption needed to break the specimen was also investigated. Loading rates ranging from 0.01 m/s to 50 m/s were considered. The effect of the loading rate on the failure process and on the energy consumption differed significantly between the case of dry and saturated wood. When assuming material properties for wood in dry condition (with no rate effects considered for the material) the effect of the loading rate was rather small. The response in the case of saturated wood was greatly influenced by the loading rate, however. The higher the loading rate, the higher the forces involved. At a loading rate of 50 m/s the maximum shear forces were about three and six times as high, respectively as the corresponding static results for the two types of specimens considered. The loading rate also had a strong effect on the energy consumption needed to break the specimen. The total energy consumption ranged from 71 to 231 mJ and 22 to 243 mJ for the two types of specimens considered.

Analyses illustrating the effect of the knife design in wood cutting processes were also carried out. The effects of the knife angle and clearance angle being studied.

At the microstructural level, the consequences of making different constitutive assumptions regarding the cell wall material were investigated, the assumptions ranging from the basic assumption of linear elasticity to more sophisticated approaches taking account both of plastic behavior as well as microcracking. Although some of the as-

sumptions and simplifications were rather crude and there were various uncertainties concerning the material data, basic differences in the deformation processes and the stress-strain relations could be shown for the various modelling techniques.

Even with the simple approach of assuming purely elastic behavior of the cell wall material, a response showing clear similarities to real behavior was obtained. The highly nonlinear response at the macrostructural level obtained when wood is loaded in compression perpendicular to the grain appears to a large extent to be related to geometrical effects at the microstructural level. The main discrepancy between the simulations and the real behavior of the wood microstructure when elastic behavior is assumed concerns the degree of strain localization. Whereas in a real structure the deformations are strongly localized, in the simulations the collapse is of a more global nature. When plastic behavior of the ray cells was taken into account, more realistic results were obtained. The deformations then were more localized and the plateau region on the stress-strain curve became flatter. Similar behavior was observed when the possibility of microcracking was included. The most accurate results were attained when plastic behavior of the ray cells was combined with the possibility of microcracking of the tracheids. There was poor agreement, however, concerning the unloading response. Better agreement could possibly be achieved by using different material data and introducing a more realistic unloading behavior into the fracture mechanics model. An additional result of the simulations was that the friction assumed in the cell lumen was found to have a small or negligible influence on the response.

8.2   Future Work

Numerical simulation of defibration processes requires proper constitutive modelling. From a mechanical point of view, wood is a very complex material. Its elastic, plastic and fracture mechanical properties, as well as its anisotropy and inhomogeneity, need to be taken into account if sufficient accuracy is to be obtained. Constitutive models that take account of all these properties are not available today. The foam plasticity model adopted in the present study has the disadvantage of being based on isotropic material behavior. The study deals only with wood loaded perpendicular to the grain. Since the difference in response between loading in the tangential and the radial directions is not very great, an isotropic foam plasticity model was employed, good agreement between the simulations and the experiments being obtained. However, in order to be able to study arbitrary loading conditions and loading directions, account must also be taken of the anisotropy of the material.

The modelling of the fracture mechanical behavior may need to be modified when the behavior in rolling shear and mixed mode conditions is better established. There is thus a need for more accurate constitutive models than those adopted here. In particular, the development of an anisotropic plasticity model suitable for wood should be given high priority in future work. The present procedure of introducing the crack elements manually is also somewhat cumbersome. Preferably some kind of automatic generation of crack elements should be employed.

It is desirable that simulations of the microstructural behaviour of real cell struc-

tures are performed and that comparisons are made with microscopic investigations. This will enable a better possibility to verify the various constitutive assumptions made in the modelling, and further, the differences obtained between using periodic fictitious cell structure models and real structures to be investigated.

Studying the complete defibration process in detail from wood chips to suitable fibres is a great challenge. A lesser task, though of considerable interest, is to perform finite element simulations for determining the flexibility properties of various fibre types. Fibre types of particular interest are those with cracks in the micro-fibrillar direction, with collapsed lumens, and fibres with "kinks", i.e. with folded cell walls.

It is important to bear in mind that all numerical simulations need to be verified by adequate experimental tests. In addition, experimental material tests concerned with elastic, plastic and fracture mechanical characterization, should be carried out for obtaining input for the material models used in simulations and for verifying the constitutive relations adopted. One of the most important observations made in the experimental study carried out here was that of the importance of taking account of differences between earlywood and latewood in applications such as those considered. Unfortunately, not much experimental work has been performed to determine the mechanical properties of earlywood and latewood separately. Such experiments should be given a very high priority in the future. They can require special specimen preparation and may also involve the need of developing completely new test methods. The mechanical properties at the wood cell level also need to be better established so that more accurate and reliable simulations of the microstructural performance of wood can be performed.

When more accurate and reliable material data become available, the numerical models can be further refined, verified and optimized. This will facilitate more accurate simulations, useful for improving and developing various industrial wood disintegration techniques, in particular, those used in mechanical pulping.

Bibliography

[1] Atack, D. and May, W. D. *Mechanical reduction of chips by double-disc refining.* Pulp and Paper Magazine of Canada, Conv. Issue, T-75, 1963.

[2] Atack, D., May, W. D., Morris, E. L. and Sproule, R. N. *The energy of tensile and cleavage fracture of black spruce.* Tappi, 44:8, pp. 555-567, 1961.

[3] Atack, D., Stationwala, M. I. and Karnis, A. *What happens in refining.* Pulp and Paper Magazine of Canada, 85:12, pp. 119-124, 1984.

[4] Atalla, R. H. and Wahren, D. *On the energy requirement in refining.* Tappi, 63:6, pp. 121-122, 1980.

[5] Barrett, J. D. *Fracture mechanics and the design of wood structures.* A Royal Society Discussion in Fracture Mechanics in Design and Service, pp. 217-226, London 1981.

[6] Bathe, K. J. *Finite element procedures.* Prentice Hall, Englewood Cliffs, New Jersey 1996.

[7] Bodig, J. and Jayne, B. A. *Mechanics of wood and wood composites.* Van Nostrand Reinhold, New York 1982.

[8] Boström, L. *Method for determination of the softening behaviour of wood and the applicability of a nonlinear fracture mechanics model.* Report TVBM-1012, Ph.D. thesis, Lund Institute of Technology, Division of Building Materials, Lund 1992.

[9] Dinwoodie, J. M. *Timber, its nature and behaviour.* Van Nostrand Reinhold, New York 1981.

[10] Dinwoodie, J. M. *Wood. Natures cellular, polymeric fibre-composite.* The Institute of Metals, London 1989.

[11] Falk, B., Jackson, M. and Danielsson, O. *The use of single and double disc refiner configurations for the production of TMP for filled super calendered and light weight coated grades.* Proc. International Mechanical Pulping Conference in Vancouver, pp. 137-143, 1987.

[12] Fengel, D. *The Ultrastructure of cellulose from wood, Part 1: Wood as the basic material for the isolation of cellulose.* Wood Science and Technology, 3, pp. 203-217, 1969.

[13] Fengel, D. *The physics and chemistry of wood pulp fibres.* Tappi, pp. 74-97, 1970.

[14] Frazier, W., C. and Williams, G., J. *Reduction of specific energy in mechanical pulping by axial precompression of wood.* Pulp and Paper Magazine of Canada, 83:6, pp. 87-92, 1982.

[15] Gerhards, C. G. *Effect of moisture content and temperature on the mechanical properties of wood: an analysis of immediate effects.* Wood and Fiber, 14:1, pp. 4-36, 1982.

[16] Gibson, L. J. and Ashby, M. F. *Cellular solids: structure and properties.* Pergamon Press, New York, 1988.

[17] Grönlund, A. *Wood machining.* Träteknik Centrum, 1985. (In Swedish).

[18] Gustafsson, P. J. *Fracture mechanics studies of non-yielding materials like concrete: modelling of tensile fracture and applied strength analyses.* Report TVBM-1007, Ph.D. thesis, Lund Institute of Technology, Division of Building Materials, Lund 1985.

[19] Gustafsson, P. J. *Some test methods for fracture mechanics properties of wood and wood adhesive joints.* Proc. RILEM TC 133-TF Workshop in Bordeaux, 1992.

[20] Gustafsson, P. J. and Enquist, B. *Strength of wooden beam at right angle notch.* Report TVSM-7042, Lund Institute of Technology, Division of Structural Mechanics, Lund 1988. (In Swedish).

[21] Hartler, N. *Aspects on curled and microcompressed fibers.* Nordic Pulp & Paper Research Journal, 1:4, 1995.

[22] Hartler, N. *Some studies on the nature of chip damage.* Svensk Papperstidning, 66:11, pp. 443-453, 1963.

[23] Heikkurinen, A., Vaarasalo, J. and Karnis, A. *Effect of initial defiberization on the properties of refiner mechanical pulp.* Journal of Pulp and Paper Science, 19:3, pp. J119-J124, 1993.

[24] Hibbitt, Karlsson & Sorensen, Inc. *ABAQUS, Version 5.6.* Pawtucket, RI., USA 1996.

[25] Hilber, H. M., Hughes, T. J. R. and Taylor, R. L. *Collocation, dissipation and 'overshoot' for time integration schemes in structural dynamics.* Earthquake Engineering and Structural Dynamics, 6, pp. 99-117, 1978.

[26] Hill, R. *The mathematical theory of plasticity.* Oxford University Press, London 1950.

[27] Hillerborg, A., Modeer, M. and Petersson, P. E. *Analysis of crack formation and crack growth in concrete by means of fracture mechanics and finite elements.* Cement and Concrete Research, 6, pp. 773-782, 1976.

[28] Holmberg, S. *Deformation and fracture of wood in initial defibration processes.* Report TVSM-3019, Lund Institute of Technology, Division of Structural Mechanics, Lund 1996.

[29] Holmberg, S., Persson, K. and Petersson, H. *Nonlinear mechanical behaviour and analysis of wood and fibre materials.* Accepted 1998 for publication in Computers and Structures.

[30] Holmberg, S. and Petersson, H. *Numerical and experimental simulations of initial defibration processes.* Proc. International Mechanical Pulping Conference in Stockholm, pp. 365-369, 1997.

[31] Holmberg, S. and Petersson, H. *Numerical simulations and experimental studies of large deformation and fracturing processes in wood.* Proc. Fifth International Conference on Computational Plasticity in Barcelona, pp. 929-936, 1997.

[32] Holmberg, S. and Petersson, H. *Numerical simulations of initial defibration of wood.* Proc. Ninth Nordic Seminar on Computational Mechanics in Lyngby, pp. 133-136, 1996.

[33] Holmberg, S., Enquist B and Petersson, H. *Initial defibration of wood - An experimental study of large deformations and fracturing.* Report TVSM-7124, Lund Institute of Technology, Division of Structural Mechanics, Lund 1998.

[34] Holmberg, S., Petersson, H. and Serrano, E. *Numerical simulations of initial defibration processes.* Report TVSM-7092, Lund Institute of Technology, Division of Structural Mechanics, Lund 1994.

[35] Htun, M., Salmén, L. and Eriksson, L. *A better understanding of wood as a material - a way to increased energy efficiency when making mechanical pulps?* In Pilavachi, P.A., editor, Energy efficiency in process technology, Elsevier Applied Science, 1993.

[36] Hughes, T. J. R. *Numerical implementation of constitutive models: rate-independent deviatoric plasticity.* In Asaro, R.J., Nemat-Nasser, S. and Hegemier, G.A., editors, Theoretical foundation for large-scale computations for nonlinear material behaviour, Martinus Nijhoff Publishers, 1984.

[37] Hughes, T. J. R. and Winget, J. *Finite rotation effects in numerical integration of rate constitutive equations arising in large-deformation analysis.* International Journal of Numerical Methods in Engineering, 15, pp. 1862-1867, 1980.

[38] Hägglund, T. H. and Höglund, H. *Recent development of CTMP for absorbent products.* The New Nonwoven World 1:1 pp. 93, 1992.

[39] Höglund, H. *Tomorrows challenges for mechanical pulp.* Proc. International Mechanical Pulping Conference in Stockholm, pp. 29-36, 1997.

[40] Höglund, H., Bäck, R., Falk, B. and Jackson, M. *Thermopulp - a new energy efficient mechanical pulping system.* Proc. International Mechanical Pulping Conference in Canada, pp. 213-225, 1995.

[41] Höglund, H. and Wilhelmsson, K. *The product must determine the choice of wood type in mechanical pulping.* Proc. International Mechanical Pulping Conference in Oslo, pp. 1-22, 1993.

[42] Johansson, L., Peng, F., Simonsson, R. and Granfeldt, T. *The effect of screw press pretreatment in CTMP pulping process.* Proc. International Mechanical Pulping Conference in Stockholm, pp. 371-375, 1997.

[43] Johnson, J. A. *Crack initiation in wood plates.* Wood Science, 6:2, pp. 151-158, 1973.

[44] Koch, P. *Wood machining processes.* Ronald Press, New York, 1976.

[45] Kollmann, F. F. P. and Côté, W. A. *Principles of wood science and technology, vol. 1.* Springer Verlag, Berlin 1968.

[46] Koran, Z. *Energy consumption in mechanical fibre separation as a function of temperature.* Transactions of the technical section, CPPA 7:2, pp. TR40-TR44, 1981.

[47] Koran, Z. *Electron microscopy of radial tracheid surfaces of black spruce separated by tensile failure at various temperatures.* Tappi, 50:2, pp. 60-67, 1967.

[48] Koran, Z. *Electron microscopy of tangential tracheid surfaces of black spruce separated by tensile failure at various temperatures.* Svensk Papperstidning, 17:71, pp. 567-576, 1968.

[49] Koran, Z. *Tensile properties of spruce under different conditions.* Wood and Fiber, 11:1, pp. 38-49, 1979.

[50] Koran, Z. and Salmen, L. *Shear strength analysis of spruce in a controlled environment.* Svensk Papperstidning, 9:88, pp. R90-R95, 1985.

[51] Krauss, T. P., Shure, L. and Little, J. N. *Signal processing toolbox, for use with MATLAB.* The MathWorks Inc. Natick, Mass., USA 1994.

[52] Krenk, S. *Non-linear analysis with finite elements.* University of Aalborg, Dept. of Building Technology and Structural Engineering, Aalborg 1993.

[53] Kretschman, D. *The effect of moisture content on mode I fracture energy for a three point bending specimen.* Proc. RILEM TC-133 Workshop in Bordeaux, 1992.

[54] Lamb, G. E. R. *Energy consumption in mechanical pulping.* Tappi, 45:5, pp. 364-368, 1962.

[55] Larsen, H. J. and Gustafsson, P. J. *The fracture energy of wood in tension perpendicular to the grain - results from a joint testing project.* Proc. CIB-W18A meeting in Lisbon, paper 23-19-2, 1990. (Errata in Proc. of CIB-W18A meeting in Oxford, 1991.)

[56] Leider, P. J. and Nissan, A. H. *Understanding the disk refiner.* Tappi, 60:10, pp. 85-89, 1977.

[57] Malvern, L. E. *Introduction to the mechanics of a continuous medium.* Prentice-Hall, Englewood Cliffs, New Jersey 1969.

[58] Marton, R., Tsujimoto, N. and Eskelinen, E. *Energy consumption in thermomechanical pulping.* Tappi, 64:8, pp. 71-74, 1981.

[59] May, W. D. *A theory of chip refining-the origin of fiber length.* Pulp and Paper Magazine of Canada, 74:1, pp. 70-78, 1973.

[60] Miles, K. B. and May, W. D. *A new plate for chip refining.* Journal of Pulp and Paper Science, 10:2, pp. 36-43, 1984.

[61] Münster, H. and Dahlqvist, G. *Operational experience with the first commercial high speed refiner at Perlen Papier AG, Switzerland.* Proc. International Mechanical Pulping Conference in Canada, pp. 197-202, 1995.

[62] Murton, K. D. *Effect of chip compression on TMP pulp properties.* Appita, 49:5, pp. 313-318, 1995.

[63] Olejniczak, P. and Gustafsson, P. J. *Rate effect in tangential tension fracture softening performance.* Proc. COST 508 Wood Mechanics Workshop on Service Life Assessment of Wooden Structures in Espoo Finland, pp. 137-147, 1994.

[64] Ottosen, P. and Petersson, H. *Introduction to the finite element method.* Prentice Hall, London 1992.

[65] Owen, D. R. J. and Hinton, E. *Finite elements in plasticity: theory and practice.* Pineridge Press Limited, Swansea, U.K. 1980.

[66] Persson, K. *Modelling of wood properties by a micromechanical approach.* Report TVSM-3020, Lund Institute of Technology, Division of Structural Mechanics, Lund 1997.

[67] Persson, K., Gustafsson, P.J. and Petersson, H. *Influence of plastic dissipation on apparent fracture energy determined by a three point bending test.* Proc. COST 508 WG Workshop on Wood: Plasticity and Damage in Limerick Ireland, 1993.

[68] Petersson, H. *Analysis of fracture propagation.* Proc. COST 508 Wood Mechanics Workshop in Bordeaux, 1992.

[69] Petersson, H., Persson, K. and Holmberg, S. *Non-linear mechanical behaviour of cellular solids.* Proc. Fourth World Congress on Computational Mechanics in Buenos Aires, 1998.

[70] Preston, R. D. *The physical biology of plant cell walls.* Chapman and Hall, 1974.

[71] Riberholt, H., Enquist, B., Gustafsson, P. J. and Jensen, R. B. *Timber beams notched at the support.* Report TVSM-7071, Lund Institute of Technology, Division of Structural Mechanics, Lund 1992.

[72] Ristinmaa, M. and Ottosen, N. *Large strain plasticity and thermodynamics.* Report TFHF-3072, Lund Institute of Technology, Division of Solid Mechanics, Lund 1996.

[73] Rug, W., Badstube, M. and Schone, W. *Determination of the fracture energie of wood for tension perpendicular to the grain.* Proc. CIB-W18A meeting in Lisbon, paper 23-19-1, 1990.

[74] Sabourin, M., Xu, E. and Musselman, R. *Evaluation of refiner disc speed, plate design and consistency on high pressure/low residence (RTS) TMP pulps.* Proc. International Mechanical Pulping Conference in Stockholm, pp. 241-249, 1997.

[75] Schreyer, H. L., Zuo, Q. H. and Maji, A. K. *Anisotropic plasticity model for foams and honeycombs.* Journal of Engineering Mechanics, 120:9, pp. 1913-1930, 1994.

[76] Smith, I. *Influence of moisture content on mode I fracture energy of plantation-grown Red Pine* Proc. IUFRO/5.02 Timber Engineering Meeting in Bordeaux, pp. 325-340, 1992.

[77] de Souza Neta, E. A., Perić, D., Dutko, M. and Owen, D. R. J. *Finite strain implementation of an elastoplastic model for crushable foam.* In Wiberg, N-E., editor, Advances in Finite Element Technology, CIMNE, Barcelona, 1995.

[78] Stationwala, M. I., Karnis, A. *Pulp grinding - a new method for producing mechanical pulp.* Tappi, 73:12, pp. 187-195, 1990.

[79] Stationwala, M. I., Miles, K., B. and Karnis, A. *The effect of first stage refining condition on pulp properties and energy consumption.* Proc. International Mechanical Pulping Conference in Minneapolis, pp. 321-327, 1991.

[80] Stefansson, F. *Mechanical properties of wood at microstructural level.* Report TVSM-5057, M. Sc. diploma thesis, Lund Institute of Technology, Division of Structural Mechanics, Lund 1995.

[81] Sundholm, J., Heikurinen, A. and Mannström, B. *The role of rate of rotation and frequency in refiner mechanical pulping.* Proc. International Mechanical Pulping Conference in Vancouver, pp. 45-51, 1987.

[82] Sveriges Skogsindustriförbund. *Paper and pulp.* SSIF Förlag 1989. (In Swedish).

[83] Uhmeier, A. *Some aspects on solid and fluid mechanics of wood in relation to mechanical pulping.* Ph.D. thesis, Royal Institute of Technology, Division of Paper Technology, Stockholm 1995.

[84] Uhmeier, A., Vansteenkiste, D. and Salmén, L. *Large transverse compression of small specimens of wet spruce.* Proc. COST 508 Wood Mechanics Workshop in Espoo, 1994.

[85] Valentin, G. H., Boström, L., Gustafsson, P. J., Ranta-Maunus, A. and Gowda, S. *Application of fracture mechanics to timber structures RILEM state-of-the-art report.* Technical Research Centre of Finland, Espoo, Research Notes 1262, 1991.

[86] Vansteenkiste, D. *Study concerning the influence of fibre morphology on the deformation and damage at large plastic deformations.* STFI report, 1994.

[87] Wernersson, H. *Fracture characterization of wood adhesive joints.* Report TVSM-1006, Ph.D. thesis, Lund Institute of Technology, Division of Structural Mechanics, Lund 1994.

[88] Wigge, B. *Unpublished experimental data.* Institutionen för Skogsproduktion, SLU, Garpenberg, Sweden.

[89] Zienkiewicz, O. C. and Taylor, R. L. *The Finite Element Method, fourth edition, Vol. 1.* McGraw-Hill, London 1989.

[90] Zienkiewicz, O. C. and Taylor, R. L. *The Finite Element Method, fourth edition, Vol. 2.* McGraw-Hill, London 1991.

Appendix A

Experimental Results

A.1   Combined Radial Compression and Shear

The stress-strain response for all the individual tests of the combined radial compression and shear tests of Section 3.2 are given in the following. The curves show filtered response. The filtering was made using the MATLAB signal processing toolbox [51] (Butterworth filtering). Examples of typical recorded stress-strain curves and the corresponding filtered response are given in Figure A.1. Figures A.2-A.3 show the results for test series Ad-Ed, Figures A.4-A.5 for test series Aw-Ew and Figure A.6 for test series Fd and Fw. The mean value curves for each test series are also given (dashed curves). The test conditions for the different test series are defined in Table 3.1. A summary of the conditions is given in Table A.1 below.

Table A.1: Summary of test conditions for the different test series.

Test series	Moisture content [%]	Loading mode, ξ [°]	Number of tests successful/total
Ad	12	0	5/5
Bd	12	22.5	5/5
Cd	12	45.0	5/5
Dd	12	67.5	5/7
Ed	12	90.0	5/7
Aw	28	0	5/5
Bw	28	22.5	5/5
Cw	28	45.0	5/5
Dw	28	67.5	6/6
Ew	28	90.0	0/4
Fd	12	0	6/6
Fw	28	0	5/6
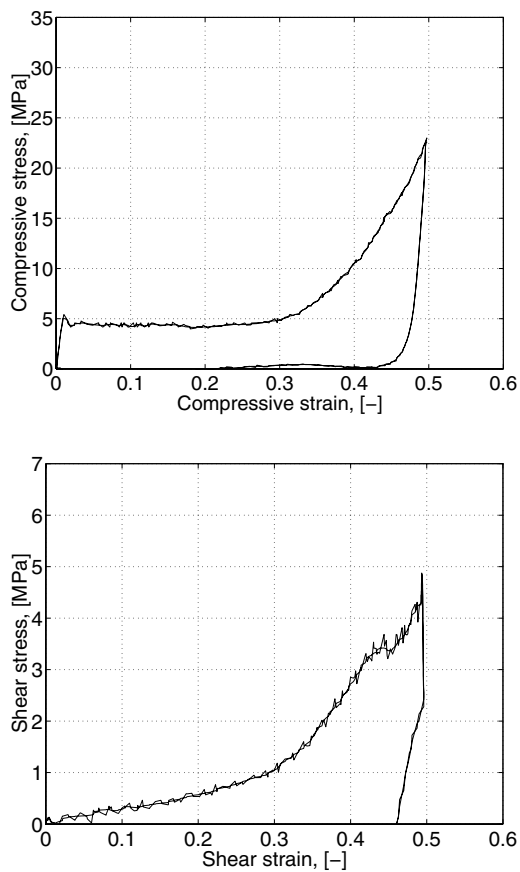
Figure A.1: Typical recorded stress-strain curves and the corresponding filtered curves.
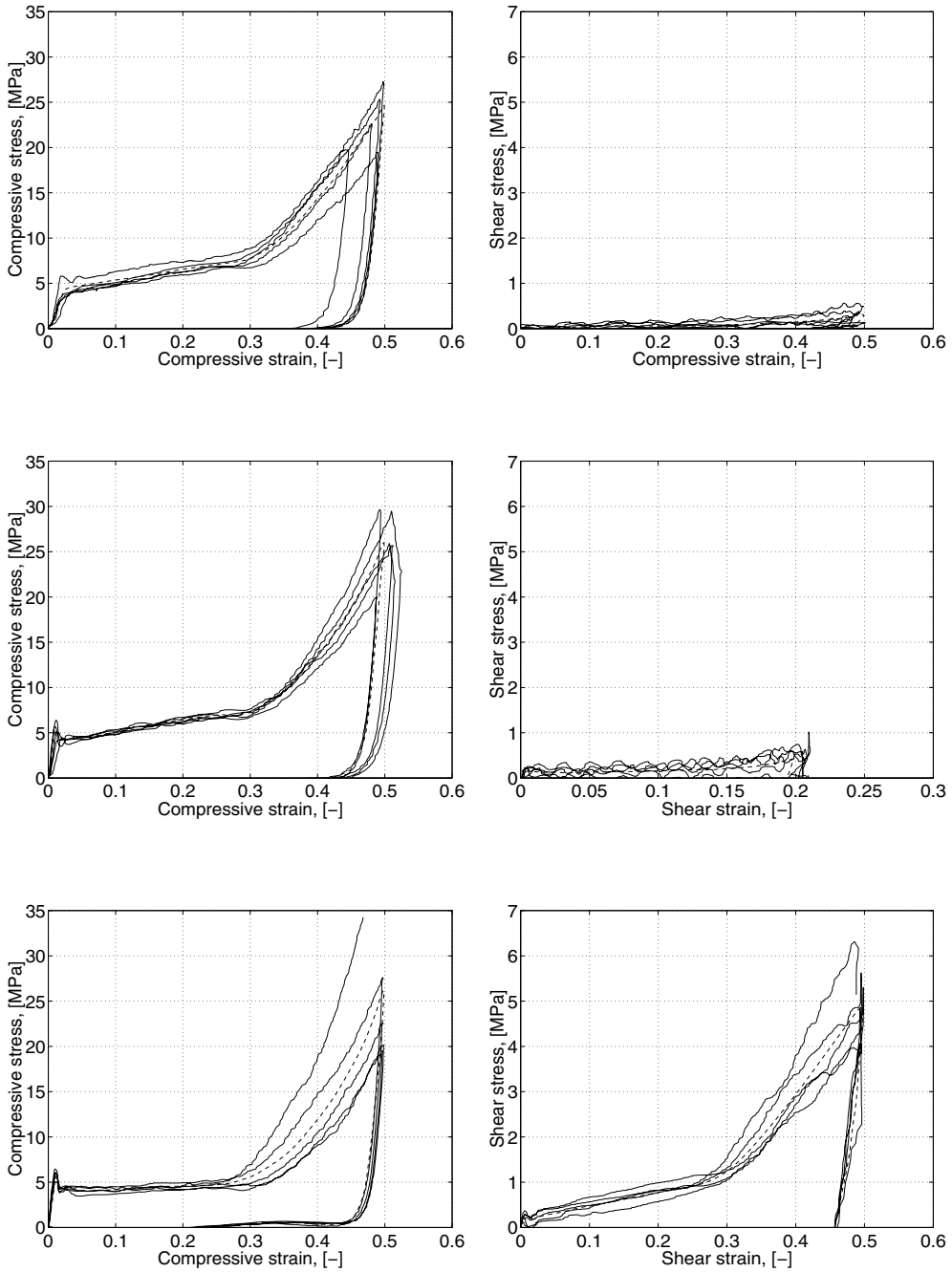
Figure A.2: Stress-strain curves for test series Ad (top), Bd (middle) and Cd (lower). The dashed lines are mean-value curves.
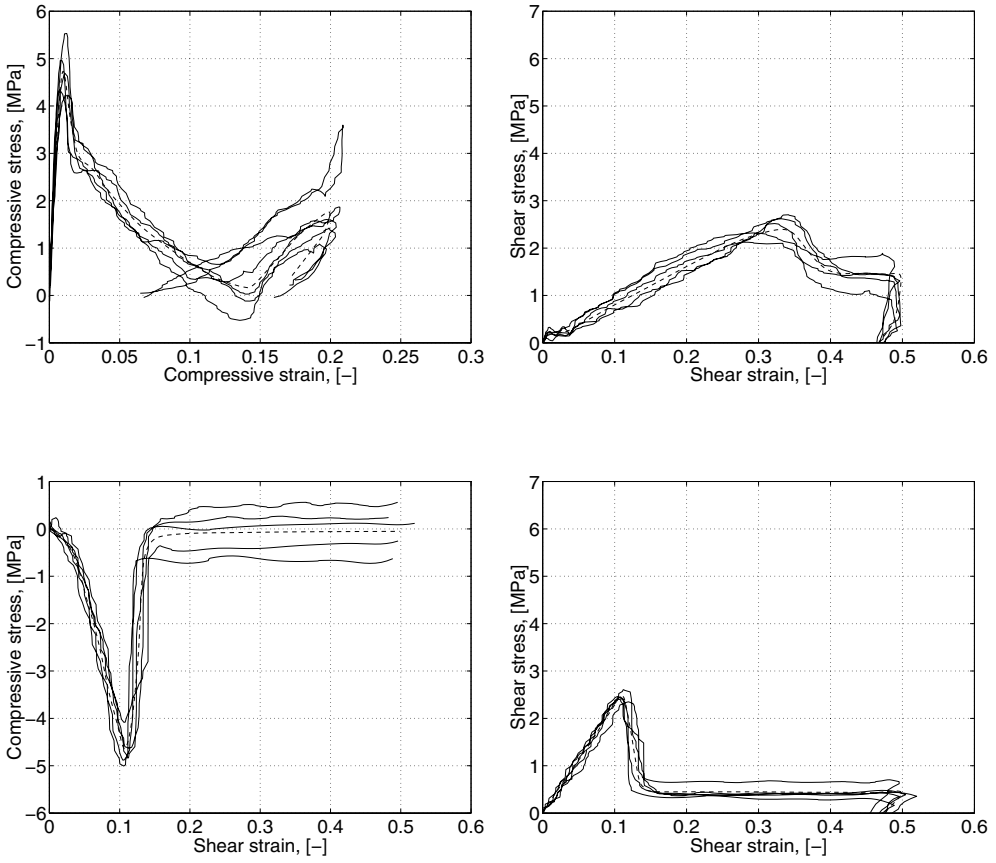
Figure A.3: Stress-strain curves for test series Dd (top) and Ed (lower). The dashed lines are mean-value curves.
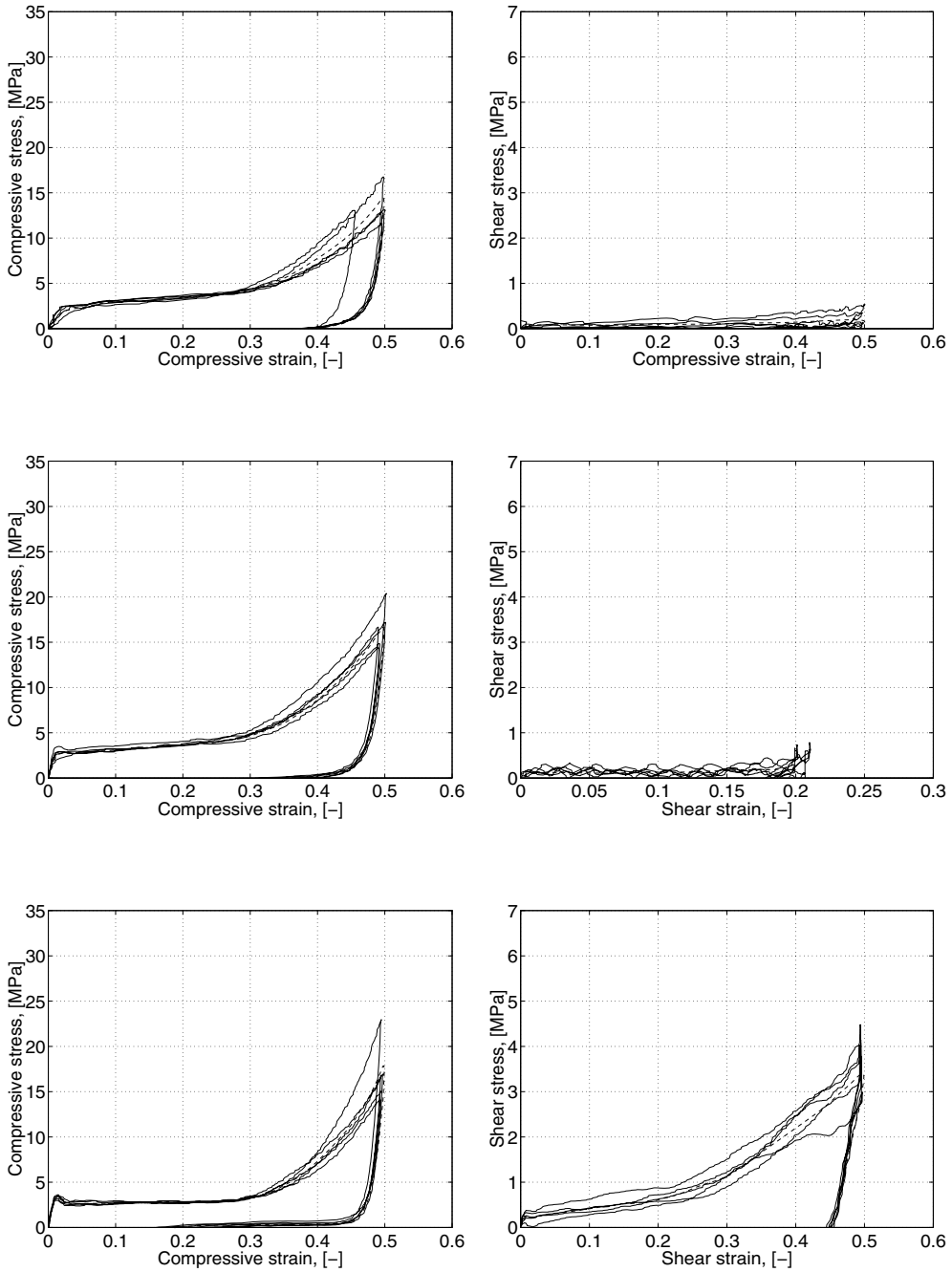
Figure A.4: Stress-strain curves for test series Aw (top), Bw (middle) and Cw (lower). The dashed lines are mean-value curves.
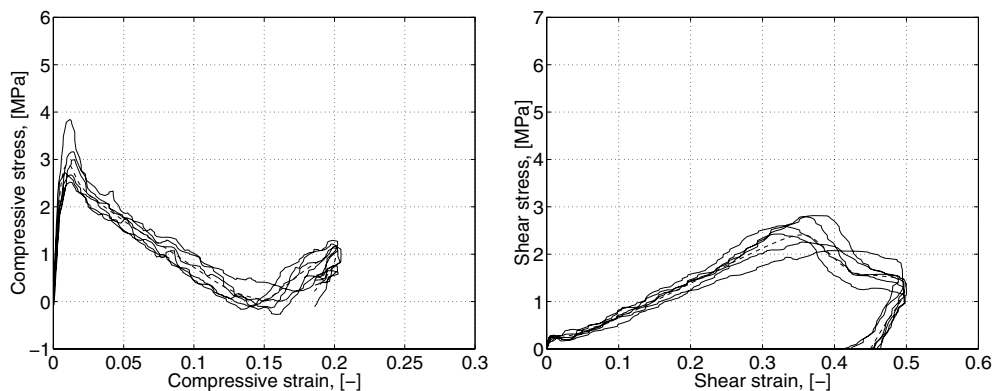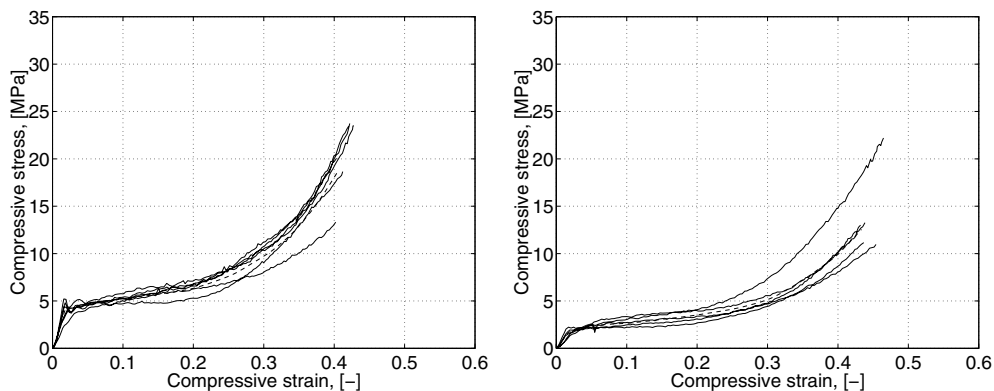
Figure A.5: Stress-strain curves for test series Dw. The dashed lines are mean-value curves.

Figure A.6: Stress-strain curves for test series Fd (left) and Fw (right). The dashed lines are mean-value curves.

A.2   Chip Shearing Tests

In the following, load-displacement curves for the individual tests of the chip shearing test of Section 3.4 are given. In most cases the curves given show filtered response. The filtering was made using the MATLAB signal processing toolbox [51] (Butterworth filtering). Examples of typical recorded load-displacement curves and the corresponding filtered responses are given in Figure A.7. In general, about 250 samplings of forces were made during testing. In a few cases (some of the tests of test series Ad, Bd, Aw and Bw) only about 50 samplings were made. For these tests raw data are presented. Figures A.8-A.9 show the results for test series Ad-Fd, Figures A.10-A.11 for test series Aw-Fw and Figures A.12-A.13 for test series Gd and Gw, respectively. The mean value curves for each test series are also given (dashed curves). The test conditions for the different test series are defined in Table 3.4. For convenience, they are repeated in Table A.2 below.

Table A.2: Test conditions for the different test series. The orientation of the specimen is defined by the angle between the radial direction and the loading direction. The superscripts e, l denote that the upper part of the specimen consists of earlywood and latewood, respectively.

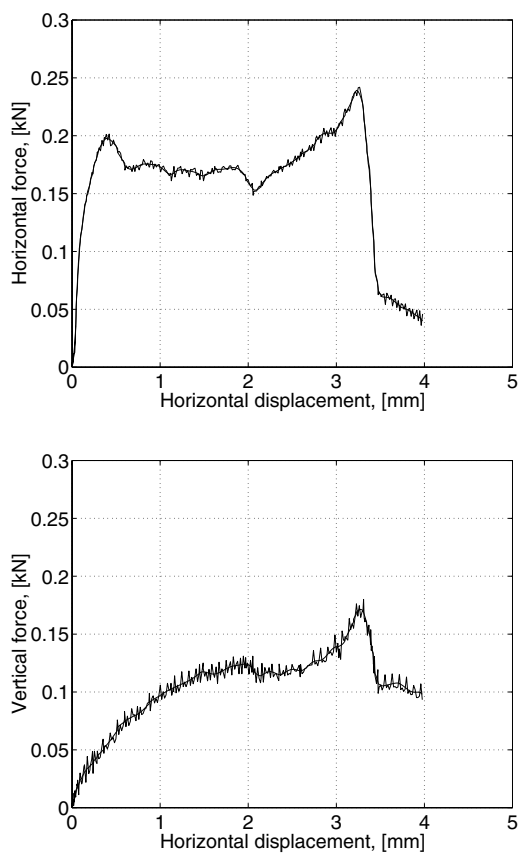| Test series	Specimen height [mm]	Specimen orient. [°]	Moisture content [%]	Angle of loading device surface [°]	Number of tests successful/total
Ad	8.1	0	12	90	8/16
Bd	5.0	0	12	90	8/12
Cd	5.0	45	12	90	4/5
Dd	5.0	90^e	12	90	5/6
Ed	5.0	90^l	12	90	5/6
Fd	5.0	135	12	90	6/6
Aw	8.1	0	28	90	6/9
Bw	5.0	0	28	90	6/6
Cw	5.0	45	28	90	5/5
Dw	5.0	90^e	28	90	6/6
Ew	5.0	90^l	28	90	4/12
Fw	5.0	135	28	90	6/6
Gd	5.0	90^e	12	30	6/6
Gw	5.0	90^e	28	30	6/6

Figure A.7: Typical recorded load-displacement curves and the corresponding filtered curves.
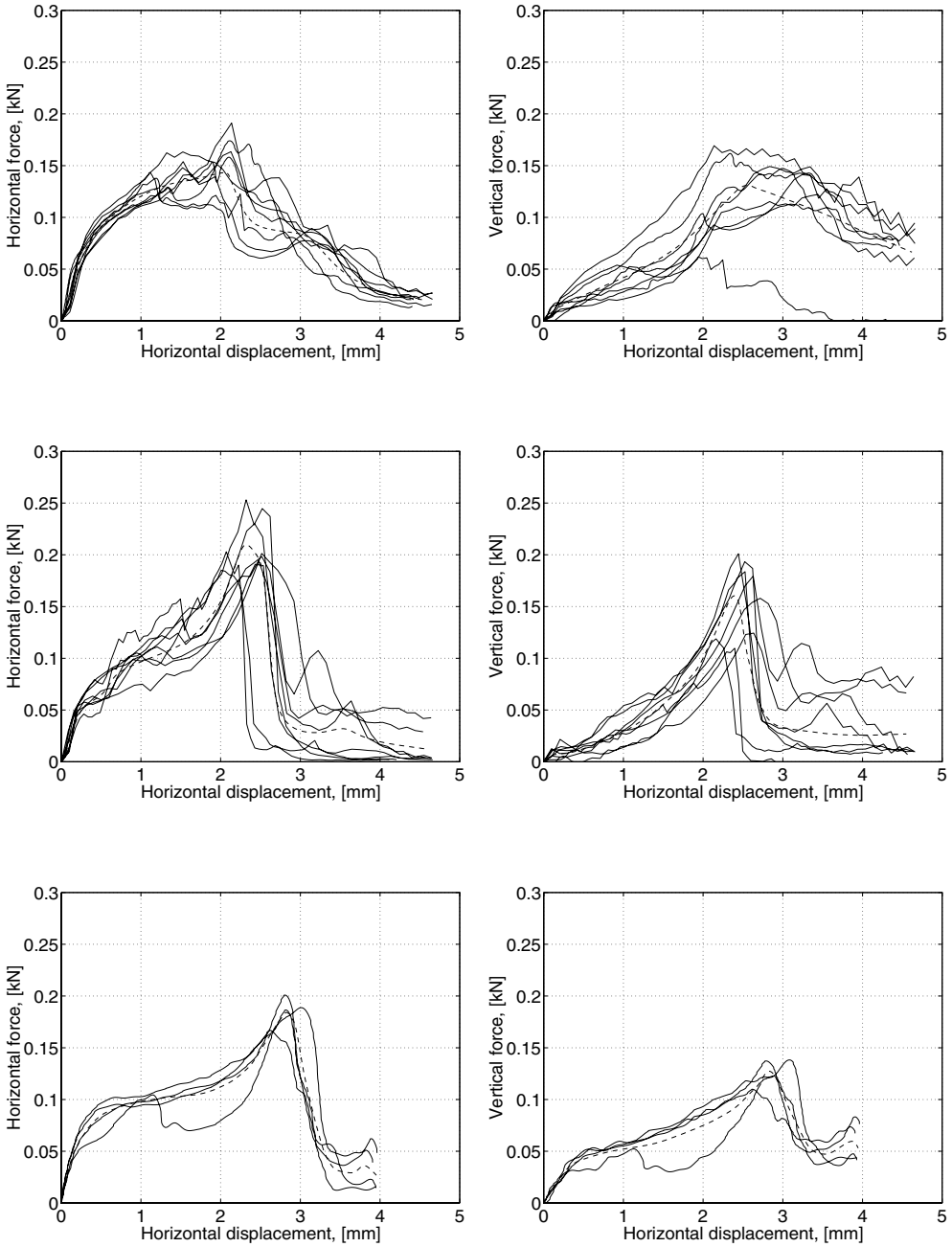
Figure A.8: Load-displacement curves for test series Ad (top), Bd (middle) and Cd (lower). The dashed lines are mean-value curves.
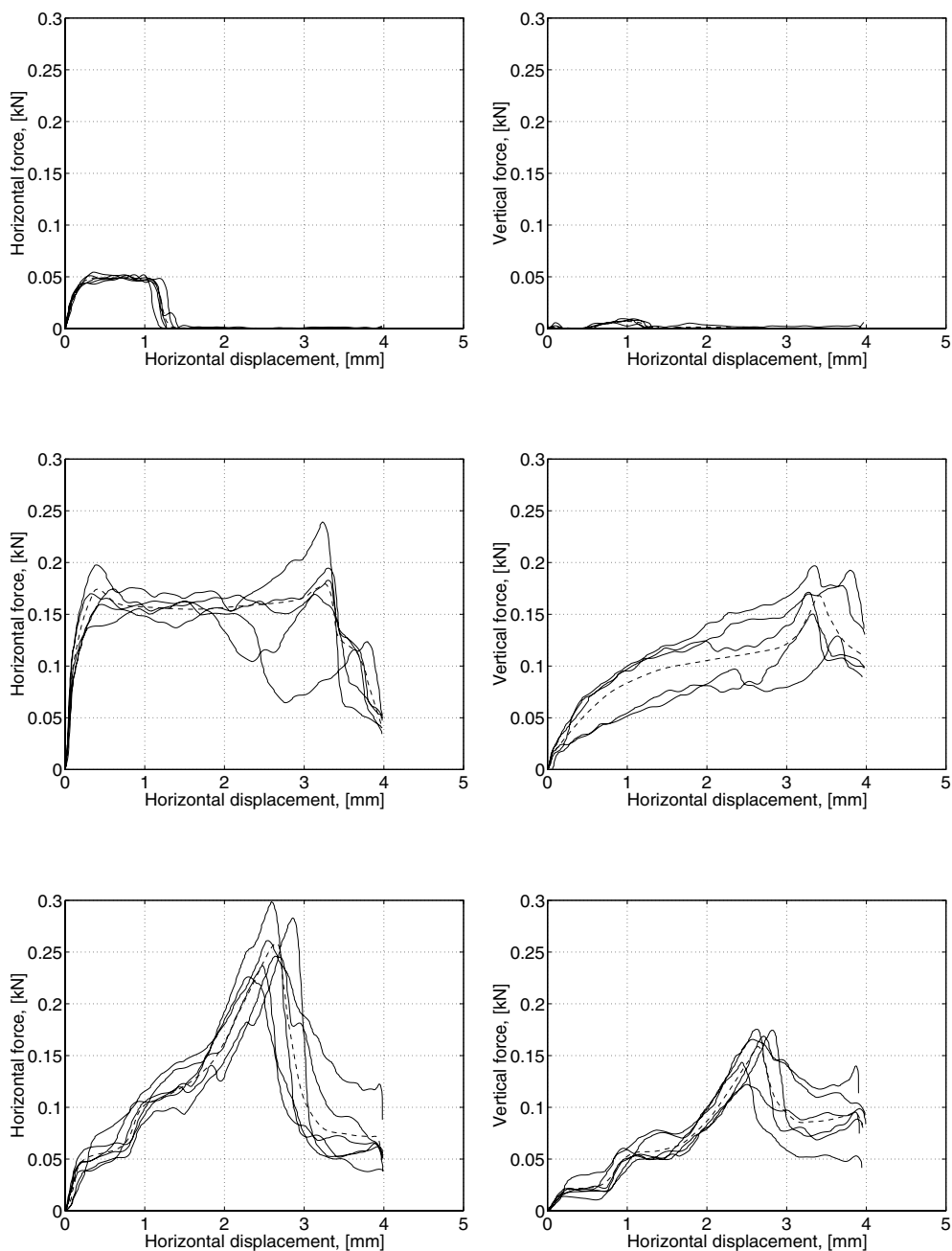
Figure A.9: Load-displacement curves for test series Dd (top), Ed (middle) and Fd (lower). The dashed lines are mean-value curves.
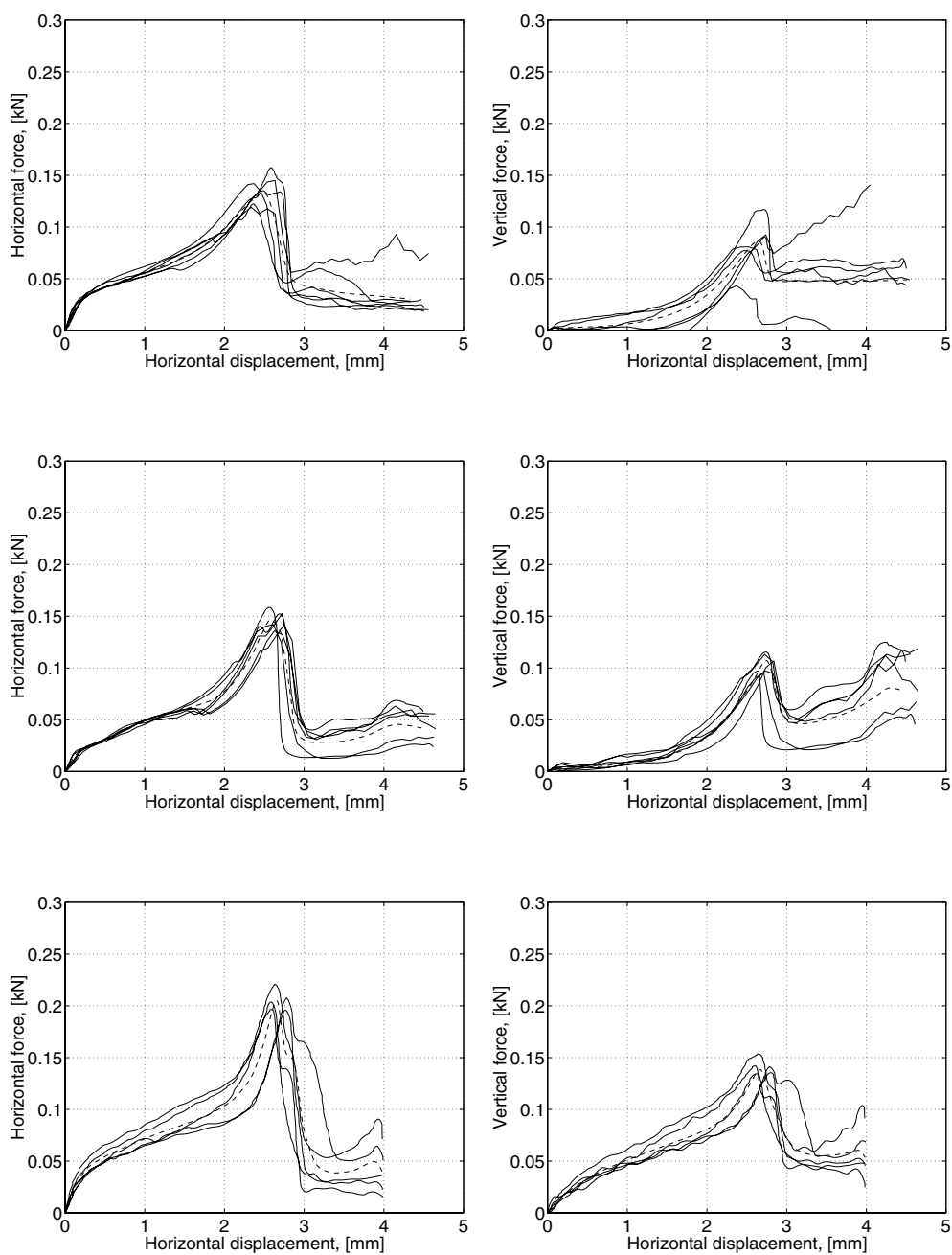
Figure A.10: Load-displacement curves for test series Aw (top), Bw (middle) and Cw (lower). The dashed lines are mean-value curves.
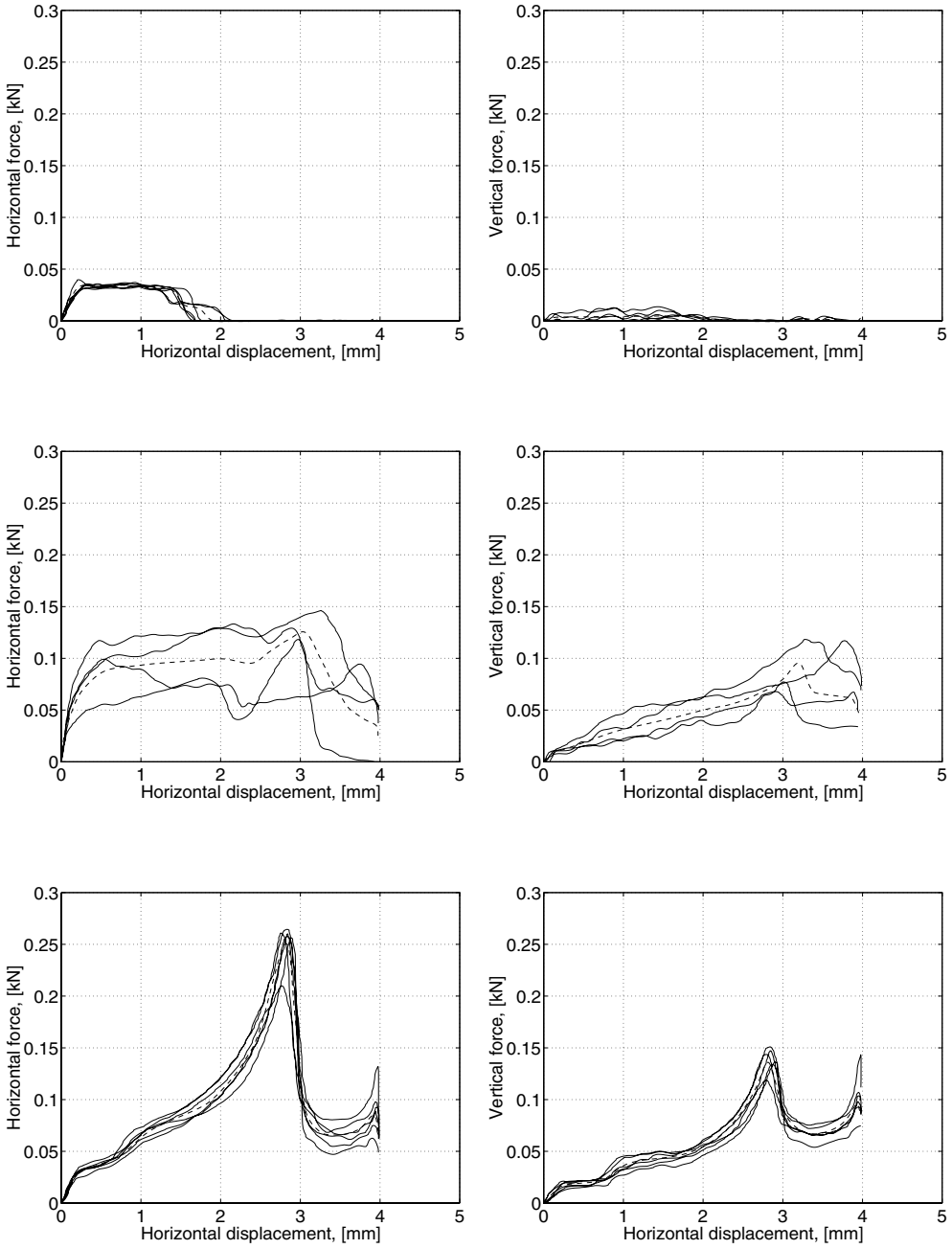
Figure A.11: Load-displacement curves for test series Dw (top), Ew (middle) and Fw (lower). The dashed lines are mean-value curves.
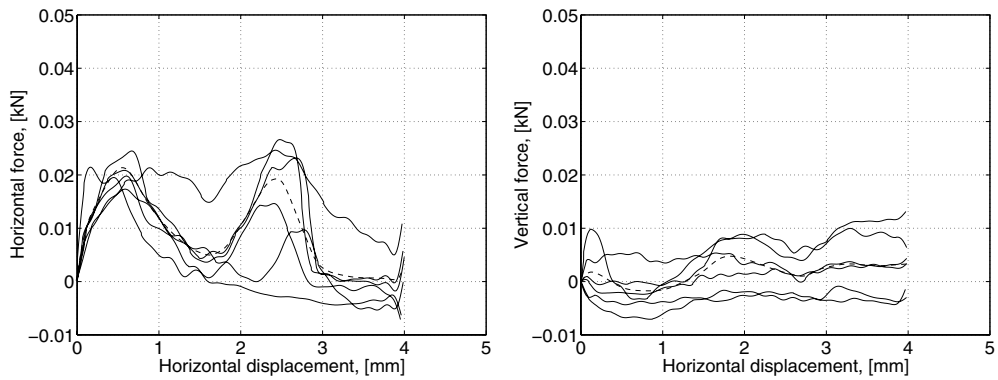
Figure A.12: Load-displacement curves for test series Gd (6 tests). The dashed lines are mean-value curves.
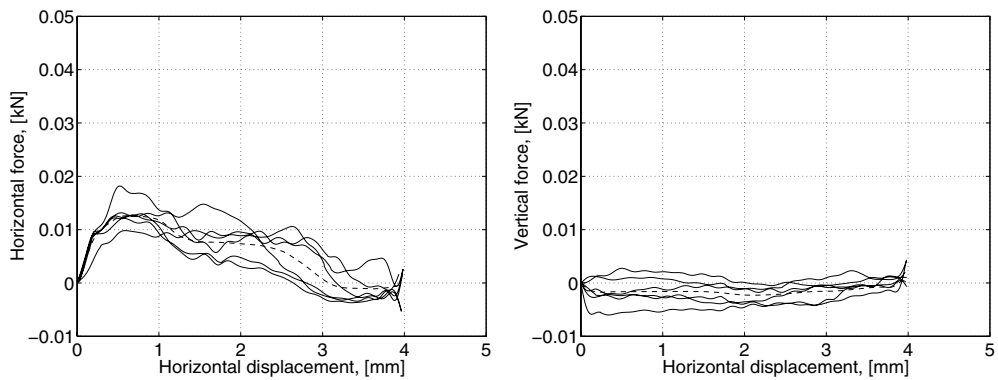

Figure A.13: Load-displacement curves for test series Gw (6 tests). The dashed lines are mean-value curves.